Carbon, oxygen, and nitrogen cycles on the Vancouver Island shelf

by

Laura Bianucci
Lic., University of Buenos Aires, 2004

A Dissertation Submitted in Partial Fulfillment
of the Requirements for the Degree of

DOCTOR OF PHILOSOPHY

in the School of Earth and Ocean Sciences

Supervisory Committee

Carbon, oxygen, and nitrogen cycles on the Vancouver Island shelf

by

Laura Bianucci
Lic., University of Buenos Aires, 2004

Supervisory Committee

Dr. Ken L. Denman (School of Earth and Ocean Sciences)
Supervisor

Dr. Adam H. Monahan (School of Earth and Ocean Sciences)
Co-Supervisor or Departmental Member

Dr. Debby Ianson (School of Earth and Ocean Sciences)
Departmental Member

Dr. Maycira Costa (Department of Geography)
Outside Member

Dr. James R. Christian (School of Earth and Ocean Sciences)
Additional Member

Abstract

Supervisory Committee
Dr. Ken L. Denman (School of Earth and Ocean Sciences)
Supervisor
Dr. Adam H. Monahan (School of Earth and Ocean Sciences)
Co-Supervisor or Departmental Member
Dr. Debby Ianson (School of Earth and Ocean Sciences)
Departmental Member
Dr. Maycira Costa (Department of Geography)
Outside Member
Dr. James R. Christian (School of Earth and Ocean Sciences)
Additional Member

A quasi-two dimensional model for the southern Vancouver Island shelf was developed with the Regional Ocean Modelling System (ROMS) to study coupling of the carbon, oxygen, and nitrogen cycles in a summer wind-driven upwelling region. The physical model is coupled to an ecosystem module that includes a simple representation of a sediment layer and considers non-fixed C:N ratios for detritus and dissolved organic matter (i.e., explicitly modelled pools of carbon and nitrogen for those variables). The model accounts for denitrification within the sediments as well as within the water column when oxygen concentrations are low (below 5 mmol-O_2 m^{-3}). The objective is to identify the dominant processes controlling the cycles, their coupling, and their sensitivity to changes in environmental forcing.

Results demonstrate how low oxygen and low pH events are tightly coupled in the coastal study region, especially through local ecosystem processes. In particular, exchange with the sediments plays a dominant role in consuming oxygen from and releasing inorganic carbon to the bottom waters on the shelf. Two key features distinguish the southern Vancouver Island shelf from other coastal regions in the California Current System and protect inner shelf waters from severe hypoxia and corrosive (i.e., undersaturated in aragonite) conditions. First, the greater width of the shelf reduces the penetration of subsurface offshore high-carbon and low-oxygen waters into shallower waters; and second, the relatively fresh Vancouver Island Coastal Current (VICC) brings oxygen-rich and carbon-poor waters to the bottom layer over the inner shelf. Sensitivity experiments show that carbon and oxygen cycles on the southern

Vancouver Island shelf may be significantly affected by an altered upwelling season, a shallower offshore Oxygen Minimum Zone, a warmer ocean, and a carbon-enriched environment. Combinations of these scenarios suggest a potential increasing risk for the development of coastal hypoxia and corrosive conditions in the future. Further sensitivity simulations indicate that sedimentary denitrification provides an additional coupling between the carbon, oxygen, and nitrogen cycles. Total alkalinity generated by sediment denitrification has the potential to buffer anthropogenic ocean acidification. However, this alkalinity effect over the Vancouver Island shelf in late spring and summer simulations is small compared with studies for other locations at annual scales. Longer time scales need to be examined in this region to confirm whether the role of alkalinity generation in the sediments is significant. In conclusion, this dissertation not only demonstrates the coupled nature of biogeochemical cycles in the coastal ocean, but also the importance of this coupling as we try to estimate how coastal ecosystems will respond to human modifications of shelf waters and the climate.

Table of Contents

List of Tables

List of Figures

Acknowledgments

My long list of acknowledgments must start with my supervisor, Ken Denman, for his guidance, support, and advice through these years, as well as for sharing with me his views of science and life. Ken is a role model, and not only as a scientist. I am also very thankful for the valuable input and availability of the rest of my committee, Debby Ianson, Adam Monahan, Jim Christian, Maycira Costa, and Katrin Meissner. A big 'Thank you!' goes to Mike Berkley for his constant computational support and help. There are many professors and researchers that shared their time, data, and experience with me at different stages of my Ph.D.: Rick Thomson, Mike Foreman, Angélica Peña, Jody Klymak, and Diana Varela. My fellow student Wendy Callendar helped me get started with the wonderful and frustrating world of ROMS. Some of the friends I made during my time in Victoria became my family away from homeland: Antonio, Carlos, Carmen, Caroll, Karla, Jany, Julio, and Valeria. My dear friends Norma and Fabian have cheered my every day for the last two years and their support and motivation has helped me through the final stage of this experience. I am also thankful for my life-long friends Natalia and Claudia who did not let the distance be an obstacle for us. I thank my brother Pablo and sister-in-law Matilde for their words of advice and for sharing their experience with me. A special mention goes to the youngest, most beautiful, new members of the family: my nephew Marco and my goddaughter Ana Sofía. I thank my grandma Lydia who gave me many reasons to remember her lovingly forever. I will never be able to thank my parents enough for all their love, dedication, and good examples. I am just so amazed by the great persons they are. Last but not least, this achievement also belongs to my wonderful husband, Diego, whose love and support mean the world to me.

Dedication

To my parents, Ruth and Hugo, because their encouragement, love, and support were transformed, somehow, in this thesis.

To my beloved husband, Diego, who has always been there for me along the way, helping me keep track of what really is important in life.

1 Introduction

1.1 Biogeochemical cycles in the coastal ocean

The coastal ocean represents only a small fraction (~ 7 %) of the global ocean surface (Gattuso et al. 1998). However, its global significance exceeds this seemingly small size. The shallow regions of the ocean contain diverse and active ecosystems that support 90 % of the world's fish catch (Pauly and Christensen 1995). They maintain higher rates of primary production than the open ocean (Smith and Hollibaugh 1993) while receiving substantial inputs of nutrients and organic matter from land (Gattuso et al. 1998). Therefore, the shallow waters of the ocean are biogeochemically active, accounting for 80 % of the global organic matter burial and 90 % of the sedimentary remineralization (Wollast 1998). Moreover, in 1990 approximately 23 % of the global human population lived within 100 km of the coastal ocean (Small and Nicholls 2003), a percentage that continues to grow. As continental shelves are in direct contact with the open ocean, they act to buffer the effects of human perturbations reaching the open ocean. Hence, biogeochemical alterations in the coastal zone may not only affect the cycling of nutrients in shallow waters, but also influence the extent of anthropogenic change experienced by the open ocean.

In the context of our changing climate, several pressing issues require deeper understanding of nutrient cycling in the coastal zone. Anoxic conditions were observed off the Oregon coast in the summer of 2006 for the first time in the historical record (Chan et al. 2008, Connolly et al. 2010). The same summer experienced the most severe low oxygen event observed on the Washington shelf (Connolly et al. 2010). Surface waters undersaturated in aragonite (the least stable form of calcium carbonate) were observed off California in July 2007 (Feely et al. 2008). Although there is no long record

of aragonite saturation measurements in the region to know how frequently this occurs, it represents a more advanced state of anthropogenic ocean acidification than expected by this time (Orr et al. 2005, Steinacher et al. 2009). Alteration of wind patterns in the coastal region may change the strength and timing of upwelling (Schwing and Mendelssohn 1997, Snyder et al. 2003, Merryfield et al. 2009), therefore affecting the input of nutrients from offshore and overall ecosystem behaviour (Bakun 1990, Bakun and Weeks 2004, Barth et al. 2007). In addition, modification of the deep ocean by a changing climate may alter the conditions of waters upwelled onto the shelves (e.g., the shoaling and strengthening of Oxygen Minimum Zones, Whitney et al. 2007, Stramma et al. 2008). In summary, there is a need to identify and understand the dominant mechanisms in coastal biogeochemical cycling under a changing environment.

The coupling of the different cycles operating in the coastal ocean (e.g., carbon, oxygen, and nitrogen) must be considered. Oxygen is produced by photosynthesis while inorganic carbon and nitrogen are consumed; the opposite occurs during aerobic remineralization of organic matter. Denitrification (anaerobic remineralization of organic matter that uses nitrate instead of oxygen as an electron acceptor) produces inorganic carbon and dinitrogen (N_2) or nitrous oxide (N_2O). Therefore, the local effect of denitrification is to remove fixed nitrogen from the water column, modifying not only the nitrogen cycle, but also the carbon and oxygen cycles through associated changes to primary production and alkalinity fluxes (Fennel et al. 2008, Thomas et al. 2009). These direct and indirect connections between biogeochemical cycles may play a role in the development or maintenance of hypoxia and/or low saturation states on continental margins.

1.2 Study area: Vancouver Island shelf

The southern Vancouver Island shelf is the study area of the present work. This shelf is at the northern end of the wind-driven upwelling regime that characterizes the California Current System (CCS) during summer months. The region experiences summer upwelling and winter downwelling (Freeland and Denman 1982), although upwelling-favourable winds in summer are not as steady or as strong as in the southern CCS (Hickey and Banas 2008). In the surface layer, an alongshore south-eastward current (speeds up to 20 cm s^{-1}) flows during summer near the shelf break in response to the prevailing winds, while an opposing current (10 – 15 cm s^{-1}) flows to the northwest closer to shore (Freeland et al. 1984). The latter is the Vancouver Island Coastal Current (VICC), a buoyancy-driven current that originates in the Juan de Fuca Strait and transports relatively fresh and nutrient-rich waters alongshore to the northwest (Thomson et al. 1989, Hickey et al. 1991). Details on the VICC are given in Chapter 2 (section 2.1). Physical forcing over the Vancouver Island shelf is not limited to local winds. Remote wind forcing in the south generates waves that propagate poleward (Battisti and Hickey 1984, Hickey et al. 1991), and upwelling is enhanced locally by submarine canyons and topographic features (Freeland and Denman 1982, Allen 2000, Waterhouse et al. 2009). Upwelling as well as inputs from the VICC provide nutrients to the shelf and maintain high productivity during summer (Whitney et al. 2005), with phytoplankton blooms dominated by diatoms (Harris 2001, Harris et al. 2009). Zooplankton populations are lower over the shelf (despite high phytoplankton mass in summer) and higher over the slope, due to offshore transport in the surface Ekman layer (Mackas 1992).

1.3 Dissertation objectives and outline

A quasi-two dimensional (quasi-2D) model of the Vancouver Island shelf was developed to examine the coupling of the carbon, oxygen, and nitrogen cycles in a seasonally upwelling margin, because numerical models can facilitate the identification of dominant processes in the ecosystem and the evaluation of their sensitivity to changing conditions.

The specific objectives of this thesis are:

1. To investigate the coupling between low oxygen and high inorganic carbon off Vancouver Island during the summer upwelling season. The magnitudes of different processes will be compared, emphasizing the relative importance of local physical, biological, and sedimentary processes as well as of the external sources of nutrients from the VICC.
2. To contribute towards understanding of the response of the Vancouver Island shelf to climate change, by studying the sensitivity of the carbon and oxygen cycles to different forcings and conditions that may exist under a future climate. The sensitivity experiments will focus on the effects of: i) intensified upwelling-favourable winds, ii) a shoaling of the Oxygen Minimum Zone immediately offshore of the shelf break, iii) higher water temperatures representative of the ocean warming by 2050, and iv) higher dissolved inorganic carbon in the ocean due to exposure to levels of atmospheric carbon dioxide projected by 2050. Conditions expected by 2050 in iii) and iv) are derived from predictions by the Canadian Earth System Model (CanESM) v1.1 (Arora et al. 2009, Christian et al. 2010) assuming the SRES 'A2' emission

scenario (Nakicenovic et al. 2000). Some sensitivity experiments (i to iv) will be combined to evaluate the non-linear response of the system to multiple forcing changes.

3. To study the effect of denitrification within the sediments on the carbon and oxygen cycles over the Vancouver Island shelf and evaluate the role of the "anaerobic pump" described by Thomas et al. (2009). The roles of total alkalinity and dissolved inorganic carbon in determining the oceanic partial pressure of carbon dioxide will be discussed, in addition to the influence of the VICC.

The next chapter (Chapter 2) addresses the first objective, along with a description of the model and its evaluation. The following chapters (Chapters 3 and 4) address objectives 2 and 3, respectively. Chapter 5 addresses the role of dissolved organic matter (DOM) in the carbon and nitrogen cycles, as well as sensitivity to the lability of DOM (i.e., labile, semilabile, refractory). This chapter also considers the export of dissolved and particulate organic matter from the shelf to the open ocean. Chapter 6 includes conclusions and an overview of the main contributions of this thesis, as well as recommendations for future work. Details of the model are presented in the appendices: Appendix A describes the model equations, Appendix B details the modelling of the VICC, Appendix C provides more information on model evaluation, and Appendix D describes the interannual variability in the model.

2 Low oxygen and high inorganic carbon on the Vancouver Island Shelf

2.1 Introduction

In the last decade, research on the role of the coastal ocean in biogeochemical cycles has been growing. There has been an increasing number of studies of different regions (e.g., Ianson and Allen 2002, Bianchi et al. 2005, Fennel et al. 2006) as well as attempts to obtain a global understanding of the role of continental margins (e.g., Smith and Hollibaugh 1993, Gattuso et al. 1998, Chen et al. 2003, Borges et al. 2005, Cai et al. 2006). Although these shallower regions of the ocean represent only ~ 7% of the global ocean surface and less than 0.5% of its total volume, they contribute about 20% of the total oceanic organic matter production and 90% of the total sedimentary remineralization (Gattuso et al. 1998, Wollast 1998). Several studies suggest that despite its comparatively small area, the coastal ocean should be included in the global carbon budget and in global carbon cycle models (Smith and Hollibaugh 1993, Chen et al. 2003, Muller-Karger et al. 2005). Considerable effort has been aimed at quantifying the amount of carbon sequestered by continental margins (Tsunogai et al. 1999, Thomas et al. 2004, Borges et al. 2005, Muller-Karger et al. 2005, Cai et al. 2006, Liu et al. 2010). More recently, the issue of coastal acidification has gained attention after Feely et al. (2008) observed corrosive waters on the shelves of western North America (i.e., undersaturated in aragonite, the mineral form of calcium carbonate in corals and some zooplankton such as pteropods, Fabry et al. 2008, with undersaturation reaching surface waters off the northern California shelf.

The west coast of North America has also drawn increased interest due to recent hypoxic events (e.g., Grantham et al. 2004, Bograd et al. 2008, Chan et al. 2008), including an anoxic event in 2006 on the inner shelf off Oregon (Chan et al. 2008). Similarly, 2006 was an anomalous year on the inner shelf off Washington, with the lowest oxygen concentrations on record since 1950 (Connolly et al. 2010). These authors show that hypoxia is a recurring feature on the Washington shelf, while it is less common off Oregon. Hypoxia causes major stress in ecosystems, with the most affected areas referred to as 'dead zones' because higher organisms are absent. Although a common cause of coastal hypoxia is anthropogenic eutrophication (Diaz and Rosenberg 2008), in upwelling regions advection of oxygen-depleted waters from offshore can be a key mechanism. Connolly et al. (2010) observe that the strength of upwelling-favourable winds was an important factor in generating the low concentrations in summer 2006. Grantham et al. (2004) suggest that hypoxia off Oregon in 2002 was due to an anomalous invasion of nutrient-rich subarctic water into the California Current System. Moreover, oxygen-poor waters at intermediate depths along eastern ocean boundaries (Oxygen Minimum Zones, OMZ) appear to be shoaling and their core oxygen concentrations are decreasing (Whitney et al. 2007, Stramma et al. 2008). These changes will eventually result in a decrease of oxygen concentrations in waters upwelled to the shelves. Chan et al. (2008) and Bograd et al. (2008) list several potential reasons for the observed decline in oxygen concentrations, however they are unable to distinguish between local and remotely forced drivers. Numerical models can help to understand the mechanisms behind the observed hypoxia.

Few studies focus simultaneously on both the carbon and oxygen cycles, although these cycles are tightly connected through biological processes such as primary production and remineralization of organic matter. Hofmann and Schellnhuber (2009) suggest that in the open ocean, ocean acidification resulting from increasing atmospheric CO_2 may contribute to the expansion of hypoxic zones by reducing mineral ballasting, thereby leading to the remineralization of sinking particulate organic carbon at shallower depths. Oschlies et al. (2008) also conclude that anthropogenic CO_2 emissions may extend tropical OMZs if the biotic carbon to nitrogen ratio (C:N) increases under elevated CO_2 conditions as observed in a mesocosm experiment.

Along the eastern margins of the oceans, equatorward winds bring offshore waters from greater depths onto the shelf, waters that have elevated dissolved inorganic carbon (DIC), low pH, and low dissolved oxygen. Furthermore, the high productivity triggered by upwelled nutrients generates a large flux of sinking particulate organic matter, particularly over the shelf (unless the offshore near-surface flow is too strong and material settles to the bottom on the slope). The remineralization of the organic matter below the euphotic zone results in elevated consumption of oxygen and production of DIC, especially over continental shelves where organic matter is confined by bathymetry to a smaller volume of water (Ianson et al. 2003). The increase of DIC leads to the reduction of pH, and the depletion of oxygen can lead to hypoxia. This link between coastal ocean acidification and hypoxia has not been thoroughly examined.

Here I present results of a study of the carbon and oxygen coupling on the Vancouver Island shelf, which represents the northern end of the wind-driven upwelling regime off western North America. This region differs from the southern regions of the California

Current System in geometry (wider shelves) and forcing (summer winds undergo direction reversals, so upwelling favourable winds are not steady; Hickey and Banas, 2008). In addition, the buoyancy-driven Vancouver Island Coastal Current (VICC) flows northward along the coast inshore of the shelf waters affected by upwelling. In summer, the VICC opposes the northwesterly winds and the wind-driven southward-flowing shelf break current (Freeland et al. 1984, Thomson et al. 1989). The main source of the VICC in summer is the relatively fresh outflow from the Juan de Fuca Strait, due mainly to snowmelt carried by the Fraser River (Thomson et al. 1989, Hickey et al. 1991). The Juan de Fuca waters are tidally mixed with deeper ocean waters entering the Strait, becoming nutrient-rich, and thus provide a source of nutrients for the shelf (Crawford and Dewey 1989, Whitney et al. 2005).

Hypoxic events have not been studied extensively on the Vancouver Island shelf, but there exists evidence of their occurrence. Crawford (2008) reports dissolved oxygen concentrations between 0.5 and 1 mL L^{-1} (~ 22 and 44 mmol-O_2 m^{-3}) in shelf waters at depths between 100 and 200 m during some summers of the historical record. Freeland and Denman (1982) suggest that concentrations below 1.5 mL L^{-1} (~ 65 mmol-O_2 m^{-3}) are likely common in the bottom waters near the region of the Juan de Fuca eddy. Furthermore, the observed decline of oxygen in the Northeast Pacific and the expansion of the OMZ may affect biogeochemical cycling in this region (Deutsch et al. 2006, Whitney et al. 2007).

The objective of this chapter is to investigate the coupling between low oxygen and high inorganic carbon (low pH, low saturation states) events on the Vancouver Island shelf with a quasi-2D model. Section 2.2 describes the model and evaluates its

performance. Section 2.3 focuses on the roles of biology and physics in the water column, as well as sediments in regulating oxygen and carbon concentrations (2.3.1) and on the role of the VICC (2.3.2). Discussion and conclusions follow in section 2.4.

2.2 Vancouver Island Shelf model

The model used here is the Regional Ocean Modelling System (ROMS) version 3.2. ROMS is a free-surface, hydrostatic, terrain-following, primitive equation ocean model. Shchepetkin and McWilliams (2005) describe the algorithms of the model's hydrodynamic kernel and Fennel el al. (2006, 2008) and Druon et al. (2009) describe the embedded ecosystem model used as a starting point in this study.

2.2.1 Model configuration

A quasi-2D configuration is used to represent wind-driven upwelling off Vancouver Island: a cross-shelf vs. depth domain (xz-plane) with uniform properties alongshore. Although 3D dynamics are important in coastal upwelling planktonic ecosystems (e.g., Gruber et al. 2006), a 2D model represents locally forced upwelling in a way that allows extensive sensitivity analysis. This 2D approach has been used previously for the Oregon shelf (Allen et al. 1995, Federiuk and Allen 1995, Spitz et al. 2003) and requires a small alongshore dimension (in this case, 5 km and 3 grid nodes; ROMS needs to be able to define alongshore gradients) and periodic open boundary conditions to maintain uniformity alongshore. In ROMS, the latter precludes applying an alongshore pressure gradient to drive a dynamic VICC. Table 2.1 contains details of the model configuration. The topography corresponds to the southern Vancouver Island shelf (~ 49ºN, Figure 2.1), along a transect that has been occupied frequently by research cruises of the Institute of

Ocean Sciences (IOS) and is known as part of the La Perouse programme 'Line D'. This region was chosen because it: a) is to the north of the Juan de Fuca eddy (a 3D feature that cannot be included in a quasi-2D model), b) experiences wind-driven summer upwelling, and c) provides existing in situ data for model evaluation. The shelf and shelf break bathymetry are approximated with an analytical function, with a minimum depth of 40 m and an offshore maximum depth of 1500 m (Figure 2.2). A modified version of Orlanski's radiation open boundary condition is applied at the offshore boundary for both 3D momentum and tracers (Raymond and Kuo 1984).

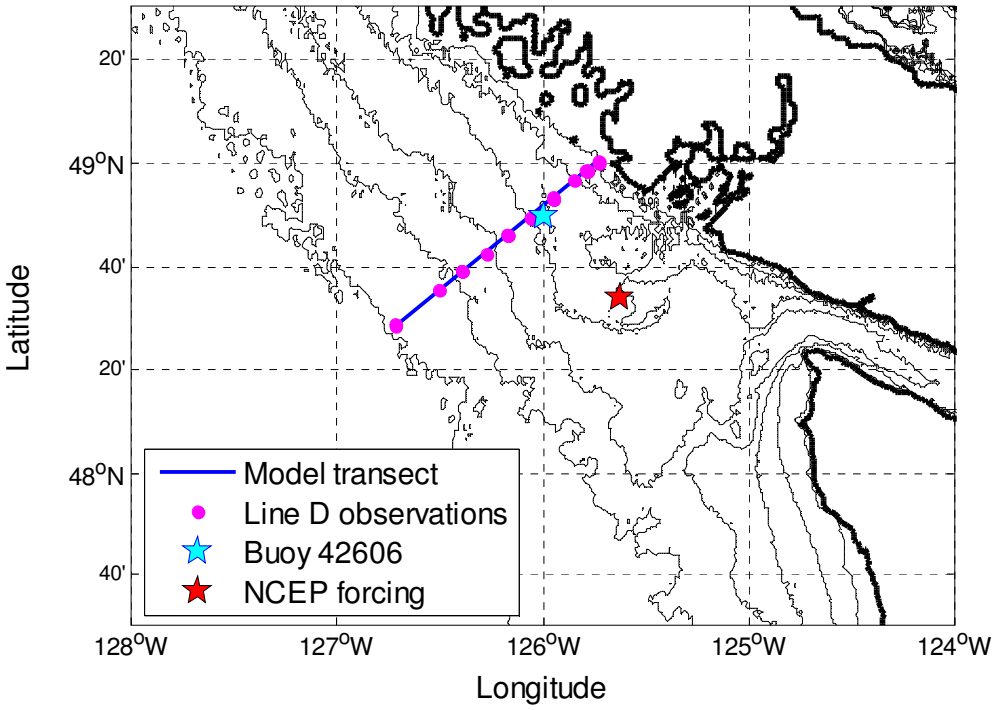

Figure 2.1: Location of model domain (blue line), Line D stations (magenta circles), and meteorological buoy 46202 (cyan star). NCEP data used to force surface net heat and shortwave fluxes are representative of a region 1.9° x 2.4° centred on the red star. Background bathymetry comes from a high resolution model for the region (Foreman et al. 2008) and shows the 25, 50, 100, 200, 1000, and 2000 m isobaths.

Table 2.1: Details of model configuration

Cross shore dimension (x)	185 km (100 km correspond to deep ocean) Number of grid nodes = 194 dx = 953 m
Alongshore dimension (y)	5 km Number of grid nodes = 3 dy = 1.67 km
Vertical dimension (z)	From 40 m at closed boundary to 1500 m in deep ocean Number of levels = 30 dz = from 1.33 m to 72.82 m

Initial conditions are horizontally uniform for all tracers and zero for velocities. Variables are initialized as the average of all available summer deep ocean profiles. Where profiles are not available, small constant values are used (phytoplankton, zooplankton, ammonium, and detritus). Sensitivity analyses were carried out for some of these constant initial conditions (e.g., NH_4 from 0.01 to 0.1 mmol-N m^{-3}), and results are independent of initial conditions after the spinup period. The sinking speed of detritus (w_D, Table 2.2) was set after sensitivity analysis performed with a 1D version of the model. The model is forced by hourly wind stress calculated from observed winds at meteorological buoy 46206 (Figure 2.1) from May 27 to September 29 1993 (the wind stress calculation follows Smith, 1988). The wind stress is filtered with a 6 hour low-pass Fast Fourier Transform (FFT) filter. Surface shortwave and net heat fluxes are daily values derived from NCEP reanalysis (Kalnay et al. 1996) at 48.57ºN, 125.62ºW for the same period (Figure 2.1). Tidal mixing is modelled implicitly by including additional eddy viscosity and diffusivity in the bottom 15 m of the water column; the eddy terms are

proportional to a turbulent dissipation rate ε (10^{-8} to 10^{-7} m^2 s^{-3}, Crawford and Dewey 1989) and inversely proportional to the local buoyancy frequency (N^2), after Osborn (1980). The Fraser River and Juan de Fuca Strait, the source of the VICC, remain outside the model domain. Therefore, the shallowest 6 km of the model domain are restored to VICC values. The restoring values of water properties and velocities are vertical profiles derived from available observations of the VICC (Appendix B).

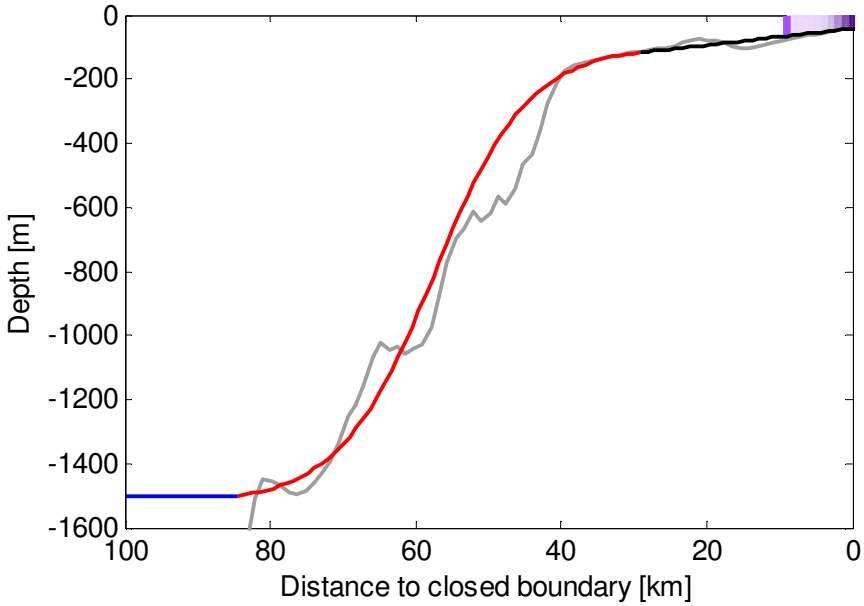

Figure 2.2: Model bathymetry represented by a combination of a linear function for the shelf (black line), hyperbolic tangent for the slope and shelf break (red line), and constant for the deep ocean (blue line) that extends for 100 km (full extension not shown here). Grey profile shows Line D bathymetry from the high resolution model (Figure 2.1). Shaded region shows the area where selected properties are restored to represent the VICC in the model. Restoring is strongest in the shallowest region (darkest color) and vanishes towards the vertical purple line (more details in Appendix B).

2.2.2 Biological model

The present study uses a modified version of the nitrogen-based model described in Fennel et al. (2006), along with an inorganic carbon component (Fennel et al. 2008). The

main additions to the version of the ROMS model downloaded from www.myroms.org are a representation of dissolved organic matter (DOM) cycling (replacing small detritus and hence eliminating their aggregation with phytoplankton to the large detritus compartment), and a sediment layer that accumulates particulate organic matter reaching the seafloor and oxidizes it with a remineralization rate. These changes aim to improve the representation of productive, coastal ecosystems. The eleven state variables are thus: phytoplankton (P), zooplankton (Z), nitrogen and carbon detritus (D_N and D_C), semilabile dissolved organic nitrogen and carbon (DON and DOC), nitrate (NO_3), ammonium (NH_4)[1], dissolved inorganic carbon (DIC), total alkalinity (TA), and oxygen (O_2). P and Z each represent a single functional group, mainly diatoms and mesozooplankton as these species dominate during the upwelling season (Mackas et al. 2004, Harris et al. 2009). Semilabile DOM represents the fraction of total DOM that decays on seasonal to annual timescales, compared to the labile (consumed within minutes to days) and refractory (biologically inert on the timescales considered) fractions of DOM (Carlson 2002). Moreover, semilabile DOM can be advected and mixed, but unlike particulate organic matter it does not sink. DOM modelling is described in Chapter 5 and is based on Christian and Anderson (2002) and Druon et al. (2009). All ecosystem processes (schematically shown in Figure 2.3) are described in Appendix A, along with the model equations for the time rate of change of ecosystem variables (parameter values are given in Table 2.2). Description of the processes that differ from those in Fennel el al. (2006, 2008) and Druon et al. (2009) follow in this section.

[1] Note that both nitrate and ammonium are charged ions (NO_3^- and NH_4^+), but for simplicity I will use the notation NO_3 and NH_4

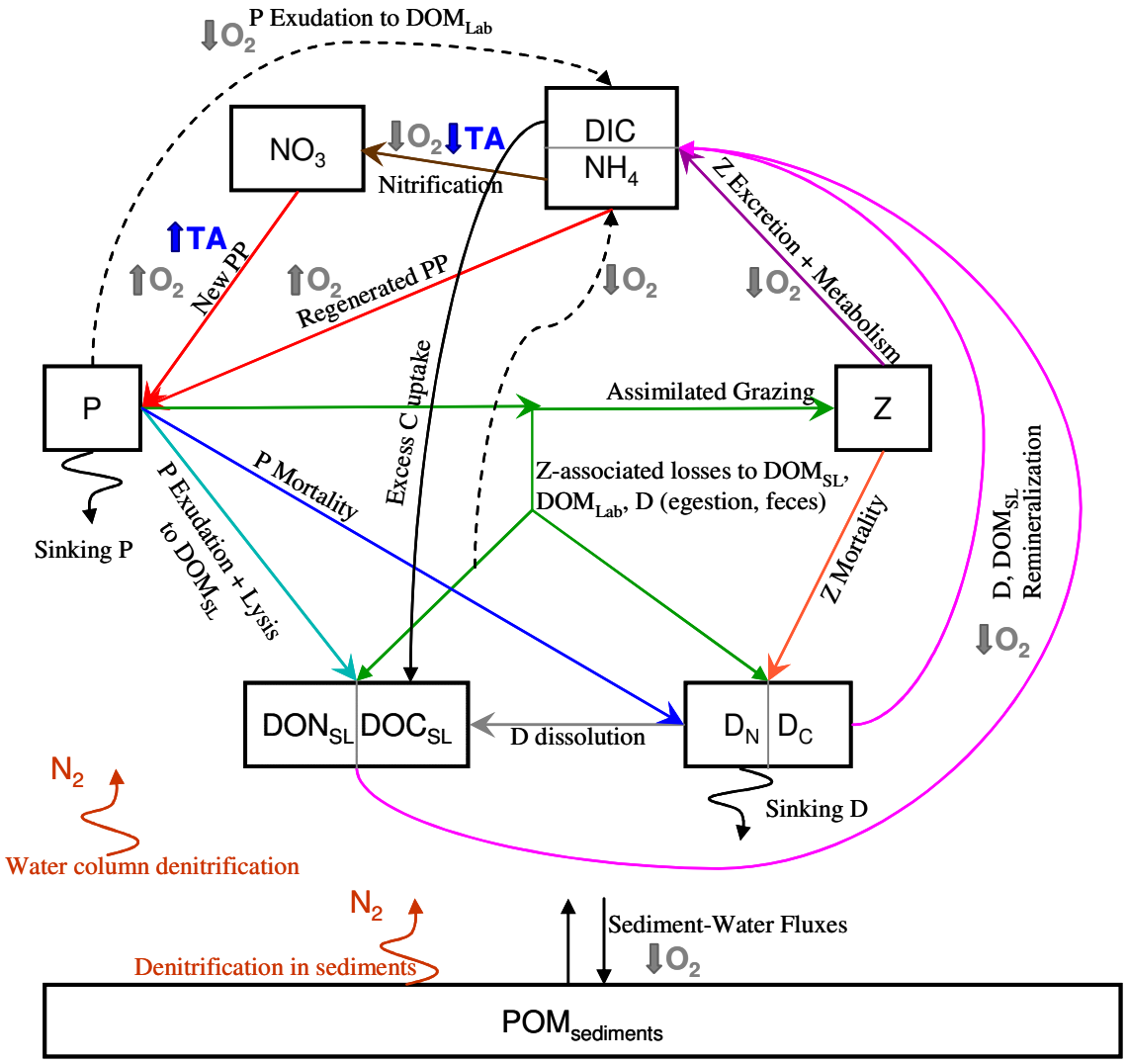

Figure 2.3: Biological model diagram. The state variables are phytoplankton (P), zooplankton (Z), nitrogen and carbon detritus (D_N and D_C), semilabile dissolved organic nitrogen and carbon (DON_{SL} and DOC_{SL}), nitrate (NO_3), ammonium (NH_4), dissolved inorganic carbon (DIC), and oxygen (O_2). Labile DOM (DOM_{Lab}) is implicitly modelled by assuming that it is instantaneously remineralized to DIC and NH_4 (dashed lines). DOM modelling is described in Chapter 5. Processes that produce (consume) O_2 are shown with up (down) bold grey arrows; processes that produce (consume) alkalinity (TA) are shown with up (down) bold blue arrows (details on TA modelling are given in Chapter 4). Grazing of P is partly assimilated by Z, partly lost as DOM_{SL} and DOM_{Lab}, and partly excreted as fecal pellets to D_N and D_C (green arrows). New primary production (New PP) also consumes DIC (arrow not shown).

Table 2.2: Biological model parameters and their values. Subscripts 'SL' and 'Lab' indicate 'semilabile' and 'labile', respectively. Details on the restoration time scale (τ) as a function of distance from the inshore boundary (x) are given in Appendix B. Superscripts next to the parameter values indicate whether they were (a) tuned with the quasi-2D model, (b) taken from Fennel et al. (2006), (c) taken from Druon et al. (2009) and references therein, (d) after Fasham (1995), or (e) taken from the standard ROMS distribution. If no exponent is shown, the parameter was tuned with a 1D version of the model.

Symbol	Parameter	Value	Units
v_0	Phytoplankton growth rate at 0ºC	1	d^{-1}
K_{NO_3}	Half saturation concentration for uptake of NO_3	$0.5^{b,e}$	mmol-N m^{-3}
K_{NH_4}	Half saturation concentration for uptake of NH_4	$0.5^{b,e}$	mmol-N m^{-3}
α	Initial slope of the photosynthesis-irradiance curve	0.025^{e}	d^{-1} (W m^{-2})$^{-1}$
g_{max}	Maximum grazing rate	0.55	d^{-1}
K_p^2	Half saturation concentration for P grazing	$2^{b,e}$	(mmol-N m^{-3})^2
m_p	Phytoplankton mortality rate	0.05	d^{-1}
β	Zooplankton assimilation efficiency	0.7	–
l_{BM}	Zooplankton basal metabolism	0.1	d^{-1}
l_E	Zooplankton specific excretion rate to NH_4	0.1	d^{-1}
m_Z	Zooplankton mortality rate	0.025	d^{-1}
r_{D_N}	Remineralization rate of nitrogen detritus	0.08^{a}	d^{-1}
r_{D_C}	Remineralization rate of carbon detritus	0.07^{a}	d^{-1}
r_{DON}	Remineralization rate of DON_{SL}	0.006^{a}	d^{-1}
r_{DOC}	Remineralization rate of DOC_{SL}	0.005^{a}	d^{-1}
n_{Nitmax}	Maximum nitrification rate	$0.05^{b,e}$	d^{-1}
K_{ox}	Half saturation concentration for O_2 dependence	2	mmol-O_2 m^{-3}

n_z, n_O	sharpness parameters for n_{Nit} and f_{ox} (eqs. 2.1, 2.2)	5, 10	–
I_0	Nitrification half light intensity level	0.5	W m^{-2}
w_P	Sinking velocity of phytoplankton	0.1	m d^{-1}
w_D	Sinking velocity of detritus	5	m d^{-1}
ε_N,ε_C	Phytoplankton exudation rate to DON_{SL}, DOC_{SL}	0.05[c]	d^{-1}
ω_N,ω_C	Phytoplankton exudation rate to DON_{Lab}, DOC_{Lab}	0.03[c]	d^{-1}
s_N	Nitrogen detritus dissolution rate to DON_{SL}	0.03[a]	d^{-1}
s_C	Carbon detritus dissolution rate to DOC_{SL}	0.01[a]	d^{-1}
k_{SW}	Diffuse light attenuation due to seawater	0.04[d,e]	m^{-1}
k_{Chl}	Diffuse light attenuation due to phytoplankton	0.06[d,e]	(mmol-N m^{-2})$^{-1}$
τ ($x = 0$)	VICC restoration time scale at inshore boundary	0.1[a]	d
r_{sed_N},r_{sed_C}	Sediment remineralization rate (nitrogen, carbon)	0.035	d^{-1}

Although earlier versions of ROMS (2.2 onwards) include O_2 cycling in the biological model, to my knowledge O_2 results have not previously been published. In the original model, O_2 is linked to the nitrogen cycle by a stoichiometric ratio of O_2:N=106:16, except for new primary production, where the model uses 138:16 (Redfield et al. 1963). The current biological model includes an excess DIC uptake when light is abundant but nitrogen nutrients (NH_4 and NO_3) are limiting, such that there is DIC consumption and O_2 production not associated with NH_4 or NO_3 drawdown. Therefore, it is more convenient to connect O_2 to the carbon cycle rather than to nitrogen. Considering that growth processes are not just the formation of carbohydrates and are not fully described by Redfield stoichiometry (Laws 1991), it is appropriate to use photosynthetic quotients (PQ) to link O_2 to carbon. These are defined as the number of moles of O_2 produced per

mole of carbon dioxide (CO_2) assimilated and have two values: PQn for new production (NO_3 based) and PQa for recycled production (NH_4 based). The values used here are PQn=1.4 and PQa=1.1 (Laws 1991), which are slightly larger than the corresponding O_2:C Redfield ratios (138:106 = 1.3 and 106:106 = 1, respectively). For the oxidation of organic matter, the respiratory quotient (RQ: moles of CO_2 produced per mole of O_2 consumed) can vary from 0.5 to 1.33, according to the type of substrate being respired (Ikeda and Hernandez-Leon 2005). Williams and del Giorgio (2005) suggest that for the more common biochemical compounds RQ falls in the range 0.67 – 1.24, and that it is usually assumed to be between 0.8 and 1.2. Here, I use $RQ = PQa^{-1} = 0.91$ to to conserve O_2 and carbon mass.

Nitrification, a process that transforms NH_4 into NO_3, consumes O_2 and is inhibited by light (Ward 2000). The original parameterization in the model produces a gradual increase in the nitrification rate with depth. Some authors have suggested that nitrification does not occur if photosynthetically available radiation (PAR) is too high, but it increases quickly as soon as PAR drops below levels that inhibit nitrifying bacteria (Denman 2003, and references therein). A formulation with a sharper transition between lit and unlit waters is implemented following Denman (2003):

$$n_{Nit} = n_{Nitmax} \cdot f_{ox} \cdot \frac{z^{n_z}}{z_{ox}^{n_z} + z^{n_z}} \qquad 2.1$$

In this equation n_{Nit} is the nitrification rate as a function of depth (z), n_{Nitmax} is the maximum rate, z_{ox} is the depth above which incoming light I_0 reduces nitrification to half its highest value (in dark conditions), and the exponent n_z determines the sharpness of the vertical gradient in n_{Nit}. Values for n_{Nitmax}, I_0, and n_z are shown in Table 2.1.

Furthermore, as low O_2 events are a main focus of this study, the model accounts for the O_2-dependence of the nitrification rate by multiplying n_{Nitmax} by a function

$$f_{ox} = \frac{{O_2}^{n_O}}{K_{ox}^{n_O} + {O_2}^{n_O}} \qquad 2.2$$

where K_{ox} is the half saturation constant and n_O is the exponent. The values of K_{ox} and n_O (2 mmol-O_2 m^{-3} and 5, respectively) are such that nitrification decreases rapidly for $O_2 < 5$ mmol-O_2 m^{-3}, following the Nevison et al. (2003) value of 4 ± 3 mmol-O_2 m^{-3}. Although concentrations are not generally below 5 mmol-O_2 m^{-3} in the experiments described in this chapter, they become as low as 1 mmol-O_2 m^{-3} over the continental slope in the sensitivity experiments of Chapter 3.

The current model also includes denitrification in the water column, i.e. the utilization of NO_3 as an electron acceptor (instead of O_2) when ambient O_2 concentrations are low (Sarmiento and Gruber 2006). The threshold O_2 concentration at which denitrification occurs in the ocean varies between 2 and 10 mmol-O_2 m^{-3} (e.g., Codispoti et al. 2005, Moore and Doney 2007, Stramma et al. 2008). It can also vary for different environments (Devol 1978). Despite the difficulty in setting an unequivocal threshold, the upper limit of O_2 concentration is probably near 5 mmol-O_2 m^{-3}, with most denitrification occurring below 2 mmol-O_2 m^{-3} (Devol 2008). Once O_2 drops below the threshold, denitrification rapidly replaces aerobic remineralization (Devol 2008). The model simulates the change from O_2-based to NO_3-based respiration in the water column once $O_2 < 5$ mmol-O_2 m^{-3} (same threshold as in nitrification) by scaling O_2 consumption due to remineralization by f_{ox} (equation 2.2) and NO_3 consumption by $1 - f_{ox}$, while assuming that the rate of oxidation of organic matter does not change. The assumption can be made because both denitrification and aerobic remineralization have similar

energy yield[2] (Sarmiento and Gruber 2006). Moreover, this assumption implies that while O_2 consumption decreases at low O_2 ambient concentrations, DIC is still produced at the same rate. The latter represents a decoupling between carbon and O_2 in low O_2 regions that leads to the potential for extra carbon enrichment even after O_2 has been depleted. Denitrification in the sediments will be described in section 2.2.3.

2.2.3 Sediment model

The sediment component described in Fennel et al. (2006) assumes instantaneous remineralization of particles reaching the bottom. This 'reflective boundary' conserves mass and is computationally efficient (Soetaert et al. 2000). However, in their evaluation of different benthic-pelagic coupling formulations, Soetaert et al. (2000) suggest that a vertically integrated dynamic sediment model provides the best balance between computational cost and system representation. In this formulation, particulate organic matter reaching the seafloor is accumulated in a sediment layer and transformed by remineralization, denitrification, and nitrification within that layer. This more complex representation is chosen because: a) it allows a time lag between deposition of organic matter and return of dissolved inorganic constituents to the water column; b) it is computationally efficient and simple enough to be implemented and run in the quasi-2D model. Nitrogen release from the sediments is based on the relationship between denitrification and sediment O_2 consumption of Seitzinger and Giblin (1996), after Fennel et al. (2006). The use of such a relationship to model denitrification in sediments is recommended for oxic environments (Fennel et al. 2009), which is usually the case on

[2] Free energy changes (in kJ mol^{-1} of CH_2O) for reduction of: O_2 =-476, NO_3=-452, MnO_2=-388, $Fe(OH)_3$=-187, SO_4^{2-}=-82, CO_2=-71. Table 6.1.2 from Sarmiento and Gruber (2006) , reprinted from Morel and Hering (1993)

the Vancouver Island shelf (Crawford 2008). The relationship assumes that NO_3 for denitrification originates from the nitrification of NH_4 (known as coupled nitrification/denitrification), thus underestimating total sediment denitrification when NO_3 is also taken up from overlying water (direct denitrification). On the Washington shelf, just south of the study region, coupled nitrification/denitrification represents about 60% of total denitrification (Devol 1991). Therefore, the Seitzinger and Giblin's linear regression may underestimate the removal of fixed nitrogen if the Vancouver Island shelf is similar to the Washington shelf. Carbon exchange between the water column and the sediments is modelled explicitly (i.e., not linked to nitrogen by Redfield ratios), while O_2 fluxes are tied to carbon fluxes through the PQa (or its reciprocal, RQ). The use of PQa (i.e., 1.1 instead of O_2:C = 106:106 = 1) leads to a small difference in the fraction of carbon oxidation that occurs through denitrification, compared with the results of Fennel et al. (2006) (14 % vs. 15 %, see Appendix A).

2.2.4 Model Evaluation

Several approaches can be used to evaluate the performance of the model. First, modelled vertical profiles are compared with nine Line D stations from 1986 and 2008 (Figure 2.4). For each comparison, the model is forced with observed hourly wind stress and surface heat fluxes, and the model profile is shown for the same day as the observations. In general, the model is able to reproduce the vertical structure of the in situ data. The model is not expected to reproduce these data perfectly, since circulation on the Vancouver Island shelf is not only forced by local wind stress (as in the model), but also by remote wind forcing further south that generates coastal trapped planetary waves and larger scale upwelling (Hickey et al. 1991). In 1986 and 2008, the model

overestimates near surface salinity and NO_3 concentrations over the shallow shelf where the VICC is being restored (Figure 2.4a). The restoring profiles (Figure B.1 in Appendix B) are strongly nudged at the shallow boundary of the model and represent an average of summer observations between 2002 and 2006 at the shallowest stations of Line C (a transect to the south of line D, see Figure B.1f in Appendix B). Thus, the modelled VICC is missing the interannual variability present in Line D in situ data. Nonetheless, the model does represent a climatological VICC: the first column in Figure 2.4a shows Line D data for the shallowest stations (D1 and D2) from eight summer transects (1986, 1988, 2004, 2006, 2008) as small grey crosses. Clearly, the model falls within the observed ranges.

Frequency distributions of modelled summer O_2 and temperature are also compared with observations (nine Line D summer transects from 1981 to 2008) to evaluate whether the statistical properties of the observations over time are represented in the model. Histograms in Figure 2.5 show modelled and observed distributions of O_2 and temperature. These model variables show a similar range of values as the observations in both the upper layers (surface to 30 m depth) and the lower layers (30 m depth to seafloor) of the shelf. Furthermore, the shapes of the frequency distributions are similar. In the upper layers, model data and Line D observations show one clear maximum (although the model is biased towards higher temperatures). Below 30 m depth, O_2 shows a broader range and both modelled and observed distributions are basically flat. The histogram for deep temperatures in the model has a short tail at low temperatures, mainly because the deep waters of the model do not fall below 4ºC (initial conditions are

such that between 300 and 1000 m temperature decreases smoothly from ~ 6 to 4.5ºC). Histograms for the remaining model variables are in Appendix C.

Finally, sea surface temperature (SST) in the model can be evaluated against observed SST from the same buoy that recorded the winds used to force the model (Figure 2.6). The quasi-2D model roughly captures surface dynamics during some time periods (e.g., in 1993 from May 27 to August 7; in 2004 up to August 25). At other times, remote forcing may generate a significant component of the flow. In 2008 the model follows the same evolution as the buoy up to ~ July 25, but there is an offset because the observed SST in late spring was lower than initial conditions in the model (which are an average of SST from available deep ocean stations).

There are difficulties in making direct quantitative comparisons between observations and model output. On one hand, observations here are taken at discrete sites during the course of a cruise (usually taking between 1 and 2 days per transect). Available observations from summer cruises on the Vancouver Island shelf come from several different years; transects are sampled usually just once per summer (twice at most). Moreover, measurements from bottle casts are spaced vertically and avoid the last several meters (sometimes tens of meters) above the seafloor to protect the instruments and the benthic environment. On the other hand, the model outputs 6-hourly data between mid July and the end of September (model days 50 to 125) over the whole shelf and slope (i.e., thousands of data points, not all independent). Observations do not sample the ocean as continuously as the model, neither in a spatial or temporal sense. For this reason, observations tend to show more isolated peaks in the tails of the distribution than model output. The model is sampled frequently, such that all events are present,

representing the shelf and slope proportionally to their areas, while the observations may represent shelf properties disproportionally. Furthermore, due to the huge discrepancy in the number of samples, it is difficult to compare distributions. One approach might be to estimate goodness of fit parameters where the model output is considered to be the parent distribution and the observations to be one estimate of that distribution.

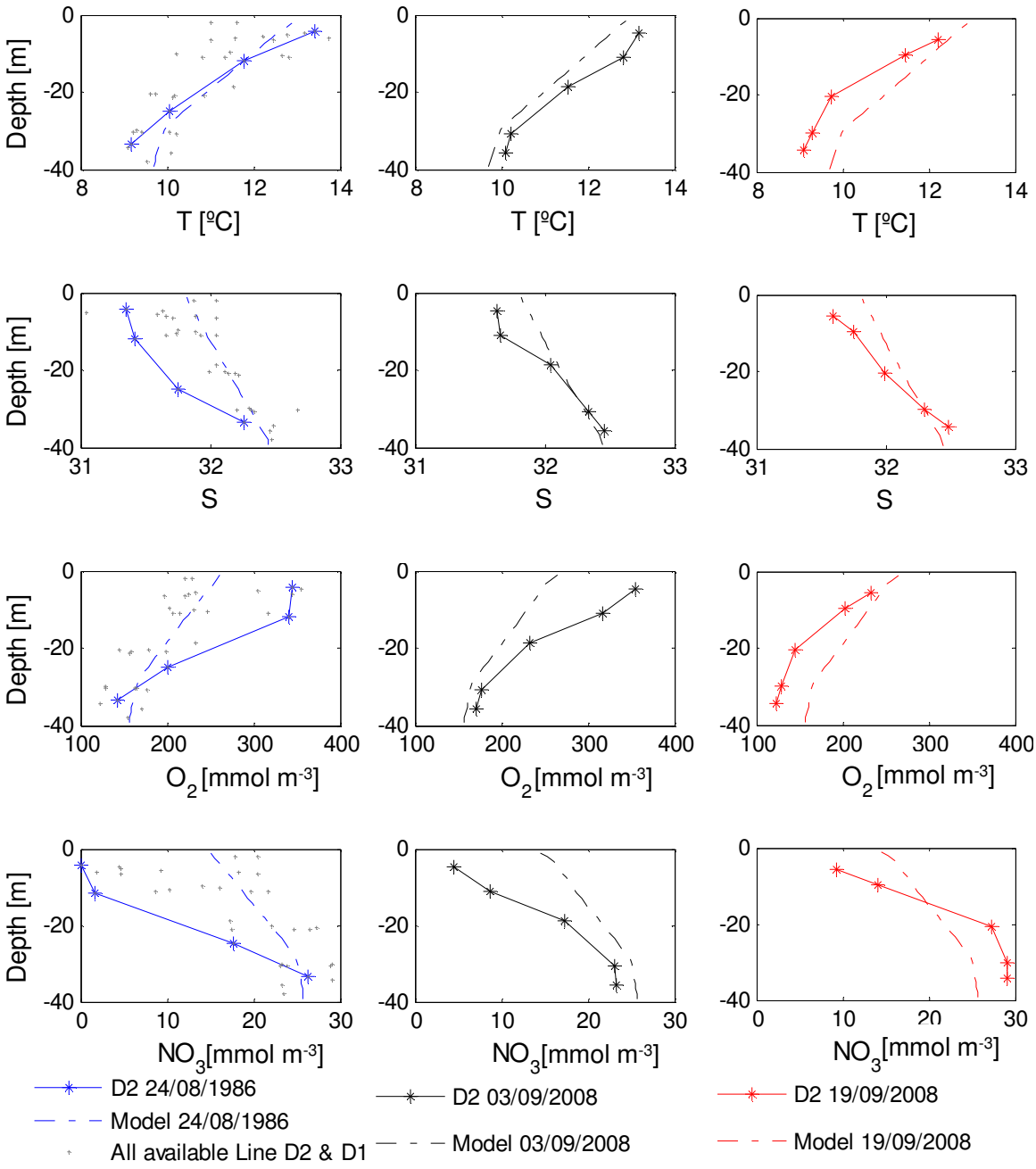

Figure 2.4a: Vertical profiles from model and Line D stations. On this page, inner shelf stations (D2) are shown. For each station, four variables are shown: temperature, salinity, O_2, and NO_3 (from top to bottom). Colour code corresponds to different transects (blue: 24 August 1986; black: 3 September 2008; red: 19 September 2008). Left hand plots show observations from eight summer D1 and D2 stations from five years between 1986 and 2008 (grey crosses). Continues…

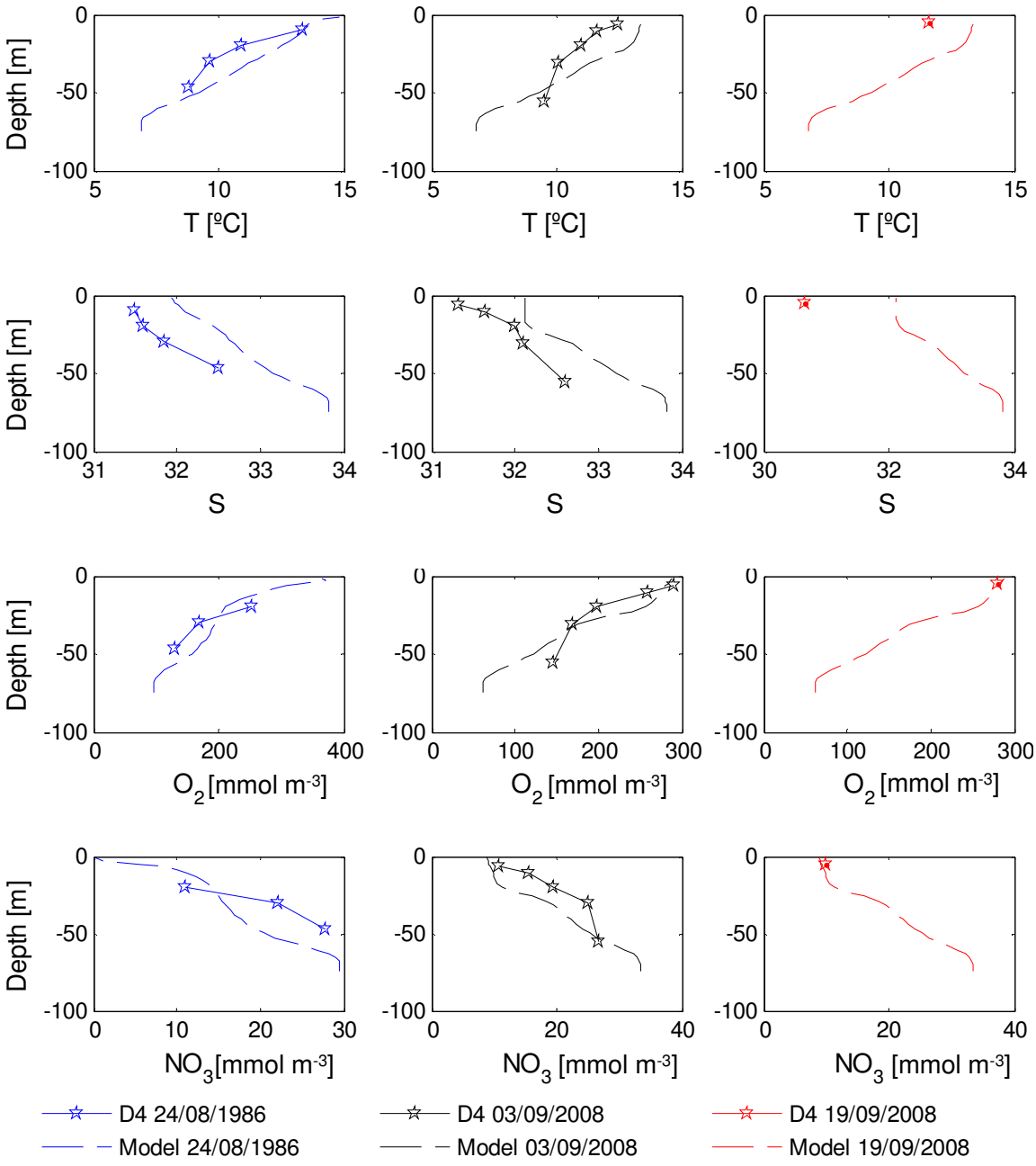

Figure 2.4b: Vertical profiles from model and Line D stations. On this page, mid shelf stations (D4) are shown. For each station, four variables are shown: temperature, salinity, O_2, and NO_3 (from top to bottom). Colour code corresponds to different transects (blue: 24 August 1986; black: 3 September 2008; red: 19 September 2008). Continues…

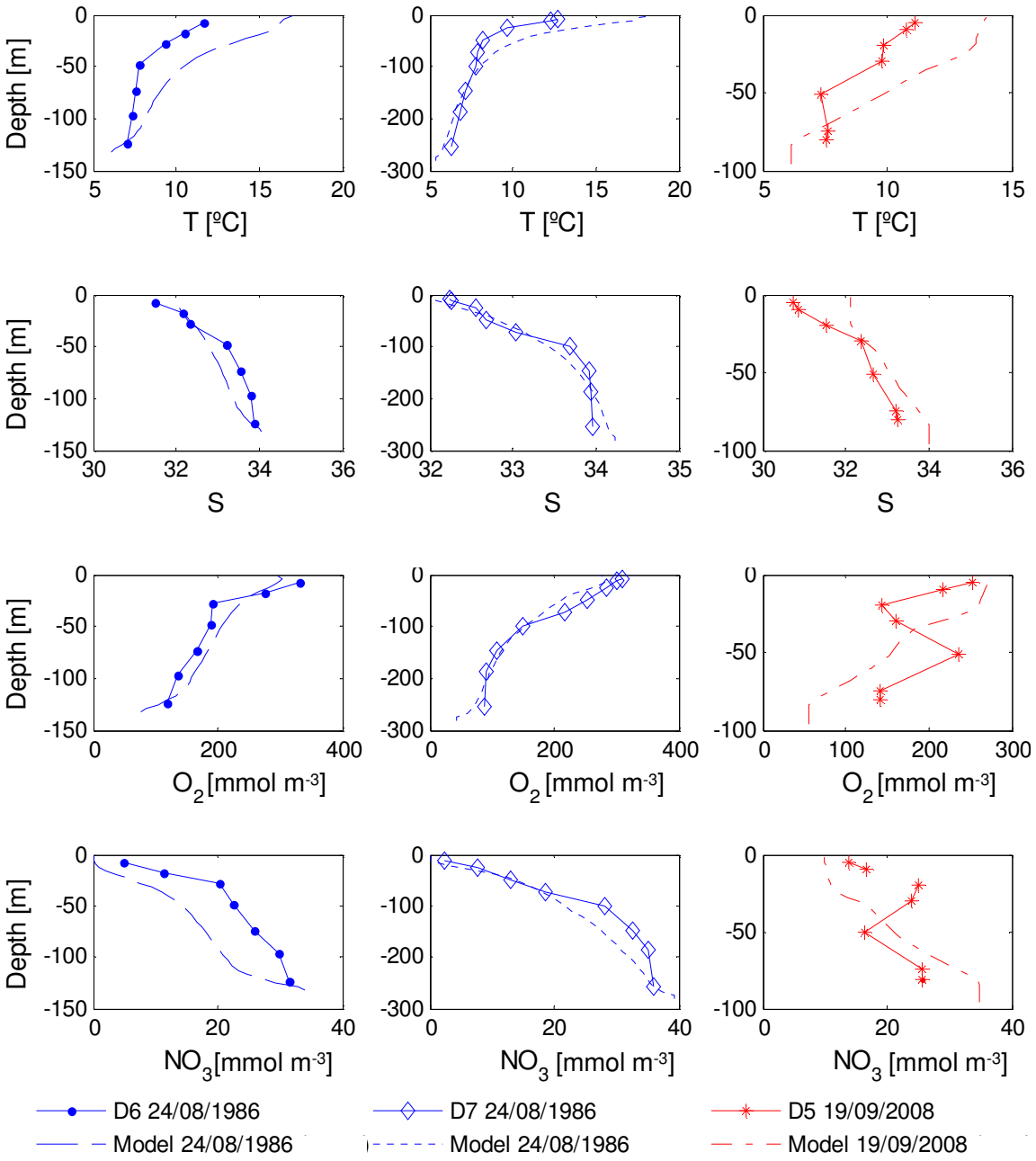

Figure 2.4c: Vertical profiles from model and Line D stations. On this page, outer shelf stations (D5 to D7) are shown. For each station, four variables are shown: temperature, salinity, O_2, and NO_3 (from top to bottom). Colour code corresponds to different transects (blue: 24 August 1986; black: 3 September 2008; red: 19 September 2008).

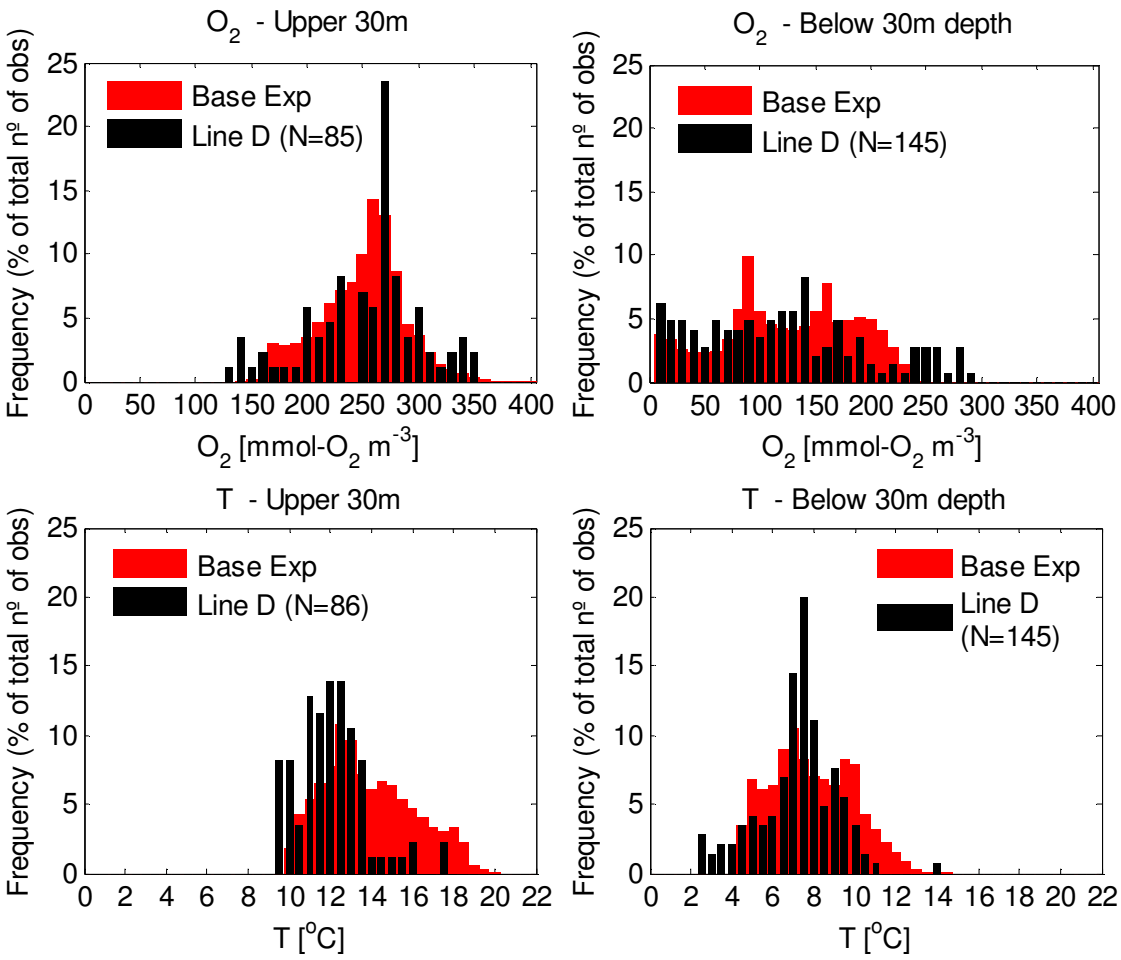

Figure 2.5: Histograms of model (red) and in situ (black) data: upper panels show O_2, lower panels temperature. Left panels present data for the upper 30 m of the shelf and slope (depth < 970 m), and right panels present data below 30 m. Model results are from the Base Experiment (forcing from 1993; more details given in section 2.3); spinup period is not included. Observations are from nine transects along Line D during 1981 to 2008; the legend shows in parentheses the number of observations (N) in each distribution.

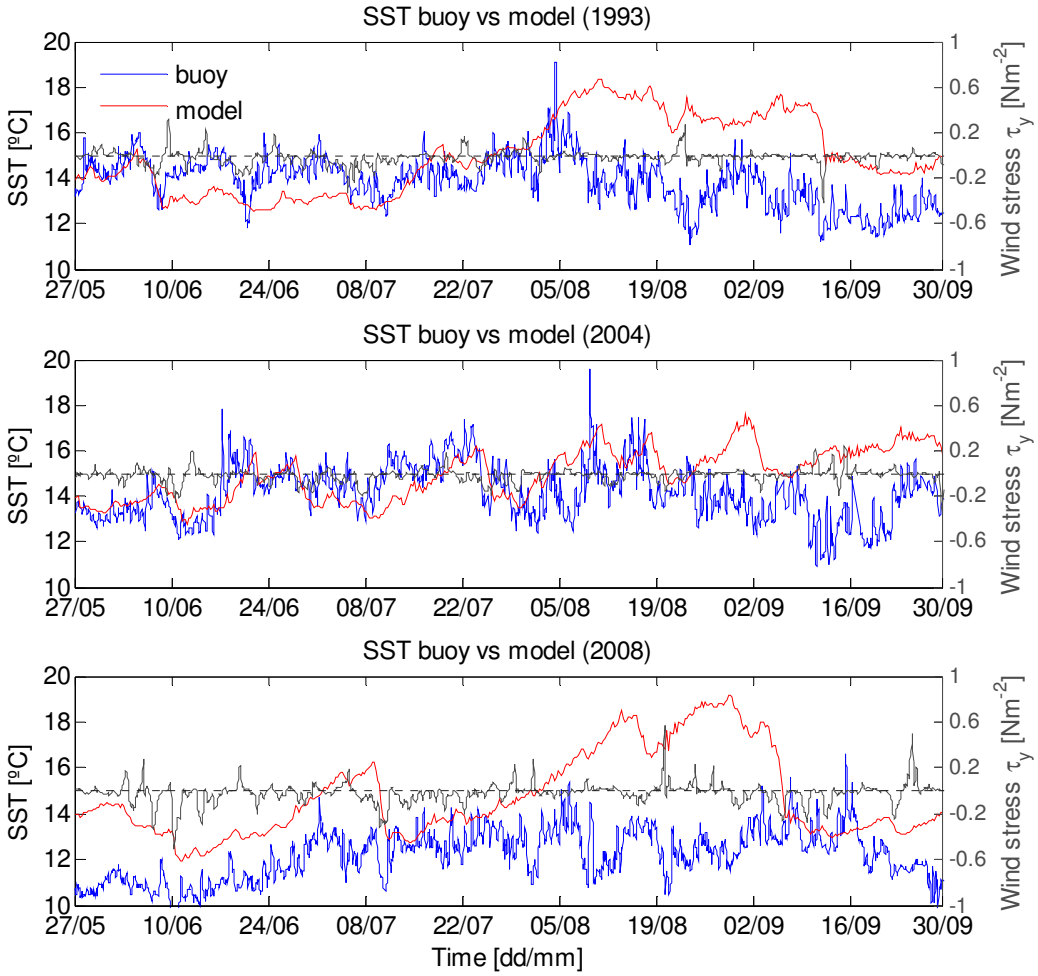

Figure 2.6: Sea surface temperature from model (red) and buoy 46206 (blue) for different years (1993 top, 2004 middle, 2008 bottom panels). Right axis indicates wind stress (dark grey line) calculated from buoy data ($\tau_y < 0$ for upwelling, $\tau_y > 0$ for downwelling). Figure 2.1 shows location of buoy 46206.

2.3 Results

The model Base Experiment is run with late spring and summer 1993 forcing because the upwelling indices for July and August of that year were close to average (Figure 2.7). The sediment layer takes ~ 40 days to 'forget' its initial conditions, so the model is initialized on 27 May to provide adequate time for spinup. The characteristic model response to wind forcing is shown in vertical sections of salinity (S) and O_2 (Figure 2.8)

during summer downwelling (upper panels) and upwelling (lower panels) wind conditions. Each plot is a snapshot at a given time, with alongshore wind stress shown in the insets (a black dot and an arrow show the wind stress at the time of the snapshot). During downwelling conditions (poleward alongshore wind stress leading to surface Ekman transport towards the coast and consequent downwelling in shallow regions), low surface S is concentrated in the VICC region (see S < 32 white contour in upper panel of Figure 2.8 pushed deeper and closer to the boundary). S near the bottom over the shelf is fresher further offshore (see S = 34 contour) due to the offshore transport of near-bottom waters from the inner shelf (note that the 33.8 contour is further onshore because of a previous intense upwelling event between days 35 to 45). High O_2 also concentrates onshore near the surface due to the advection of waters that experienced elevated primary production (second panel).

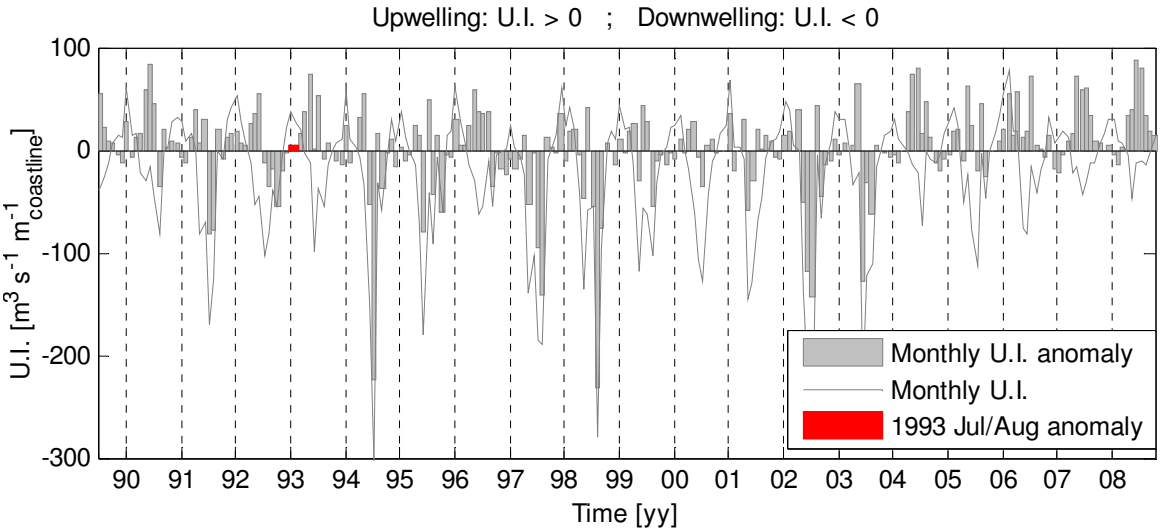

Figure 2.7: Monthly upwelling index (U.I.; grey curve) and monthly U.I. anomaly (grey bars) from 1990 to 2008. The dashed vertical lines indicate July of each year. The small red bars for 1993 indicate a year where upwelling was close to average during July and August (small monthly anomalies).

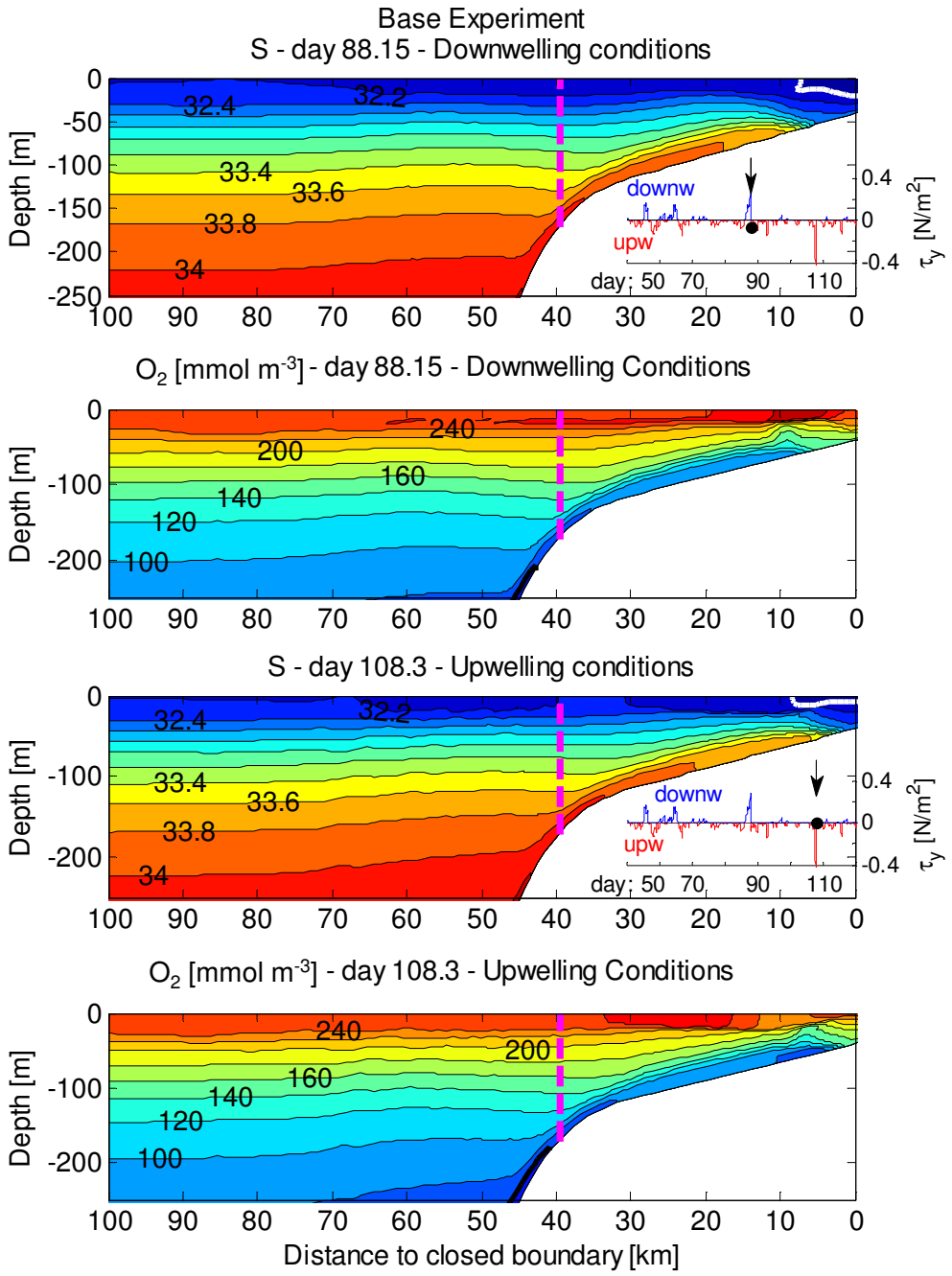

Figure 2.8: Vertical sections of salinity (S) and oxygen (O_2) for different wind conditions. Upper two panels show S and O_2 immediately after a strong downwelling event (23 August); lower two panels, immediately after a strong upwelling event (23 September). Insets in S plots show alongshore wind stress evolution (black dot and arrow indicate the exact time of the snapshot). These times are also shown with black arrows in Figure 2.9 and Figure 2.10. The bold black contour in the O_2 plot shows the hypoxic threshold (60 mmol m^{-3}); the bold white contour in the S plot shows S = 32. The dashed magenta line shows the location of the shelf break (172 m depth).

When upwelling conditions prevail (equatorward alongshore wind stress producing surface Ekman transport offshore), offshore surface transport carries low S and high O_2 concentrations from the inner shelf offshore towards the mid shelf (third and fourth panels). These plots show how the model represents the effect of the VICC in the upper layer, advecting its fresh, O_2-rich waters (also nutrient-rich) offshore when upwelling favourable winds prevail. Moreover, under these wind conditions, the high salinity/low O_2 tongue near the bottom on the shelf penetrates farther onshore into shallower waters. However, there is a relative O_2 minimum near the bottom on the inner shelf that it is not directly connected to the upwelling tongue. As it will be discussed later, this feature results from local biogeochemical processes.

The time evolution of O_2 concentrations in the near-bottom layer of the model domain (Hovmöller plot) shows the response of near-bottom concentrations to wind forcing (Figure 2.9). Given the σ vertical coordinates of the model, the near-bottom layer is 1.4 m thick near the shallowest boundary, 5 m at the shelf break (magenta line in bathymetry profiles in Figure 2.9), and 42 m thick in the open ocean. Despite the substantial change in thickness, the near-bottom layer represents the bottom boundary layer (BBL) well in most of the domain (the modelled BBL thickness (~ 10 m) agrees with observations of the coastal upwelling system off Oregon, Perlin et al. 2005). Several vertical levels describe the BBL over the outer and mid shelf; two to five levels usually represent the BBL over the inner shelf, except within the shallowest 3 km of the domain. This is the region where the nutrient- and O_2-rich VICC is restored most strongly (Figure B.2), seen in Figure 2.9 as high and homogeneous O_2 concentrations close to the inshore boundary. During downwelling events bottom VICC concentrations

penetrate further offshore in the bottom layer, showing displacements out to the 69 m depth contour (~ 10 km from inshore boundary). In general, these events lead to higher near-bottom O_2 concentrations over the whole shelf (region to the right of the magenta dashed line in Figure 2.8 and Figure 2.9), while upwelling leads to the penetration of lower O_2 waters onto the shelf (as previously described for Figure 2.8). As expected during late spring and summer, O_2 over the near-bottom of the shelf decreases as time progresses. Replacing small detritus with semilabile DOM, and hence removing aggregation to the faster sinking large detritus, may reduce temporal variability in the near bottom layer dynamics.

The bold black contour ($O_2 = 60$ mmol m^{-3}) indicates the onshore limit of hypoxic bottom waters (Gray et al. 2002, Whitney et al. 2007, Stramma et al. 2008). Although this value is a commonly used hypoxic threshold, many species have thresholds (either lethal or sublethal) at higher O_2 concentrations (Vaquer-Sunyer and Duarte 2008). Recently, Brewer and Peltzer (2009) have suggested that partial pressure of carbon dioxide (pCO_2) should also be considered when defining stress thresholds. They define a Respiration Index:

$$RI = log_{10}\left(pO_2 / pCO_2\right) \qquad 2.3$$

This index is linearly related to available energy in basic oxic respiration and considers the effects of not only O_2, but also pCO_2 when defining ocean dead zones (regions where marine animals are excluded). These authors argue that elevated pCO_2 may impose a physiological strain on higher animals, and that the use of an O_2 limit to define a dead zone implicitly assumes that pCO_2 levels are low and inversely proportional to O_2. The basic hypothesis is that both lower ambient O_2 and higher ambient pCO_2 impose a higher

energy requirement on the organisms to transfer O_2 and CO_2 across the cell membrane (i.e., O_2 into and CO_2 out of the cells). According to equation 2.3, as atmospheric pCO_2 rises and more carbon is absorbed by the ocean, dead zones could expand even if O_2 levels were not affected. The yellow thick contour in Figure 2.9 shows RI = 1 (RI < 1 inside the contour), which Brewer and Peltzer (2009) argue may be the approximate value that delimits the aerobic stress zone (only some species can tolerate RI ~ 1; the onset of denitrification occurs at RI ~ 0.4 to 0.7). Near-bottom waters with RI ≤ 1 are found where the OMZ intersects the continental slope, and disappear due to horizontal advection of O_2 around day 55 in response to a strong upwelling event (note however that waters with RI ≤ 1 are mostly present during spinup, i.e. day 0 to 50, following closely a contour of O_2 = 13 mmol m^{-3}). The results show a clear separation between the location of RI = 1 and the hypoxic threshold O_2 = 60 mmol m^{-3} (Figure 2.9). According to these model results, the latter is a more conservative index of ecosystem impacts, as the area with $O_2 \leq 60$ mmol m^{-3} is more extensive than for RI ≤ 1. However, these results could change as ambient pCO_2 levels increase.

Hovmöller plots for O_2, saturation state of aragonite (Ω_A), pH, and pCO_2 show the simultaneous responses of O_2 and inorganic carbon after the spinup period (Figure 2.10). The value of Ω_A describes whether the waters are oversaturated ($\Omega_A > 1$) or undersaturated ($\Omega_A < 1$) with respect to aragonite; therefore, $\Omega_A = 1$ can be considered a critical value that delimits the regions of precipitation or dissolution of this form of calcium carbonate. The general pattern for all variables follows that of O_2. This figure will be compared with similar figures for different model experiments (described in Table 2.3) throughout this chapter.

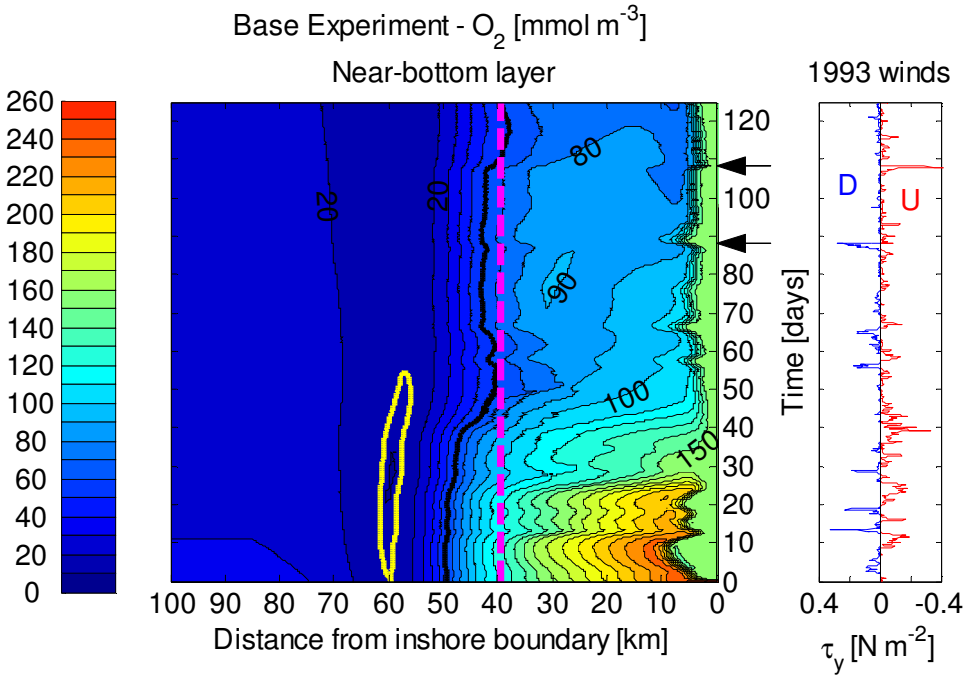

Figure 2.9: Hovmöller plot for O_2 concentrations in the near-bottom layer of the model. The panel on the right shows alongshore wind stress (upwelling/downwelling in red/blue, respectively). The bold black contour is the hypoxic threshold (60 mmol-O_2 m^{-3}), the bold yellow contour indicates the Respiration Index (RI) = 1, and the dashed magenta line represents the location of the shelf break (172 m depth) as in Figure 2.8. Day 0 is 27 May 1993. Black arrows on the right show the downwelling and upwelling events of Figure 2.8

Table 2.3: Description of model sensitivity experiments

Experiment	Description
Base	Control experiment with 1993 late spring and summer forcing (Day 0 is 27 May 1993)
No Biology	Turn off local sources and sinks. Biological tracers are only advected and mixed. O_2 and CO_2 are exchanged at the surface
Reflective Sediment Boundary	No mass accumulation in sediment layer. Particles reaching the seafloor are instantaneously remineralized
No VICC	No coastal current

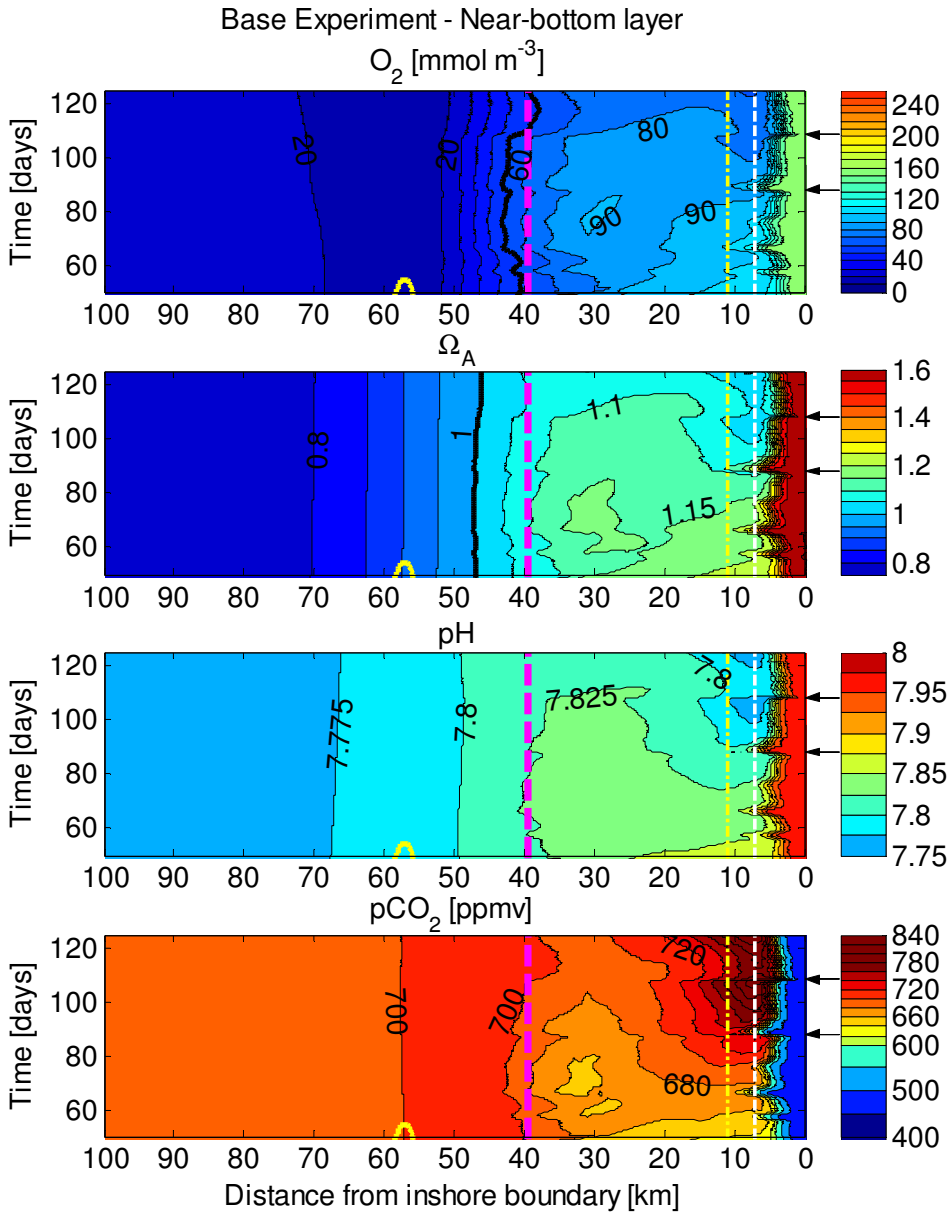

Figure 2.10: Hovmöller plots for near-bottom layer values of O_2, Ω_A, pH, and pCO_2. The closed inshore boundary is on the right; the dashed magenta line shows the location of the shelf break (172 m depth). The yellow contour is RI = 1; the bold black contours show the hypoxic threshold (60 mmol-O_2 m^{-3}) and the limit for aragonite dissolution (Ω_A = 1). The vertical dash-dotted yellow and dashed white lines show 69 and 59 m depth contours, respectively. The two arrows on the right of each panel show the downwelling and upwelling events of Figure 2.8 (23 August and 12 September, respectively).

2.3.1 Roles of water column and sediment processes

Examining the sources and sinks in the bottom ~ 10 m of the water column will help to understand which processes regulate the near-bottom concentrations of O_2 and inorganic carbon in the model (Figure 2.11). Two shelf locations, one with a total depth of 59 m (dashed white line in Figure 2.10, inside the area where the VICC is being restored in the model), and another with a total depth of 69 m (dash-dotted yellow line in Figure 2.10, shallowest point with no VICC restoration), are shown. At the shallower location (Figure 2.11a and c), advection is the leading (and most variable) term in the balance for both O_2 and DIC during strong wind events, and leads to the conditions described previously: increasing O_2 (decreasing DIC) in the bottom shallow waters of the model during downwelling, and the opposite during upwelling. For DIC, advection dominates the balance during most of the record, increasing carbon concentrations as winds are upwelling-favourable most of the time. Sediments contribute to a lesser extent to the rise in DIC, while diffusion and the VICC flux tend to diminish it. Remineralization of detritus and DOM produce DIC, although these terms are about half the sediment flux and approximately one order of magnitude smaller than the flux due to advection. The budget of near-bottom O_2 at 59 m depth differs from DIC: although advection plays a role, O_2 drawdown by the sediments is at times the largest sink (especially during weak upwelling after day 100). At the location outside the VICC restoration region (69 m depth; Figure 2.11b and d), advective fluxes are reduced compared with those at the inshore location. Although advection is still significant, it is of the same order of magnitude as the diffusive and sediment fluxes. The smaller advective fluxes result from the smaller property gradients outside the VICC region. After day 95, although winds remain mainly upwelling-favourable, advection increases O_2 and decreases DIC,

especially in response to the upwelling event on day 108. This opposite effect can be explained by the local O_2 minimum and inorganic carbon maximum that occur over the inner shelf (Figure 2.10), such that upwelled waters advect onshore waters from the mid shelf that are higher in O_2 and lower in DIC than the waters closer to the shore. At these times, the sediments become the main O_2 sink and DIC source outside the VICC region.

An additional model experiment with all biological processes 'turned off' (No Biology Experiment, see Table 2.3), allows separating the contributions resulting from physical and biological processes. Hovmöller plots for this simulation (Figure 2.12) can be compared with those for the Base Experiment (Figure 2.10): in the No Biology Experiment, near-bottom O_2, Ω_A, and pH are higher over the shelf, while pCO_2 is lower. These results respond to the lack of biological consumption of O_2 and production of DIC in the bottom layer of the water column and in the sediments, as shown by the net change in O_2 and DIC concentrations due to physical and biological processes for the bottom 11 m at the 69 m depth contour (Figure 2.13). The changes due to physical processes result from the integration from day 50 to 125 of advective plus diffusive fluxes (Figure 2.13, black and orange arrows for Base and No Biology Experiments, respectively). The net change due to biological processes (only in the Base Experiment) is the time integral of the sum of all ecosystem sources and sinks (Figure 2.13, purple arrow). In the Base Experiment, O_2 decreases and DIC increases from day 50 to 125 as a result of biological processes, while physical processes generate opposite changes, mainly by vertical mixing (Figure 2.11b and d) as layers above the bottom ~ 10 m are richer in O_2 and lower in DIC. When biology is removed from the model, the net change in O_2 and DIC from physical processes only (orange arrow) opposes the net change in the Base Experiment

(red arrow). Therefore, although upwelling brings carbon-rich and O_2 depleted waters onto the shelf, it is not sufficient to maintain low O_2 and high inorganic carbon concentrations (i.e., high pCO_2 as well as low Ω_A and pH) on the mid and inner shelf (it should be noted that in the Base Experiment, waters that are advected or mixed to the location of the budget estimate have themselves been modified by biological processes). The dashed grey line in Figure 2.13 represents the ΔO_2:ΔC ratio equal to PQa (1.1, see section 2.2.2); not all biological processes follow this ratio (e.g., nitrification, denitrification within the sediments), so the purple arrow does not fall on the grey line. There is no a priori reason why changes in O_2 and DIC resulting from physical processes should maintain ΔO_2:ΔC = PQa. Physical processes mix and transport waters that have been biologically modified, so the ratio of changes ΔO_2:ΔC should be close to (but not necessarily the same as) that of biological processes. Note that if an integration period different from 50 – 125 days is used and/or a different spatial location is analyzed, the black arrow in Figure 2.13 (i.e., changes due to physics in the Base Experiment) does not fall exactly on the dashed grey line (not shown).

In the Reflective Sediment Boundary Experiment (Table 2.3), particulate organic matter reaching the seafloor is instantaneously remineralized. This type of bottom boundary is only realistic if remineralization time scales are short compared to the time scales of study or in the unlikely case of constant organic matter deposition (Soetaert et al. 2000). This formulation has been used in coastal (e.g., Fennel et al. 2006, 2008) and global (e.g., Najjar et al. 1992, Matear and Holloway 1995) biogeochemical model studies, so it is worth analysing it. Compared to the Base Experiment (Figure 2.10), O_2, Ω_A, and pH in the near-bottom layer decrease and pCO_2 increases in the Reflective

Sediment Boundary Experiment (Figure 2.14), because this parameterization increases sedimentary remineralization (Figure 2.15). Each bar in Figure 2.15 represents the time integral of a flux between days 50 and 125 (red/cyan bars are for the Base/Reflective Sediment Boundary Experiments) at a location 69 m deep (dash-dotted yellow line in Figure 2.14). In the case of the Base Experiment, the bars represent the time integral of the different budget terms in Figure 2.11b and d (except that Figure 2.15 distinguishes between water column detritus and semilabile DOM remineralization and nitrification). Exchanges with the sediments in the Reflective Boundary simulation are 26% larger than in the Base Experiment in the 75-day period, since organic matter cannot be accumulated in the sediments. If both simulations were averaged over sufficiently long time scales, the release of DIC and the consumption of O_2 from the sediments would become nearly equal because neither experiment considers permanent sequestration of organic matter in the sediments. Nevertheless, at the timescales of interest here, the difference is enough to lead to aragonite undersaturation and corrosive waters ($\Omega_A < 1$) in near-bottom waters over the inner shelf. Nonetheless, both experiments show that exchange between the water column and sediments represents the largest term contributing to net consumption of O_2 and production of DIC (Figure 2.15). As a result, sediments play a significant role in tightening the connection between O_2 and inorganic carbon in the near-bottom layers over the shelf. All of these results indicate that the role of sediments in the cycling of carbon, nitrogen, and O_2 must be considered when working in coastal environments.

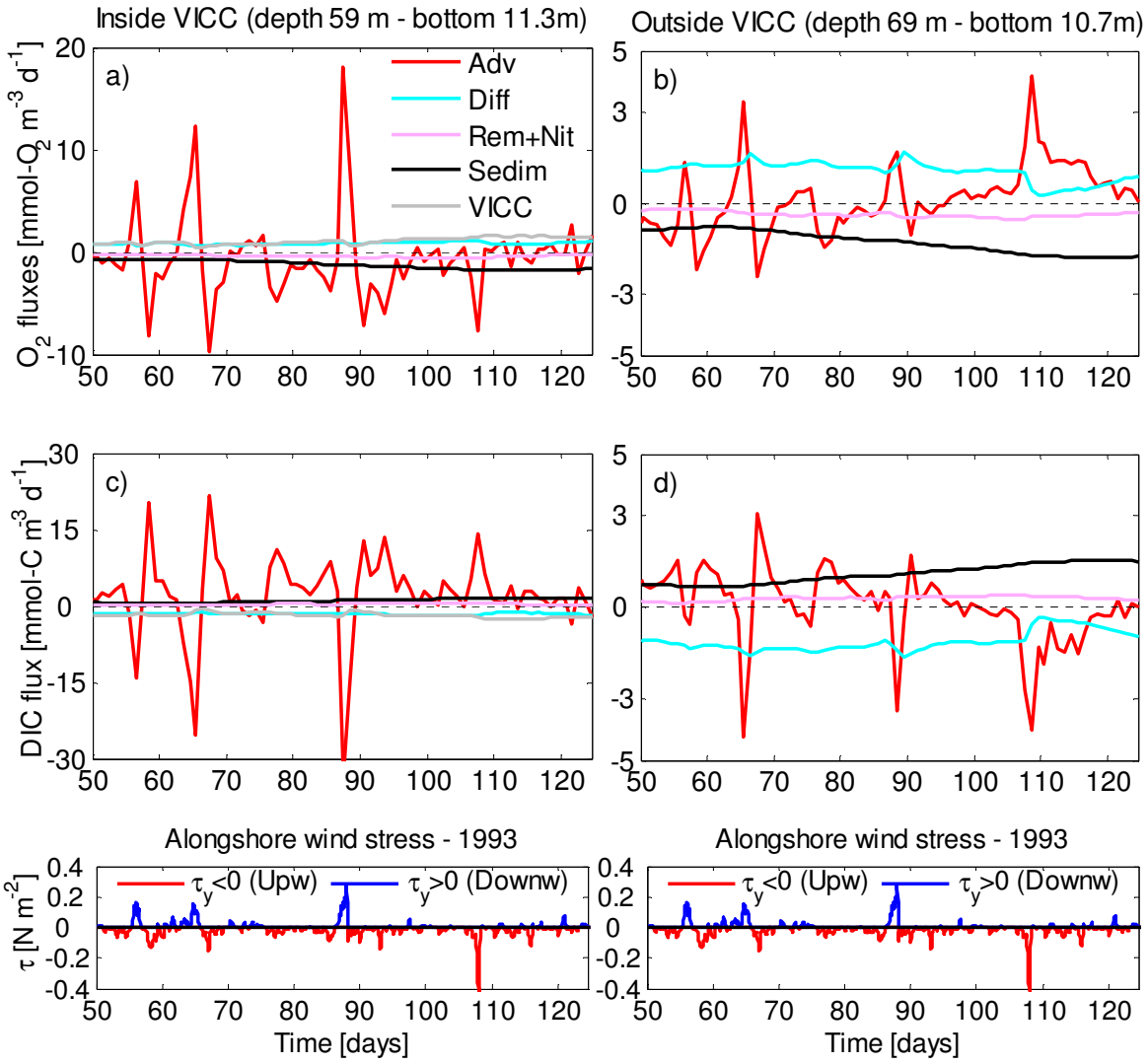

Figure 2.11: Source and sink fluxes of (a, b) O_2 and (c, d) DIC in the bottom ~ 10 m of a water column of (left) 59 and (right) 69 m depth for the Base Experiment. The shallower location (left) belongs to the VICC restoring region; the other location (right), lies outside the VICC region. The VICC (grey line) is the restoring flux, so it is zero at 69 m depth (although all the processes are affected by the presence of the VICC in the shallow waters). Advective (Adv, red) and diffusive (Diff, cyan) fluxes as well as water column remineralization (detritus and semilabile DOM) plus nitrification (Rem+Nit, pink), remineralization within the sediments (Sedim, black), and VICC flux (grey) are shown. Both bottom panels show 1993 alongshore wind stress (upwelling/downwelling in red/blue).

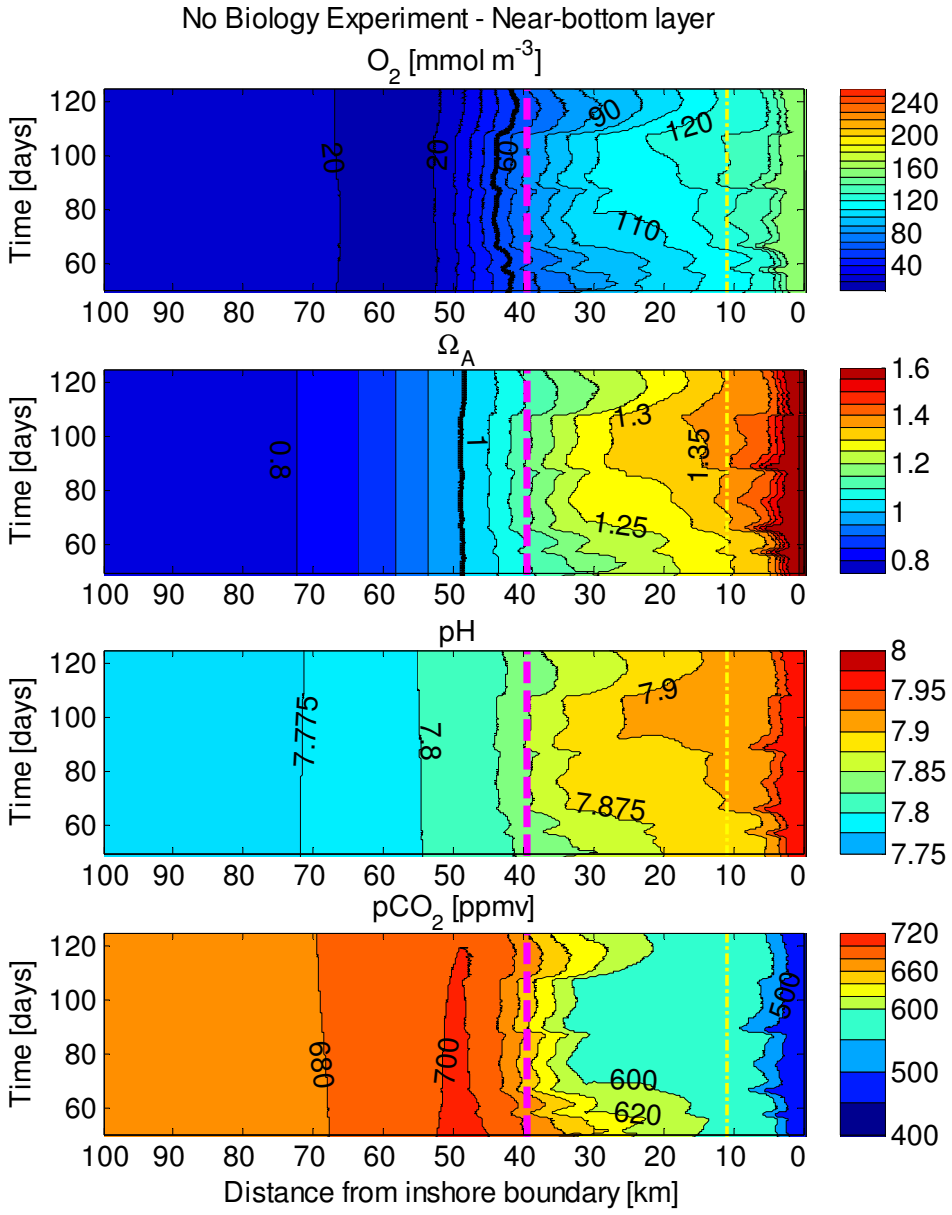

Figure 2.12: Hovmöller plots for near-bottom layer O_2, Ω_A, pH, and pCO_2 for the No Biology Experiment (see Table 2.3). As in Figure 2.9, the dashed magenta line indicates the position of the shelf break and the bold black contours show the hypoxic threshold $O_2 = 60$ mmol m^{-3} and $\Omega_A = 1$. RI in this experiment is always greater than 1 (therefore not shown). The dash-dotted yellow line shows the location of the 69 m isobath.

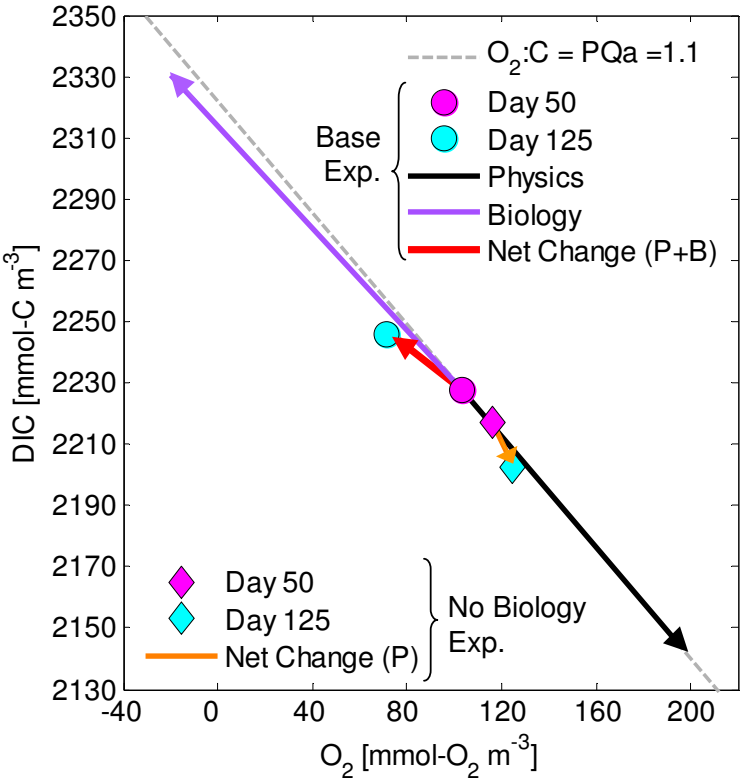

Figure 2.13: Total changes in DIC and O_2 from day 50 to 125 in the bottom ~ 10 metres of the water column at the 69 m depth contour for the Base Experiment (red arrow from magenta circle to cyan circle) and the No Biology Experiment (orange arrow from magenta diamond to cyan diamond). DIC and O_2 changes during the Base Experiment result from the vector sum of advection and mixing (black arrow) and biological processes in the water column plus sedimentary remineralization (purple arrow). The dashed grey line shows the O_2 to carbon ratio (PQa).

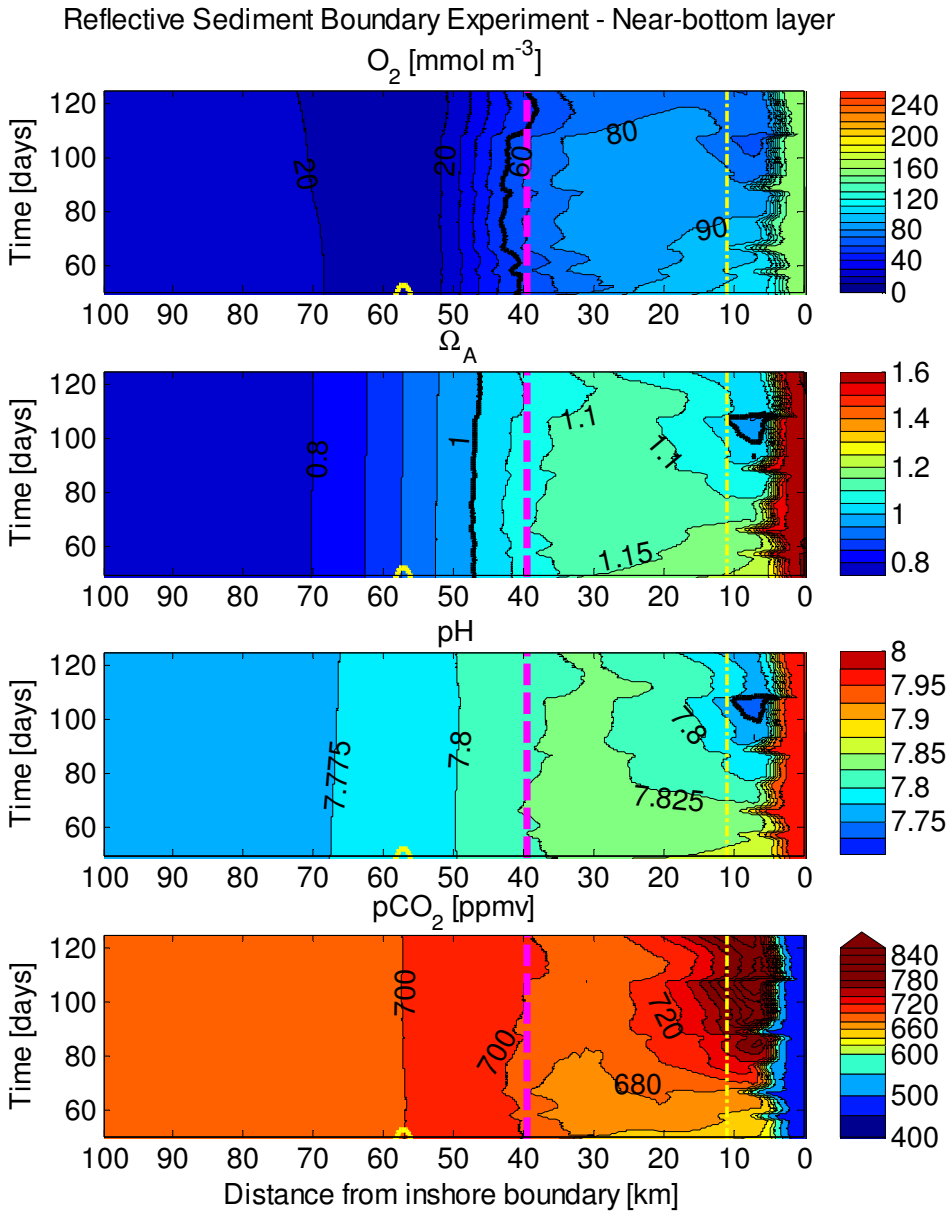

Figure 2.14: Hovmöller plots for near-bottom layer O_2, Ω_A, pH, and pCO_2 for the Reflective Sediment Boundary Experiment (see Table 2.3). As in Figure 2.9, the dashed magenta line indicates the position of the shelf break, the bold yellow contour shows RI = 1, and the bold black contours show the hypoxic threshold $O_2 = 60$ mmol m^{-3} and $\Omega_A = 1$. This experiment shows $\Omega_A < 1$ and pH < 7.75 over the inner shelf, indicating corrosive waters (the bold black contour in the pH plot shows pH = 7.75). The dash-dotted yellow line shows the location of the 69 m isobath.

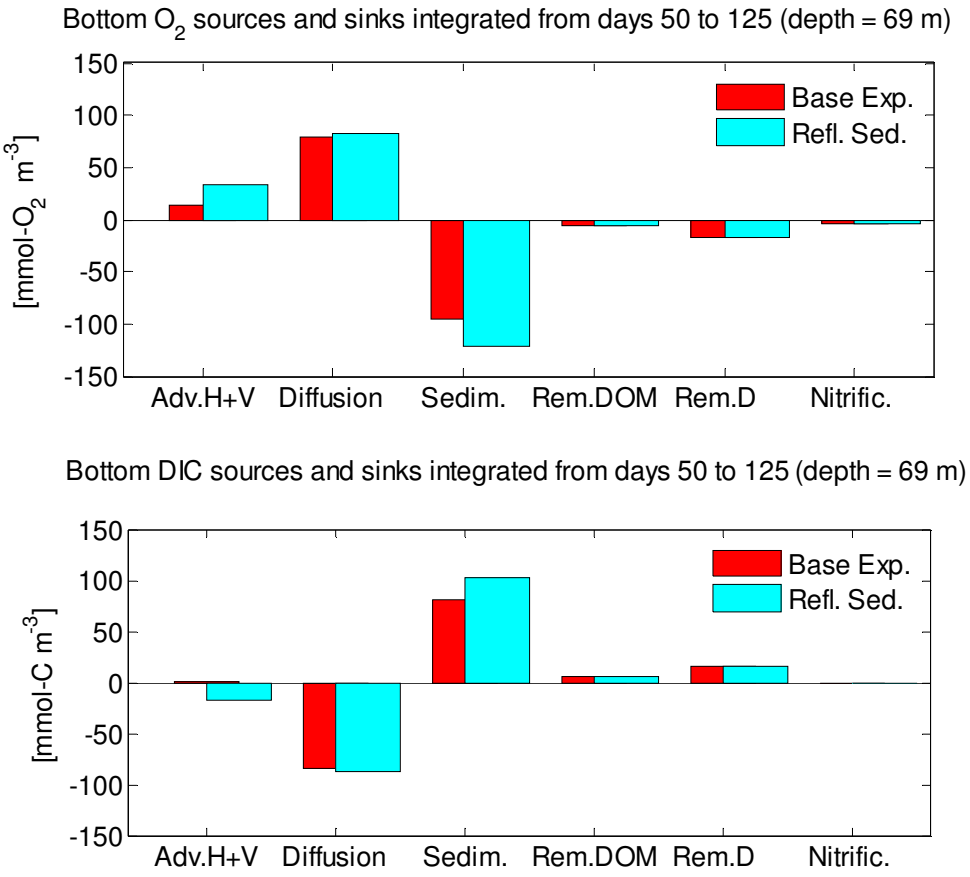

Figure 2.15: Source and sink fluxes in the bottom ~ 10 m of the water column at a location 69 m deep for O_2 and DIC (upper and lower panels, respectively), integrated from day 50 to 125. Base and Reflective Sediment Boundary Experiments in red and cyan bars, respectively. The horizontal axis reads: advection (horizontal plus vertical), diffusion, exchanges with the sediments, water column remineralization of semilabile DOM and D, and water column nitrification.

2.3.2 The role of the Vancouver Island Coastal Current

The influence of the VICC is studied by comparing the Base Experiment with one that does not include the current (No VICC Experiment): there is no restoring in the shallow waters to VICC properties, so all ecosystem variables respond to a solid wall at the inshore boundary. This simulation could be analogous to the modelling of shelves further south in the CCS. In this simulation, near-bottom shelf waters contain less O_2 and more inorganic carbon (Figure 2.16) compared with the Base Experiment (Figure 2.10). The

VICC is a source of O_2-rich waters for the shelf, while DIC concentrations in the bottom layers of the VICC are lower than in near-bottom layers over the mid and outer shelf (Figure B.4). Time integrated fluxes (from day 50 to 125) in the bottom 11 m of the water column at a location 59 m deep (Figure 2.17) show how the VICC supplies O_2 and removes DIC (the VICC flux is the restoring term that represents the current in the quasi-2D model). This direct effect of the VICC is partially counterbalanced by the larger exchange with the sediments and remineralization of detritus observed in the Base Experiment compared with the No VICC simulation. The increase in these fluxes responds to the enhanced primary production when the VICC is included (Figure 2.18). Moreover, the influence of the VICC is also seen indirectly in the physical fluxes, as the presence of this current in shallow waters of the model increases horizontal and vertical gradients, thus enhancing advection and mixing. Near-bottom waters over the inner shelf become hypoxic as well as undersaturated in aragonite (i.e., corrosive) in the experiment without the coastal current. This emphasizes the important role of the VICC in this ecosystem, as it not only provides nutrients that enhance primary production in the euphotic zone, but also supplies O_2 to and removes DIC from the bottom layers.

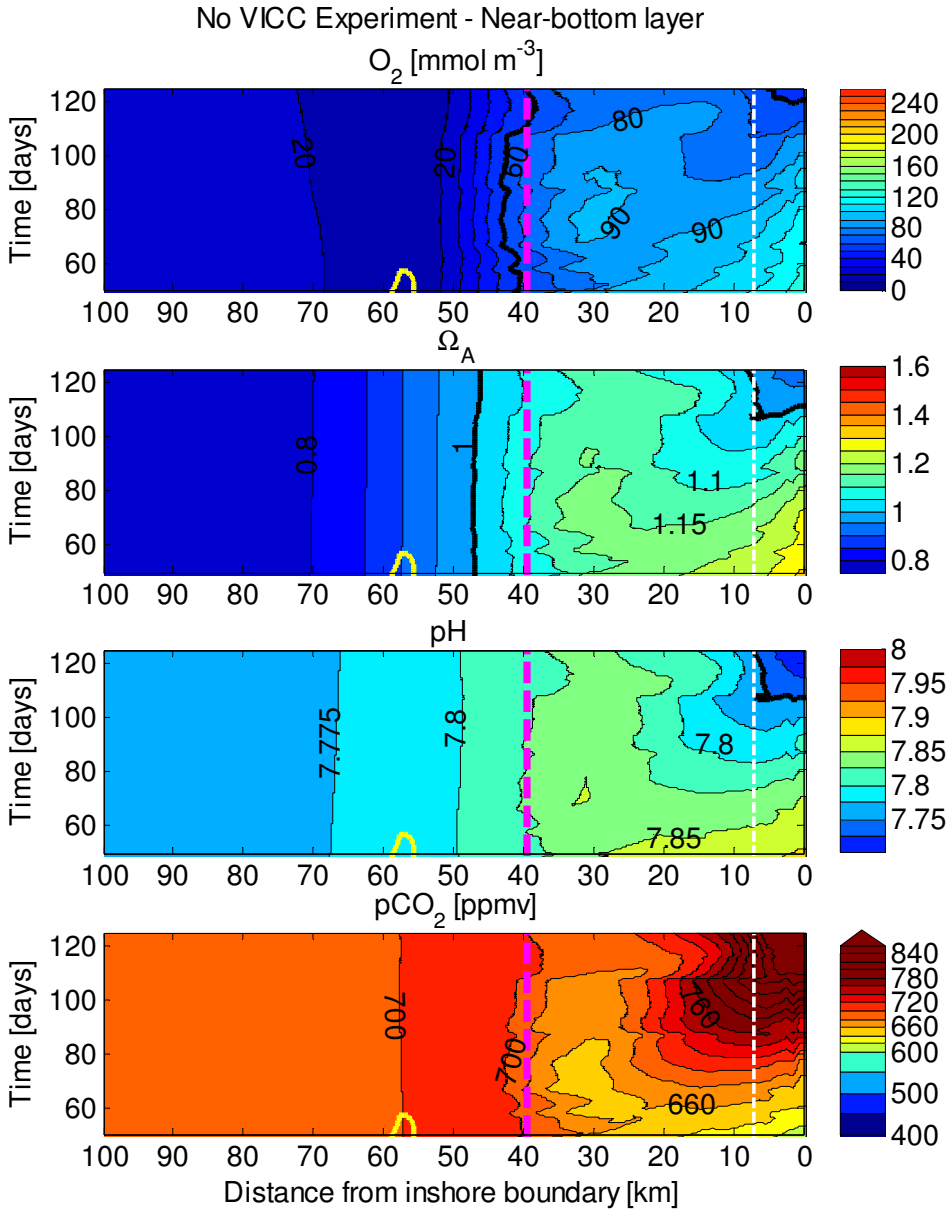

Figure 2.16: Hovmöller plots for near-bottom layer O_2, Ω_A, pH, and pCO_2 for the No VICC Experiment (see Table 2.3). As in Figure 2.9 and Figure 2.14, the dashed magenta line indicates the position of the shelf break, the bold yellow contour shows RI = 1, and the bold black contours show the hypoxic threshold $O_2 = 60$ mmol m^{-3}, $\Omega_A = 1$, and pH = 7.75. The dashed white line shows the location of the 59 m isobath.

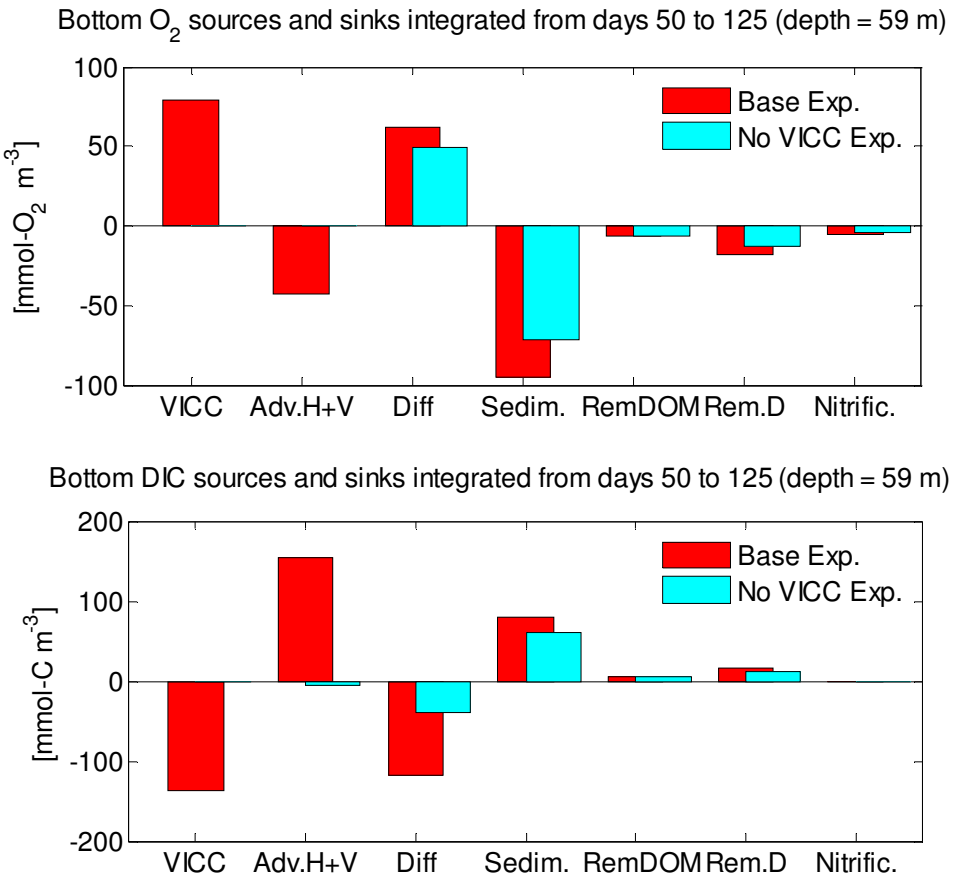

Figure 2.17: Source and sink fluxes in the bottom ~ 10m of the water column at a location 59 m deep for O_2 and DIC (upper and lower panels, respectively), integrated from day 50 to 125. Base and No VICC experiments are red and cyan bars, respectively. The horizontal axis reads: VICC flux, advection (horizontal plus vertical), diffusion, exchanges with the sediments, water column remineralization of semilabile DOM and D, and water column nitrification. The VICC flux results from restoring properties to VICC values; the presence of the VICC also enhances advection and diffusion as it increases O_2 and DIC gradients (advective fluxes in the No VICC Experiment is ~ 2 orders of magnitude smaller than in the Base Experiment).

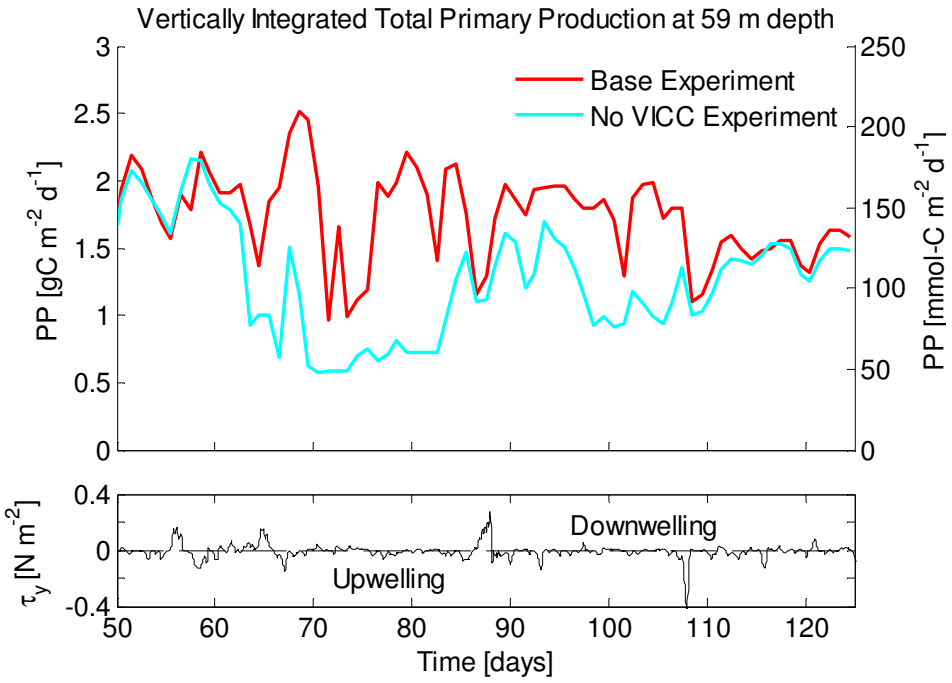

Figure 2.18: Time series of vertically integrated primary production (PP) at a location 59 m deep for Base and No VICC experiments (red and cyan curves, respectively). Left axis shows PP units in gC m^{-2} d^{-1} and right axis, in mmol-C m^{-2} d^{-1}. Lower panel shows alongshore wind stress evolution during the same time period (negative: upwelling, positive: downwelling favourable winds).

2.4 Discussion and Conclusions

O_2 and carbon are tightly coupled on the shelf. All spatial and temporal trends in O_2 are accompanied by opposing trends in inorganic carbon, i.e. decreases in O_2 take place simultaneously with decreases in pH and Ω_A (increasing DIC) and vice versa. The model allows us to examine the different processes individually (in particular, linking hypoxia and changes in acidity), in a way that is difficult to do from in situ observations alone.

First of all, the model shows that local ecosystem processes are required to achieve the low O_2 and high carbon concentrations observed on the shelf. Physical transport processes are important because upwelling triggers high primary production, but physical

processes alone cannot drive down O_2 or pH to the levels observed. This result agrees with Connolly et al. (2010), who show that seasonal hypoxia over the Washington shelf from 2003 to 2006 was dominated by biochemical processes in the water column and sediments. The upwelling of O_2-poor and carbon-rich waters from the open ocean affects the outer shelf region (as can be seen for instance in the near-bottom hypoxic threshold contour in Figure 2.9 and in the O_2 contours of Figure 2.12), but does not strongly influence the shallower regions of this wide shelf. Results from the Base Experiment do not show hypoxia, aragonite undersaturation, or corrosive waters over the inner shelf. It has been suggested that open ocean-shelf exchange can trigger coastal hypoxia (Grantham et al. 2004, Monteiro et al. 2006, 2008). The next chapter will focus on sensitivity analysis to determine whether advection of lower O_2 and higher DIC waters (stronger and deeper upwelling, or a shallower OMZ) could lead to hypoxia or acidification over the shelf off southern Vancouver Island.

In this model, remineralization within the sediments is the dominant process consuming O_2 and releasing DIC within the bottom layer over the shelf (~ 78 % of total O_2 sink and DIC source). This is similar to a recent study off the Washington shelf (Connolly et al. 2010), where water column processes and sediment remineralization were estimated to contribute equally (~ 50 % each) to the total consumption of O_2 in near-bottom water. Despite the differences between the two studies (i.e., the use of observations vs. modelling, the locations), both studies emphasize the importance of the sediments in coastal environments.

The reflective sediment model described in Fennel et al. (2006) produces sediment fluxes 26 % higher than the dynamic but simple sediment layer formulation used here,

which accumulates mass and remineralizes DIC back to the water column at a constant rate per unit mass. This difference leads to lower O_2 and higher DIC on the shelf in the Reflective Sediment Boundary Experiment, especially on the inner shelf where bottom layers become undersaturated with respect to aragonite during some periods (Figure 2.14). Although the reflective boundary is commonly used in global biogeochemical models (Najjar et al. 1992, Matear and Holloway 1995, etc), sediment remineralization does not occur instantaneously in nature, so Soetaert et al. (2000) recommended the vertically integrated dynamic sediment model implemented here. Disadvantages of this formulation are: a) two poorly constrained rates are needed (nitrogen and carbon remineralization rates within the sediments); and b) it takes a longer time to spin up, increasing the computational cost. As long as the model is relatively simple or the domain is small enough, this parameterization of a sediment layer is straightforward to implement and dynamically more correct than a reflective boundary. A caveat with respect to this sediment model is that it is more appropriate for low energy regions where resuspension is low and sediments can accumulate. Over the Vancouver Island shelf, little organic matter is expected to accumulate on the bottom, as currents are strong causing frequent resuspension (Macdonald and Pedersen 1991). A different sediment parameterization may be more suitable for this shelf, indicating an important direction for future studies. The two sediment models presented here probably represent the upper and lower ranges for the rate of sedimentary remineralization on the Vancouver Island shelf. Nonetheless, this work indicates the importance of including a representation of sediment processes when modelling coastal environments.

Thomas et al. (2009) propose that the capacity to store carbon in the coastal ocean is increased by the alkalinity generated by anaerobic degradation of organic matter in the sediments. The sedimentary production of alkalinity can also increase pH in the bottom layers over the shelf. Chapter 4 will focus on these effects of sedimentary denitrification. Other biological O_2 sinks such as remineralization of semilabile DOM and detritus, as well as nitrification (also sources of DIC, except for nitrification) are considerably smaller than the fluxes from the sediments.

The buoyant VICC coastal current is not only a persistent characteristic of the Vancouver Island shelf, but the model results suggest that it also plays a clear role in maintaining O_2 concentrations above hypoxia and lowering inorganic carbon levels, such as to avoid aragonite undersaturation. In the experiment without the VICC, exchanges with the sediment layer are not counterbalanced by the O_2 source and DIC sink associated with restoring to VICC properties, which leads to hypoxia and acidification (VICC near-bottom DIC concentrations are lower than near-bottom concentrations on the mid shelf, Figure B.4). The presence of the VICC may be a key difference between the Vancouver Island shelf and other shelves to the south in the California Current System (CCS), where coastal acidification and hypoxia have been observed (Grantham et al. 2004, Bograd et al. 2008, Chan et al. 2008, Feely et al. 2008, Connolly et al. 2010). The CCS includes other sources of buoyant waters, the largest being the Columbia River, which enters the ocean along the boundary between the states of Washington and Oregon. A main difference between the Columbia River and the VICC is that the latter occupies the whole water column inshore of the ~ 100 m isobath (Thomson et al. 1989, Hickey et al. 1991), while the Columbia River plume is shallow (~ 15 m) in summer (Hickey et al. 2005). The

strong tidal mixing in the channels through the San Juan and Gulf Islands generates this characteristic of the VICC. Therefore, the VICC and its associated mixing affect bottom waters over the shelf more efficiently than the shallow Columbia River plume. Some additional differences are the variable direction of the flow of the Columbia River plume in summer (Hickey et al. 2005) as well as the lower salinity and NO_3 as well as the higher sediment content of this plume compared with the VICC (Hickey and Banas 2008). Another important difference between the southern Vancouver Island shelf and regions to the south in the CCS is the width of the shelf, as upwelling can penetrate closer to the shoreline over a narrower shelf. The shelves in the northern part of the CCS, and especially off southern Vancouver Island, are typically wider (Hickey and Banas 2008). The effect of a wide shelf can be seen in the Base Experiment, where offshore O_2 conditions penetrate only ~ 10 km onto the shelf (depths of ~ 120 m) during upwelling events (Figure 2.9).

In conclusion, the model results indicate that low O_2 concentrations in the shelf occur simultaneously with low pH and Ω_A. Acidified O_2-depleted bottom waters have been observed in a semi-enclosed coastal sea in Japan (Taguchi and Fujiwara 2010). Hypoxia and acidification can severely affect ecosystems, and under a changing climate where O_2 depletion, carbonate dissolution, and pH decline continue to progress, it will be crucial to assess how marine ecosystems will respond to these phenomena occurring individually and together. Many past studies focus on either acidification or hypoxia, but the strong connection between the carbon and O_2 cycles must be considered as we try to predict how shelf ecosystems will adapt to a future climate.

3 Carbon and oxygen cycles: Sensitivity to changes in environmental forcing

3.1 Introduction

Future climate change will affect every aspect of the ocean, from its physics to its chemistry and its biology. In particular, biogeochemical cycles will not only be altered directly by the rising partial pressure of carbon dioxide (pCO_2) in the atmosphere, but also by indirect effects, such as higher temperatures and changes in wind strength and patterns (Bakun 1990, Falkowski et al. 2000, etc). For instance, the increase in sea surface temperatures and the strengthening of stratification as global climate warms is expected to be sufficient to intensify existing hypoxia and generate hypoxia in new areas (Rabalais et al. 2010). If the biotic carbon to nitrogen ratio (C:N) increases under elevated CO_2 conditions (as observed in a mesocosm experiment), anthropogenic CO_2 emissions may extend tropical oxygen (O_2) deficient zones (Oschlies et al. 2008). Models project a decline in O_2 concentrations in the oceans during the 21st century (Frölicher et al. 2009) and over the next 100,000 years (Shaffer et al. 2009). Recent warming in the 1990s has already produced an estimated global oceanic O_2 outgassing of $0.3 \pm 0.4\ 10^{14}$ mol-O_2 yr^{-1} (Keeling and Garcia 2002).

Oxygen Minimum Zones (OMZ) are permanently hypoxic regions of the open ocean ($O_2 < 60$ mmol m^{-3}), typically along the continental margins of the eastern Pacific, eastern Atlantic, and Indian oceans (Helly and Levin 2004, Stramma et al. 2008). In these areas, respiration of marine animals is limited (Brewer and Peltzer 2009). Helly and Levin (2004) identified regions where OMZs affect outer continental shelves and upper slopes, suggesting that changes in these OMZs could impact shallower waters.

Decline of O_2 concentrations in different OMZs as well as shoaling of their upper boundaries has already been observed (Whitney et al. 2007, Stramma et al. 2008). The shoaling of the OMZ in the northeast Pacific may be a cause of the recently observed hypoxic events in the coastal waters off Oregon and California (Grantham et al. 2004, Bograd et al. 2008, Chan et al. 2008), which in some cases turned the shelves into "dead zones" due to the widespread mortality of benthic animals. As not only low O_2, but also high pCO_2 may impose a physiological strain in marine animals, the combined effect of increasing pCO_2 and decreasing O_2 may lead to the expansion of regions unsuitable for aerobic marine life in the future (Brewer and Peltzer 2009). Identifying the key drivers of coastal hypoxia from in situ observations only is difficult; hence, modelling efforts can help to achieve this goal.

Cycling of carbon in the ocean is also expected to change as the climate changes. Declines in pH and increases in surface pCO_2 have already been observed in two > 20-year time series, at stations ALOHA in the central North Pacific (Dore et al. 2009) and BATS, off Bermuda in the North Atlantic (Bates 2007), as well as in a 10 year-long record at station ESTOC (100 km north off Gran Canaria Island in the North Atlantic, Santana-Casiano et al., 2007). These stations show that surface ocean pCO_2 has increased at rates indistinguishable from the atmospheric increase (Bindoff et al. 2007). Model simulations indicate a pH decrease of ~ 0.1 off the US west coast since pre-industrial times (Hauri et al. 2009). Corrosive waters have been observed on the shelves off western North America, where undersaturation with respect to aragonite (the less stable form of calcium carbonate ($CaCO_3$) found in corals for example) occurred at depths between 40 and 120 m, even reaching the surface along one transect off northern

California (Feely et al. 2008). These observations support two global model projections that predicted surface undersaturation for aragonite by 2050 in the Southern Ocean (Orr et al. 2005) or when atmospheric CO_2 exceeds 409 ppm (probably within next decade) in the Arctic Ocean (Steinacher et al. 2009). The decrease of pH and $CaCO_3$ saturation due to the cumulative addition of CO_2 to the ocean from the burning of fossil fuels is referred to as 'ocean acidification'. The ecosystem response to this phenomenon is complex: although the probability of replacement of calcareous species by other species usually increases at lower pH, decreases of competitors or of predators may favour some calcareous species (Wootton et al. 2008). Overall, the potential for marine organisms to adapt to ocean acidification and the implications for ocean ecosystems are not well understood (Doney et al. 2009).

It is uncertain how carbon and O_2 cycles in the coastal ocean will respond to climate change and what mechanisms lie behind the changes observed so far. To improve our understanding of how these cycles may change in a future climate, this study uses a coastal model to investigate their sensitivity to different forcings. A quasi-2D configuration represents summer upwelling over the southern Vancouver Island shelf, as described in the previous chapter. Four experiments aim to determine the model sensitivity to changes in upwelling, the depth of the OMZ, ocean temperature, and inorganic carbon concentration. The experiments are detailed in section 3.2 and the results for each are given separately in section 3.3. A discussion follows in section 3.4.

3.2 Design of sensitivity experiments

I have developed a quasi-2D application of the Regional Ocean Modelling System (ROMS) to model wind-driven upwelling on the Vancouver Island shelf. The domain represents a transect perpendicular to the isobaths (i.e., cross-shore distance vs. depth) at ~ 49ºN (Figure 2.1). The previous chapter describes in detail the model configuration as well as the biological and sediment modules coupled to the physical component. Appendix B explains how the Vancouver Island Coastal Current (VICC, a northward buoyancy current on the inner shelf) is represented. In the present chapter, a set of model experiments helps to determine the sensitivity of the carbon and O_2 cycles to different forcing and changing conditions. By changing one aspect of the model at a time, I can compare the changes with respect to a Base Experiment. The list below describes the sensitivity simulations performed, which are summarized in Table 3.1. Surface incoming shortwave radiation and net heat fluxes are specified in all experiments as daily values from NCEP reanalysis for the period 27 May to 29 September 1993, at 48.57ºN, 125.62ºW. Wind stress is calculated from observed hourly winds at meteorological buoy 46206 (48.83ºN, 126ºW, Figure 2.1) following Smith (1988), and filtered with a 6 hour low-pass Fast Fourier Transform (FFT) filter.

- **Base Experiment:** Wind and surface heat forcing corresponds to late spring and summer 1993, a year representing a 'normal upwelling summer' with upwelling indices for July and August close to the climatological means (i.e., small upwelling index anomalies, Figure 3.1). Observed deep ocean summer profiles from the study region are used to create average depth profiles to initialize scalar properties (i.e., they are horizontally uniform) and initial velocities are set to zero. To provide

sufficient time for spinup, the experiment starts on 27 May 1993 (day 0). Analysis will start on 16 July (day 50), since sediments take more than a month to approach equilibration (section 2.3).

- **Stronger Upwelling:** Increasing trends in upwelling intensity have been observed in some major coastal upwelling systems of the world during the 20th Century (e.g., Bakun 1990, Schwing and Mendelssohn 1997, McGregor et al. 2007). Intensified summer upwelling due to increased atmospheric pCO_2 is predicted by a regional climate model with high resolution over the coastal region of California (Snyder et al. 2003). Off the Vancouver Island shelf, an ensemble of 18 climate models predicts increased upwelling summer winds in the 21st century (Merryfield et al. 2009). Therefore, it is worth testing the sensitivity of the O_2 and carbon cycles in the model to increased upwelling. The summer of 2002 experienced higher than normal upwelling-favourable winds off Vancouver Island (Figure 3.1). Mean alongshore wind stress was 28 % greater in 2002 than in 1993 for the period 27 May to 29 September (-0.018 N m^{-2} in 1993 vs. -0.023 N m^{-2} in 2002; see Figure 3.2 for a time series of alongshore wind stress). For the period 16 July to 29 September (the period of analysis following 50 days of spinup), mean alongshore wind stress almost tripled in 2002 relative to 1993 (-0.009 N m^{-2} vs. -0.026 N m^{-2}). The Stronger Upwelling Experiment is forced with 2002 wind stress in two simulations: a) with the same spinup as in the Base Experiment (first 50 days with 1993 wind stress); b) forcing the entire simulation with 2002 winds. The first approach allows a comparison of results after a common forcing during the 50 day

spinup period; the second allows examining the effect of using different forcing during spinup.

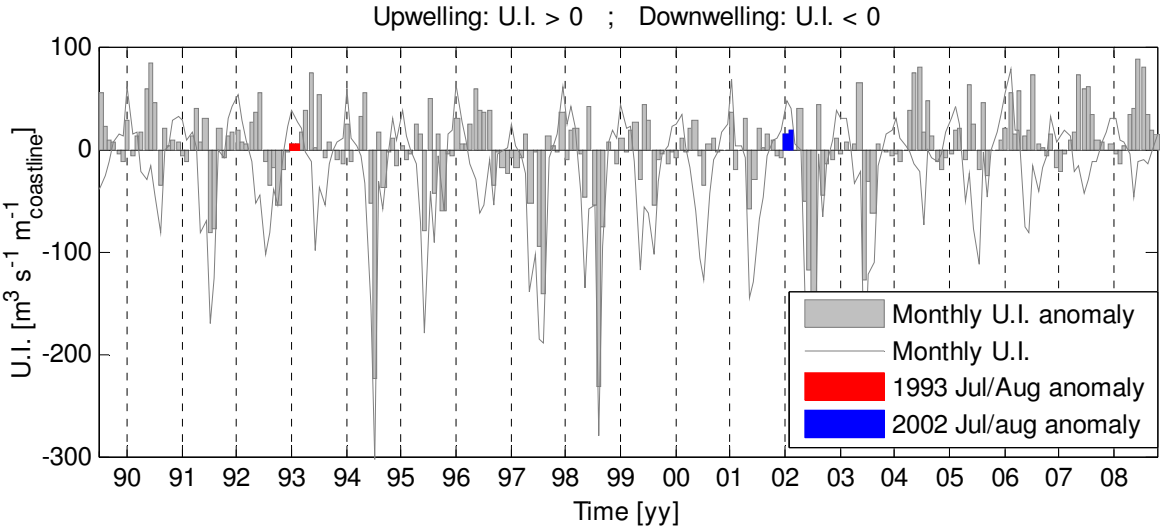

Figure 3.1: Monthly upwelling index (U.I.; grey curve) and monthly U.I. anomaly (grey bars) for 1990 to 2008. The dashed vertical lines indicate July of each year. The red bars for 1993 indicate a year where upwelling was close to normal during July and August (small monthly anomalies). The blue bars for 2002 show a year when upwelling was strong in both July and August (large monthly anomalies for both months).

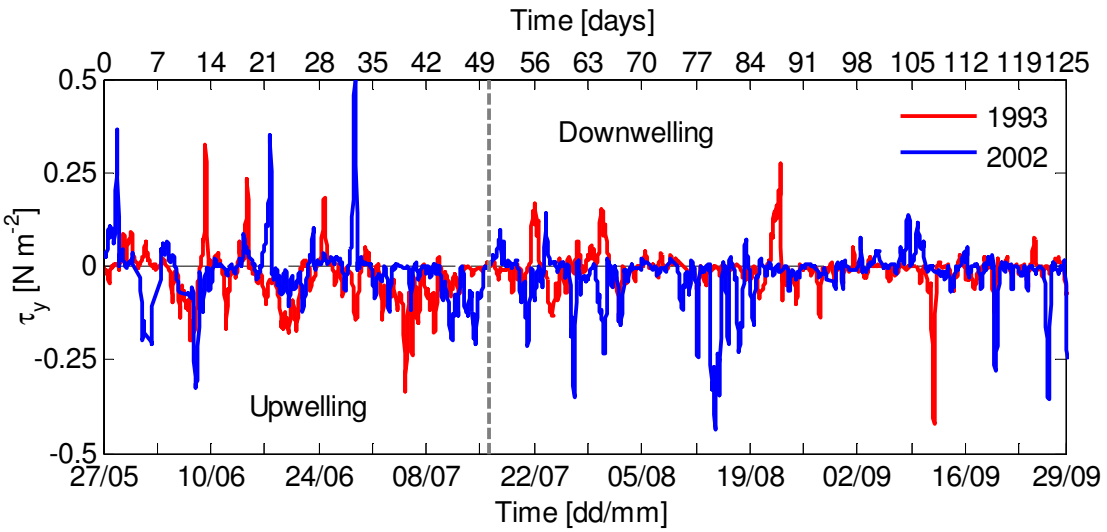

Figure 3.2: Alongshore wind stress for 1993 (red) and 2002 (blue). One of the simulations ('Stronger Upwelling (spinup: 1993) Experiment') uses 1993 winds up to day 50 (dashed grey line), and 2002 winds afterwards.

- **Shallower Oxygen Minimum Zone (OMZ):** Although not all species have the same tolerance to low O_2 concentrations (Vaquer-Sunyer and Duarte 2008), hypoxia is commonly defined as waters with $O_2 < 60$ mmol-O_2 m^{-3} (= 60 μM-O_2 ~ 60 μmol-O_2 kg^{-1} ~ 1.4 mL L^{-1}; Gray et al. 2002, Whitney et al. 2007, Stramma et al. 2008). Whitney et al. (2007) find that the hypoxic threshold at Ocean Station Papa (OSP) has shoaled roughly by 100 m from 1956 to 2006 (from 300 to 400 m). The southern California Current System (CCS) has experienced a similar shoaling of up to 90 m in the period 1984-2006 (Bograd et al. 2008). Moreover, O_2 concentrations in the OMZ are decreasing with observed rates of 0.18 mmol-O_2 m^{-3} yr^{-1} at a depth of 800 m at OSP and 0.15 mmol-O_2 m^{-3} yr^{-1} at a depth of 500 m in the southern CCS region (Whitney et al. 2007, Bograd et al. 2008). To analyze the effect of a shallower and more intense OMZ on the southern Vancouver Island shelf system, I initialize the O_2 field with a hypoxic threshold 100 m shallower than in the original profile and with a minimum concentration of 1.3 mmol-O_2 m^{-3} (Figure 3.3). This value implies a decrease of ~ 9 mmol-O_2 m^{-3}, which represents an O_2 decay for 50 years at the observed rate at 800 m at OSP (consistent with the 100 m shoaling).
- **Warmer Environment Scenario:** The global ocean heat content has been increasing due to increasing concentrations of greenhouse gases in the atmosphere (Levitus et al. 2001, 2009). In the Northeast Pacific, wintertime sea surface temperature (SST) is projected to increase by up to 1.4ºC by 2050 (relative to the 1980-1999 mean), according to an ensemble of 10 IPCC models forced with the A1B emissions scenario (Overland and Wang 2007, Wang et al. 2010). An experiment with higher initial temperature allows studying the response of

biogeochemical cycles on the Vancouver Island shelf to a warmer environment. The amount of warming in the initial conditions represents the depth-dependent temperature increase expected in 50 years (2000 to 2050), as predicted in a global climate model (Canadian Earth System Model (CanESM) 1.1 with emission scenario A2; Arora et al. 2009 and Christian et al. 2010) at the model location closest to the Vancouver Island shelf (50ºN, 130ºW). Figure 3.4 shows temperature profiles from the climate model at that location (means for the decades centred on 2000 and 2050) and their difference (panels a and c, respectively). The latter is added to the initial temperature profile for the Base Experiment. Surface heat fluxes remain as in the Base Experiment, assuming they do not change.

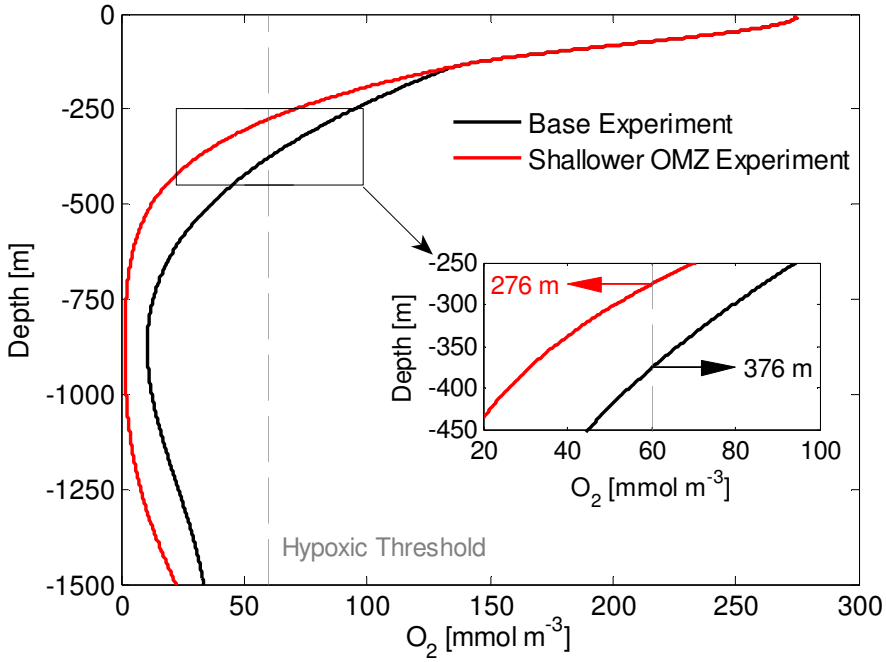

Figure 3.3: Initial O_2 profiles for the Base and Shallower OMZ Experiments (black and red lines, respectively). The inset shows the region where the profiles intersect the hypoxic threshold (vertical dashed grey line at 60 mmol-O_2 m^{-3}). Initial conditions for Base Experiment are based on stations D9 and D11 (1060 and 1590 m deep).

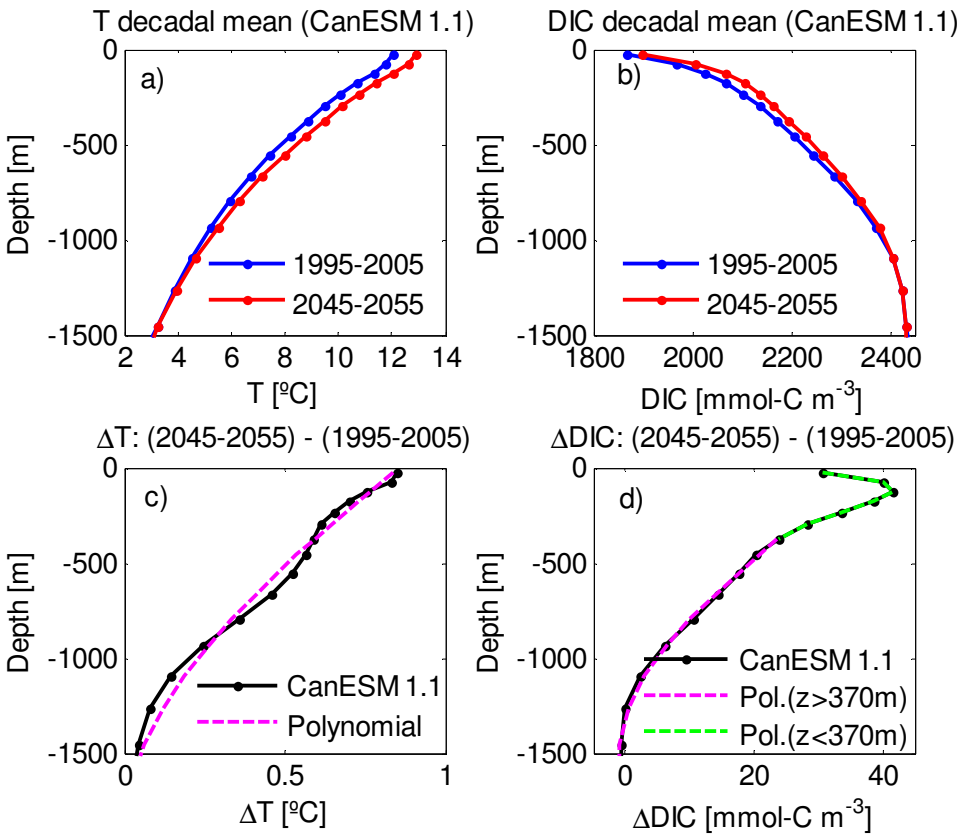

Figure 3.4: Profiles of decadal means centred on years 2000 and 2050 for a) temperature and b) DIC from the Canadian Earth System Model (CanESM 1.1), and profiles of the differences (c: temperature, d: DIC). Dashed curves in c and d are polynomial functions used to represent the increase in temperature and DIC in the initial conditions (Warmer Environment and Higher Carbon Experiments).

- **Higher Carbon Scenario:** As CO_2 increases in the atmosphere due to anthropogenic activities, around one third of emissions are absorbed by the ocean (Sabine et al. 2004, Sabine and Feely 2007). The Higher Carbon Experiment examines the effect of increased atmospheric CO_2 (pCO_{2atm}) and ocean DIC on biogeochemical cycles in the model. The increments correspond to the predicted changes in DIC and pCO_{2atm} over the period 2000 to 2050 from CanESM 1.1 (analogous to the temperature increase in the Warmer Environment Experiment;

Figure 3.4b and d). The pCO_{2atm}, which is set as a constant boundary condition, increases by 143 ppmv relative to the Base Experiment (from 370 to 513 ppmv).

Table 3.1: Description of model sensitivity experiments. CanESM 1.1 stands for Canadian Earth System Model version 1.1 (Arora et al. 2009, Christian et al. 2010). Day 0: 27 May, Day 50: July 16; Day 125 (final day of experiments): 29 September. In the Warmer Environment Experiment, surface heat fluxes are as in the Base Experiment.

Experiment	Description
Base	Control experiment based on 1993 late spring and summer forcing (Day 0: 27 May 1993)
Stronger Upwelling (spinup: 1993)	1993 wind stress (Base Exp.) during spinup (day 0 to 50) 2002 wind stress (increased upwelling) after day 50
Stronger Upwelling (spinup: 2002)	2002 wind stress from day 0
Shallower OMZ	Initial conditions for O_2 with a shallower OMZ (100 m) and lower O_2 concentration.
Shallower OMZ + Stronger Upwelling	Combination of the Shallower OMZ and the Stronger Upwelling (spinup: 2002) Experiments.
Warmer Environment	Higher temperature initial conditions in the ocean (expected 2000 to 2050 warming from CanESM 1.1 'A2' simulation).
Higher Carbon	Higher pCO_{2atm} and DIC initial conditions (expected 2000 to 2050 changes from CanESM 1.1 'A2' simulation)

3.3 Results

3.3.1 Effect of increased upwelling

The overall effect of stronger upwelling can be seen in the fields averaged from day 50 (16 July, first day with 2002 winds) to the end of the experiments (day 125 or 29 September). Time and vertical averages of O_2 and pCO_2 across the shelf are compared for the Base and Stronger Upwelling (spinup: 1993) Experiments (blue and red lines, respectively, in Figure 3.5). The upper 30 m water column experiences higher O_2 concentrations under intensified upwelling over most of the shelf (Figure 3.5a), while below 30 m depth these wind conditions decrease O_2 concentrations (Figure 3.5c). The inner shelf concentrations are similar in both simulations because of restoring to VICC properties. pCO_2 is higher in the bottom layers in the Stronger Upwelling Experiment (Figure 3.5d) and mostly lower in the upper 30 m (Figure 3.5b). However, there is a region of the inner shelf (~ 10 – 25 km from inshore boundary) with higher upper-layer pCO_2 under intensified upwelling; moreover, approximately in the same region O_2 is lower under stronger upwelling relative to the Base Experiment. This result is due to the position of phytoplankton blooms in both simulations, as will be discussed later in this section. Atmospheric pCO_2 concentration is set as a constant boundary condition (pCO_{2atm} = 370 ppmv, dashed grey line in Figure 3.5b). On average, pCO_2 in the upper ocean is lower than pCO_{2atm} over the mid and outer shelf in both experiments, so air-sea CO_2 fluxes are from the atmosphere to the ocean in that region. However, the high DIC concentrations in the VICC lead to pCO_2 higher than pCO_{2atm} on the inner shelf. Note that Figure 3.5b shows the average for the top 30 m of the water column; the surface-layer distribution of time-integrated pCO_2 has a similar pattern but lower values. CO_2

outgassing occurs on the inner 4 km of the model domain in the Base Experiment and within 6 km in the Stronger Upwelling Experiment.

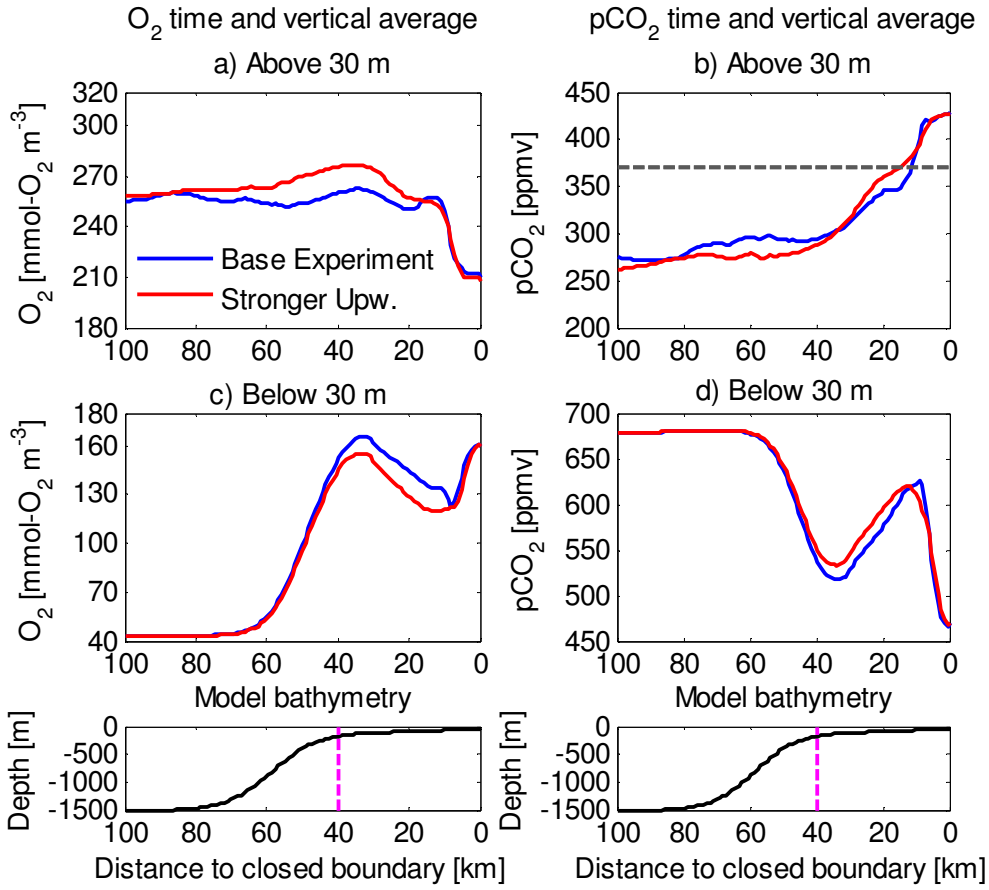

Figure 3.5: Across-shelf distribution of time and vertically averaged (a, c) O_2 and (b, d) pCO_2 for Base (blue) and Strong Upwelling (spinup:1993) (red) Experiments. Time average is for days 50 to 125, after the spinup period. Vertical averages are shown for the upper 30 m of the water column (a, b) and from 30 m to the seafloor (c, d). Bottom panels show the bathymetry, with a magenta vertical line indicating the edge of the shelf break. The dashed grey line in (b) indicates atmospheric pCO_2 (370 ppmv).

To show the evolution over time for the two wind forcing cases, spatial and temporal distributions (Hovmöller plots) are presented in Figure 3.6 for O_2 in the near-bottom layer of the model. The thickness of this layer changes from 1.4 m near the shallowest boundary to 5 m at the shelf break (magenta line in bathymetry profiles in Figure 3.5) due

to the σ vertical coordinates of the model, but it represents correctly the bottom boundary layer (except within the shallowest 3 km of the domain, see section 2.3). The first 50 days are the same in Figure 3.6a and b, since 1993 wind forcing during spinup is used in both experiments (spinup not shown). Under more intense upwelling, low O_2 concentrations develop in the bottom layer over the shelf. In particular, the hypoxic boundary (60 mmol-O_2 m^{-3}, bold black contour) spreads inshore across the shelf after the intense upwelling-favourable wind event centred on day 80 (Figure 3.6b). Onshore advection causes the O_2 decrease with time on the outer shelf in both experiments: Figure 3.7b and d show O_2 sinks and transport fluxes in the bottom ~ 10 m of a 130 m deep water column (shown as a dashed white line in Figure 3.6) for each simulation. In the Stronger Upwelling (spinup: 1993) Experiment (Figure 3.7d), the persistently southward alongshore winds result in a consistent advection of low O_2 water onto the shelf. In contrast, weaker summer winds in the Base Experiment (Figure 3.7b) lead to weaker advection that is balanced by vertical mixing (which is always positive, bringing higher O_2 from overlaying layers in both simulations). Biological O_2 sinks (nitrification and remineralization in the water column and sediments) do not contribute significantly to the balance at this depth in either experiment, as little organic matter reaches the seafloor. However, over the mid shelf biological O_2 demand in the sediments contributes to maintaining low concentrations near the bottom, as can be seen in Figure 3.7a and c, which show the O_2 sinks and transport fluxes in the bottom ~ 10 m at a location 90 m deep (dashed black line in Figure 3.6). Over most of the last 75 days of the Base Experiment, O_2 consumption within the sediment layer (black line) is the largest sink of O_2 (Figure 3.7a). In the Strong Upwelling Experiment, onshore advection near the

bottom initiates the hypoxic event at day ~ 85, while O_2 demand in the sediments maintains low O_2 concentrations once winds decay after day 90 (Figure 3.7c).

Between days 100 and 115 of the Stronger Upwelling Experiment, O_2 increases slightly over the near-bottom of the outer shelf (Figure 3.6b) and DIC decreases (not shown) in response to relaxation of upwelling before and during that period. Most of the O_2 increase is due to vertical mixing with overlying layers (Figure 3.7d), which is also responsible for the DIC decrease.

The wind forcing used for spinup during the first 50 days of the Stronger Upwelling Experiment can modify the results. An intense upwelling event between days 35 to 45 in 1993 (~ first week of July), advects the hypoxic threshold closer to the shelf break. Therefore, if 1993 winds are used during spinup, waters on the shelf become more hypoxic than if 2002 winds are used from day 0 (Figure 3.6b and c show near-bottom O_2 concentrations for the two Strong Upwelling Experiments with spinup winds from different years). Hence, the timing of the onset of the upwelling season is another factor determining both the timing and magnitude of hypoxia (and analogously, of events with increased acidity).

Carbon concentrations in the near-bottom layer over the shelf respond to the same processes: dissolved inorganic carbon (DIC) increases due to advection of high DIC from offshore, while sediment remineralization maintains high DIC over the mid shelf during relaxation and periods with weak winds (DIC budget terms not shown). To illustrate the time evolution of the carbon state in the near-bottom layer, Figure 3.8 shows Hovmöller plots for aragonite saturation state (Ω_A). Aragonite is the less stable form of $CaCO_3$ in the ocean and its degree of saturation can be defined by

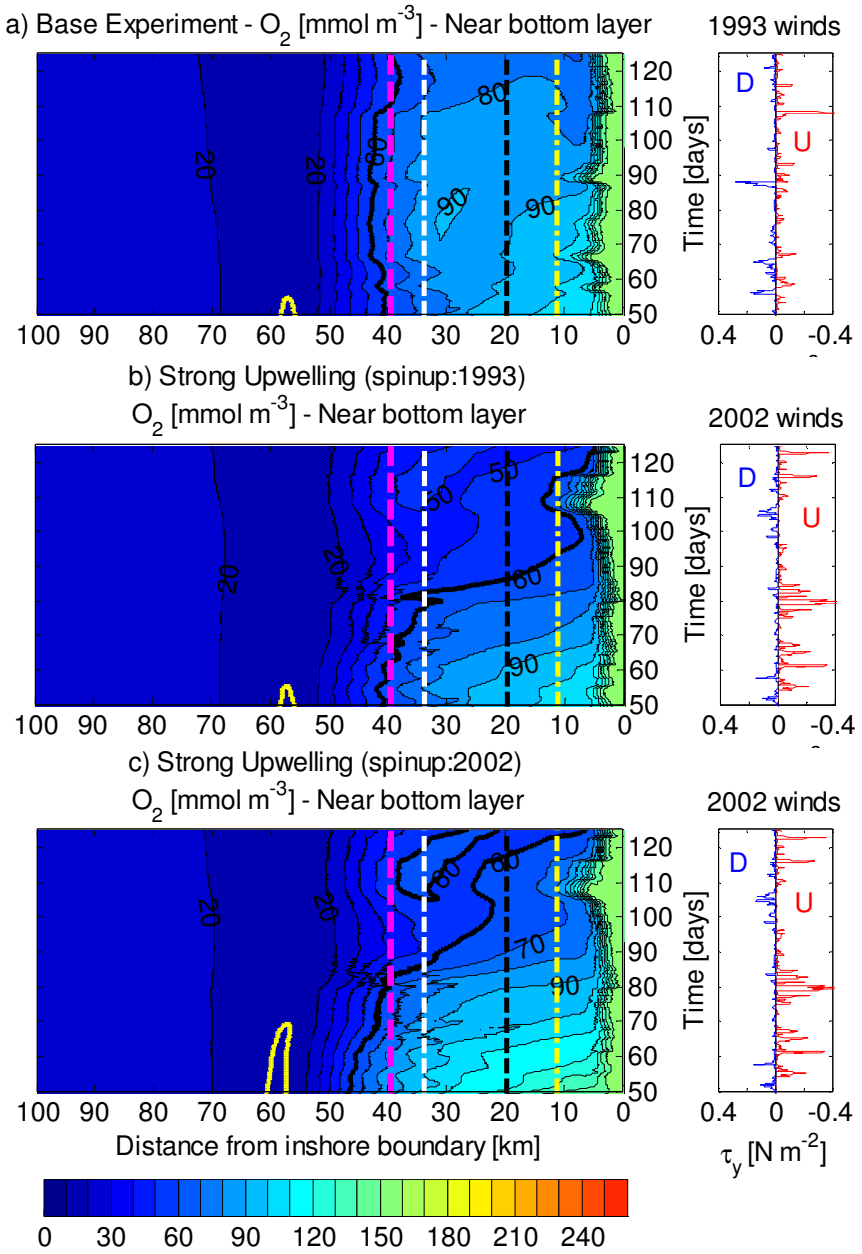

Figure 3.6: Hovmöller plots for near-bottom O_2 concentrations: a) Base, b) Strong Upwelling (spinup: 1993), and c) Strong Upwelling (spinup: 2002) Experiments. Panels on the right show alongshore wind stress for each experiment (upwelling/downwelling in red/blue). Spinup period (first 50 days; common forcing for a and b) not shown. The bold black contour is the hypoxic threshold (60 mmol-O_2 m^{-3}), the bold yellow contour is RI = 1, and the dashed magenta line represents the location of the shelf break. The three sets of dashed lines on the shelf (yellow, black, and white) indicate the 69, 90, and 130 m isobaths.

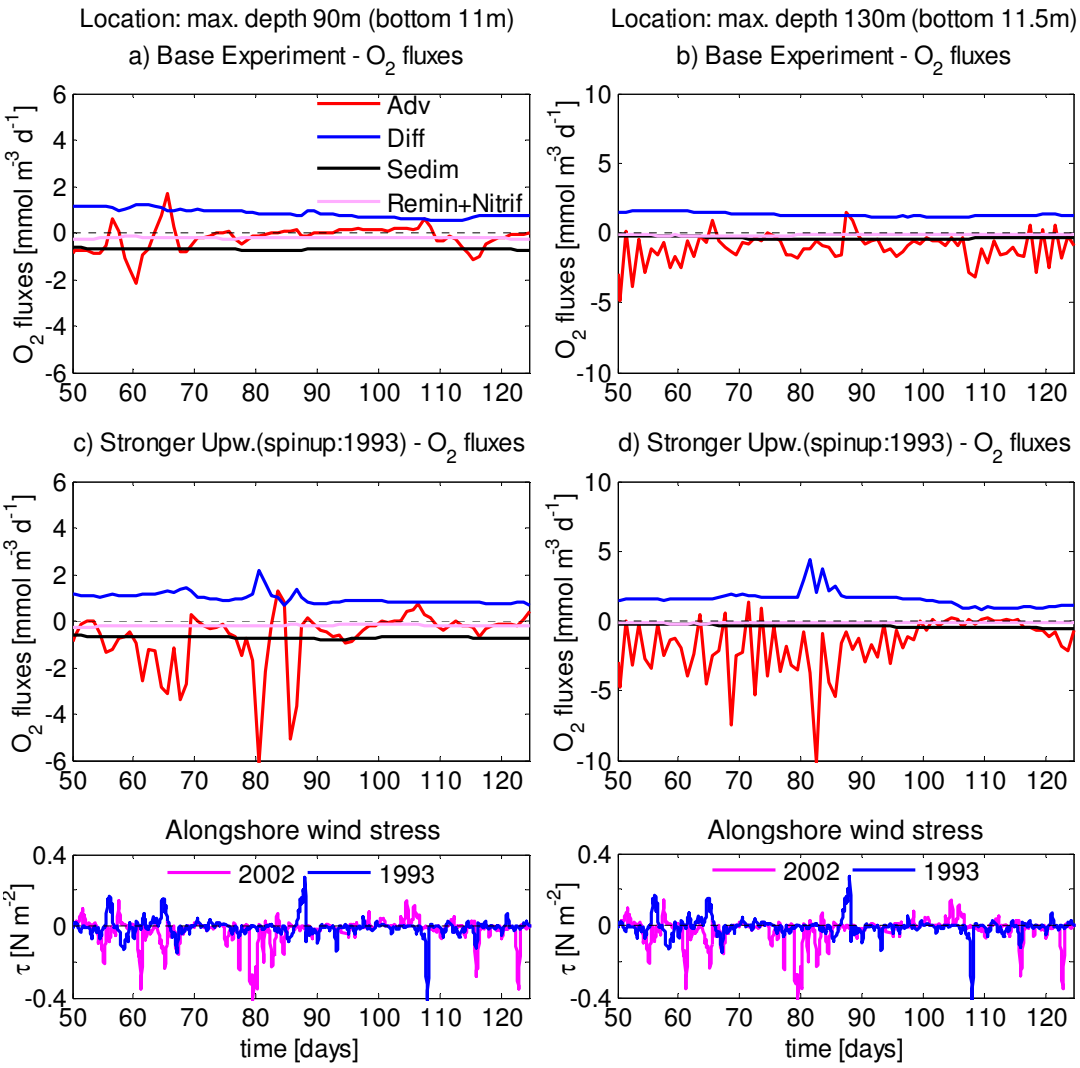

Figure 3.7: Time series of advection (red), diffusion (blue), and biological O_2 sinks (black: remineralization within the sediments, pink: remineralization plus nitrification in the water column) in bottom ~ 10 m of the water column for Base (a,b) and Strong Upwelling (spinup: 1993) (c,d) Experiments. (a,c) at 90 m isobath (dashed black line in Figure 3.6); (b,d) at 130 m isobath (dashed white line in Figure 3.6). Positive (negative) fluxes indicate a gain (loss) of O_2. Bottom panels show alongshore wind stress for both experiments (1993: blue, 2002: magenta), such that upwelling occurs when $\tau < 0$. The initial 50 day spinup (not shown) is the same in both simulations.

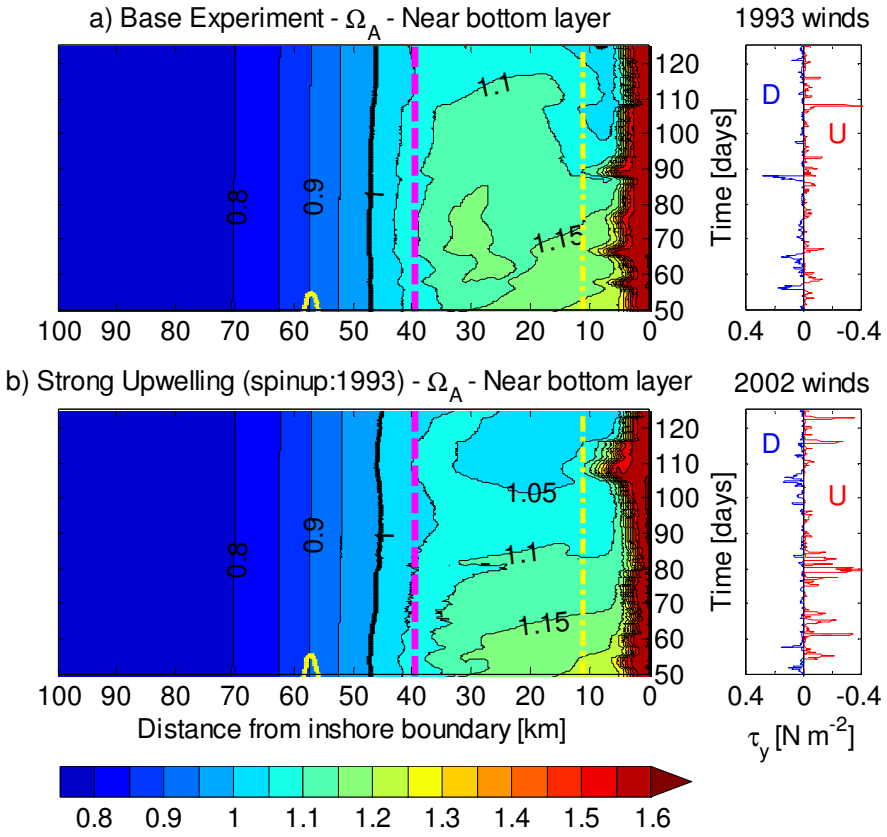

Figure 3.8: Hovmöller plots for near-bottom Ω_A levels: a) Base and b) Strong Upwelling (spinup:1993) Experiments. Panels on the right show alongshore wind stress for each experiment (upwelling/downwelling in red/blue). Spinup period (first 50 days; common forcing for a and b) not shown. The bold black contour is the boundary between saturation and undersaturation ($\Omega_A = 1$), the bold yellow contour is RI = 1. The dashed magenta line indicates the location of the shelf break; the dash-dotted yellow line on the shelf indicates the 69 m isobath.

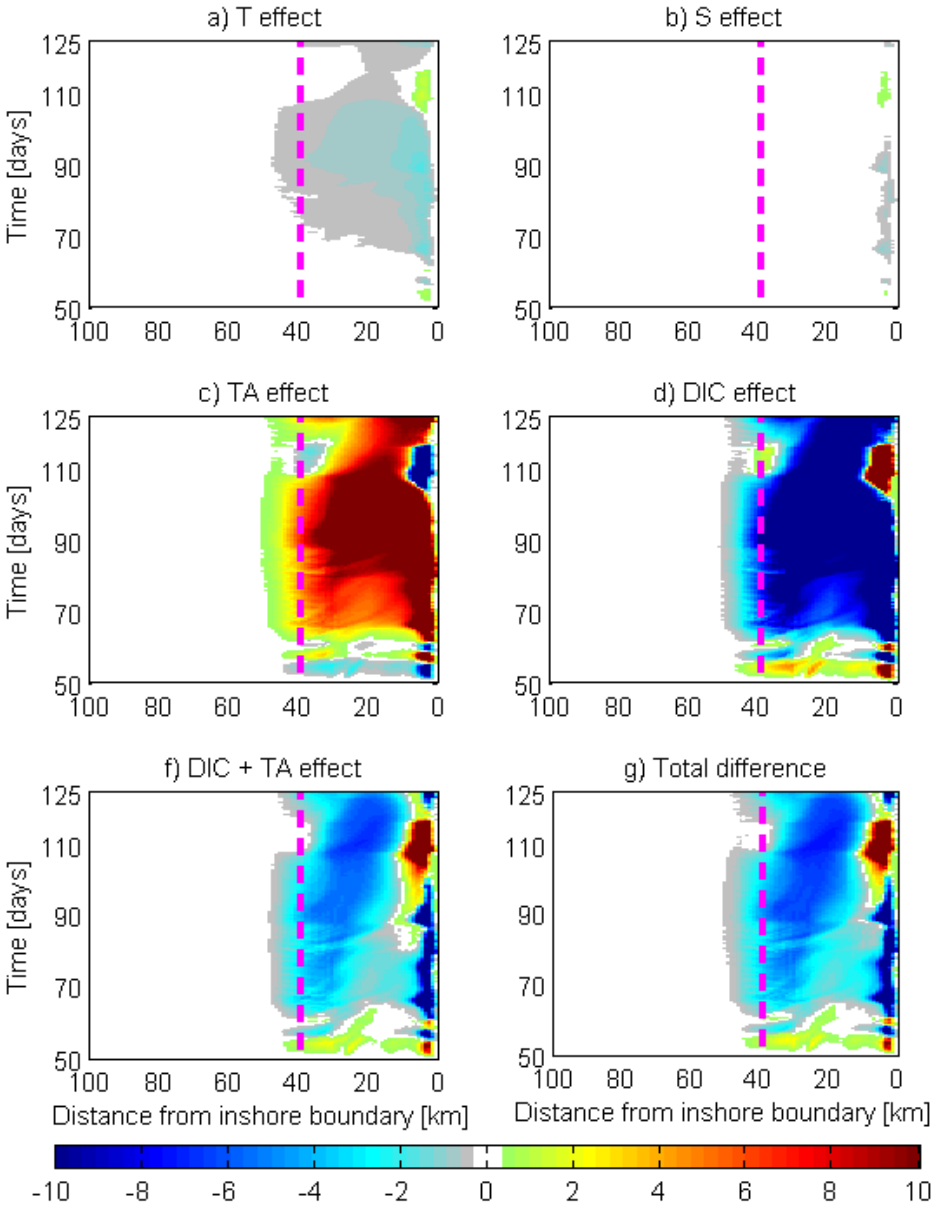

Figure 3.9: Change in near-bottom layer Ω_A [%] between Base and Stronger Upwelling (spinup: 1993) Experiments due to the contributions of each variable (a: temperature, b: salinity, c: total alkalinity (TA), d: DIC), the combination of DIC and TA (e), and all variables taken together (f). The dashed magenta line indicates the location of the shelf break.

$$\Omega_A = \frac{\left[Ca^{2+}\right]\left[CO_3^{2-}\right]}{\left[Ca^{2+}\right]_{sat}\left[CO_3^{2-}\right]_{sat}} \approx \frac{\left[CO_3^{2-}\right]}{\left[CO_3^{2-}\right]_{sat}} \qquad 3.1$$

where [ ] and $[\ ]_{sat}$ represent the concentrations of the carbonate and calcium ions in ambient seawater and at saturation. When $\Omega_A > 1$ (< 1), seawater is supersaturated (undersaturated) with respect to aragonite and favours calcification (dissolution). In the Stronger Upwelling (spinup: 1993) scenario, Ω_A decreases in the near-bottom layer over the shelf near day 90 (bottom panel of Figure 3.8), relative to the Base Experiment (top panel of Figure 3.8).

Hovmöller plots in Figure 3.9a to d depict the change in Ω_A with respect to the Base Experiment (in %), each panel showing the effect of only one variable: temperature, salinity, DIC, and total alkalinity (TA). Figure 3.9e and f show the combined effect of DIC and TA and the total change in Ω_A between experiments. The increase in DIC is primarily responsible for the drop in Ω_A (Figure 3.9d), while the change in TA cancels out about 40 % of the DIC effect (Figure 3.9c). Upwelling also brings colder waters from offshore that reduce the temperature near the bottom over the shelf by up to 3ºC (the mean cooling over the near-bottom shelf is 0.63ºC), which tends to decrease Ω_A by increasing $[CO_3^{2-}]_{sat}$. The reduction in Ω_A due to cooling (Figure 3.9a) is small compared with the change due to DIC (Figure 3.9d). The changes in salinity due to stronger upwelling do not significantly affect Ω_A over the near-bottom of the shelf outside the VICC region (Figure 3.9b). The combined effect of DIC and TA (Figure 3.9e) accounts for essentially all of the change in near-bottom Ω_A between the Base and Strong Upwelling Experiments (Figure 3.9f).

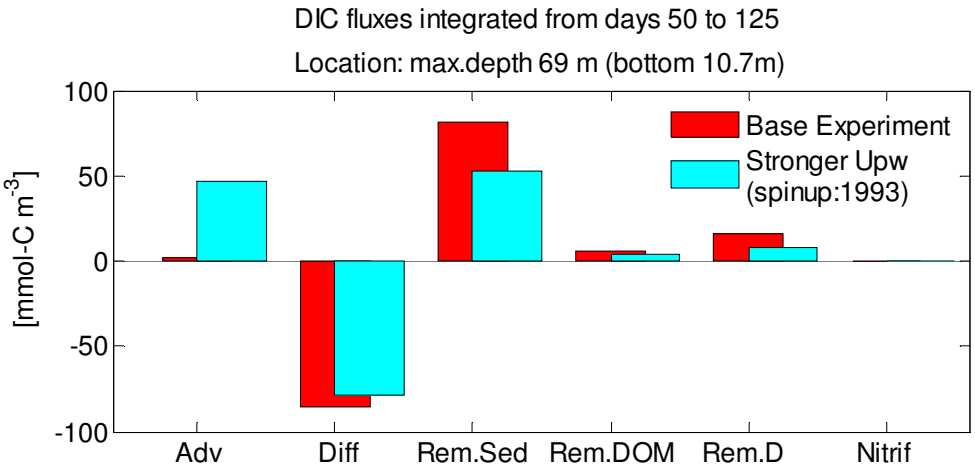

Figure 3.10: Biological sources and physical fluxes of DIC in the bottom ~ 10 m of the water column at a shallow location 69 m deep, integrated from day 50 to 125. Base Experiment in red, Stronger Upwelling (spinup: 1993) Experiment in cyan. The x-axis reads: advection (horizontal + vertical), diffusion, remineralization within the sediments, remineralization of semilabile DOM and detritus, and nitrification.

Over the shallower part of the shelf, stronger upwelling-favourable winds increase the magnitude of the mean advective fluxes between day 50 and 125. Figure 3.10 shows time integrated near-bottom DIC budget terms (sources, mixing, and transport) in the bottom 10 m at a location 69 m deep (dash-dotted yellow line in Figure 3.8). Net advection in the Base Experiment is small: transport of high DIC from the mid shelf during upwelling is almost balanced by transport of low DIC from the VICC during downwelling (although the VICC is DIC-rich relative to shelf waters at similar depths, the bottom layers of the mid and outer shelf have higher DIC than the bottom layers of the VICC, Figure B.4). Note that the Base Experiment undergoes more downwelling events after day 50 than the Stronger Upwelling Experiment (see Figure 3.6a and b). Exchanges with the sediments dominate DIC production, as well as O_2 consumption (not shown) over the shallower part of the shelf in the Base Experiment (Figure 3.10, red bars). In the Stronger Upwelling (spinup: 1993) Experiment (cyan bars) mean exchanges

with the sediments decrease and become comparable with advection. Overall, all biological sources decline with 2002 wind forcing at this location, responding to decreased primary production in shallow waters. Figure 3.11 shows the total primary production for both simulations. During intense upwelling events, phytoplankton are advected offshore in the near surface layers, so the bulk of the primary production occurs over the mid and outer shelf (between 10 and 40 km). This response explains the higher mean O_2 and lower mean pCO_2 concentrations in the upper 30 m of the water column over the outer and mid shelf in Figure 3.5 (offshore of ~ 30 km) for the Strong Upwelling (spinup: 1993) Experiment. Moreover, high primary production over the mid shelf leads to more organic matter reaching the seafloor at those depths, enhancing the exchange of O_2 and DIC with the sediments (between 20 and 30 km from the inshore boundary, i.e., at bottom depths between 90 and 115 m, O_2 and DIC exchange with the sediments increases up to 50 % and ~ 8 % on average).

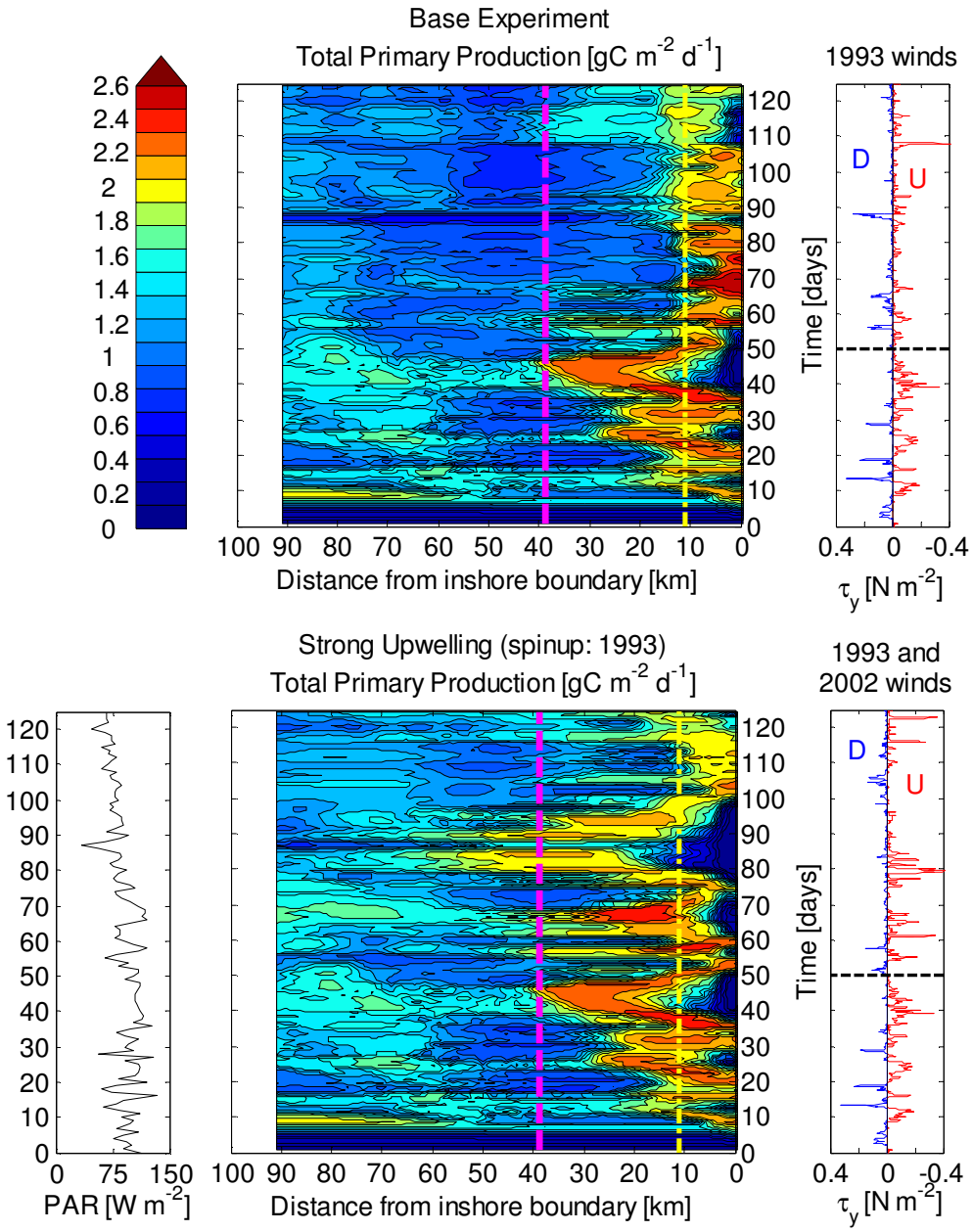

Figure 3.11: Hovmöller plots for total water column primary production in Base and Strong Upwelling (spinup: 1993) Experiments (top and bottom panels, respectively). The dashed magenta line represents the location of the shelf break and the dash-dotted yellow line indicates the 69 m isobath. On the right, alongshore wind stress for each experiment (upwelling/downwelling in red/blue) is shown; the horizontal dashed line at day 50 denotes the end of spinup period with common 1993 forcing. The bottom left panel shows the photosynthetically available radiation (PAR) for both experiments.

3.3.2 Phytoplankton bloom response to wind forcing

Different upwelling events trigger different responses in primary production (Figure 3.11). A simple linear regression between the cross-shelf position of the maximum primary production for the Strong Upwelling (spinup: 1993) Experiment and the corresponding alongshore wind stress (τ_y) shows highest correlation with a lag of 3 days ($r^2 = 0.29^*$, figure not shown). However, phytoplankton do not respond solely to the alongshore wind at a given time, but to recent cumulative forcing. Figure 3.12 shows the time evolution of the cross-shelf position of maximum primary production in blue (left axes; same curve for all four panels), along with a running average of the most recent alongshore wind stress (τ_y) over different averaging periods (1, 5, 9, and 13 days) in green (right axes). The correlation coefficient (r^2) increases with longer averaging periods (T) up to T = 9 days ($r^2 = 0.67^*$). For longer periods, r^2 decreases slightly (T from 1 to 18 days were implemented, although I show only four examples here). Hence, the position of the bloom depends on the winds of at least the last 9 days. The mean τ_y of the previous 9 days for any given time is centred at 4.5 days before that particular time, representing a lag between the position of the phytoplankton blooms and the mean τ_y of ~ 5 days. A linear regression between the 9-day running average of τ_y and the position of the maximum primary production (Figure 3.13), predicts a displacement of the maximum primary production of ~ 20 km from the inshore boundary for a mean alongshore southward wind stress of 0.05 N m^{-2} in the previous 9 days. Note that the difference in the magnitude of primary production cannot be linked unequivocally to the strength of upwelling because surface photosynthetically available radiation (PAR) declined after

* Significance levels for these correlations are very high (i.e., $p < 0.001$), because data points are not independent but serially correlated. Nevertheless, if the series is subsampled in time for the correlations (e.g., taking every 10^{th} data point), p values are still less than 0.05.

day 70 (see inset in Figure 3.11 for PAR time series). Following the weakening (relaxation) of upwelling-favourable winds, the blooms move inshore towards the closed boundary. When upwelling remains weak for a long period of time (e.g., between days 60 and 105 in the Base Experiment, Figure 3.11 upper panel), higher primary production occurs in the shallower near-shore region of the shelf fuelled by the VICC.

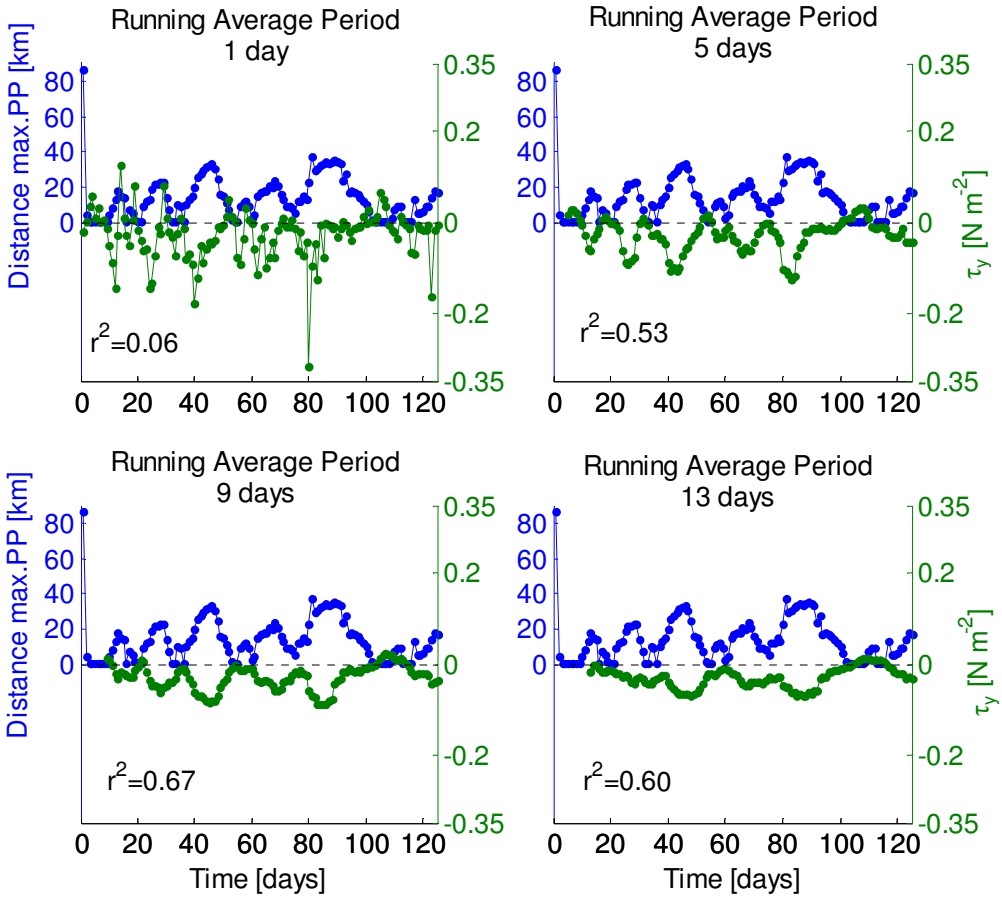

Figure 3.12: Time series of the distance of maximum primary production from the inshore boundary (blue; same curve in all plots) and the running average of the alongshore wind stress (τ_y) for the following averaging periods (green): 1 day (top left), 5 days (top right), 9 days (bottom left), and 13 days (bottom right). Each plot shows the r^2 of the correlation ($p < 0.05$ even when taking every 10^{th} data point); time series are based on the Strong Upwelling (spinup: 1993) Experiment.

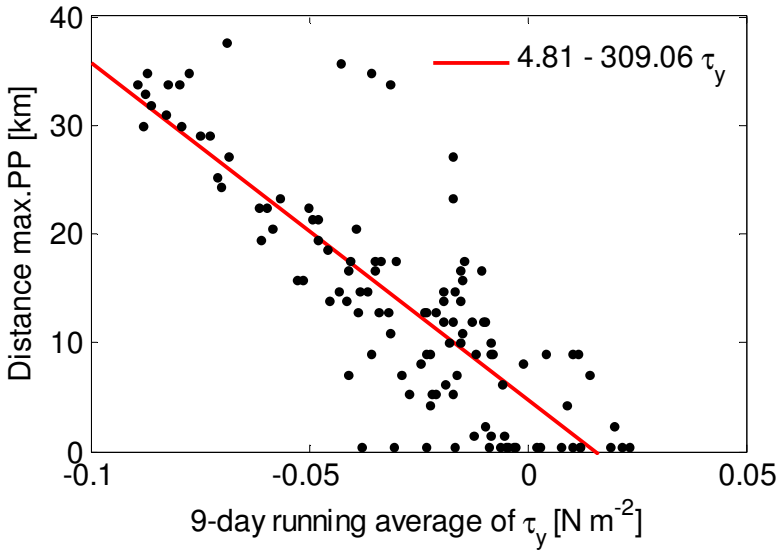

Figure 3.13: Scatter plot of the 9-day running average of alongshore wind stress (τ_y) vs. the cross-shelf location of maximum primary production on the shelf. The red line indicates the linear regression.

3.3.3 Effect of a shallower offshore OMZ

Figure 3.14 compares the vertical across-shelf sections of O_2 concentrations averaged over days 50 to 125 for the Base Experiment (upper panel) and the Shallower OMZ Experiment (middle panel; refer to Figure 3.3 to see the different O_2 initialization in this experiment). In the latter simulation, the mean hypoxic threshold (60 mmol-O_2 m^{-3}, bold black line) reaches the shelf break, penetrating up to ~ 135 m. Moreover, over most of the shelf, the near-bottom layer has a lower O_2 concentration than in the Base Experiment (top panel). The upper layers of both simulations remain similar, since their initialization is the same (Figure 3.3) and the changes in deeper waters do not greatly modify biology in the upper layers or air-sea O_2 exchange. The shoaling of the OMZ does not significantly affect the carbon cycle either, e.g. differences between Base and Shallow OMZ experiments for pCO_2 and Ω_A are < 0.6 % and 0.4 %, respectively (not shown). Once O_2 reaches concentrations lower than 5 mmol-O_2 m^{-3} in the model, denitrification

replaces aerobic remineralization (section 2.2.2). Therefore, DIC is still produced despite O_2 depletion. As mentioned in the previous chapter, this approach assumes that the rate of denitrification is equal to the rate of aerobic remineralization in terms of the rate of oxidation of organic matter. The assumption is based on the similar energy requirements of both reactions (Sarmiento and Gruber 2006).

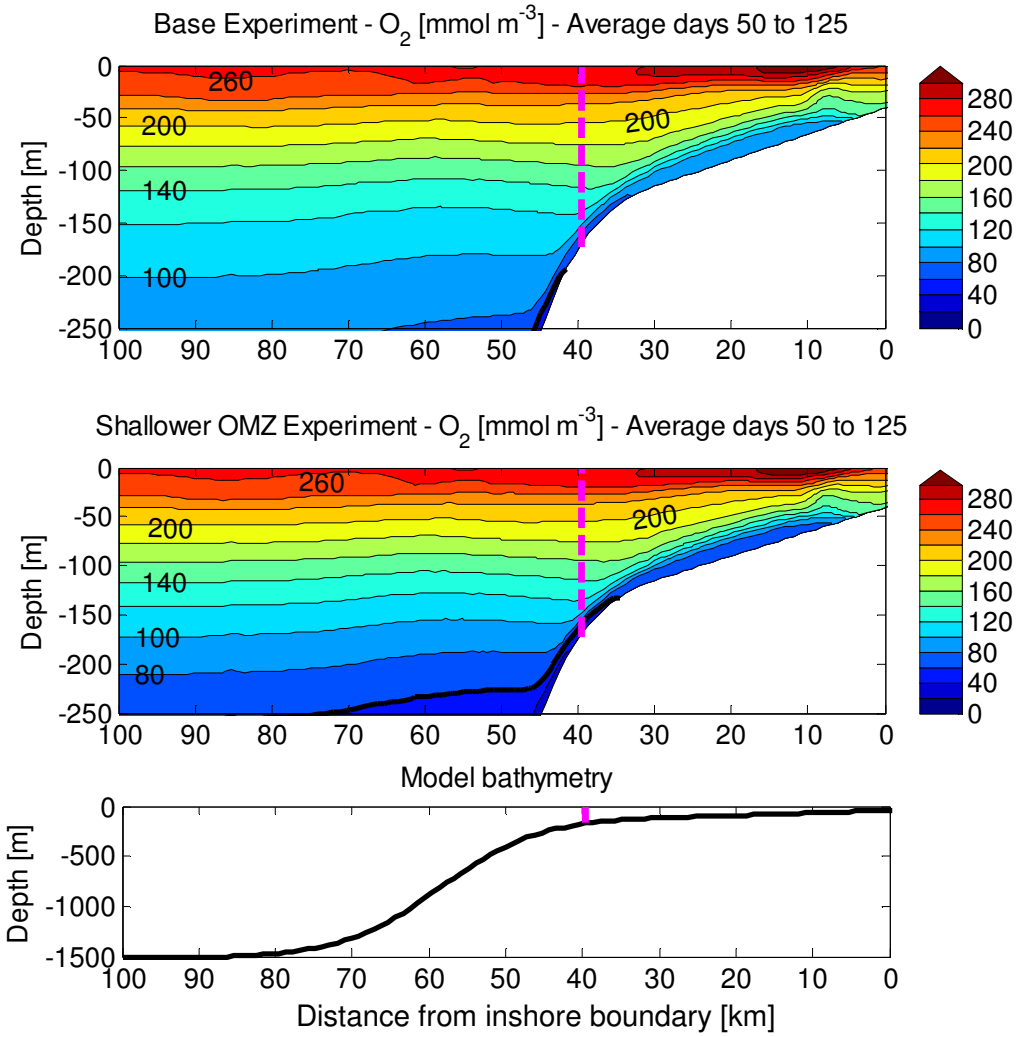

Figure 3.14: Mean O_2 vertical sections (average for days 50 to 125) for Base (upper) and Shallower Oxygen Minimum Zone (OMZ, middle) Experiments, down to 250 m. The bold black contour is the hypoxic threshold (60 mmol-O_2 m^{-3}); the dashed magenta line indicates the position of the shelf break. Lower panel shows full bathymetry profile.

The Hovmöller plot for the Shallower OMZ Experiment shows that after spinup the near-bottom hypoxic threshold is either near the shelf break or over the outer shelf (bold black contour in Figure 3.15a; compare with Base Experiment in Figure 3.6a). In particular, the threshold penetrates onshore after strong upwelling events (after days ~ 40 and 108). Figure 3.16 shows time integrated O_2 budget terms in the bottom ~ 10 m of the water column for three locations across the shelf (bottom depths of 69, 90, and 130 m; spinup is removed from budget). The difference in near-bottom O_2 concentrations between Base and Shallow OMZ Experiments is mainly caused by physical processes, since biological sinks (both in the water column and the sediments) remain largely unchanged for the three locations. In particular, decreasing concentrations of O_2 in the Shallow OMZ Experiment result mostly from the enhanced advection of low O_2 from offshore onto the mid and outer shelf (middle and bottom panels in Figure 3.16). The increase in the vertical diffusive flux partially balances the increased loss to advection (as near-bottom O_2 decreases, vertical gradients are stronger and mixing can transport more O_2 downwards from overlying layers). Over the inner shelf (Figure 3.16, top panel), advective fluxes increase O_2 in the near-bottom layer mainly due to downwelling events after day 50, which introduce high O_2 from the VICC to the bottom layers. In the Shallower OMZ Experiment, the advective O_2 flux decreases relative to the Base Experiment due to onshore transport of lower O_2 water from the mid shelf during upwelling events, counterbalancing the input of O_2 from the VICC during downwelling.

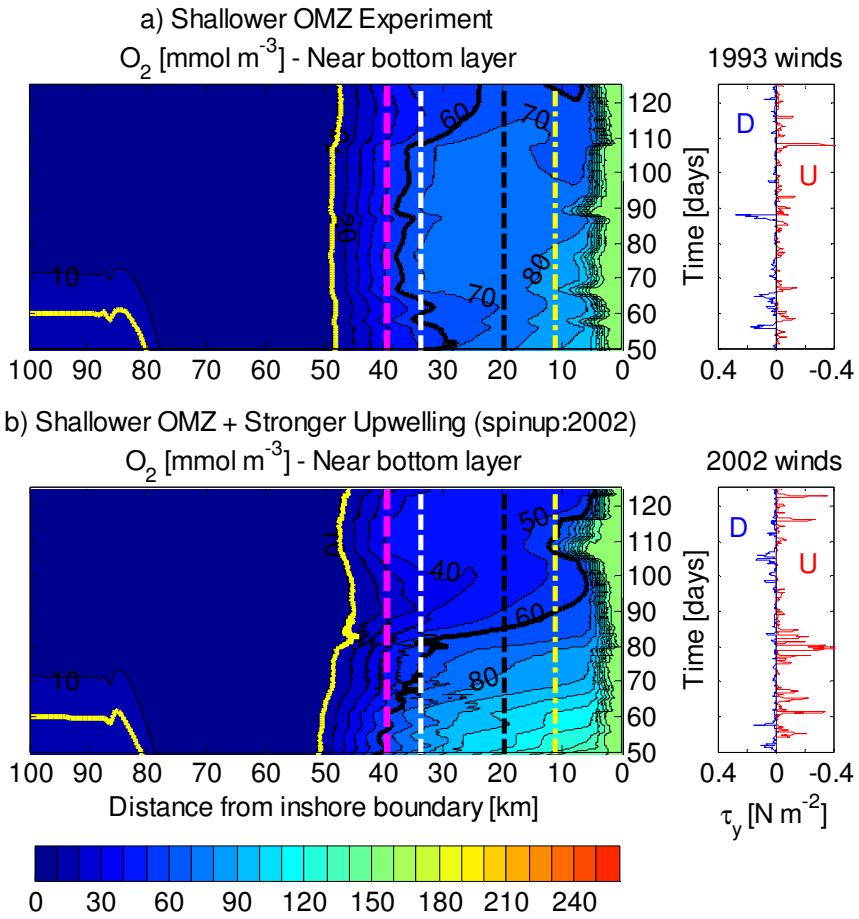

Figure 3.15: Hovmöller plots for near-bottom O_2 concentrations: a) Shallower OMZ and b) Shallower OMZ plus Strong Upwelling (spinup:2002) Experiments. Panels on the right show alongshore wind stress for each experiment (upwelling/downwelling in red/blue). Spinup period (first 50 days) not shown. The bold black contour is the hypoxic threshold (60 mmol-O_2 m^{-3}), the bold yellow contour is RI = 1, and the dashed magenta line indicates the location of the shelf break. The three dashed lines on the shelf (yellow, black, and white) indicate the 69, 90, and 130 m isobaths.

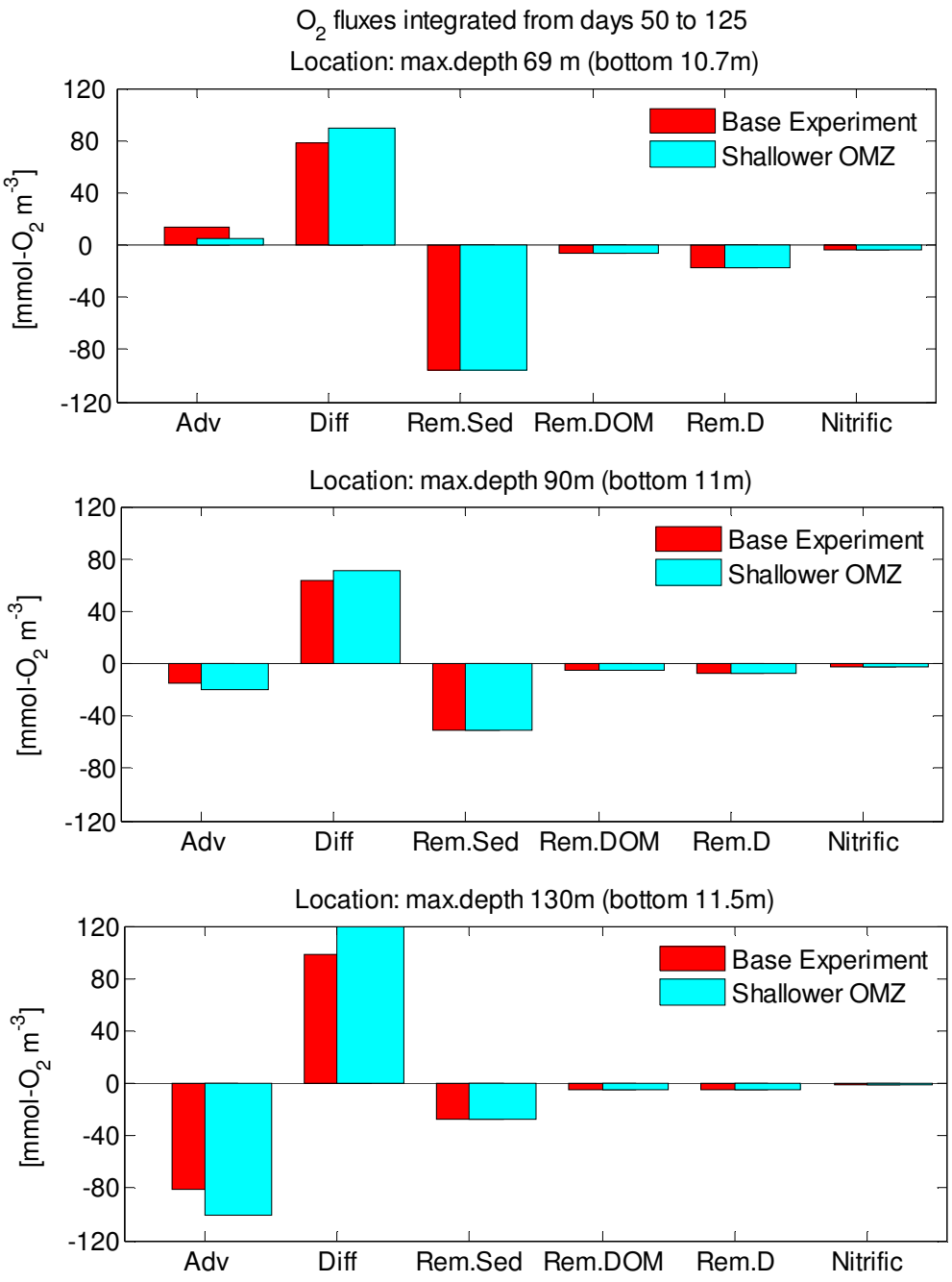

Figure 3.16: Biological sinks and physical fluxes of O_2 in the bottom ~ 10 m of the water column at three locations (top: 69 m, middle: 90 m, and bottom: 130 m deep), integrated from day 50 to 125. Base Experiment in red, Shallower OMZ in blue. The x-axis reads: advection (horizontal + vertical), diffusion, remineralization within the sediments, remineralization of semilabile DOM and detritus, and nitrification.

If the Shallower OMZ and Stronger Upwelling Experiments are combined (using winds from 2002 from day 0), O_2 concentrations decrease even further in the near-bottom layer over the shelf (Figure 3.15b; compare with Strong Upwelling (spinup: 2002) Experiment in Figure 3.6c). The bold yellow contours in all panels of Figure 3.15 and Figure 3.6 represent the $RI = 1$ boundary that delimits the aerobic stress zone (Brewer and Peltzer 2009). In the Shallower OMZ Experiments ((Figure 3.15a and b), the region with $RI \leq 1$ expands greatly compared with the Base and Stronger Upwelling Experiments (Figure 3.6a to c) due to the lower O_2 concentrations in the near-bottom of the open ocean (pCO_2 does not change significantly).

3.3.4 Effect of a warmer environment

The cross-shelf distribution of time (day 50 to 125) and vertical averages of O_2 and pCO_2 allow comparison of the Warmer Environment Experiment (i.e., higher initial temperatures, see section 3.2 and Table 3.1) with the Base Experiment (Figure 3.17; Base Experiment in blue, Warmer Environment Experiment in red). In the case of mean O_2 concentrations, the experiments differ mainly in the upper 30 m of the water column (Figure 3.17a), with lower O_2 concentrations in the warmer scenario. Differences in O_2 are negligible below 30 m depth (Figure 3.17c). On the other hand, mean pCO_2 is higher both above and below 30 m depth (Figure 3.17b and d, respectively), although differences are somewhat larger in the lower layers.

Both O_2 and pCO_2 are affected directly by increases in temperature (e.g., by changes in solubility at the air-sea interface), as well as by indirect effects (e.g., changes in O_2, DIC, and total alkalinity (TA) due to altered primary production associated with warmer waters; note that remineralization rates are not temperature dependent). In the case of

pCO_2, another direct effect of increasing temperature is the modification of the dissociation constants of carbonic acid, which shifts the equilibrium among the three constituents of DIC toward higher pCO_2. Hovmöller plots in Figure 3.18 separate out the effects of TA, DIC, and temperature on the increase in pCO_2 in the near-bottom layer (Figure 3.18a, b, and c, respectively; changes in salinity are negligible, so do not affect pCO_2). Figure 3.18d shows the total pCO_2 change between the experiments (as a percentage).

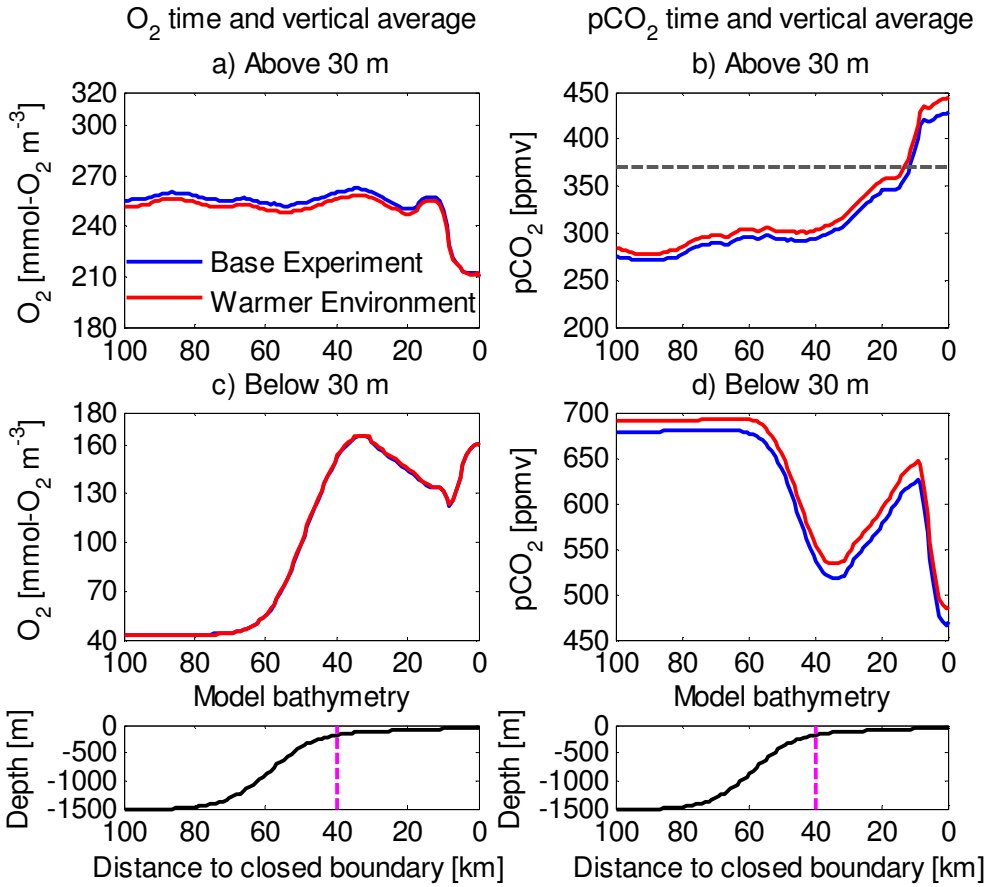

Figure 3.17: Across-shelf distribution of time and vertically averaged (a, c) O_2 and (b, d) pCO_2 for Base (blue) and Warmer Environment (red) Experiments. Time average is for days 50 to 125, after the spinup period. Vertical averages are shown for the upper 30 m of the water column (a, b) and below 30 m until the seafloor (c, d). Bottom panels show the bathymetry profile, with a magenta vertical line indicating the location of the shelf break. The dashed grey line in (b) indicates the atmospheric pCO_2 (370 ppmv).

The direct effect of temperature dominates the pCO_2 change near the bottom, while the effects of changes in DIC and TA are smaller (the DIC effect opposes that of temperature for the most part). The histograms in Figure 3.18 (e and f) show the frequency distribution of individual contributions to the changes in pCO_2 in the near-bottom layer over the shelf (as a percentage). In Figure 3.18e, the similar distributions of the blue (combined effect of all variables) and red (temperature effect only) bars emphasize the dominant role of temperature. In Figure 3.18f, the histogram combines temperature and DIC effects (grey bars) to highlight the DIC contribution.

Similarly, temperature dominates the reduction in pH in the bottom layer over the shelf, but not of Ω_A. Histograms in Figure 3.19c and d show the individual contributions to changes in pH and Ω_A in the deepest layer of the model. Blue and red bars are similar for pH (meaning that warming can explain most of the pH reduction in the near-bottom layer over the shelf), while both temperature and DIC contribute to the Ω_A increase. Note that warming decreases pH (i.e., 'acidifies' the system) while increasing Ω_A (i.e., favours calcification by moving the system towards supersaturation). This seemingly contradictory effect results from the decrease in $[CO_3^{2-}]_{sat}$ with higher temperature, which counter-balances the decrease in $[CO_3^{2-}]$ (see equation 3.1).

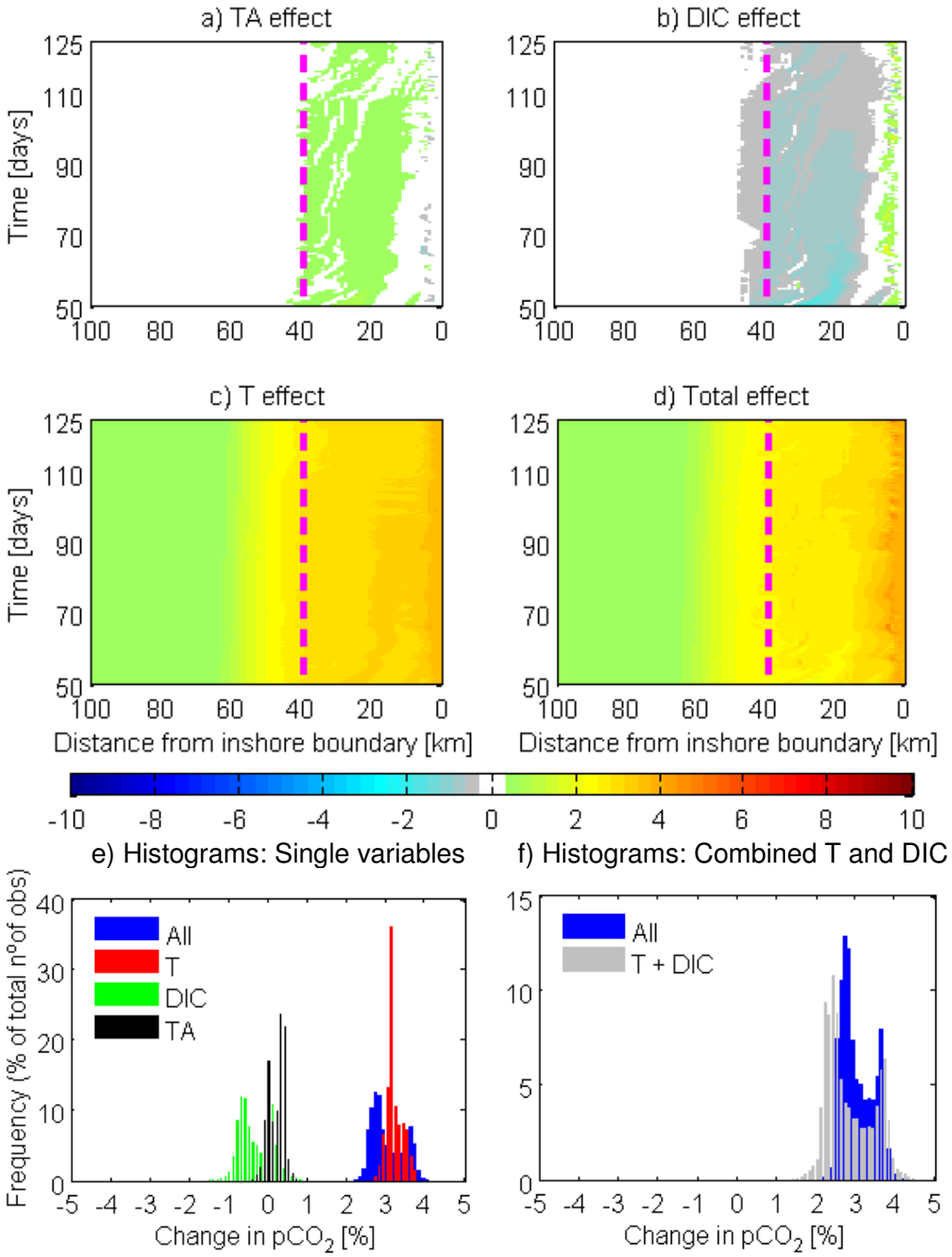

Figure 3.18: Change in near-bottom layer pCO_2 [%] between the Base and Warmer Environment Experiments due to the effect of changes in (a) TA, (b) DIC, (c) temperature, and (d) all combined. The initial 50 days (spinup time) are not shown; the dashed magenta line indicates the location of the shelf break. Histograms show the distribution of these changes over the shelf (except area with strong VICC restoring on inner 3 km) for each individual variable (e) and for the combined effect of temperature and DIC (f). Blue bars in both histograms represent the total change between the experiments (note different vertical scales in e and f).

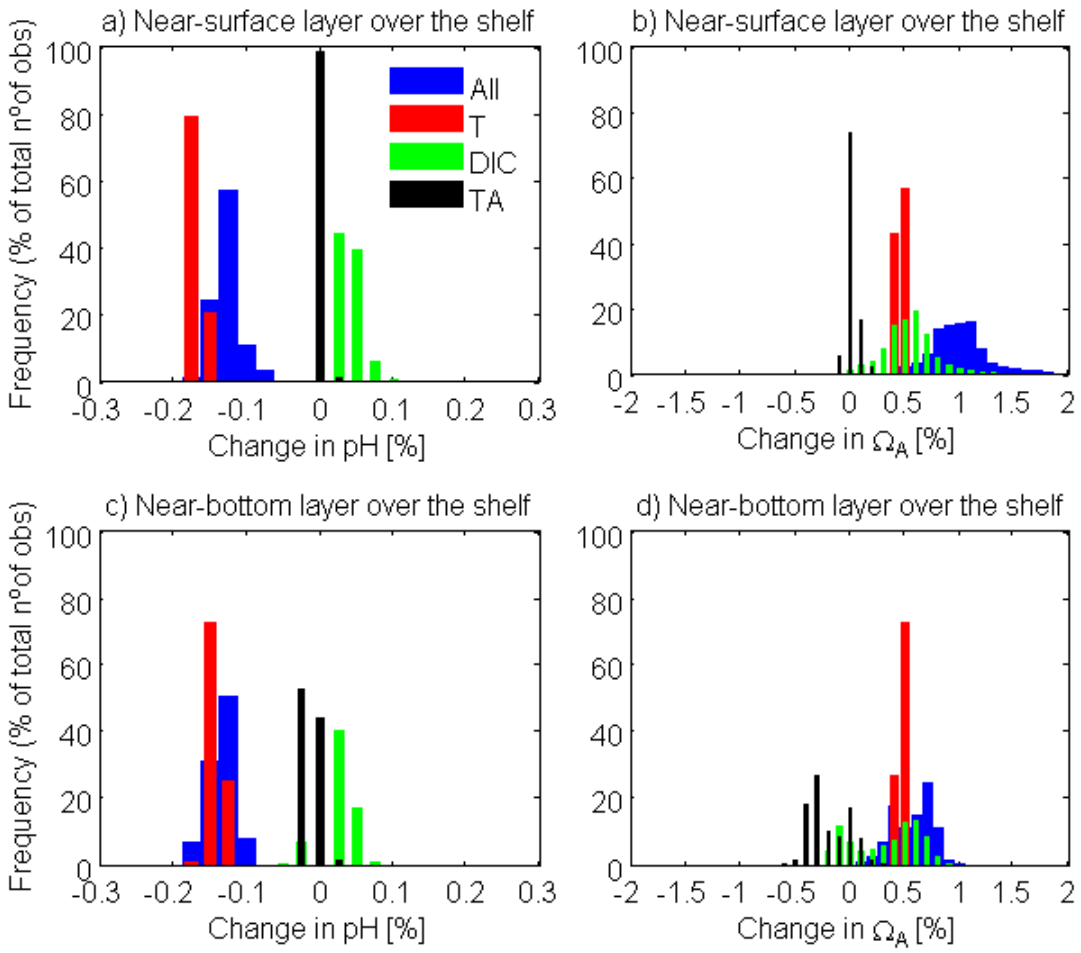

Figure 3.19: Histograms of the change in pH and Ω_A [%] between the Base and Warmer Environment Experiments due to changes in each variable (temperature in red, DIC in green, and TA in black), and the combined effect off all variables (i.e., the net difference between experiments, blue bars). Left (a, c): pH; Right (b, d): Ω_A; Upper (a, b): near-surface layer; Lower (c, d): near-bottom layer. The histograms represent the frequency distribution between days 50 and 125 over the shelf, except for the area with strong VICC restoring (i.e., from ~ 3 km to 40 km, at the magenta line in Figure 3.18).

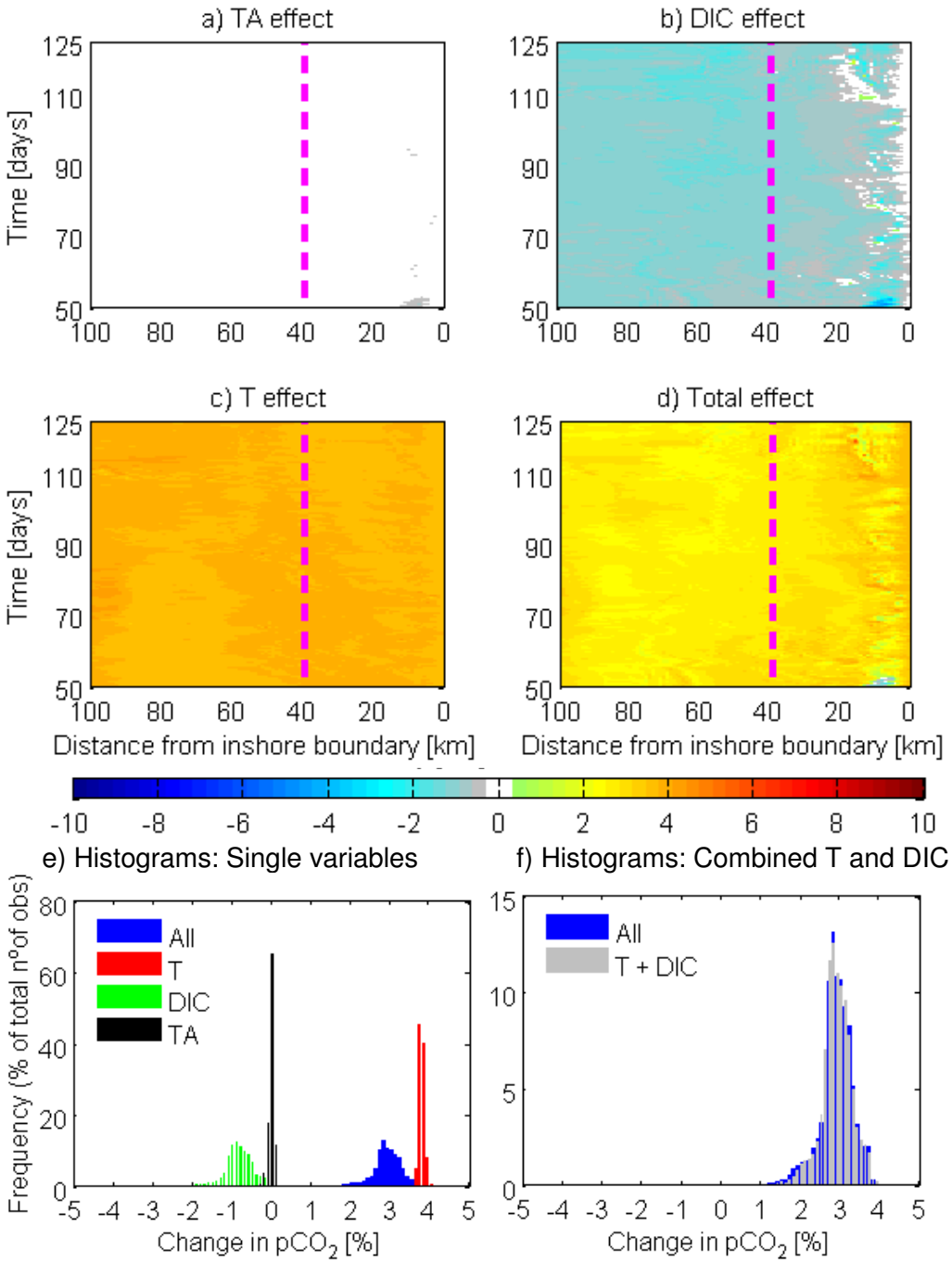

Figure 3.20: Change in near-surface layer pCO_2 [%] between the Base and Warmer Environment Experiments due to the effect of changes in (a) TA, (b) DIC, (c) temperature, and (d) all combined. The initial 50 days (spinup time) are not shown; the dashed magenta line indicates the location of the shelf break. Histograms show the distribution of these changes over the shelf (except area with strong VICC restoring on inner 3 km) for each individual variable (e) and for the combined effect of temperature and DIC (f). Blue bars in both histograms represent the total change between the experiments (note different vertical scales in e and f).

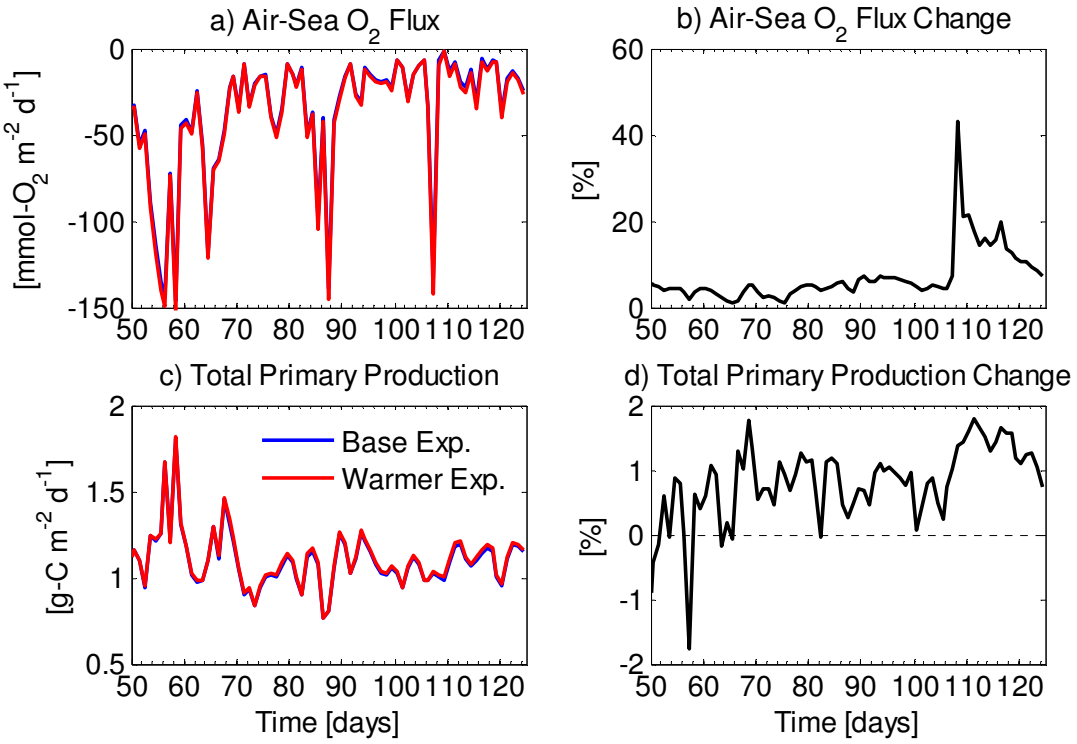

Figure 3.21: Time series of (a) air-sea O_2 fluxes and (c) total primary production for the Base (blue) and Warmer (red) Environment Experiments averaged over the shelf, as well as the changes between simulations (b: air-sea O_2 flux into the ocean; d: total primary production). Changes in b and d are in percentages (positive/negative changes indicate the intensification/ reduction of primary production or air-sea flux into the ocean).

The increase in near-surface pCO_2 can also be examined in terms of the individual effects of TA, DIC, and temperature (Figure 3.20). Temperature and DIC changes together are responsible for the net pCO_2 change in the Warmer Environment Experiment. The two effects are opposed: increasing temperature increases pCO_2, while temperature-associated changes in DIC reduce it. Higher temperature affects DIC in the near-surface in two ways: i) warmer waters reduce the solubility of CO_2 and therefore reduce the absorption of atmospheric CO_2; and ii) the maximum phytoplankton growth rate (ν) increases with temperature (Eppley (1972) and equation A.3).

For O_2, warmer temperature lowers the saturation concentration, which implies an increase in O_2 outgassing from surface layers (Figure 3.21a and b). In addition, when phytoplankton growth is enhanced, O_2 production increases and intensifies outgassing to the atmosphere (Figure 3.21c and d).

3.3.5 Higher Carbon Experiment

Higher DIC initial conditions (see Figure 3.4 and Table 3.1 for a description of the experiment) increase pCO_2 throughout the model domain, as shown in the across-shelf sections in Figure 3.22: the top and middle panels present pCO_2 (averaged between days 50 and 125) for the Base and Higher Carbon Experiments, respectively. The bold black contours represent the atmospheric pCO_2 in each experiment (370 ppmv in the Base Experiment and 513 ppmv in the Higher Carbon Experiment, which is representative of the year 2050, see section 3.2), showing that over most of the shelf the surface ocean is in average undersaturated in both simulations and absorbs CO_2 from the atmosphere. However, surface VICC waters within 4 km from the inshore boundary are oversaturated in the Base Experiment (releasing CO_2 to the atmosphere), in contrast to the Higher Carbon Experiment. The downward air-sea flux of CO_2 (positive in the model convention) increases across the shelf in the Higher Carbon Experiment, compared with the Base Experiment (Figure 3.23). In particular, during the strong upwelling event around day 108, the inner shelf location (69 m deep, upper panel Figure 3.23) releases CO_2 to the atmosphere (negative air-sea flux) in the Base Experiment (blue), due to the offshore transport of high DIC waters from the VICC. During the same event at the same location in the Higher Carbon Experiment (red), air-sea CO_2 fluxes into the ocean are reduced but not reversed.

Aragonite undersaturation expands considerably over the shelf in this scenario: the saturation state is below unity after day 50 in the near-bottom layer over the whole shelf seaward of 8 km from the inshore boundary (Figure 3.24), where the VICC carries waters with lower DIC relative to near-bottom waters over the shelf. In the Base Experiment, near-bottom waters with $\Omega_A \leq 1$ are found offshore of ~ 45 km from the inshore boundary (Figure 3.8). Moreover, the saturation horizon shoals ~ 250 m in the deep ocean offshore, and is found over the shelf up to ~ 30 m above the seafloor (averaged pCO_2 values of 710 and 800 ppmv coincide with the average saturation horizon in the Base and Higher Carbon Experiments, respectively. Note that the 710 ppmv pCO_2 level lies below 250 m depth in the Base Experiment and therefore does not appear in the upper panel of Figure 3.22, while 800 ppmv water occupies almost the whole near-bottom of the shelf in the Higher Carbon Experiment).

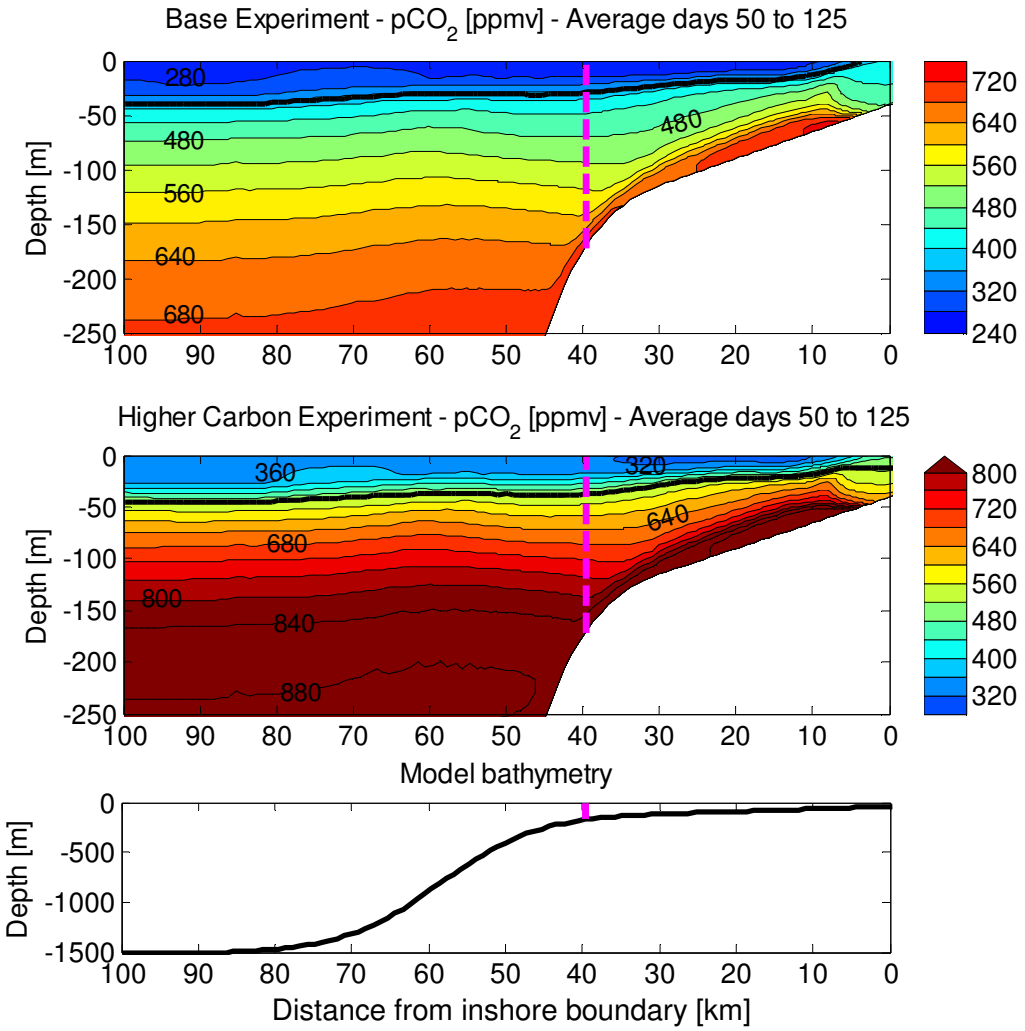

Figure 3.22: Mean pCO_2 vertical sections (average for days 50 to 125) for Base (top) and Higher Carbon (middle) Experiments, down to 250 m. The bold black contour indicates the atmospheric pCO_2 in each experiment (370 and 513 ppmv for the Base and Higher Carbon Experiments, respectively; the latter simulation represents the year 2050, see experiment description in section 3.2). The colour scale is the same in both vertical sections; the dashed magenta line indicates the position of the shelf break. Lower panel shows full bathymetry profile.

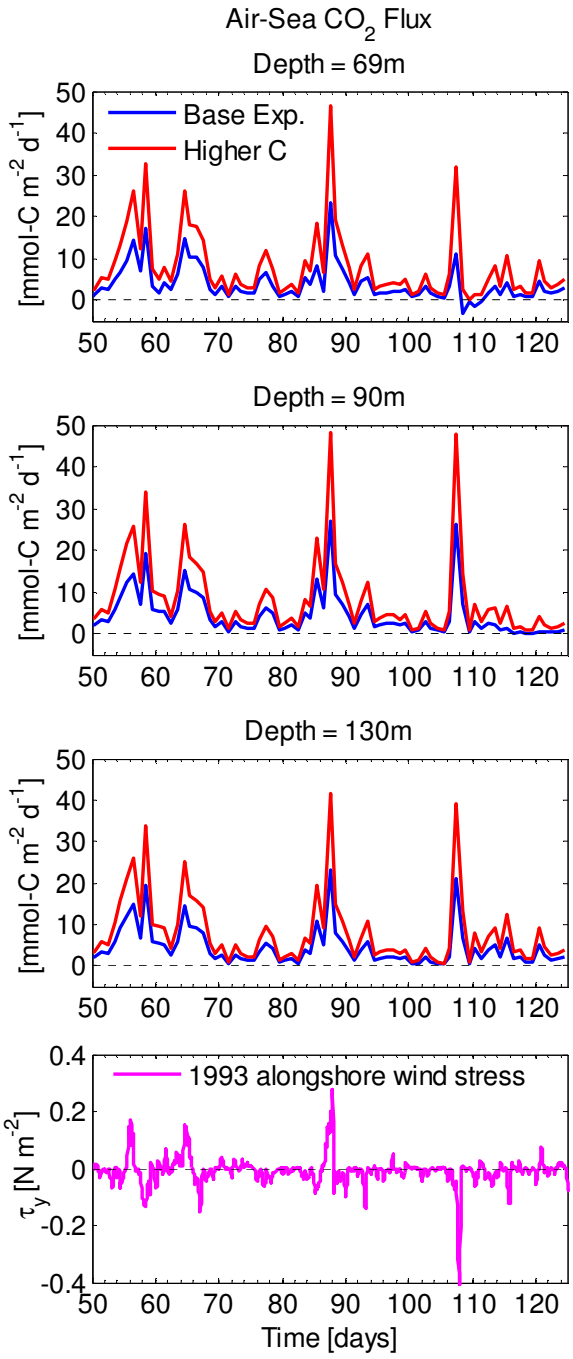

Figure 3.23: Time series of air-sea CO_2 flux into the ocean for the Base (blue) and Higher Carbon (red) Experiments for 3 locations: 69, 90, and 130 m isobaths. Bottom panel shows the alongshore wind stress for the experiments (1993 winds in both cases). Positive fluxes indicate absorption by the ocean.

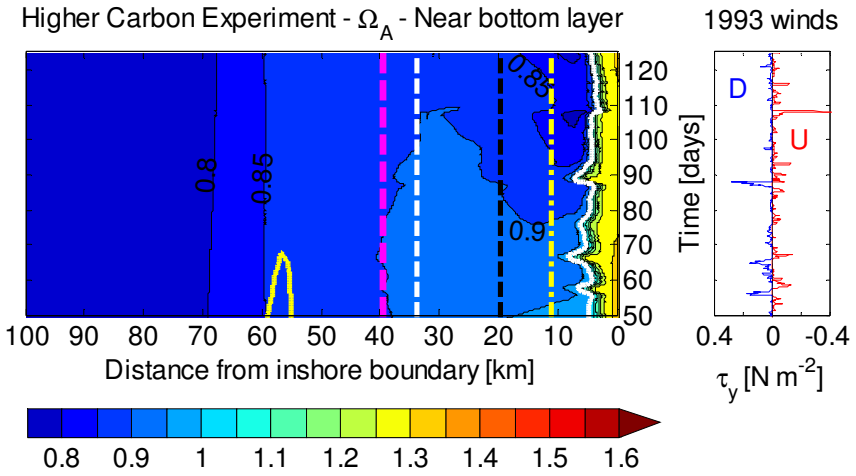

Figure 3.24: Hovmöller plot for near-bottom Ω_A in the Higher Carbon Experiment. Right hand panel shows alongshore wind stress (upwelling/downwelling in red/blue). Spinup period (first 50 days) not shown. The bold white contour represents the boundary between saturation and undersaturation (Ω_A = 1), the bold yellow contour represents the location of RI = 1, and the dashed magenta line indicates the location of the shelf break. The three dashed lines on the shelf (yellow, black, and white) indicate the 69, 90, and 130 m isobaths, respectively. Compare this figure with Figure 3.8 for the Base Experiment (note the Ω_A = 1 contour is white here to improve visualization).

3.4 Discussion and conclusions

The experiments described in this chapter provide insight into the sensitivity of the carbon and O_2 cycles to different forcing or initial conditions in a seasonal upwelling region. The ultimate goal is to understand how biogeochemical cycles will respond to climate change in the coastal ocean, in order to provide input into planning for mitigation and adaptation. While 3D models will eventually be required, the present work contributes towards the goal by focusing on the sensitivities of biogeochemical cycling to environmental factors, individually and collectively, that may change (in most cases, certainly will) as the anthropocene evolves. The experiments aim to identify important processes that will regulate the state of the coastal ocean as the climate changes.

Lower O_2, pH, and Ω_A in the near-bottom layers are triggered by advection of low O_2 and high DIC from offshore (especially after a strong upwelling event such as the one at day ~ 80 in the Stronger Upwelling Experiment). These lower values are efficiently maintained after that by remineralization in the sediments. Under intensified upwelling, O_2 consumption and DIC production in the sediments are enhanced on the mid shelf due to offshore transport of near-surface phytoplankton blooms (which increases deposition of organic matter to the seafloor over the mid shelf). The Ω_A decrease in the Stronger Upwelling Experiment (as well as the pH decrease, not shown) responds mainly to the DIC increase (and is partially compensated by the increase in TA), while advection of cooler waters has a second order effect. These results emphasize the potential negative impact that increased upwelling may have on benthic ecosystems, along the lines of the consequences first hypothesized by Bakun (1990). O_2 concentrations in particular are demonstrated to be sensitive to intensified upwelling, since hypoxia develops in the near-bottom waters on the shelf in both Strong Upwelling Experiments.

Differences between the two Stronger Upwelling Experiments with different wind conditions during the first 50 days (spinup period) demonstrate the effect of the timing of the onset of the upwelling season. If summer upwelling is stronger and starts earlier ("spinup: 1993" case), O_2-poor and DIC-rich near-bottom waters are advected upwards closer to the shelf break earlier in the season. Thus, subsequent upwelling events further reduce O_2, pH, and Ω_A in the near-bottom layers over the shelf. A regional climate model with 40 km horizontal resolution projects a one-month delay for the onset of upwelling on the northern California shelf for increased CO_2 conditions (560 to 686 ppmv), as well as intensified upwelling (Snyder et al. 2003). In the context of the present

study, a delayed upwelling season would reduce the potential for hypoxia and acidification on the Vancouver Island shelf. Nevertheless, Barth et al. (2007) reported on the negative consequences of a one-month delay in the 2005 transition to upwelling-favourable wind stress on the California and Oregon shelves (warm waters, low nutrient levels, low primary productivity, and low recruitment of rocky intertidal organisms).

The effect of a shallower OMZ is straightforward: it moves the hypoxic threshold closer to the shelf break, so upwelling events bring waters of lower O_2 concentration onto the shelf. Therefore, the combination of stronger upwelling and a shallower OMZ would further reduce O_2 concentrations on the shelf, representing a potential stressor for ecosystems. The present model represents the wide shelf off Vancouver Island: despite the considerable shelf width, the influence of a shallower OMZ still reaches the inner shelf. The effect could be more severe on narrower shelves, where upwelling can transport offshore waters to even shallower depths onshore. The expected overall decrease in O_2 concentration in the subsurface open ocean would lead to an expansion of the region with $RI < 1$, implying a larger area where aerobic marine life would be under stress (Brewer and Peltzer 2009). In none of the experiments performed did RI reach values below unity over the shelf (although O_2 levels did decline below the 60 mmol-O_2 m^{-3} hypoxic threshold). $RI = 1$ may be a better indicator of the onset of 'severe hypoxia', usually considered to be 0.5 mL/L ~ 20 mmol-O_2 m^{-3} (e.g., Monteiro et al. 2006, Chan et al. 2008, Diaz and Rosenberg 2008).

In the Warmer Environment Experiment, the direct effect of higher temperature leads to an increase in pCO_2 and a reduction in pH. Indirect effects on DIC play a role near the surface, partially offsetting the pCO_2 increase and pH decrease due to warming (DIC

diminishes due to enhanced primary production and reduced invasion of CO_2 from the atmosphere). It appears that warming would lead to a small net reduction in pH. However, higher temperatures actually increase Ω_A, so the overall effect in this experiment is to move the system away from aragonite dissolution, emphasizing the complexity of the carbonate system in the ocean. Nevertheless, future warming of ocean waters will occur along with other environmental changes, so we may not observe these opposing changes in pH and Ω_A (i.e., decreasing pH and increasing Ω_A). For instance, if warming occurs together with an increase in DIC (i.e., a combination of the Warmer Environment and Higher Carbon Experiments), the effect of DIC dominates Ω_A changes (not shown). The increase in stratification due to preferential surface warming (Figure 3.4c) is only moderate in the Warmer Environment Experiment. Future simulations could assess the effect of increased stratification, in particular evaluating its role relative to increased upwelling (as in Auad et al., 2006).

Currently, the model employs remineralization rates that do not depend on temperature. Consequences for both carbon and O_2 cycles could be enhanced if remineralization increased with temperature (more O_2 consumption and DIC production, especially in the lower layers and in the sediments, leading to further development of hypoxia and acidification).

Under the Higher Carbon Experiment, near-bottom waters over the shelf (beyond the area of influence of the VICC) become corrosive after 50 days (the period considered as spinup time), i.e., Ω_A drops below unity. As most of the DIC increase was imposed over the upper 1000 m of the water column (Figure 3.4), DIC at greater depths of the ocean does not change appreciably, providing an explanation for why the area with $RI < 1$

expands only modestly compared with the Base Experiment (only deep waters exhibit low RI values). In the current model configuration, no biological process depends on DIC concentration, so the increase of DIC in the ocean does not affect the O_2 or nitrogen cycles directly. There is no calcification in the model and decreased calcification in a carbon-rich ocean may affect photosynthesis and phytoplankton community structure (Paasche 1962, Sikes et al. 1980, Paasche 2001), providing a potential link between O_2 and carbon. Furthermore, the model is missing a negative feedback in the carbon cycle that could potentially reduce acidification: a reduction of calcification (increase of $CaCO_3$ dissolution) reduces the production (enhances the consumption) of CO_2 in seawater through the reaction:

$$2\ HCO_3^- + Ca^{++} \longleftrightarrow CO_2 + CaCO_3 + H_2O \qquad 3.2$$

where the reaction proceeding from left to right represents calcification, and the reverse reaction represents dissolution of $CaCO_3$ shells. Most of the literature agrees on the reduction of calcification rates with higher pCO_2, although a recent paper by Iglesias-Rodríguez et al. (2008) reported the opposite and aroused some controversy (see Riebesell et al., 2008). Nevertheless, blooms of calcifiers (e.g., coccolithophorids) are not frequent over the Vancouver Island shelf, although they have been observed (Debby Ianson, personal communication).

In conclusion, in the model experiments performed here, the O_2 and carbon cycles are coupled through their sensitivity to upwelling and warming. On the other hand, only O_2 concentrations respond to the shoaling of the OMZ, and only the carbon cycle responds to changes in the oceanic DIC inventory. Nonetheless, changes in the depth of the OMZ and carbon content of the ocean will not be independent of each other, as both respond to the increase in atmospheric CO_2 from human activities. The response of the

"acidification state" of the coastal ocean to climate change will be complex due to the nonlinear dependence of Ω_A and pH on changes in temperature, salinity, DIC, and TA. The perturbations analysed here (increased upwelling, shallower OMZ, warming, and higher DIC and pCO_{2atm} concentrations) consistently drive the system towards lower O_2, pH, and Ω_A states (except for the increase in Ω_A in the Warmer Environment Experiment). Therefore, this sensitivity analysis would suggest that a region such as the Vancouver Island shelf could potentially develop hypoxia and corrosive conditions ($\Omega_A < 1$) in the future. Full 3D biogeochemical modelling as well as continuous and simultaneous observations of carbon and O_2 are needed to assess the current state of these cycles in the coastal ocean and how they vary in time and space.

4 Coupled O_2 and carbon effects due to denitrification

4.1 Introduction

The coastal ocean acts as a buffer region between the land and the deep ocean, exposed to many anthropogenic alterations before they reach open waters. The shallow waters of the ocean support diverse and active ecosystems, as well as a significant fraction of the world's fisheries (Pauly and Christensen 1995). There have been several estimates of the amount of carbon that the continental margins sequester from the atmosphere (Tsunogai et al. 1999, Cai et al. 2003, Thomas et al. 2004, Cai and Dai 2004, Borges et al. 2005, etc); recent studies suggest that exchanges with the bottom sediment layer may be critical to the potential uptake of atmospheric carbon dioxide (CO_2) by the coastal ocean (Fennel et al. 2008, Thomas et al. 2009).

Below the oxygenated upper few millimetres of the sediment layer and where oxygen (O_2) concentrations in the water column are low, anaerobic processes become important. Nitrate (NO_3^-) is the first electron acceptor used in place of O_2 in the decomposition of organic matter because of its higher energy yield (Sarmiento and Gruber 2006). The remineralization of organic matter using NO_3^- is known as 'denitrification'. In contrast to aerobic remineralization, denitrification produces forms of inorganic nitrogen that cannot be readily utilized by most primary producers (e.g., dinitrogen or nitrous oxide, N_2 and N_2O, respectively). Thus, denitrification represents a loss of bioavailable nitrogen from the ecosystem, with repercussions for the carbon cycle (Fennel et al. 2008, Thomas et al. 2009).

This chapter addresses the role of denitrification in carbon and O_2 cycles off the southern Vancouver Island shelf, a seasonal upwelling-driven margin off western Canada. Before describing the specific goals of this study, some aspects of carbon chemistry in seawater must be introduced.

4.1.1 Carbon chemistry, alkalinity, and denitrification in seawater

The nitrogen cycle indirectly affects the carbon cycle through changes in total alkalinity (TA), which is defined as the excess of proton acceptors over proton donors in seawater (Dickson 1981). TA is subjected to mixing and advection, and it is modified by biogeochemical processes such as calcium carbonate precipitation and dissolution, nutrient uptake, organic matter remineralization, nitrification, etc. Wolf-Gladrow et al. (2007) present an explicit conservative expression for TA (in units of mmol of charged equivalents per cubic meter, or for convenience, mmol m^{-3}):

$$TA = [Na^+] + 2\,[Mg^{2+}] + 2\,[Ca^{2+}] + [K^+] + 2\,[Sr^{2+}] + \ldots - [Cl^-] - [Br^-] - [NO_3^-] \qquad 4.1$$
$$- \ldots + TPO_4 + TNH_3 - 2\,TSO_4 - THF - THNO_2$$

where the last five terms in the right hand side represent total phosphate, ammonia, sulphate, fluoride, and nitrite (e.g, total ammonia, $TNH_3 = [NH_3] + [NH_4^+]$), which are conservative quantities (i.e., even though the concentrations of various phosphate species can change with pressure or temperature, total phosphate does not change). Note that equation 4.1 represents a combination of the more typical TA equation (Dickson 1981) and the concept of electroneutrality (Wolf-Gladrow et al. 2007).

From this expression it is straightforward to understand how different biogeochemical processes alter TA. Figure 4.1 (modified from Zeebe and Wolf-Gladrow, 2001) summarizes changes in TA and dissolved inorganic carbon (DIC) resulting from the most

relevant processes. Primary production always consumes DIC, and can take up either nitrate or ammonium (NO_3^- and NH_4^+, respectively; hereafter referred to as NO_3 and NH_4 in the text (not in the equations) for simplicity):

$$106\ CO_2 + 16\ NO_3^- + H_3PO_4 + 138\ H_2O \rightarrow \text{Organic Matter} + 138\ O_2 + 16\ OH^- \quad 4.2$$

(New primary production)

$$106\ CO_2 + 16\ NH_4^+ + H_3PO_4 + 106\ H_2O \rightarrow \text{Organic Matter} + 106\ O_2 + 16\ H^+ \quad 4.3$$

(Regenerated primary production)

(equations from Sarmiento and Gruber, 2006). Therefore, new primary production increases TA by 1 mole per each mole of NO_3 consumed, while regenerated primary production decreases TA by 1 mole per mole of NH_4 consumed (see Figure 4.1 and opposing signs for NH_4 and NO_3 in equation 4.1, where NH_4 is included in TNH_3). The effect of aerobic organic matter remineralization (the reverse reaction of equation 4.3) is the opposite of primary production (Figure 4.1). Nitrification, which is the aerobic oxidation of NH_4 to NO_3 (does not change DIC), follows the reaction:

$$NH_4^+ + 2\ O_2 \rightarrow NO_3^- + H_2O + 2\ H^+ \quad 4.4$$

(Sarmiento and Gruber 2006). For every mole of NO_3 formed, nitrification consumes 1 mole of NH_4, reducing TA by 2 moles (see equation 4.1, where NH_4 and NO_3 have different signs, and Figure 4.1). Discussion of the effects on TA and DIC of other biogeochemical process (such as calcification, phosphorus assimilation and remineralization, etc) can be found in Wolf-Gladrow et al. (2007).

Denitrification occurs within the sediments and in severely hypoxic ocean waters. The O_2 threshold at which denitrification occurs in the water column varies with different environments (Devol 1978), but denitrification probably starts to take place when O_2 concentrations drop to about 5 mmol-O_2 m^{-3}, with most denitrification occurring below

2 mmol-O_2 m^{-3} (Devol 2008). This process still produces 1 mole of inorganic carbon per mole of organic carbon oxidized, but releases gaseous forms of nitrogen as well:

$$OM + 100.8\ H^+ + 84.8\ NO_3^- \rightarrow 106\ CO_2 + 42.4\ N_2 + 16\ NH_4^+ + H_3PO_4 + 148.4\ H_2O \quad 4.5$$

(Fennel et al. 2006) assuming organic matter (OM) to be $C_{106}H_{263}O_{110}N_{16}P$ (Redfield et al. 1963).

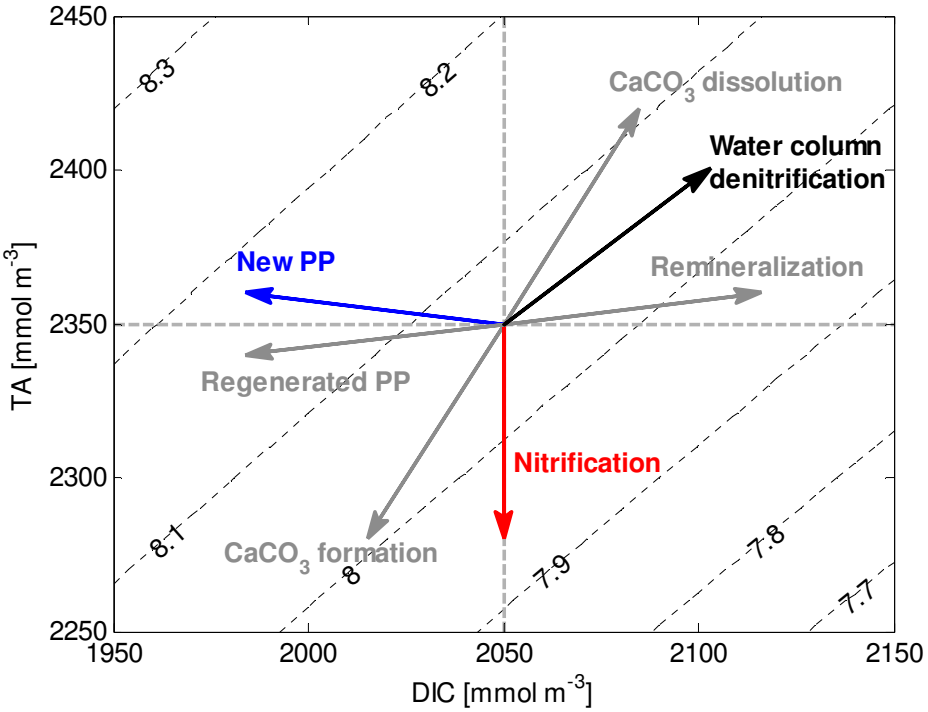

Figure 4.1: Effect of various processes (arrows) on dissolved inorganic carbon (DIC) and total alkalinity (TA), modified from Zeebe and Wolf-Gladrow (2001). The only sources or sinks of TA currently modelled are new primary production (New PP, blue) and nitrification (red). Water column denitrification (black) is also modelled (equation 4.5), but does not occur in the Base Experiment (O_2 concentrations are higher than 5 mmol-O_2 m^{-3}). The grey arrows correspond to processes not included as sources or sinks of TA in the model (some, such as $CaCO_3$ formation and dissolution, are not included in the model at all; see discussion in section 4.2). The dashed black lines indicate pH levels as a function of DIC and TA (for constant temperature and salinity of 25ºC and 33.2, respectively). Absorption of atmospheric CO_2 (release of CO_2 to the atmosphere) by the ocean increases (decreases) DIC, but does not change TA (arrows not shown).

By consuming NO_3 and producing N_2, denitrification represents a loss from the marine fixed nitrogen pool (also referred to as bioavailable nitrogen), since N_2 is biologically inert (note that denitrification could release N_2O instead of N_2, with different stoichiometry than in equation 4.5). Hence, this anaerobic process links the O_2, nitrogen, and carbon cycles by modifying primary production, nitrification, and as a result TA (see discussion associated with the TA equation (4.1) and Figure 4.1). Note that the amount of DIC produced by the oxidation of organic matter is not affected by the remineralization pathway (i.e., whether it is aerobic remineralization or anaerobic denitrification): equations 4.2, 4.3, and 4.5 all produce 106 moles of CO_2 per 106 mol-C in organic matter oxidized. Moreover, denitrification rates are assumed equal to aerobic remineralization rates, as both processes have similar energy yields (see Chapter 2 and Sarmiento and Gruber, 2006).

Fennel et al. (2008), using a high resolution numerical model, analyzed connections between denitrification, TA, and air-sea CO_2 fluxes in the Mid-Atlantic Bight (MAB). They found that decrease of fixed nitrogen concentrations in the water column by denitrification within the sediments can limit primary production and reduce the flux of CO_2 from the atmosphere into the ocean. However, the increase in TA due to denitrification partially counteracts the effect of reduced primary production on air-sea CO_2 fluxes in their simulations (and even intensifies the atmospheric CO_2 flux into the ocean on the inner MAB). Furthermore, Thomas et al. (2009) use observations from the North sea to argue that in the shallower areas TA provides a stronger control on the pH and surface partial pressure of CO_2 (pCO_2) than does DIC. They suggest that anaerobic degradation in the sediments (i.e., denitrification and/or sulphate reduction) supplies most

of the TA in the shallower regions, as also proposed by Chen and Wang (1999) for the East China Sea. Thomas et al. (2009) propose that this "anaerobic pump" may constitute a major control on the uptake of atmospheric CO_2 in shallow coastal seas.

4.1.2 Objectives

The effect of denitrification on air-sea CO_2 fluxes in the summer upwelling system off Vancouver Island is examined, distinguishing the roles of the different processes that affect TA and DIC. Another objective is to assess the effects of denitrification on O_2 concentrations on the shelf. To the best of my knowledge, no publications exist on the latter connection. A model with a simple physical configuration and a biogeochemical module that couples the carbon, nitrogen, and O_2 cycles is used for these purposes.

4.2 Description of model experiments

A quasi-2D implementation of the Regional Ocean Modelling System (ROMS) is used to simulate summer upwelling off the Vancouver Island shelf and to evaluate the role of denitrification. The model configuration consists of a cross-shelf transect (xz-plane) at ~ 49ºN and uniform conditions alongshore. A biogeochemical module embedded in ROMS, includes nitrogen, carbon, and O_2 cycling as well as a representation of the bottom sediment layer. Details of the model and the forcing are given in Chapter 2 and references therein.

In the model, denitrification occurs in ocean waters where O_2 concentrations fall below 5 mmol-O_2 m^{-3} (see section 4.1.1 and Chapter 2 for details) and in the sediment layer. To study the role of denitrification in the system, I take the Base Experiment from Chapters 2 and 3 and compare it with a No Denitrification Experiment (where the only change is

the absence of this process). As the Base Experiment has O_2 levels above 5 mmol-O_2 m^{-3} everywhere (in agreement with observations, Crawford 2008), denitrification is only active in the sediment layer. Hereafter, I will refer to this simulation as the Denitrification Experiment. Both simulations start in late spring (27 May 1993) and continue until early fall (29 September 1993). Experiments are compared starting on day 50 (16 July), to allow for spinup.

The formulation of denitrification within the sediments assumes coupled nitrification/ denitrification (i.e., all NO_3 denitrified is provided by previous nitrification of NH_4; for more modelling details, refer to Chapter 2), as opposed to direct denitrification (NO_3 taken up from the overlying water). In addition to O_2 consumption by aerobic remineralization, the sediments take up extra O_2 from the overlying water for nitrification. Hence, in the Denitrification Experiment a decrease in O_2 would be expected in the near-bottom layers over the shelf relative to the No Denitrification Experiment, which only considers O_2 consumption in the sediments by aerobic remineralization. The simultaneous changes in primary production and nitrification due to sedimentary denitrification also affect the O_2 cycle, a feedback whose importance will be evaluated.

TA is initialized in the model as a linear regression on salinity developed for the region by Ianson et al. (2003). The current version of the model assumes that for every mole of NO_3 produced by nitrification of NH_4, TA is reduced by one mol; uptake of NO_3 by phytoplankton increases TA by the same amount (Goldman and Brewer 1980). This approach neglects sources and sinks of NH_4 as sources or sinks of TA, respectively (see section 4.1.1 as well as Wolf-Gladrow et al., 2007; Hofmann, 2008). The assumption

behind this calculation is that the sum of all sources and sinks of NH_4 fluxes tends to be smaller than that of NO_3 (i.e., production of NH_4 will likely be balanced by consumption, generating no net change in TA). However, it remains an assumption to be assessed in future experiments.

Table 4.1: Calculations of changes in pCO_2 due to denitrification in the sediments. The aim is to separate out the individual effects of changes in total alkalinity (TA) and dissolved inorganic carbon (DIC). T and S stand for temperature and salinity, which are equal in both simulations; the subscript Den (NoDen) indicates a variable from the Denitrification (No Denitrification) Experiment. The same procedure can be carried out for any variable of the carbon system (e.g., Ω_A). The function to calculate pCO_2 is described by van Heuven et al. (2009).

pCO_{2Den}	= function (T, S, TA_{Den}, DIC_{Den})
pCO_{2NoDen}	= function (T, S, TA_{NoDen}, DIC_{NoDen})
pCO_{2TA}	= function (T, S, TA_{Den}, DIC_{NoDen})
pCO_{2DIC}	= function (T, S, TA_{NoDen}, DIC_{Den})

To separate out the effects of denitrification on pCO_2 due to changes in either TA or DIC, pCO_2 is computed from the output of the simulations in four different ways (Table 4.1). The comparison of pCO_{2TA} (pCO_{2DIC}) and pCO_{2NoDen} yields the approximate effect of only TA (DIC) changes due to denitrification. These can then be compared with the total change in pCO_2 due to denitrification (pCO_{2Den} vs. pCO_{2NoDen}). This approach neglects that changes in TA can affect air-sea exchange of CO_2; however, it allows the evaluation of most of the changes between pCO_{2Den} and pCO_{2NoDen}. Analogous calculations are performed for the saturation state of aragonite (Ω_A), the less stable form of calcium carbonate in the ocean, and could be carried out for any carbon system variable (pH, saturation state of calcite, etc).

It is useful to understand what changes are expected in pCO_2 and Ω_A from variations in TA and DIC. At constant temperature and salinity, an expression for how pCO_2 varies as a function of TA and DIC can be obtained after some approximations to the equations of the carbon system in seawater (Sarmiento and Gruber 2006):

$$pCO_2 \sim \frac{(2 \cdot DIC - TA)^2}{TA - DIC} \quad 4.6$$

From this equation it can be shown that an increase in DIC increases pCO_2, while an increase in TA reduces pCO_2. Ω_A can be approximated by

$$\Omega_A \sim [CO_3^{2-}] / [CO_3^{2-}]_{sat} \quad 4.7$$

where $[CO_3^{2-}]$ and $[CO_3^{2-}]_{sat}$ represent the concentrations of the carbonate ion in seawater and at saturation, respectively (see full expression for Ω_A in equation 3.1). Seawater is supersaturated (undersaturated) with respect to aragonite when $\Omega_A > 1$ (< 1), favouring calcification (dissolution). The dependence of $[CO_3^{2-}]$ with TA and DIC is closely approximated by

$$[CO_3^{2-}] \sim TA - DIC \quad 4.8$$

(Najjar 1992). Therefore, Ω_A will decrease with increasing DIC, while it will increase with increasing TA, at constant temperature and salinity.

4.3 Results

4.3.1 Surface

The spatial and temporal distribution (Hovmöller plot) of the total primary production change due to denitrification in the sediments shows that the removal of inorganic nitrogen by denitrification reduces primary production throughout in the model domain (Figure 4.2a), as in Fennel et al. (2008). Note that denitrification only occurs in the

sediments, as O_2 concentrations in the water column are above 5 mmol-O_2 m^{-3}. A reduction in primary production decreases DIC uptake in the euphotic zone and could lead to higher pCO_2 in the surface layer of the ocean. Thus, a reduction in the absorption of atmospheric CO_2 over the shelf would be expected, except in the VICC region (inshore ~ 8 km which is a source of CO_2 to the atmosphere), where air-sea CO_2 fluxes would be increased. However, sometimes air-sea CO_2 fluxes into the ocean are increased on the mid and inner shelf (positive values in Figure 4.2b), outside of the VICC region.

The changes in air-sea CO_2 flux between the two experiments can only be due to changes in DIC and/or TA (note that atmospheric pCO_2, winds, salinity, and temperature are the same for both experiments). Figure 4.3 shows the individual effects of changes in each of these variables on surface pCO_2 as well as the total change due to denitrification, following the method described in section 4.2 (see Table 4.1). The effect of DIC (Figure 4.3b) dominates the net change in surface pCO_2 (Figure 4.3c). However, TA plays a role on the mid and inner shelf (Figure 4.3a), especially after the upwelling event on day 108 (see alongshore wind stress in Figure 4.2). There, the increase in surface TA reduces pCO_2 (equation 4.6) and results in the enhanced air-sea flux into the ocean observed in Figure 4.2b.

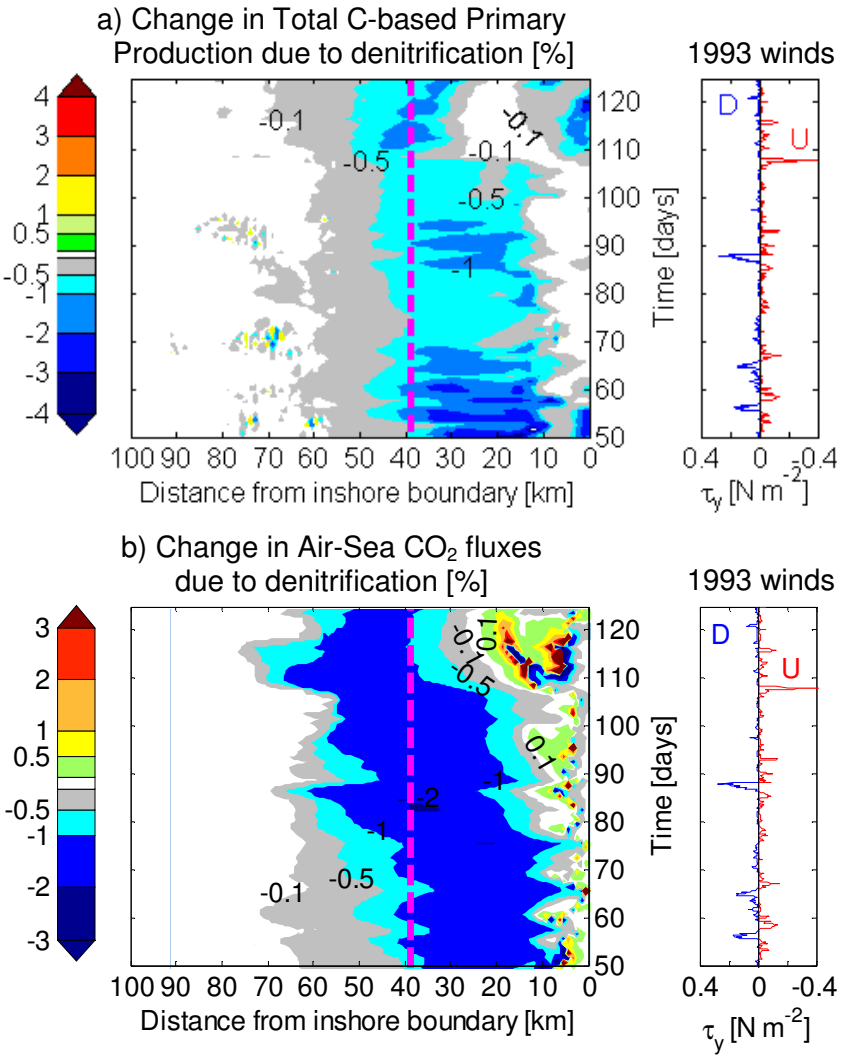

Figure 4.2: Hovmöller plots for the changes [%] due to denitrification in the sediments in: a) total primary production; b) air-sea CO_2 fluxes (which are mostly into the ocean, except in the inner ~ 8 km where the VICC is oversaturated in CO_2). Plots start at day 50 after the spinup period. The dashed magenta line indicates the location of the shelf break. Alongshore wind stress is shown in the right hand panels (blue/red denotes downwelling/ upwelling favourable winds). Positive (negative) changes indicate intensification (reduction) of primary production or air-sea CO_2 fluxes.

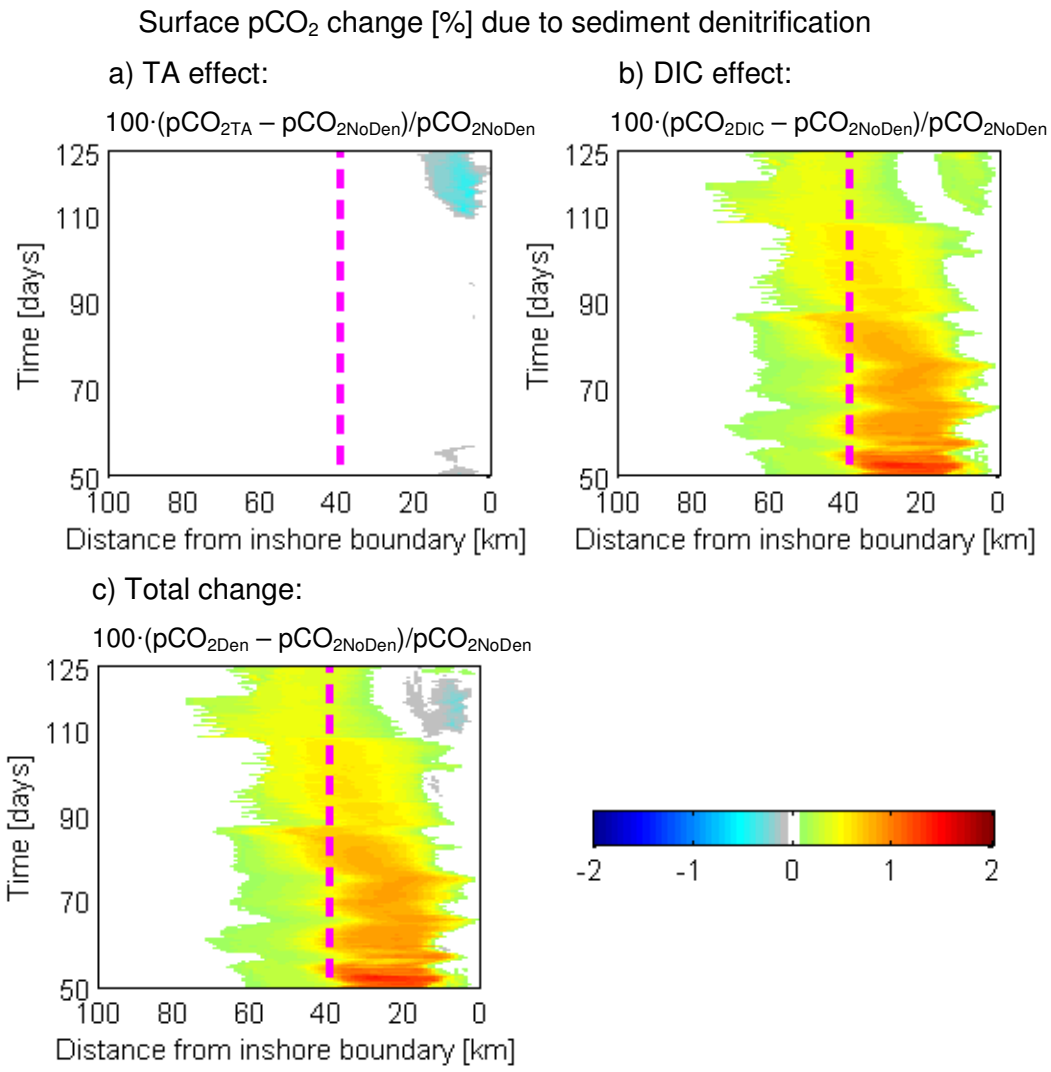

Figure 4.3: Hovmöller plots showing the change [%] in surface pCO_2 between the Denitrification and No Denitrification Experiments due to: a) changes only in TA, b) changes only in DIC, c) total change (i.e., combined TA and DIC effects). Plots start at day 50 after the spinup period. The dashed magenta line indicates the location of the shelf break.

4.3.2 Bottom

In the near-bottom layer over the shelf, Ω_A increases due to denitrification (Figure 4.4c) and pCO_2 decreases (not shown). Here, TA rather than DIC drives the changes (Figure 4.4a and b, respectively).

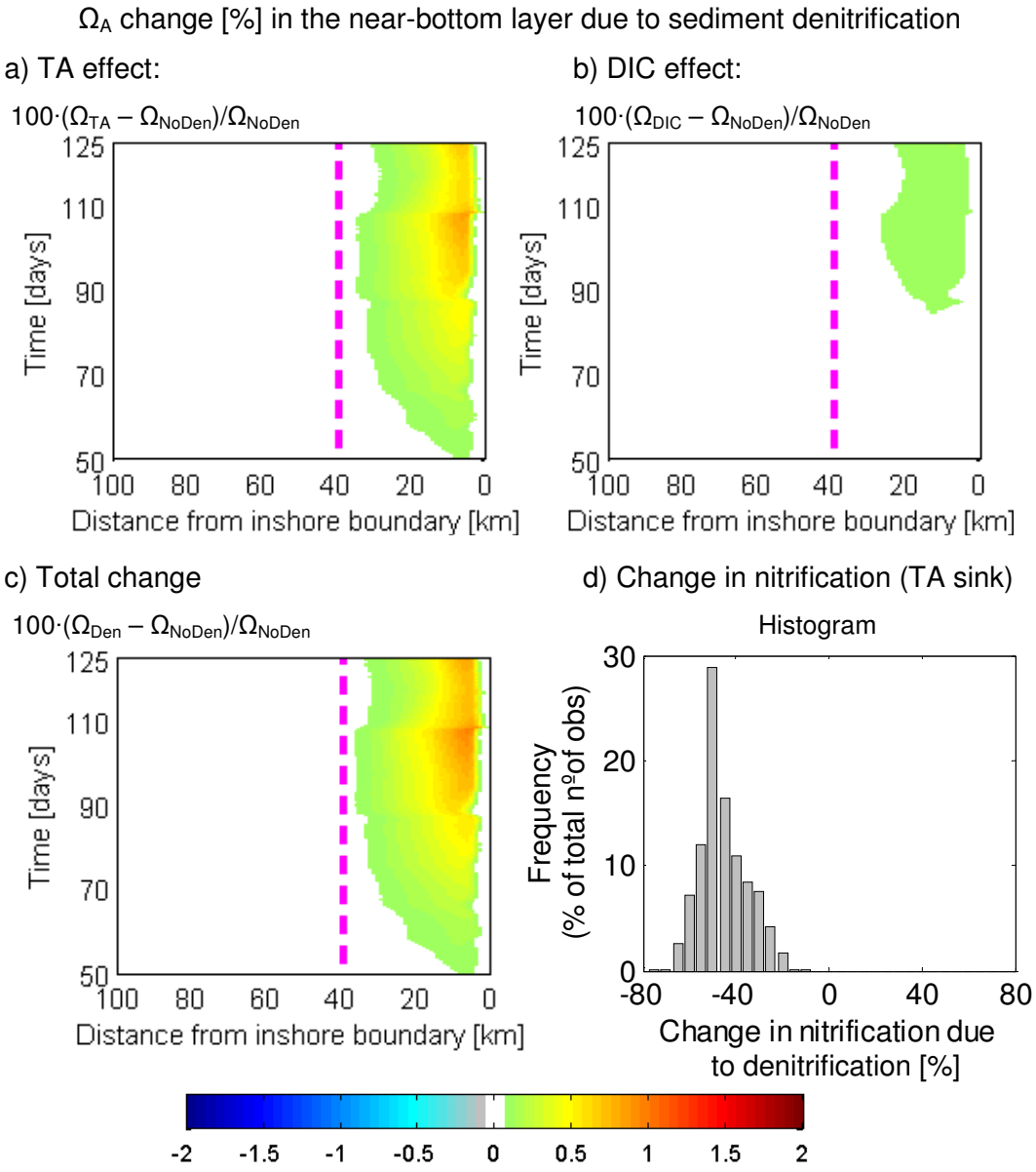

Figure 4.4: Hovmöller plots showing the Ω_A change [%] in the near-bottom layer of the model between the Denitrification and No Denitrification Experiments due to: a) changes only in TA, b) changes only in DIC, c) total change (i.e., combined TA and DIC effects). Plots start at day 50 after the spinup period. The dashed magenta line indicates the location of the shelf break. Panel d) shows the histogram of the changes [%] in nitrification (which is a sink of TA) between both experiments (i.e., due to denitrification) in the near-bottom layer over the shelf (from the inshore boundary to the shelf break). Negative changes indicate a reduction in nitrification (thus, a reduction in the sink of TA) due to denitrification.

Nitrification is the main biogeochemical process regulating TA in the deepest layer of the model, as new primary production is negligible in waters close to the bottom (remember that only these two biological processes modify TA in the model, as O_2 concentrations are above the threshold for water column denitrification). As mentioned in section 4.1.1, nitrification transforms NH_4 into NO_3, thus decreasing TA (equation 4.1 and Figure 4.1). Nitrification in the near-bottom layer over the shelf is reduced due to denitrification (Figure 4.4d), because of the overall decrease of the nitrogen pool when denitrification within the sediments is included in the model. Therefore, TA increases in the Denitrification Experiment in response to the decrease in nitrification, leading to the Ω_A increase in Figure 4.4a (see relationship between TA and Ω_A in equations 4.7 and 4.8).

Changes in DIC provide a secondary control on Ω_A in the near-bottom layer over the shelf (Figure 4.4b), increasing Ω_A (by decreasing DIC, equations 4.7 and 4.8) when there is denitrification in the sediments. The reduction of DIC is indirectly linked to denitrification: as primary production decreases due to the reduced availability of fixed nitrogen in the presence of sediment denitrification (Figure 4.2a), the sinking flux of organic matter is reduced. Therefore, there is less remineralization in bottom waters over the shelf and within the sediments, which reduces the source of DIC in the deepest layer of the model. Figure 4.5 shows the changes (as percentages) of the DIC sources in the bottom ~ 10 m of the water column at two locations on the shelf (69 and 90 m depth): remineralization of detrital carbon (D_C; blue line) and semilabile dissolved organic carbon (DOC; red line), as well as the production of DIC from remineralization within the sediments (grey line).

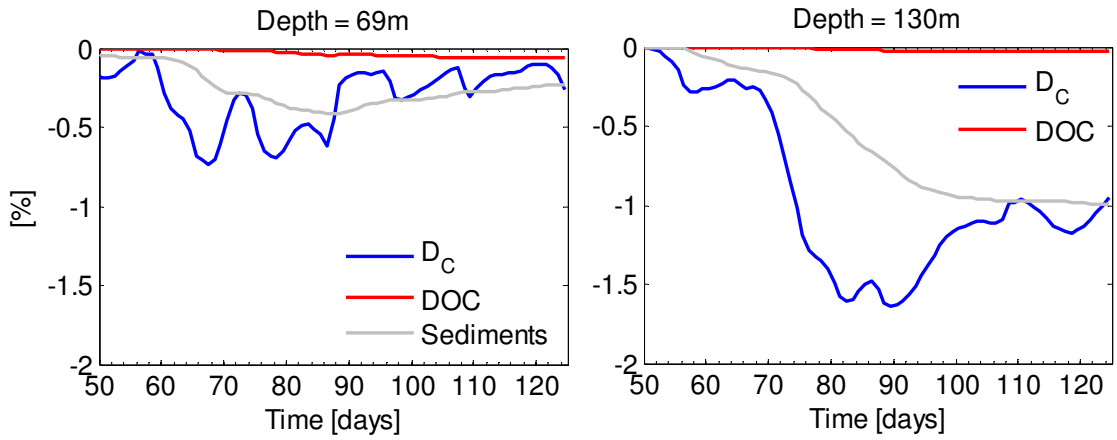

Figure 4.5: Time series of changes [%] in DIC sources in the bottom ~ 10 m of the water column due to sediment denitrification: water column remineralization of detritus (D_C; blue) and of semilabile dissolved organic carbon (DOC; red) as well as DIC production from remineralization within the sediments (grey). Two locations are shown (see the dashed black lines in Figure 4.6) indicating water depths of 69 m (left) and 130 m (right).

4.3.3 Oxygen changes over the bottom

O_2 concentrations in the near-bottom layer of the shelf decrease as time progresses in both experiments, as expected due to biological activity during summer conditions (see Hovmöller plot for near-bottom O_2 in the Denitrification Experiment in Figure 2.9). O_2 is slightly lower in the Denitrification Experiment over most of the shelf due to sedimentary denitrification, but not everywhere (Figure 4.6). The processes leading to the differential effect of sedimentary denitrification in near-bottom O_2 is illustrated by the time integrated sources and sinks of O_2 in the bottom ~ 10 m at two locations on the shelf (Figure 4.7; dashed black lines in Figure 4.6 show locations at 69 and 130 m depth). The O_2 demand by the sediments is enhanced in the Denitrification Experiment (red bars) compared with the No Denitrification Experiment (cyan bars) at both locations, as expected from extra O_2 consumption by coupled nitrification/denitrification in the sediments. However, in the shallower region (69 m depth) O_2 drawdown by nitrification

(see equation 4.4) is reduced in the Denitrification Experiment relative to the No Denitrification Experiment (Figure 4.7 top panel). Therefore, O_2 concentrations in near-bottom waters at the 69 m depth contour are slightly higher due to sedimentary denitrification (Figure 4.6; see 69 m depth isobath shown as dashed black line ~ 10 km from the inshore boundary). The same mechanism (i.e., reduction of O_2 consumption by nitrification) applies for the slope (figure of sinks and sources not shown).

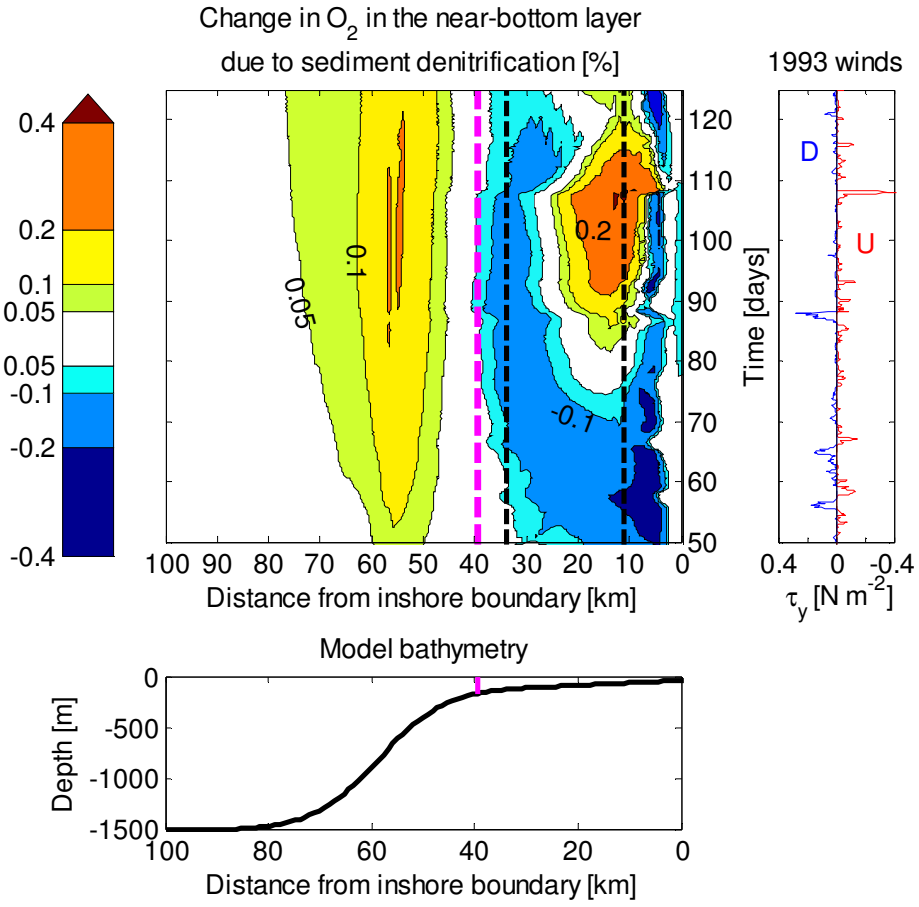

Figure 4.6: Hovmöller plot for the change in near-bottom O_2 concentrations [%] due to sediment denitrification (starting on day 50 after the spinup period). The dashed magenta line indicates the location of the shelf break (depth 172 m); the dashed black lines indicate the 130 and 69 m isobaths. Alongshore wind stress is shown on the right (blue/red denotes downwelling/ upwelling winds). The bottom panel shows the bathymetry profile and the location of the shelf break. Positive (negative) changes indicate higher (lower) O_2 concentration in the Denitrification Experiment relative to the No Denitrification Experiment.

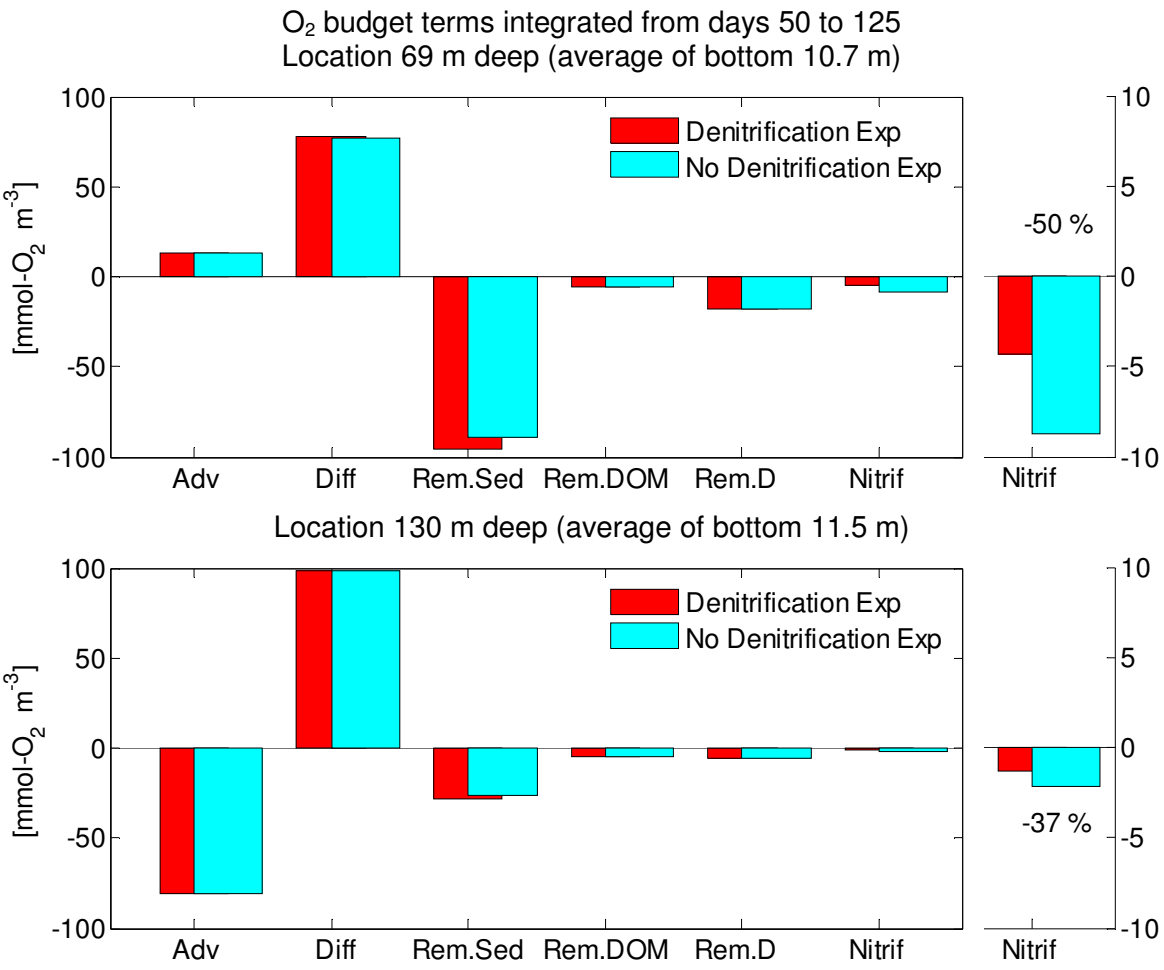

Figure 4.7: Time integrated (from day 50 to 125) biological sinks and physical fluxes of O_2 in the bottom ~ 10 m of the water column at two locations (upper panel: 69 m isobath; lower panel: 130 m isobath; see dashed black lines in Figure 4.6 for location). Denitrification Experiment in red, No Denitrification Experiment in cyan. The x-axis reads: advection (horizontal + vertical), diffusion, remineralization within the sediments, remineralization of semilabile DOM and detritus, and nitrification (the axes on the right show the nitrification sink of O_2 in the same units but with another vertical scale; their change due to denitrification is given as a percentage).

The stronger reduction in near-bottom nitrification due to sediment denitrification on the inner shel compared with the outer shelf (-50 and -37 %, respectively; see axes on the right in Figure 4.7) depends on the depth of the shelf and the spatial distribution of the sediments: sediment mass is higher at shallower depths, where organic matter can reach the seafloor before substantial remineralization can occur in the water column.

Therefore, NH_4 in bottom layers is greater over the mid and inner shelf, as remineralization within the sediments represents its main source. When denitrification is present in the sediments, NH_4 in the near-bottom layer decreases everywhere due to the loss as N_2 or N_2O (equation 4.5); NH_4 decreases proportionally more in shallower regions where sediment mass is larger. Thus, nitrification decreases more on the mid and inner shelf (except in the VICC region; Figure 4.8a) as there is less production of NH_4, leading to less consumption of O_2 (see equation 4.4) and the associated higher O_2 concentrations over near-bottom waters in the Denitrification Experiment relative to the No Denitrification case (Figure 4.6).

On the other hand, sedimentary denitrification leads to less O_2 over the near-bottom waters in the VICC region (Figure 4.6). Primary production is maintained there by the inflow of new nutrients from the VICC (as will be discussed in more detail in section 4.4 and Table 4.3). Therefore, although the reduction in primary production due to denitrification decreases the flux of organic matter to the sediments in the Denitrification Experiment, in the VICC region sediment mass does not decrease as much as on the rest of the shelf (Figure 4.8b). Therefore, the extra O_2 demand by sedimentary denitrification overrides the decreased O_2 consumption by nitrification in the Denitrification Experiment and leads to the decrease in near bottom O_2 concentrations in the VICC region relative to the No Denitrification Experiment (Figure 4.6). If both model experiments (with and without denitrification) are run without the VICC, the relative increase in near-bottom O_2 concentrations due to sedimentary denitrification occurs from the mid shelf to the inshore boundary (not shown). Finally, Figure 4.8a also shows that reduced nitrification due to sedimentary denitrification in the near-bottom layer of the slope (50 – 60 km from the

inshore boundary) is responsible for the higher O_2 in that region relative to the simulation without denitrification (Figure 4.6). Although sediment mass is smaller over the slope, it does not change substantially between simulations, especially compared with the shelf break (dashed magenta line) and outer shelf regions (Figure 4.8b). In the balance between increased O_2 demand by sediment denitrification and reduced nitrification, the latter effect leads to the relative O_2 increase observed on the slope (not shown).

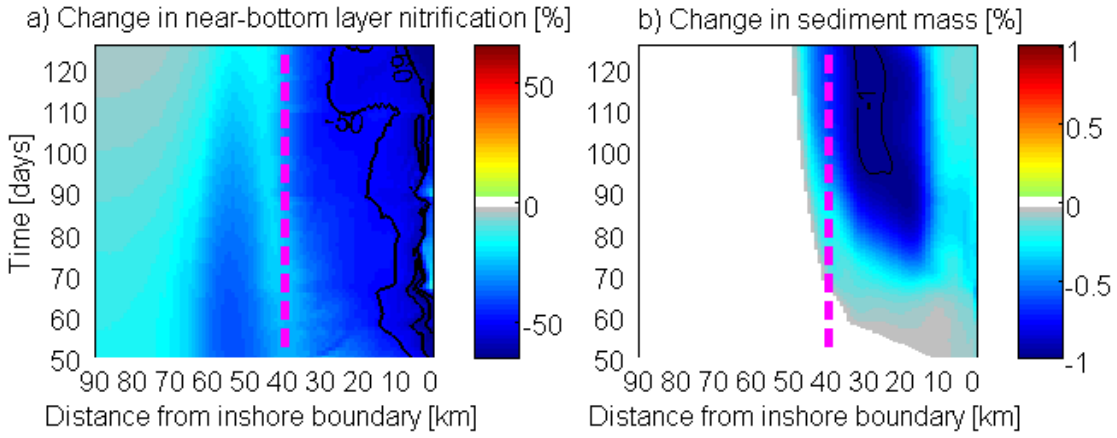

Figure 4.8: Hovmöller plots showing changes due to sediment denitrification [%] in: a) nitrification in the near-bottom layer of the model; b) nitrogen content in the sediment layer. The dashed magenta line indicates the position of the shelf break; the bold black curves are labelled contours.

4.4 Discussion and conclusions

The changes observed due to sediment denitrification in these model simulations are small (usually less than 5 %, and sometimes, less than 1 %). The rates of nitrogen loss due to sediment denitrification do, however, fall within the ranges reported by Fennel et al. (2009) in their compilation of available data sets and by Devol (1991) from observations on the shelf off Washington, south of the present study area (Table 4.2).

Table 4.2: Sediment denitrification rates (i.e., loss of bioavailable nitrogen) from published data for the Washington shelf (Devol 1991), the data compilation by Fennel et al. (2009), and this study. Model values are calculated only for the shelf (region shallower than the shelf break shown as a magenta line in Figure 4.2) and do not include the initial 50 days of spinup. The estimate from Seitzinger et al. (2006) is taken from their Figure 9.

[&]data from 7 stations.

[*]range where most observations fall in their Figure 1c (negative values indicate N_2 fixation within the sediments).

Sediment Denitrification (sink of nitrogen)	Mean [mmol-N m^{-2} d^{-1}]	Median [mmol-N m^{-2} d^{-1}]	Min – Max [mmol-N m^{-2} d^{-1}]
Devol (1991)[&]	3.20	3.11	0.78 – 5.27
Fennel et al. (2009)	2.16	1.45	-5.00 – 10.00[*]
This study	1.40	1.26	0.24 – 5.00
Seitzinger et al. (2006) estimate for Vancouver Island			2.33 – 21.60

The latter work represents observations closest to the southern Vancouver Island shelf. However, sedimentary dynamics differ in, for example, coastal fiords and canyons on the Vancouver Island shelf, which trap most of the sediments from terrigenous sources (Macdonald and Pedersen 1991). Seitzinger et al. (2006) employ a model (Seitzinger and Giblin 1996) that links coupled nitrification/denitrification in continental shelf sediments to depth-integrated primary production using annual averages estimated from SeaWiFS satellite imagery. For the Vancouver Island shelf, their estimate of denitrification rates falls within their two categories with largest rates (between 2.3 and 21.6 mmol-N m^{-2} d^{-1}). If nitrogen losses calculated from the southern Vancouver Island model (Table 4.2, third row) were extrapolated to an annual estimate assuming that denitrification has no strong seasonal pattern (Laursen and Seitzinger 2002), a 75-km long shelf would lose 0.03 TgN yr^{-1}. This annual extrapolation would imply a significant production of

gaseous denitrification products (either N_2 or N_2O), with potential consequences for greenhouse gas emissions by the ocean due to the fraction released as N_2O. The simulations presented here show the direction of change driven by denitrification, the spatial gradients across the shelf, and the processes behind these changes.

The increase of near-surface DIC due to reduced primary production in the presence of denitrification dominates the reduction in air-sea CO_2 flux into the ocean. However, TA plays a role in shallower waters, leading to an increased absorption of atmospheric CO_2 by the ocean (in particular, in the last ~ 20 days of the experiment, after an upwelling event that triggers high primary production). This result agrees with Fennel et al. (2008), who saw an increase in air-sea CO_2 flux into the ocean on the inner MAB due to changes in TA (their Table 2), although they do not discuss the reasons for the leading role of TA there. Thomas et al. (2009) also determined that TA plays a role in regulating air-sea CO_2 exchange over shallow regions of the North Sea. What drives the TA increase on the inner shelf in the Denitrification Experiment? The answer is the coastal current. Table 4.3 shows sources and sinks of TA integrated over time (after the spinup period, i.e. starting at day 50) in the upper ~ 10 m of the water column on the inner shelf at 59 m depth (~ 7 km from the inshore boundary). This isobath lies inside the VICC region, where nutrients are restored to simulate their input from the coastal current. The integration of the sum of all TA sources and sinks shows a net increase in TA with time in the upper layers in both experiments. However, the increment is slightly larger for the Denitrification Experiment, driven by higher new primary production (nitrification is light inhibited, thus its effect in the upper layers is small).

Table 4.3: Time-integrated (day 50 to 125) sources and sinks of TA in the upper 10 m of the water column at a location 59 m deep for both experiments (D=Denitrification, ND=No Denitrification Experiment) and the difference between them (D-ND). New PP stands for New Primary Production. Last row (in italics) is not a TA change, but the NO_3 input from the coastal current (in mmol-N m^{-3}).

$\frac{1}{10\text{m}}\int_{0}^{-10}\int_{50}^{125}(TA_{fluxes}$ at 59 m depth) dt dz	D [mmol m^{-3}]	ND [mmol m^{-3}]	D-ND [mmol m^{-3}]
All processes	11.12	10.94	0.18
Physics (advection + diffusion)	-96.99	-95.64	-1.35
Biology (new PP + nitrification)	120.26	118.53	1.73
VICC TA	-2.12	-1.92	-0.20
VICC NO_3	*9.31*	*9.02*	*0.29*

Increased production is fuelled by more NO_3 introduced by the VICC when denitrification occurs in the sediments (last row in Table 4.3). The modelled VICC restores NO_3 to a typical profile within the coastal current, so when the nitrogen pool decreases due to denitrification, the strength of the VICC source increases (Appendix B gives more detailed information on the modelling of the VICC). Although this buoyancy current dilutes TA in the shallow waters, the enhancement of new primary production dominates the balance and leads to even higher TA in surface waters in the Denitrification Experiment in the VICC region. Outside this region, the VICC still influences the increase of TA in upper layers through changes in advection. Although this result depends on how the VICC is represented in the model, the main conclusion is that the input of new nutrients will always fuel new primary production in shallow waters and change TA (section 4.1.1 and Figure 4.1). Borges and Gypens (2010) find that the increase of primary production due to eutrophication is the main driver of changes in the

carbonate system in the Belgian Coastal Zone (even larger than acidification due to increasing atmospheric CO_2), although they do not discuss changes in TA. The research conducted here also emphasizes the effect of external sources of nutrients on the carbon cycle not only through the direct enhancement of primary production, but also indirectly through changes to TA.

Denitrification increases Ω_A in the near-bottom layer over the shelf (Figure 4.4). Higher TA is the main cause of this effect (driven by the decrease in nitrification due to the reduced availability of NH_4). A reduction in near-bottom DIC contributes to the overall effect, due to reduced remineralization resulting from reduced primary production. The effect of changes in sources and sinks of NH_4 on TA remains to be assessed, but they may be important where the largest changes in NH_4 are observed. Increases in Ω_A due to sediment denitrification could lead to a potential control on ocean acidification from CO_2 sequestration, although changes in Ω_A estimated here are small (< 1.5 %). Note that only coupled nitrification/denitrification is considered here within the sediments; if direct denitrification were important, the consumption of nitrate from the sediments would further increase TA, providing a stronger buffering of shelf waters. Longer model experiments and more in situ observations are needed to confirm the effect of denitrification in the carbonate system off the Vancouver Island shelf. The role of TA generation by the sediments in ocean acidification has been discussed previously for the Mid Atlantic Bight (Fennel et al. 2008) and the North Sea (Thomas et al. 2009), where the authors suggest that it has a larger effect than the acidification by deposition of atmospheric reactive nitrogen and sulphur considered by Doney et al. (2007). More

regional studies should evaluate the magnitude of the buffering effect of TA generation by sedimentary denitrification, before we can assess its global significance.

Results presented here indicate that sedimentary denitrification alters O_2 in the near-bottom layers of the shelf, relative to a simulation without denitrification (Figure 4.6). The changes in near-bottom O_2 due to denitrification (given as a percentage in Figure 4.6) are small (± 0.4 %); the mean change in the 75-day period of the simulations varies from -0.15 to 0.05 mmol-O_2 m^{-3} over different areas of the shelf. If the mean changes were representative of the whole year, the extrapolated rates of near-bottom O_2 change due to sediment denitrification would be between -0.75 and 0.26 mmol-O_2 m^{-3} yr^{-1}. These rates would be comparable with the rates of O_2 decline reported for different continental margins (e.g., -1.47 mmol-O_2 m^{-3} yr^{-1} at ~ 168 m depth at the North Pacific station P4, Whitney et al. 2007; -1.5 mmol-O_2 m^{-3} yr^{-1} on the southern California shelf at depths of 50 to 200 m, Bograd et al. 2008). This comparison emphasizes that, although small, changes in O_2 concentrations due to denitrification could be significant. In conclusion, the loss of bioavailable nitrogen in the water column through sediment denitrification may locally contribute towards increasing or decreasing O_2 levels on the shelf, depending on the local balance between the excess O_2 consumption by denitrification within the sediments and the reduced nitrification in overlying water layers. In general, this balance tends to increase O_2 bottom concentration over the inner and mid shelf for depths less than ~ 100 m (except in the VICC region where primary production is supported by external sources of nutrients) and to decrease it elsewhere.

To sum up, this study emphasizes the tight coupling between O_2, carbon, and nitrogen cycles in the coastal ocean. The loss of fixed nitrogen by sedimentary denitrification not

only increases the coastal ocean buffering capacity, but also affects air-sea CO_2 fluxes and near-bottom O_2 concentrations. The "anaerobic pump" suggested by Thomas et al. (2009) contributes marginally towards the control of acidification on the southern Vancouver Island shelf and the absorption of extra atmospheric CO_2 in shallow regions. The net decrease in CO_2 exchange with the atmosphere due to denitrification reduces the total amount of carbon temporarily sequestered on the shelf during late spring and summer in the Denitrification Experiment by 0.5 %. Longer simulations are needed to evaluate the effect of denitrification on carbon sequestration on annual scales. The leading role of TA in reducing surface pCO_2 (i.e., enhancing CO_2 fluxes into the sea) is limited to the region where the inflow of new nutrients from the coastal current maintains new primary production. Moreover, denitrification in the sediments can either increase or decrease near-bottom O_2 concentrations depending on the depth of the shelf and the external input of nutrients. The VICC influences the spatial distribution of changes due to denitrification, and as climate change modifies the VICC source waters (e.g., reduced snowmelt flow in summer to the Strait of Georgia), both the absorption of CO_2 from the atmosphere and the near-bottom O_2 concentrations could be affected. Extrapolations of regional studies to global scales are challenging, due to the strong dependence of the carbonate system in coastal zones on location-specific properties, such as sources of nutrients, sediments, and fresh waters.

5 DOM cycling on the Vancouver Island shelf

5.1 DOM cycling in the model

The distinction between dissolved and particulate organic matter (DOM and POM, respectively) is generally operational: DOM passes through a filter of a nominal pore size (usually 0.45 μm, though it can range from 0.2 to 1 μm; Benner 2002), while POM is caught on the filter (Sarmiento and Gruber 2006). Generally, DOM is transported and mixed by physical processes but does not sink. Depending on the size and density of the particles, some POM sinks and some does not, unless aggregation processes come into play. DOM is usually enriched in carbon compared with POM (i.e., DOC:DON > POC:PON), although these ratios have large ranges due to the variable composition of DOM and variable remineralization times (Hill and Wheeler 2002, Hopkinson et al. 2002). Three types of DOM can be distinguished according to their rates of decay in the ocean (Carlson 2002):

- Labile DOM (DOM_{Lab}): decays rapidly (minutes to days) through bacterial consumption or breakdown and is only observed in low concentrations in surface waters. Loss rates: ~ 0.1 – 10 d^{-1}.
- Semilabile DOM (DOM_{SL}): decays on seasonal to annual timescales, so it can be transported by advection and mixing. Thus, vertical and horizontal gradients can develop, with decreasing concentrations at depth and away from areas of formation. Loss rates: ~ 0.005 – 0.01 d^{-1}.

- Refractory DOM: is almost biologically inert, with timescales of centuries to millennia. It provides a background DOM pool that makes up most of the bulk DOM at depth (~ 34 mmol-C m^{-3}, C:N ratios ~ 14 – 20).

The Regional Ocean Modelling System (ROMS, version 3.2) was modified in this study to include the cycling of DOM_{Lab} and DOM_{SL}, following the Druon et al. (2009) modification of ROMS and incorporating further recommendations by Christian and Anderson (2002). DOM_{Lab} is implicitly represented: it is assumed to turn over rapidly enough to be transformed immediately into dissolved inorganic carbon (DIC) and ammonium (NH_4^+, hereafter NH_4). On the other hand, DOM_{SL} is explicitly modelled with two pools for dissolved organic nitrogen (DON_{SL}) and carbon (DOC_{SL}) with different remineralization rates. The refractory fraction of DOM is considered inert on the time scales of my experiments (Anderson and Williams 1999, Carlson 2002) and not included in the model. The schematic diagram shown in Figure 2.3 (Chapter 2) shows the fluxes between the different pools of nitrogen and carbon in the model; in particular, it depicts fluxes to both DOM_{Lab} (dashed lines) and DOM_{SL}. These processes and their parameterizations are briefly described below; equations are given in Appendix A.

Excess carbon uptake: Sambrotto et al. (1993) observed that organic carbon and nitrogen production occur at ratios larger than the typical C:N Redfield ratio. The assumption made here is that phytoplankton can still take up carbon when light is abundant but nitrogen nutrients are limiting, which is transformed into carbohydrate over-production (Anderson and Williams 1998, Ianson and Allen 2002, Druon et al. 2009). Therefore, in the model there is an extra photosynthetic uptake of carbon during nutrient limitation that goes directly into the DOC_{SL} pool (equation A.14).

Phytoplankton exudation to DOM_{Lab} and DOM_{SL}: This process represents the continuous loss of organic matter through permeable cell membranes and its rate is proportional to phytoplankton biomass (Bjørnsen 1988). Different proportionality factors are used for exudation to DOM_{Lab} and DOM_{SL} (Druon et al. 2009, see Table 2.2).

Zooplankton-associated losses to DOM_{Lab} and DOM_{SL}: A fraction of grazed material is directed to DOM_{Lab} and DOM_{SL}, representing zooplankton-associated losses such as direct sloppy feeding, egestion, and dissolution of feces (Christian and Anderson 2002). The fraction of DOC released by sloppy feeding is larger when copepods graze on large diatoms (usually representative of the spring bloom) than on smaller prey (Møller et al. 2003, Møller 2005). Assuming that high grazing rates occur only when the diatom biomass is high (Druon et al. 2009), the fraction of unassimilated grazed material released as DOC (both labile and semilabile) by zooplankton is formulated as

$$Q = 0.71\frac{g}{g_{max}} = 0.71\frac{P^2}{P^2 + K_P^2}$$

where g is the grazing rate, g_{max} the maximum grazing rate, P stands for phytoplankton and K_P^2 is the half saturation concentration for P ingestion. The remaining unassimilated grazed material (i.e., 1 – Q) is released as detritus (D). The maximum fraction of DOC release (71 %) represents the largest values for Q observed when copepods graze on blooms of large diatoms (Møller et al. 2003). The same approach is used for DON (i.e., a Q fraction of unassimilated grazing directed to DON, and 1 – Q directed to D). From the zooplankton-associated losses directed to DOC and DON, a fraction δ_C (δ_N) is DOC_{SL} (DON_{SL}) and the remaining 1 – δ_C (1 – δ_N) is DOC_{Lab} (DON_{Lab}). The parameters δ_C and δ_N represent the fractions of total DOC and DON that are DOC_{SL} and DON_{SL} and are set to 0.55 and 0.30, respectively, following Druon et al. (2009) and references therein.

Detritus dissolution to DOM_{SL}: The dissolution of POM to DOM_{SL} is modelled as a first order decay of detritus. A preferential dissolution of nitrogen over carbon detritus that is consistent with the increased C:N ratios of POM with depth (Christian et al. 1997).

DOM_{SL} remineralization to inorganic nutrients (DIC and NH_4): Turnover of DOM_{SL} is modelled analogously to remineralization of detritus (i.e., first order decay), although rates are at least one order of magnitude smaller to represent the longer time scales of DOM_{SL} (Table 2.2).

Light absorption by DOM: The chromophoric fraction of DOM (CDOM) absorbs photosynthetically available radiation (PAR), affecting the downward penetration of PAR in the water column. In coastal environments, CDOM originates mainly from terrestrial sources and is negatively correlated with salinity (Blough and Vecchio 2002). In the model, a third attenuation coefficient (K_{CDOM}) is required to represent the absorption by CDOM (in addition to the light attenuation by seawater and phytoplankton) as a function of salinity (S):

$$K_{CDOM} = 0.5329 - 0.02669\ S + 0.0003395\ S^2 \qquad \text{(Druon et al. 2009)}$$

Section 5.2 will describe the analysis of carbon and nitrogen fluxes in the model, with emphasis on DOM. In particular, it will investigate whether there is net export of organic carbon to the deep ocean during the summer upwelling season. Section 5.3 will describe three sensitivity experiments to explore the role of DOM in the continental shelf ecosystem off Vancouver Island, examining the effect of DOC in the residence time of organic carbon and the role of DOM as a source of nutrients.

5.2 Carbon and nitrogen fluxes

5.2.1 Carbon and nitrogen balance in the experiments

The short duration of the experiments performed here (i.e., summertime simulations) precludes calculation of annual fluxes. Figure 5.1 shows a summary of the exchanges during the last 75 days of the simulations (from 16 July to 29 September in the Base Experiment, after the spinup period of 50 days) between the open ocean, atmosphere, sediments, coastal current, and shelf domains. The dominant source for both carbon and nitrogen on the shelf is the onshore transport of dissolved inorganic components (DIC and DIN) in layers below 50 m depth (in agreement with annual fluxes in a box model by Ianson and Allen, 2002). The next largest sources for carbon are the influx of atmospheric carbon dioxide (CO_2, ~ 1 % of the deep DIC source) and for nitrogen, the input from the Vancouver Island Coastal Current (VICC, ~ 13 % of the deep DIN source).

Most of the carbon input is exported from the shelf to the open ocean in the upper 50 metres as DIC (~ 82 %, similar to annual fluxes in Ianson and Allen, 2002), and a smaller percentage (~ 5 %) as DOC_{SL} and POC. The remainder is transported away by the VICC (~ 5 %), stored temporarily in the sediments (~ 0.4 %; the sediments can accumulate mass but there is no permanent burial), or increases the total carbon content of the waters over the shelf (~ 7 %). In contrast, the bulk of the imported nitrogen accumulates in shelf waters (~ 55 %), while similar fractions are exported to the open ocean in the upper 50 m as DON_{SL} or lost from the system by denitrification within the sediments (each ~ 18 %). Smaller amounts are exported in the upper 50 m to the open ocean as particulate organic nitrogen (PON; ~ 7 %) and stored in the sediments (~ 2 %).

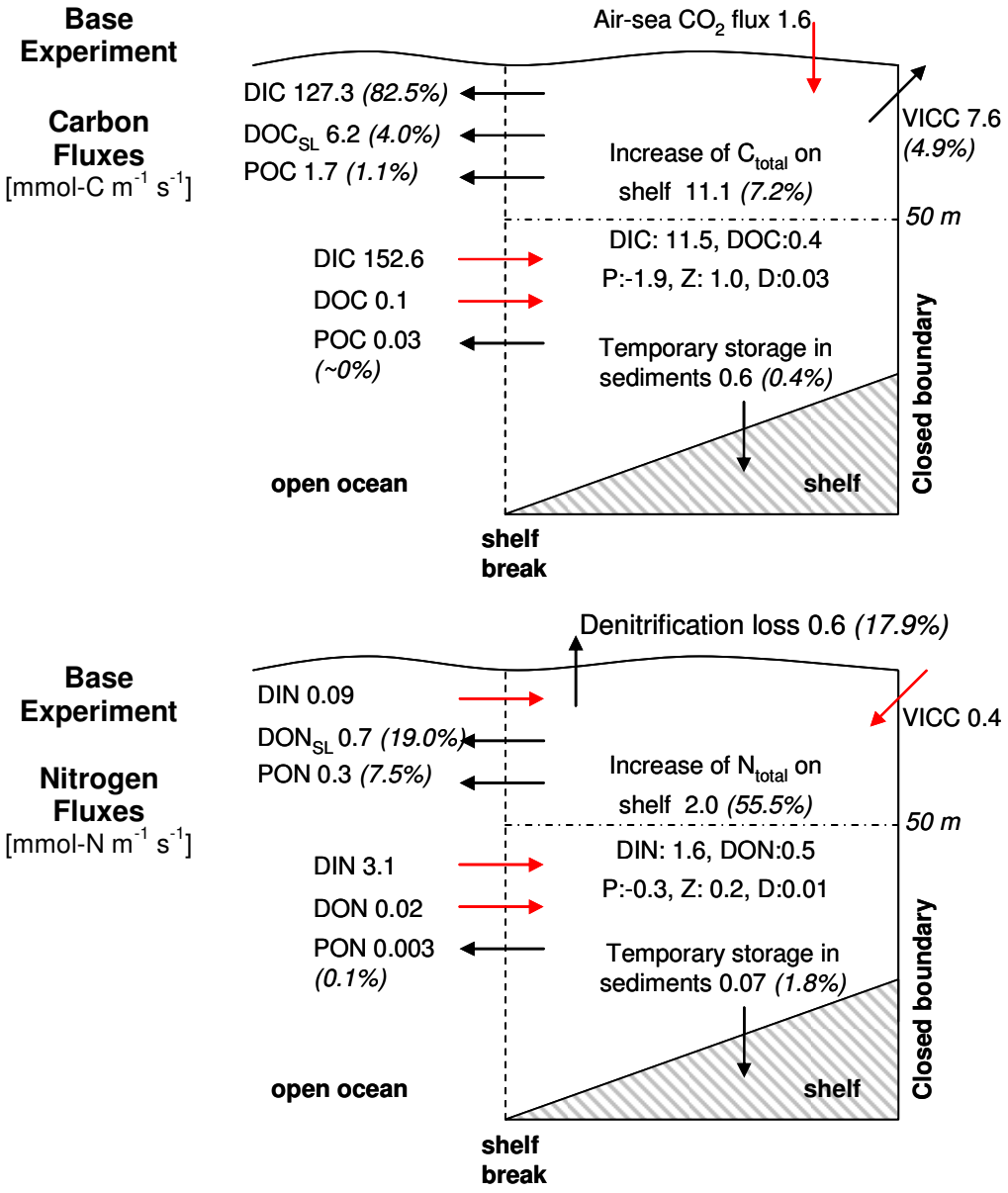

Figure 5.1: Net exchanges between shelf, open ocean, sediments, and atmosphere for all carbon (top) and nitrogen (bottom) components of the model in the Base Experiment (phytoplankton, zooplankton, and detritus are included in particulate organic pools POC and PON). DIC and DIN exchanges with the VICC and accumulation of total carbon and nitrogen over the shelf are also shown (increases on the shelf are divided into individual components as well). Sediment denitrification represents a loss of bioavailable nitrogen (as N_2 or N_2O) from the system, possibly outgassing to the atmosphere eventually. Red (black) arrows indicate sources (sinks) for the shelf. Numbers represent mean fluxes during the last 75 days of the Base Experiment in mmol of C or N per metre of coastline per second (mmol m^{-1} s^{-1}). Parentheses in italics show the percentage of the total incoming flux that each outgoing flux or increase in pool size represents.

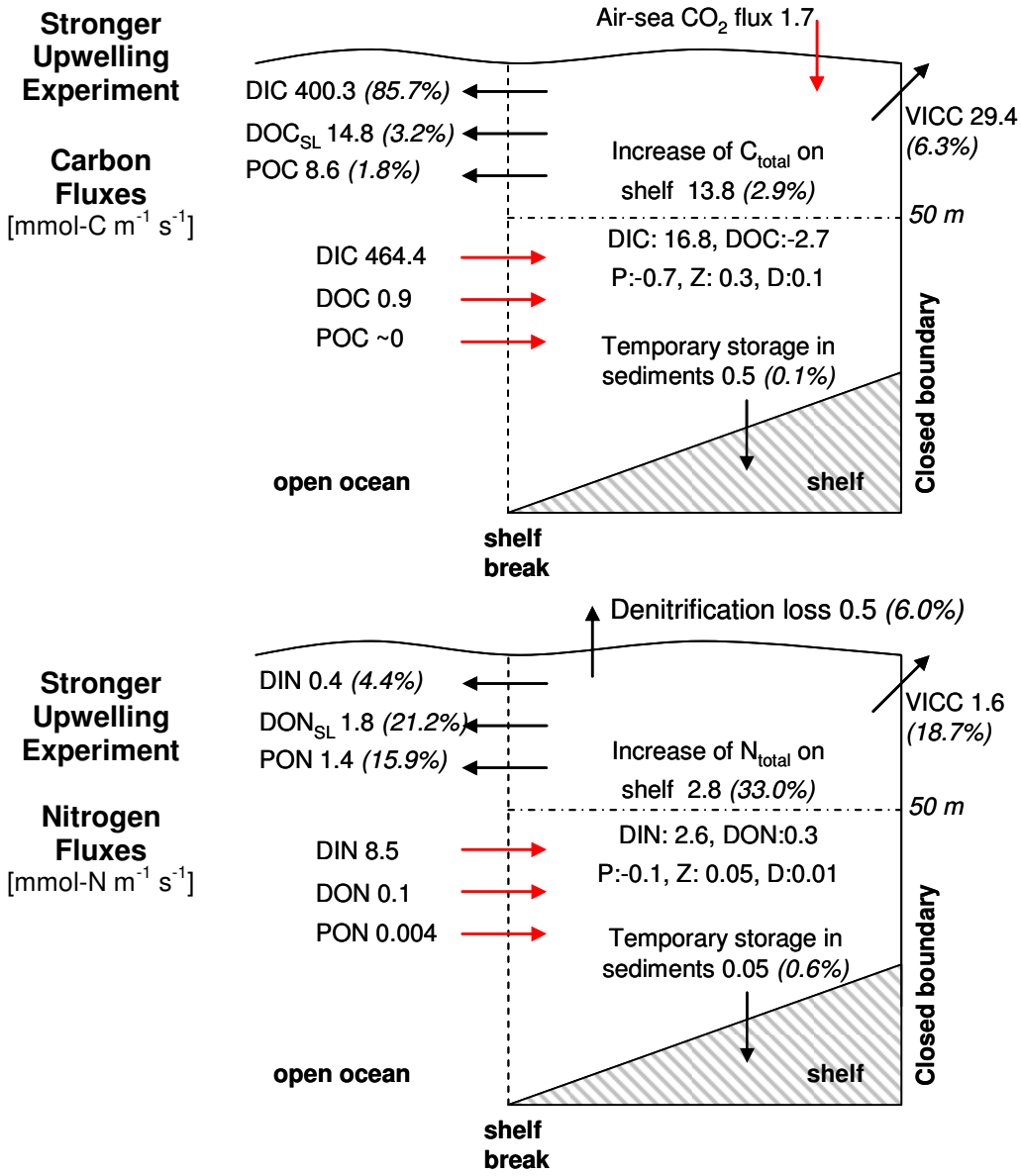

Figure 5.2: Net exchanges between shelf, open ocean, sediments, and atmosphere for all carbon (top) and nitrogen (bottom) components of the model in the Stronger Upwelling (spinup: 1993) Experiment (phytoplankton, zooplankton, and detritus are included in POC and PON). DIC and DIN exchanges with the VICC and accumulation of total carbon and nitrogen over the shelf are also shown (increases on the shelf are divided into individual components as well). Sediment denitrification represents a loss of bioavailable nitrogen (as N_2 or N_2O) from the system, possibly outgassing to the atmosphere eventually. Red (black) arrows indicate sources (sinks) for the shelf. Numbers represent mean fluxes during the last 75 days of the Stronger Upwelling Experiment in mmol of C or N per metre of coastline per second (mmol m^{-1} s^{-1}). Parentheses in italics show the percentage of the total incoming flux that each outgoing flux or increase in pool size represents.

The experiment with increased upwelling-favourable winds (Stronger Upwelling Experiment with 1993 spinup, see Chapter 3) increases the onshore fluxes of DIC and DIN from the open ocean below 50 m by a factor of 3 and 2.7, respectively (compare Figure 5.2 with Figure 5.1). The outgoing flux of DIC from the surface is increased by a factor of 3.1, representing ~ 86 % of the total incoming carbon (which is mostly the deep flux of DIC, as in the previous simulation). These results also agree with those from an intensified upwelling experiment in the region by Ianson and Allen (2002). Most of the DIN that enters the shelf below 50 m leaves it in the upper 50 m as DON_{SL} (~ 21 %) and PON (~ 16 %). In this experiment, the VICC removes a significant fraction of incoming nitrogen (~ 19 %) via "diffusion" simulated by restoring to the VICC values. This change in the direction and magnitude of the VICC flux is due to the offshore displacement of phytoplankton blooms, which under stronger upwelling occur over the mid shelf rather than over the inner shelf close to the VICC (see Chapter 3). Therefore, in this experiment nutrients are not consumed as rapidly in the near-shore region, leading to an excess of nitrate that is removed by "diffusion" into the VICC.

The offshore displacement of phytoplankton biomass in the Stronger Upwelling Experiment also alters the sediment distribution with respect to the Base Experiment (not shown): sediment mass decreases in the shallow waters (where productivity is reduced) and increases over the mid shelf (where productivity is enhanced). The net effect is to reduce the amount of carbon and nitrogen temporarily stored in the sediments over the shelf by roughly 20 %. As a consequence, nitrogen loss due to sediment denitrification also decreases under stronger upwelling-favourable winds. In addition, as incoming DIN

increases by almost a factor of 2.8, the percentage of nitrogen removal by denitrification drops to 6 % (compared with ~ 18 % in Figure 5.1).

These results would indicate that there is no net carbon export to the deep layers of the open ocean during summer, either as DIC, POC or as DOC_{SL}. Most of the transport of organic matter towards the open ocean occurs in the upper 50 m as DOM_{SL}, as was hypothesized for the Oregon shelf by Wetz et al. (2008) and observed in the Iberian upwelling system by Alvarez-Salgado et al. (2001). The following section will deal with variability in the cross-shelf transport of carbon.

5.2.2 Cross-shelf transport of Carbon

Figure 5.3 shows the time series of alongshore wind stress and carbon transport across the shelf break for DIC, DOC_{SL}, and POC (the latter merges phytoplankton, zooplankton, and detritus). Fluxes are shown for layers above and below 50 m. As expected from the balance in Figure 5.1, transport is predominantly onshore (i.e., positive fluxes) in the deeper layers and offshore (i.e., negative fluxes) above 50 m. In particular, this pattern is emphasized during upwelling events (peaks of southward (negative) alongshore wind stress, e.g. on ~ day 108). When downwelling winds prevail, flux directions are reversed (e.g. on ~ day 88). For DIC and DOC_{SL}, deep offshore flow of carbon increases rapidly with strong downwelling wind events. However, POC export to the open ocean is stronger with the weaker downwelling events between days 50 to 70, which results from enhanced primary production associated with a previous strong upwelling event between days 35 and 45 (see alongshore wind stress in Figure 2.9 in section 2.3, chapter 2). The time delay between upwelling events and increased POC concentrations below 50 m depth is a function of the POC pulse sinking through the water column (sinking speeds

are 5 and 0.1 m d^{-1} for detritus and phytoplankton, respectively). The effect of enhanced POC export during this particular downwelling event (days 50 to 70) is the small net outflow of POC below 50 m depth observed in the carbon balance shown in Figure 5.1.

Hales et al. (2006) suggest a mechanism for cross-shelf transport of POC: it accumulates in the bottom boundary layer (BBL) of the shelf during upwelling events and then is advected offshore to the shelf break during periods of relaxation as the BBL moves seaward. Figure 5.4 shows POC transport at the shelf break below 50 m depth for the Base and Stronger Upwelling Experiments. In both cases, although upwelling winds dominate, reversal of wind direction is frequent between upwelling events. Offshore transport of POC occurs during downwelling rather than during relaxation of upwelling in both simulations. However, in the Stronger Upwelling Experiment the weak wind reversals between upwelling peaks generate offshore transport fluxes similar to those during downwelling events (e.g., compare negative fluxes between days 60 and 70 vs. downwelling event at day ~ 105). As previously mentioned, these deep offshore fluxes respond to the increased downward flux of POC due to stronger upwelling. However, the more intense upwelling winds enhance the transport of POC onto the shelf during these events, so the overall effect of the Stronger Upwelling Experiment is to increase the onshore flux of POC onto the shelf in the deeper layers (compare Figure 5.2 with Figure 5.1). In conclusion, the hypothesis by Hales et al. (2006) is not confirmed by the quasi-2D model, since significant near-bottom offshore currents do not occur in the model during relaxation. Note, however, that resuspension of POC from the sediments likely occurs in nature, while it is not a process included in the model.

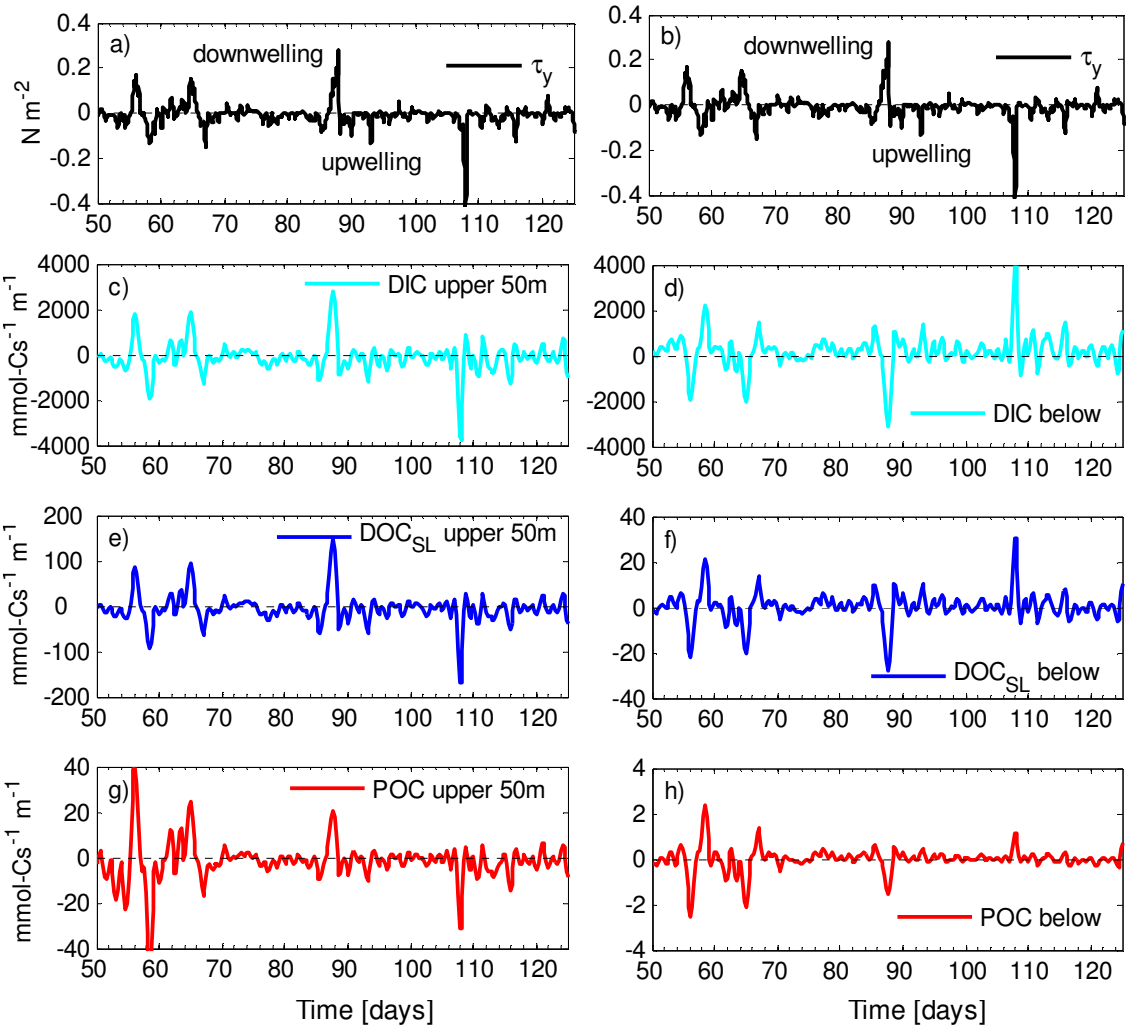

Figure 5.3: Transport of carbon across the shelf break (depth 172 m) in the Base Experiment. (a, b) show alongshore wind stress from 1993 (both panels are the same). Carbon transport is separated into (c, d) DIC, (e, f) DOC_{SL}, and (g, h) POC. Left hand panels (c, e, g) show transport in the upper 50 m of the water column; right hand panels (d, f, h), below 50 m. Positive (negative) fluxes are towards the shelf (open ocean). Transport units are mmol of carbon per second per meter of coastline (mmol-C s^{-1} m^{-1}). Note that for DOC_{SL} and POC, the left and right hand plots have different vertical scales.

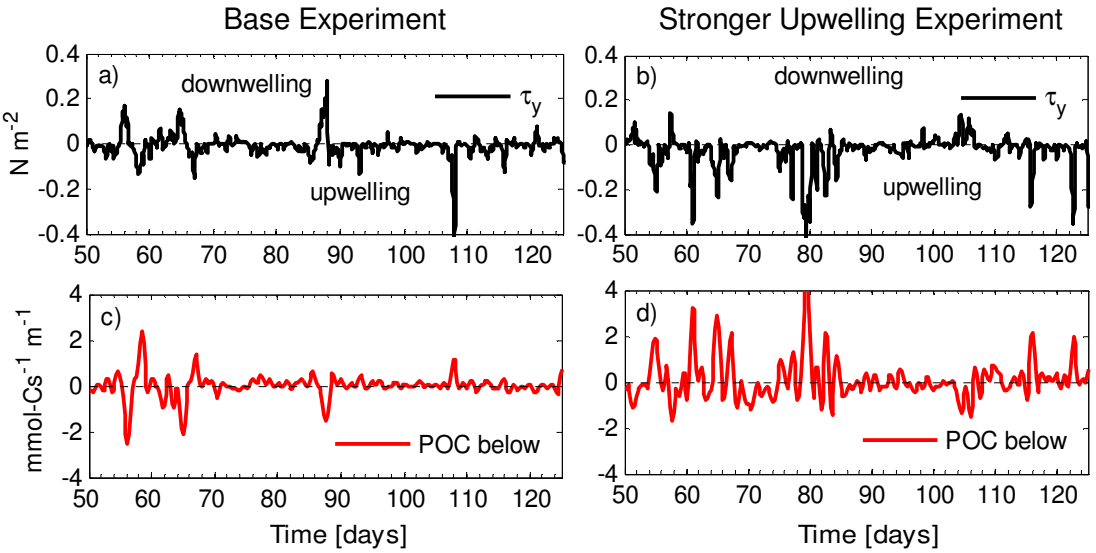

Figure 5.4: Cross-shelf transport of POC at the shelf break below 50 m depth for (c) the Base and (d) Stronger Upwelling (spinup: 1993) Experiments. Panels a) and b) show alongshore wind stress for each experiment (in N m^{-2}). Positive (negative) fluxes are towards the shelf (open ocean). Transport units are mmol of carbon per second per metre of coastline (mmol-C s^{-1} m^{-1}).

5.3 The role of DOM on the Vancouver Island shelf

One process that creates DOM_{SL} is excess DIC uptake by phytoplankton under nitrogen nutrient limitation (Christian and Anderson 2002, Ianson and Allen 2002, Druon et al. 2009). This carbohydrate over-production is given by the nutrient limitation and is proportional to

$$\text{Excess-C production} \sim v^* f_I P (1 - L_{Tot})$$

where v^* is the maximum phytoplankton growth rate (equation A.3), f_I represents the light limitation term (depth dependent, see equation A.4), P is the phytoplankton biomass, and L_{Tot} is the nitrogen-nutrient limitation term[3] (equation A.6), i.e., the sum of nitrate (NO_3^-, hereafter NO_3) and NH_4 limitations (L_{NO_3} and L_{NH_4}, respectively; see complete parameterization of Excess-C production in equation A.14). L_{Tot} approaches unity when

[3] L_{Tot} actually indicates the availability of total nitrogen nutrient ranging from 0 to 1.

either NO_3 or NH_4 is high and approaches zero when both NO_3 and NH_4 concentration are low (see equation A.6). Therefore, the term $(1 - L_{Tot})$ represents the role of excess DIC uptake during nitrogen nutrient limitation, and is close to unity (zero) when NO_3 and NH_4 concentrations are low (high). In contrast, new and regenerated primary production are higher (lower) when NO_3 and NH_4 concentrations are high (low):

$$\text{New Primary Production} = v^* f_I P L_{NO_3}$$

$$\text{Regenerated Primary Production} = v^* f_I P L_{NH_4}$$

Thus, as long as light is not limiting, Excess-C uptake increases when new and regenerated primary production decrease (i.e., $1 - L_{Tot} \sim 1$, while $L_{NO3}, L_{NH4} \sim 0$). The latter can be seen in Figure 5.5c and e, which show new, regenerated, and Excess-C primary production at two different locations on the shelf (69 and 90 m depth, respectively). During the periods of Excess-C uptake increase, this process can represent up to 35 % of total primary production (Figure 5.5d and f show the fraction of Excess-C to total production for both locations). Similarly, Wetz and Wheeler (2003) determined from on-deck incubations of one diatom species (*Chaetoceros* sp.) that 38 % (± 8.5 %) of total organic carbon was accumulated as DOC after NO_3 depletion.

The excess uptake of DIC results in production of DOC_{SL}, which has a longer residence time before release back into DIC. Moreover, it decouples the carbon and nitrogen cycles relative to a model using fixed C:N ratios. Figure 5.5g depicts the evolution of PP_C:PP_N for a location 90 m deep on the mid shelf (grey curve), while the Redfield ratio of 106:16 is shown as a dashed magenta line.

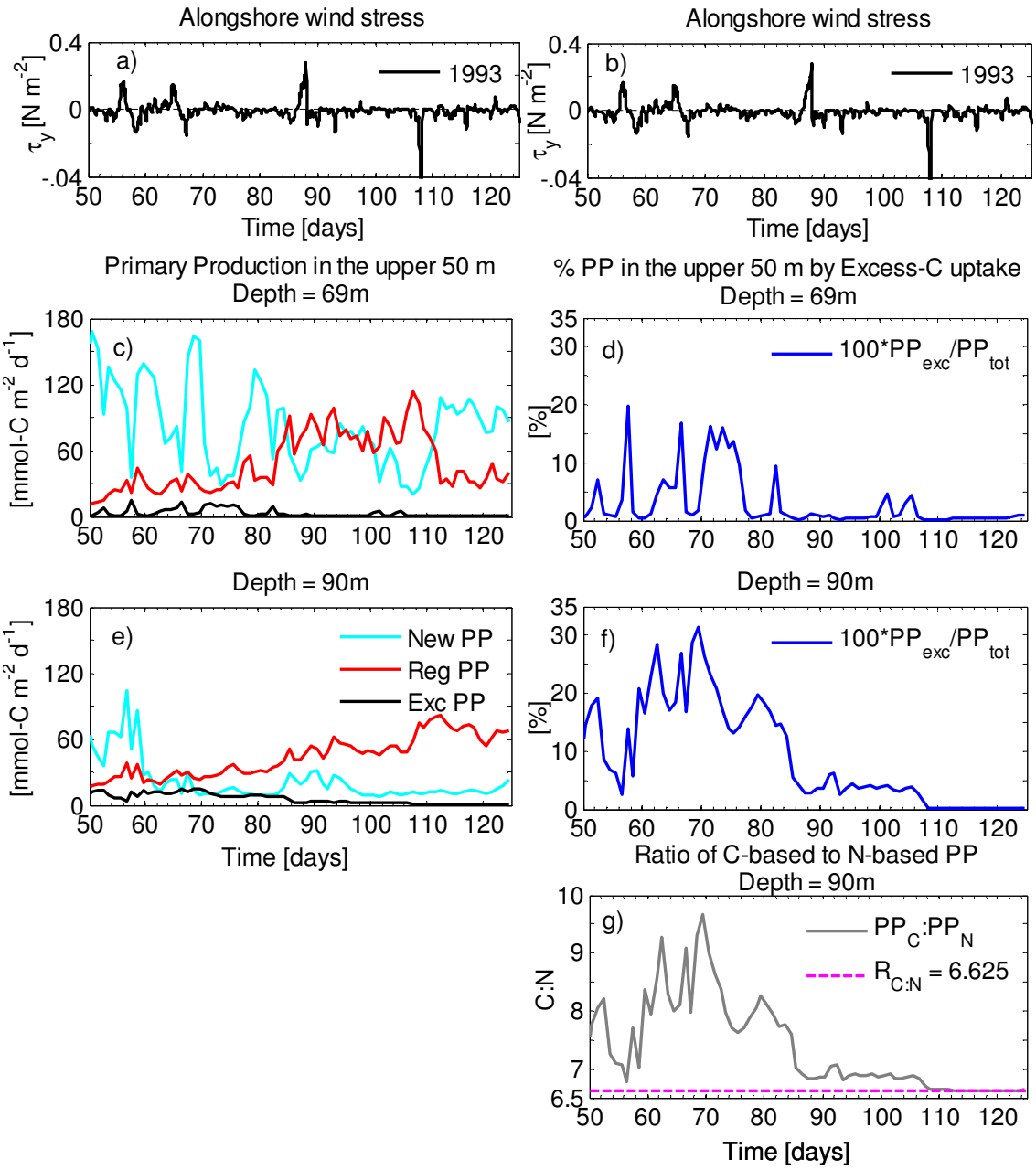

Figure 5.5: (a, b) Alongshore wind stress for the Base Experiment. (c, e) Time series of new (cyan), regenerated (red), and excess carbon (black) primary production in the upper 50 m for the Base Experiment: c) 69 m and e) 90 m isobaths. (d, f) Time series of fraction of Excess-C with respect to total primary production (blue): b) 69 m and d) 90 m isobaths. (g) Time series of ratio of carbon- to nitrogen-based primary production (grey) at the 90 m isobath. The dashed magenta line indicates a constant Redfield ratio of 106:16.

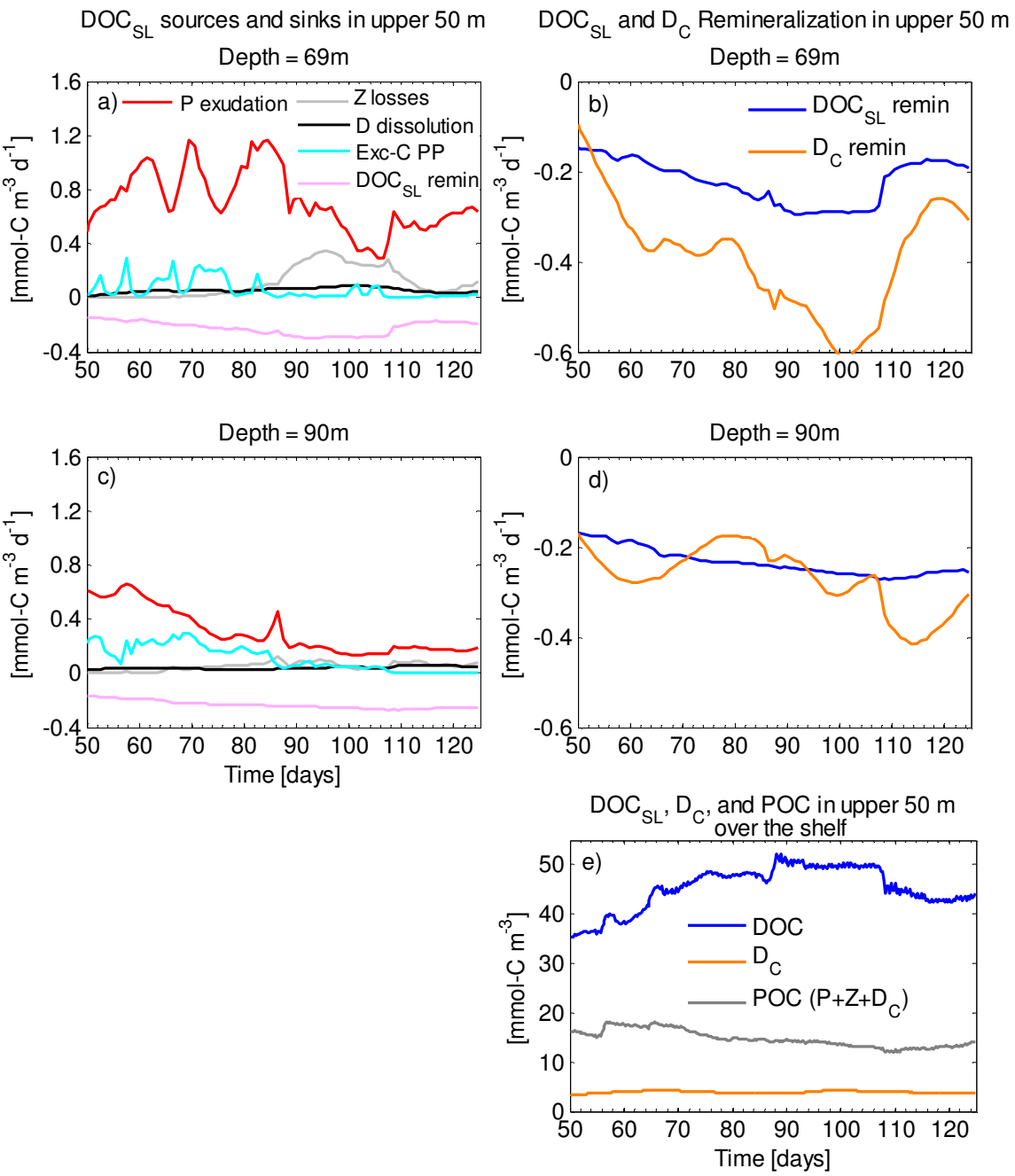

Figure 5.6: (a, c) Time series of sinks and sources of DOC_{SL} in the upper 50 m of the water column for the Base Experiment: a) 69 m and c) 90 m isobaths. The legend in a) reads: phytoplankton exudation of DOC_{SL} (red), zooplankton losses to DOC_{SL} (grey), detritus dissolution to DOC_{SL} (black), excess-C production of DOC_{SL} (cyan), and remineralization of DOC_{SL} (pink). (b, d) Time series of remineralization of DOC_{SL} (blue) and carbon detritus (D_C, orange) in the upper 50 m: b) 69 m and d) 90 m isobaths. (e) Time series of DOC_{SL} (blue), D_C (orange), and POC (dark grey) averaged in the upper 50 m over the whole shelf.

Other processes also contribute towards the production of carbon as DOC_{SL}: Figure 5.6a and c show sinks and sources of DOC_{SL} in the upper 50 m of the water column for two locations of the shelf (69 and 90 m isobaths, respectively). Exudation by nutrient replete phytoplankton is the largest source of DOM_{SL} (and also the largest source of DON_{SL} which is not shown), followed by excess carbon uptake (only for DOC_{SL}, as the Excess-C photosynthesis does not generate DON_{SL}). These two processes show different variability over time since the former is proportional to phytoplankton biomass while the latter is a variable fraction of the nutrient-limited primary productivity. Dissolution of detritus and zooplankton-associated losses to DOM_{SL} are generally minor sources of DOM_{SL}, except on the inner shelf between days 90 and 110 (Figure 5.6a), when zooplankton biomass increases (increased grazing on the previous phytoplankton bloom).

Remineralization of DOM_{SL} does not vary as rapidly as remineralization of detritus due to its slower turnover rates (Figure 5.6b and d show remineralization of DOC_{SL} and D_C in the upper 50 m at the 69 and 90 m isobaths, respectively). Remineralization rates of DOC_{SL} and D_C (in units of mmol-C m^{-3} d^{-1}) are of the same order of magnitude due to the larger mass of DOC_{SL} compared with D_C (see Figure 5.6e, which shows the time series of DOC_{SL}, D_C, and POC in the upper 50 m of the water column). The slower rates of DOC_{SL} and DON_{SL} remineralization affect the carbon and nitrogen cycles by allowing a longer residence time of organic matter in the dissolved form before release back to the water column as inorganic constituents. This increased residence time can be seen from the continuous accumulation of DOC_{SL} in the upper 50 m over the whole shelf between days 50 and 100 compared with the slightly decreasing trend of POC (Figure 5.6e).

Analogously, the oxygen cycle is affected by the slower turnover of DOM_{SL}, introducing a longer time scale for oxygen consumption during remineralization.

Figure 5.7 shows the time series for all DIC sources in the upper and lower 10 m of the water column at two locations (69 and 90 m isobaths). In the upper layer (panels a and c), the flux to DOC_{Lab} from phytoplankton (P) exudation is the leading source during periods of elevated new primary production (see new primary production time series in Figure 5.5 and compare with P exudation of DOC_{Lab} in Figure 5.7): nutrient replete blooms increase P biomass, and consequently P exudation of DOC_{Lab}. Once the blooms start to decay and P biomass starts to decrease due to grazing by zooplankton (Z), excretion of DIC by Z becomes the largest source in the upper 10 m. At the 69 m depth contour (Figure 5.7a), Z-associated losses to DOC_{Lab} are also important once Z biomass increases (Z biomass not shown, but its increase is approximately proportional to the rise in Z excretion, see equation A.8). At other times, Z-associated losses and remineralization of carbon detritus (D_C) are the smallest fluxes. DOC_{SL} remineralization is a consistent source of DIC in the upper 10 m at the two locations shown.

In the bottom 10 m at the two different locations (Figure 5.7b and d), the source of DIC from sediment remineralization is the largest term, and its relative importance decreases with increasing water depth. At the 69 m isobath (Figure 5.7b) remineralization of D_C produces more DIC than DOC_{SL} remineralization; at the 90 m isobath, these two fluxes are of similar magnitude. The main difference between remineralization of D_C and DOC_{SL} is their variability over time: D_C can sink, so its mass in the bottom layers responds more quickly to changes in primary production; moreover, as D_C breaks down more rapidly than DOC_{SL}, its remineralization fluxes are also more variable. The sources

of NH_4 respond to the same processes as DIC, and the relative importance of the different sources is analogous to that shown for DIC in Figure 5.7.

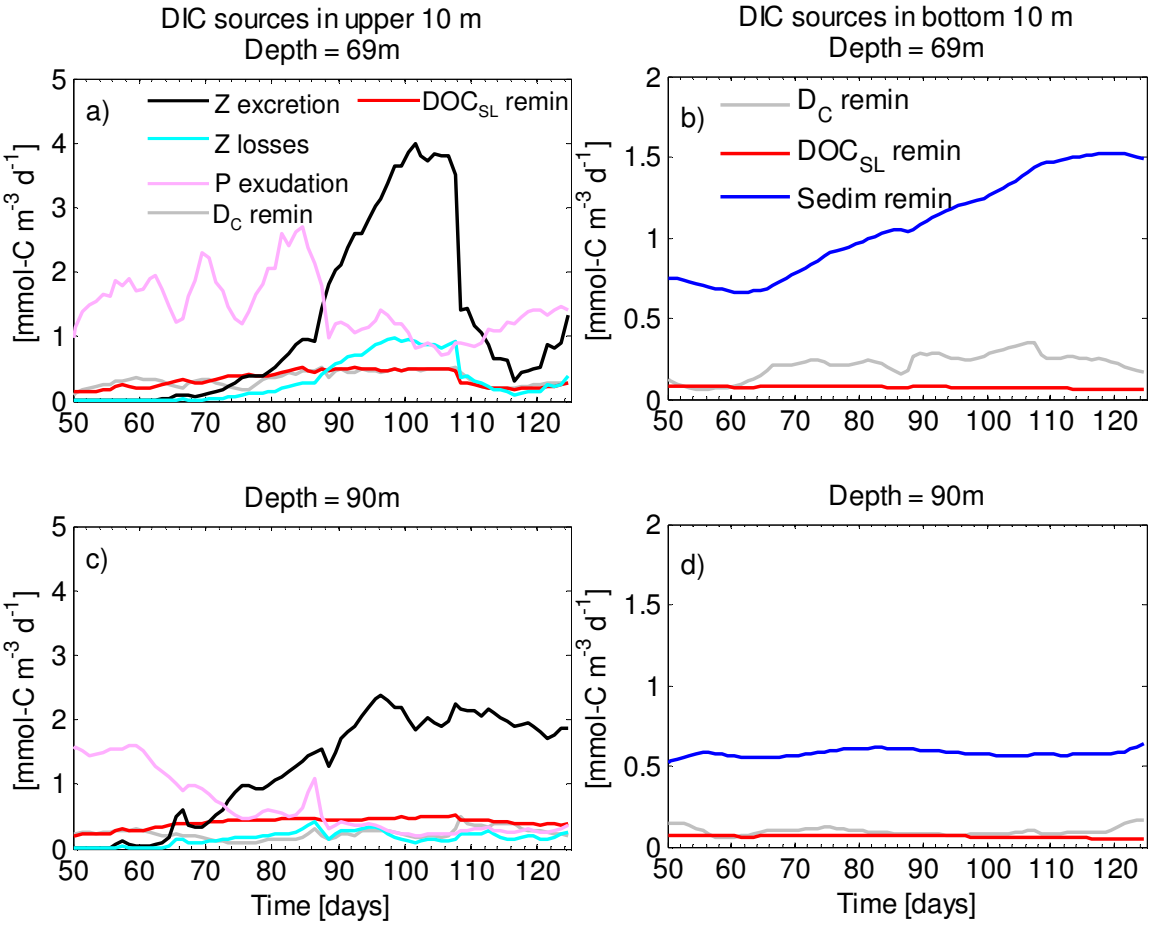

Figure 5.7: Time series of DIC sources in the (a, c) upper and (b, d) lower 10 m of the water column for the Base Experiment at two locations: (a, b) 69 m and (c, d) 90 m isobaths. The legend for panels a) and c) reads: zooplankton (Z) excretion (black), Z associated losses to DOC_{Lab} (cyan), phytoplankton exudation of DOC_{Lab} (pink), carbon detritus (D_C) remineralization (grey), and DOC_{SL} remineralization (red); for panels b) and d): D_C (grey) and DOC_{SL} (red) remineralization, and remineralization of carbon within the sediments (blue).

In conclusion, the cycling of DOM plays a role in this ecosystem model, by providing a source of nutrients, mainly through P exudation of DOM_{Lab}, Z-associated losses, and DOM_{SL} remineralization, and by increasing the carbon residence time of the system by consuming extra DIC under nitrogen nutrient limitation (Excess-C uptake) and

transforming it to DOC_{SL}. Slower turnover rates of DOM_{SL} also enhance carbon and nitrogen residence time, as it takes longer to remineralize DOM_{SL} back to DIC and NH_4 relative to D_C and nitrogen detritus (D_N). DOM_{SL} remineralization also introduces a time lag in the consumption of oxygen, compared with the more rapid changes in oxygen demand associated with degradation of detritus. The reciprocal of remineralization rates gives characteristic turnover times of 14 and 200 days for D_C and DOC_{SL}, respectively. Lastly, DOM uncouples the carbon and nitrogen cycles not only due to the generation of DOC_{SL} by excess DIC uptake, but also through:

- different ratios of DOM_{SL} to total DOM for carbon and nitrogen (see section 5.1; $\delta_C = 0.55$, $\delta_N = 0.30$).
- different dissolution rates of D_C and D_N (see Table 2.2: $S_C = 0.01\ d^{-1}$, $S_N = 0.03\ d^{-1}$). These values were chosen after sensitivity analysis and assuming that there is a preferential solubility of D_N over D_C (Christian et al. 1997).

5.4 Sensitivity experiments

Since DOM modelling is based on still poorly understood processes (Benner 2002, Christian and Anderson 2002), the model sensitivity to DOM processes should be examined. For instance, some of the questions to ask are: How important are the slow remineralization rates of DOM for the ecosystem?; How sensitive is the model to fractions of DOM with different lability?. To address these questions, three extreme scenarios were simulated and compared with the Base Experiment (see Table 2.2 and Appendix A for the description of the different parameters):

1. **Equal DOM_{SL} and D Remineralization Experiment.** Remineralization rates of DON_{SL} and DOC_{SL} increased such that they are equal to those of D_N and D_C (represents a scenario of fast DOM_{SL} remineralization): $rDON = rD_N = 0.08\ d^{-1}$, $rDOC = rD_C = 0.07\ d^{-1}$ (Base Experiment: $rDON = 0.006\ d^{-1}$, $rDOC = 0.005\ d^{-1}$).
2. **Only DOM_{SL} Experiment.** Model only DOM_{SL} by removing sources and sinks of DOM_{Lab} (i.e., remove processes shown as dashed lines in Figure 2.3): $\omega_N = \omega_C = 0$, $\delta_N = \delta_C = 1$ (Base Experiment: $\omega_N = \omega_C = 0.03\ d^{-1}$, $\delta_N = 0.3$, $\delta_C = 0.55$).
3. **Only DOM_{Lab} Experiment.** Model only DOM_{Lab} by removing sources and sinks of DOM_{SL} (i.e., remove processes shown as arrows to and out of DOM_{SL} in Figure 2.3): $\sigma_C = 0$, $\varepsilon_N = \varepsilon_C = 0$, $\delta_N = \delta_C = 0$, $rDON = rDOC = 0$, $s_N = s_C = 0$ (Base Experiment: $\sigma_C = 0.45$, $\varepsilon_N = \varepsilon_C = 0.05\ d^{-1}$, $\delta_N = 0.3$, $\delta_C = 0.55$, $rDON = 0.006\ d^{-1}$, $rDOC = 0.005\ d^{-1}$, $s_N = 0.03\ d^{-1}$, $s_C = 0.01\ d^{-1}$). Note that DOM_{SL} remains in the system as a conservative tracer.

The spatial and temporal evolution of the saturation state of aragonite (Ω_A) in the near-bottom layer over the shelf is shown in Figure 5.8 for the four simulations; Figure 5.8a corresponds to the Base Experiment. If DOM_{SL} remineralization rates are increased to match detritus rates, Ω_A decreases more rapidly in the near-bottom layer over the shelf (Figure 5.8b) than in the Base Experiment. If only DOM_{SL} or DOM_{Lab} is modelled (Figure 5.8c and d, respectively), the decrease in Ω_A over the shelf is faster than in the Base Experiment, but not as rapid as in the Equal DOM_{SL} and D Remineralization Experiment (the cumulative decrease is greater if only DOM_{Lab} is modelled).

The stronger decrease in Ω_A in the Equal DOM_{SL} and D Remineralization Experiment responds to the faster decomposition of DOM_{SL}, especially during the first 40 days of the simulation, when most of the initial DOC_{SL} (which is the same in all experiments) is remineralized to DIC (red curve in Figure 5.9a and its inset; time series in Figure 5.9 correspond to a shallow region of the model (69 m depth) where Ω_A decreases the most). The fast remineralization of initial DOC_{SL} produces the lower Ω_A at day 50 in Figure 5.8b compared with the other simulations. Actually, DOC_{SL} concentrations in the bottom 10 m remain low after day 40 in this experiment (not shown), since production of DOM_{SL} cannot balance the rapid turnover. In the Only DOM_{SL} and Only DOM_{Lab} Experiments, the increase in DIC that leads to the faster decrease in near-bottom Ω_A compared with the Base Experiment, responds to the enhanced remineralization of D_C and to DIC exchange with the sediments rather than directly to changes in DOC_{SL} remineralization. Figure 5.9 compares these three DIC sources for all experiments for the 69 m depth contour of the model. If only DOM_{SL} is modelled, the lack of a P loss to inorganic nutrients (i.e., exudation to DOM_{Lab}) increases P biomass and consequently enhances D_C and sediment mass, leading to higher remineralization of D_C and of organic carbon within the sediments (black curves in Figure 5.9). In the case of the Only DOM_{Lab} Experiment (cyan curves in Figure 5.9), the larger sources of DIC from remineralization of D_C and exchange with the sediments respond to enhanced primary production (Figure 5.11). The larger source of DIC by remineralization of D_C (Figure 5.9b) and exchange with the sediments (Figure 5.9c) in the Only DOM_{Lab} Experiment explains the faster decrease of Ω_A in this experiment compared to the Only DOM_{SL} Experiment (Figure 5.8d and c, respectively).

Changes in the cycling of DOM also affect O_2 concentrations in the near-bottom layer over the shelf (Figure 5.10). The rapid remineralization of DOM_{SL} in the Equal DOM_{SL} and D Remineralization Experiment also leads to a large increase in O_2 demand (especially during the first 40 days) and subsequently lower O_2 concentrations in the near-bottom layer over the shelf: Figure 5.10b shows that a large fraction of the shelf develops hypoxia in this experiment (compare with Base Experiment in Figure 5.10a). The Only DOM_{SL} and Only DOM_{Lab} experiments enhance inshore O_2 demand to a smaller degree and hence lead to more moderate decreases in near-bottom O_2 concentrations (Figure 5.10c and d, respectively; as in the case of Ω_A, hypoxia development is more extensive in the Only DOM_{Lab} Experiment).

The effect of changing the DOM decay rates (either as changes in remineralization rates or modifications in the lability of DOM) on primary production can be observed from the histograms in Figure 5.11. In the Equal DOM_{SL} and D Remineralization Experiment, total primary production is enhanced compared with the Base Experiment by the faster turnover of DOM_{SL} into inorganic nutrients (Figure 5.11a). However, total primary production decreases slightly if only DOM_{SL} is considered (Figure 5.11b), as it lacks the instantaneous source of nutrients represented by DOM_{Lab} (partly compensated by higher P biomass discussed above). If only DOM_{Lab} is modelled, productivity increases to some extent relative to the Base Experiment due to an enhanced source of nutrients (Figure 5.11c).

In conclusion, the cycling of DOM affects ecosystem function by altering the timing and distribution of remineralization in the water column. Both labile and semilabile fractions play a role in the overall nitrogen, carbon, and O_2 cycling, as could be seen by

removing separately each of those components. DOM cycling is still poorly understood (Benner 2002, Christian and Anderson 2002), which makes modelling of DOM not only difficult but also important. Models allow assessing the importance of DOM in biogeochemical cycling for a variety of remineralization scales and, therefore, help guide field programmes by identifying periods and locations where DOM samples are needed. This research demonstrates the possible range of influence of DOM in the coastal ocean by changing assumptions about its various pathways in the ecosystem. Future studies are needed to increase our understanding of DOM in regional coastal and shelf ecosystems, in order to improve the representation of DOM in models.

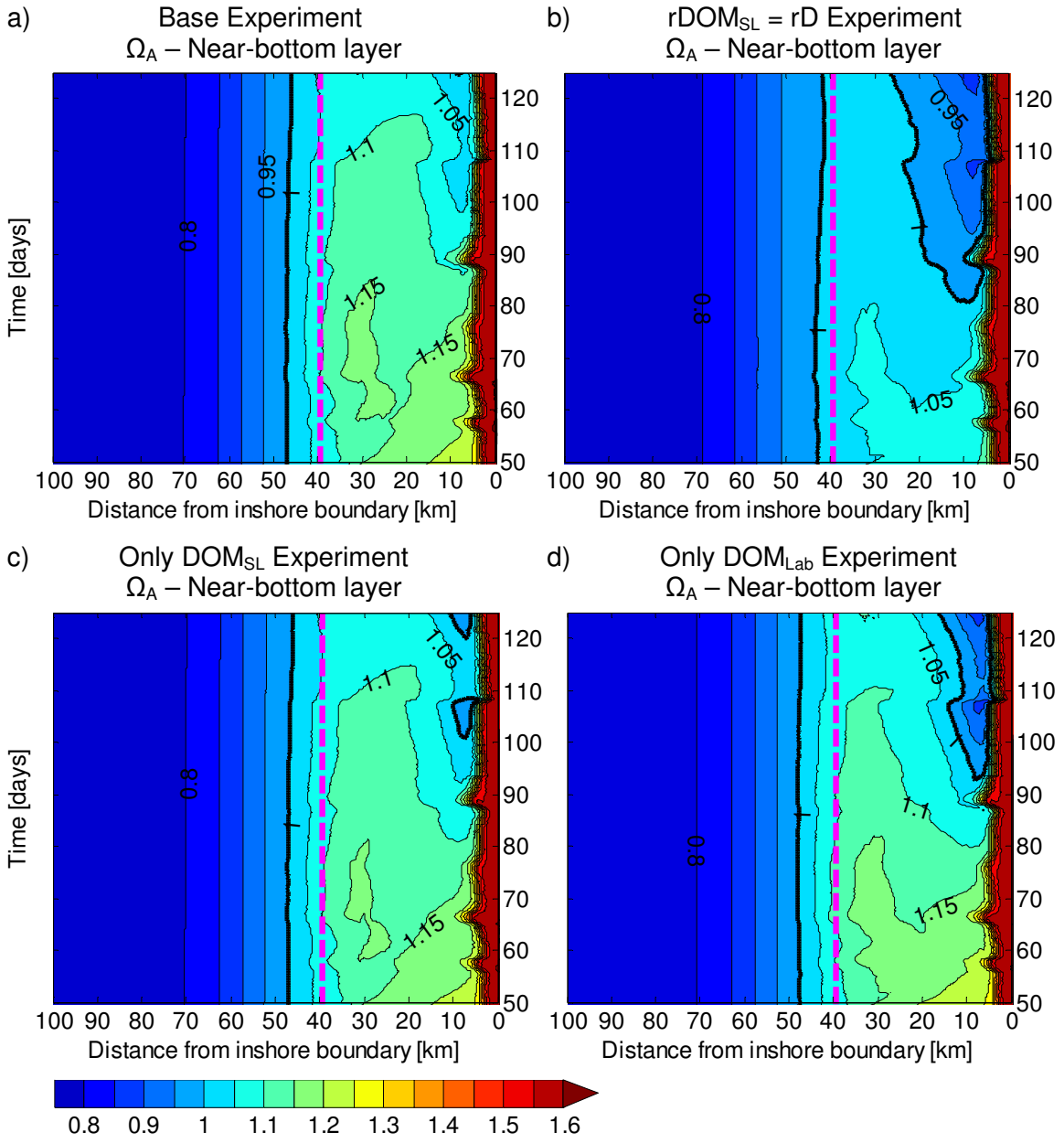

Figure 5.8: Hovmöller plots of saturation state of aragonite (Ω_A) in the near-bottom layer of the model domain for the four experiments described in the text (a: Base; b: Equal DOM$_{SL}$ and D Remineralization; c: Only DOM$_{SL}$; d: Only DOM$_{Lab}$). The thick black contours indicate the threshold for aragonite dissolution (Ω_A = 1). The dashed magenta lines show the position of the shelf break (depth 172 m).

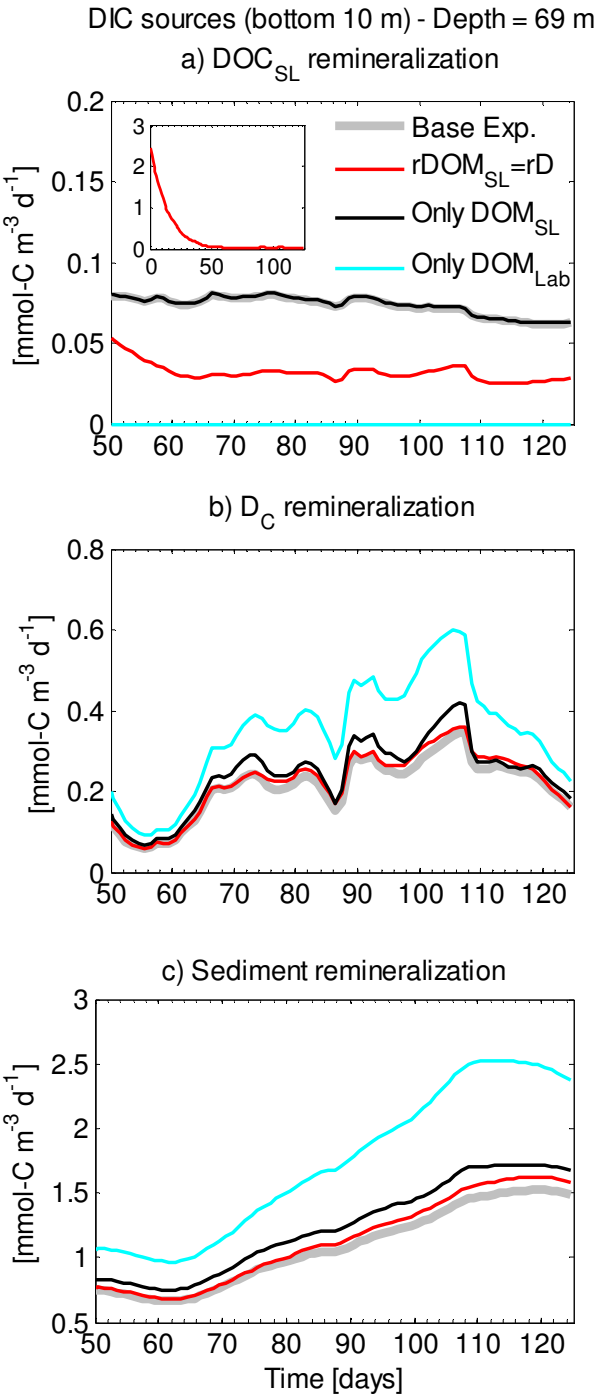

Figure 5.9: Time series of DIC sources in the bottom 10 m of the water column at the 69 m isobath (dash-dotted yellow in Figure 2.10): (a) remineralization of DOC_{SL}, (b) remineralization of D_C, and (c) remineralization of organic carbon within the sediments. Four simulations shown: Base (bold grey), Equal DOM_{SL} and D Remineralization (red), Only DOM_{SL} (black), and Only DOM_{Lab} (cyan) Experiments. Inset in (a) shows the large source of DIC due to remineralization of DOC_{SL} during spinup (first 50 days) in the Equal DOM_{SL} and D Remineralization Experiment.

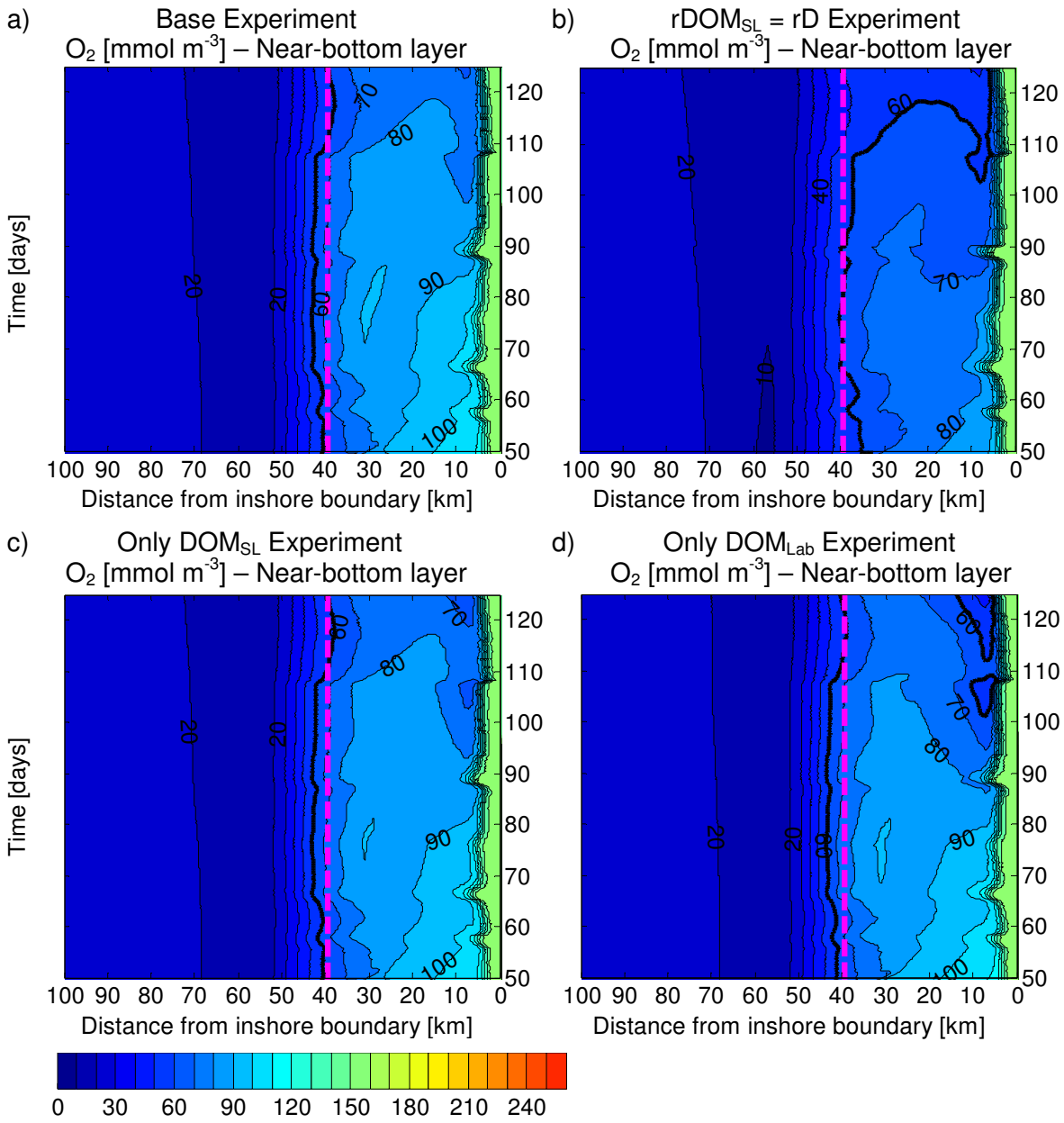

Figure 5.10: Hovmöller plots of O_2 (in mmol-O_2 m^{-3}) at the bottom of the model domain for the four experiments described in the text (a: Base; b: Equal DOM_{SL} and D Remineralization; c: Only DOM_{SL}; d: Only DOM_{Lab}). The thick black contours indicate the hypoxic limit (60 mmol-O_2 m^{-3}). The dashed magenta lines show the position of the shelf break (depth 172 m).

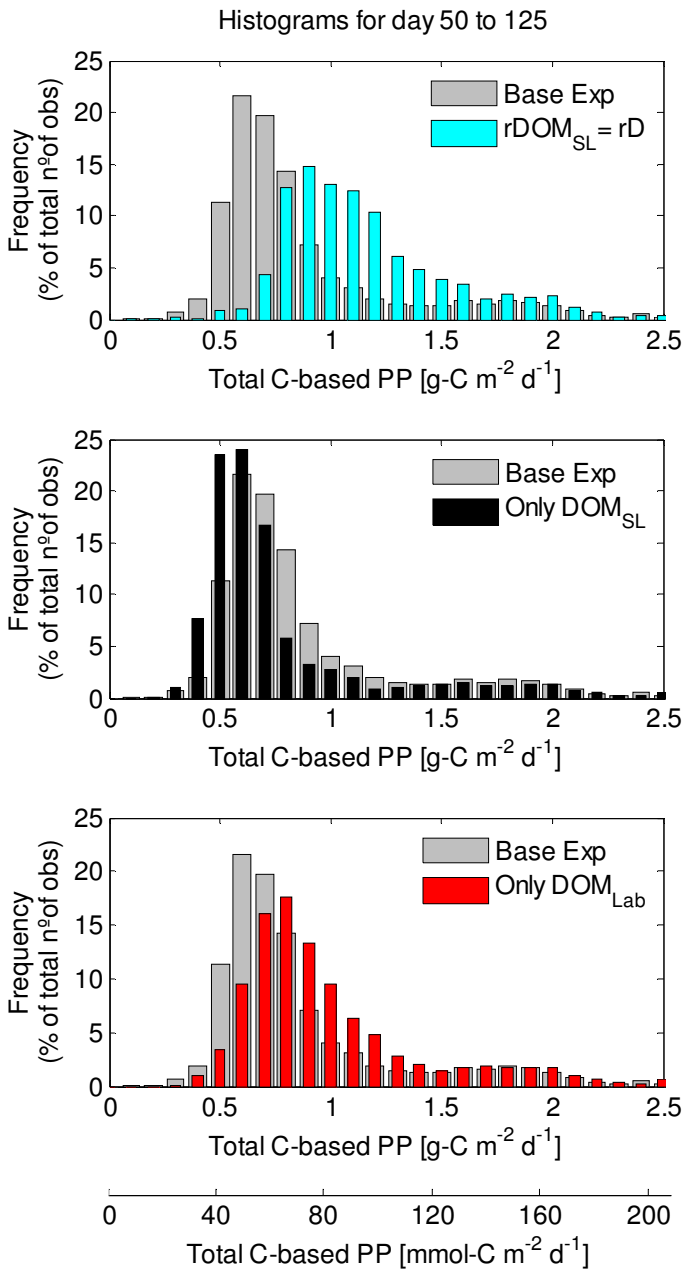

Figure 5.11: Histograms of total carbon based primary production (in g-C m^{-2} d^{-1}) on the shelf for the Base (grey bars in all plots), Equal DOM_{SL} and D Remineralization (cyan bars, upper panel), Only DOM_{SL} (black bars, middle panel), and Only DOM_{Lab} (red bars, bottom panel) Experiments. Bottom horizontal axis shows units in mmol-C m^{-2} d^{-1}. Histograms consider days 50 to 125 (i.e., after spinup period).

6 Discussion and conclusions

Although biogeochemical cycles are tightly coupled in the ocean, most previous studies have focused on either carbon, nitrogen, or oxygen (O_2). This thesis examines the interactions between these three cycles on the Vancouver Island shelf during the summer upwelling season, through the implementation of a quasi-2D numerical model. The experiments performed allow the identification of the dominant processes controlling each cycle and their coupling, as well as the examination of their sensitivity to changes in environmental forcing.

6.1 Main results and limitations

Chapter 2 focuses on the coupling between carbon and O_2 cycles over the shelf, particularly on the connection between low O_2 events and high inorganic carbon. Sensitivity experiments show that local ecosystem processes are key to maintaining low O_2 concentrations and pH (i.e., without the influence of biology, O_2 and pH remain unrealistically high). In particular, the simulations point towards the dominant role of remineralization within the sediments, similar to observations off the Washington shelf (Connolly et al. 2010). Two key aspects distinguish the Vancouver Island shelf from coastal regions to the south in the California Current System (CCS): the greater width of the shelf (Hickey and Banas 2008) and the presence of the Vancouver Island Coastal Current (VICC) flowing poleward on the inner shelf. Results from the quasi-2D model suggest that a narrower shelf would be influenced more strongly by offshore conditions (i.e., lower O_2 and higher DIC) under wind-forced upwelling. Moreover, the VICC brings relatively fresh, O_2-rich, and DIC-poor waters to the bottom layers over the inner

shelf, preventing the shelf from becoming hypoxic and undersaturated in aragonite (also known as 'corrosive' waters).

Chapter 3 investigates the sensitivity of the carbon and O_2 cycles on the shelf to environmental forcing that is expected to change with a changing climate. O_2 concentrations in the near-bottom layer over the shelf are sensitive to stronger upwelling in summer and a shallower Oxygen Minimum Zone (OMZ) offshore (the most severe hypoxic conditions in the simulations occur over the shelf when these two scenarios are combined, with concentrations as low as 30 mmol-O_2 m^{-3} at depths shallower than 130 m). The saturation state of aragonite (Ω_A) in near-bottom waters decreases under stronger summer upwelling and in a higher carbon environment (DIC and atmospheric pCO_2 conditions expected by 2050). In the latter simulation, the near-bottom layer of whole shelf (except in the VICC region) shows undersaturation, with Ω_A as low as 0.78. The experiment that considers a warmer ocean (as predicted for 2050) emphasizes the complexity of the carbon system: although pCO_2 increases and pH decreases in the near-bottom layer over the shelf in this simulation relative to the baseline, Ω_A increases slightly (i.e., reducing the risk for aragonite dissolution). Nevertheless, as DIC enrichment will occur along with warming in the ocean, a decrease in Ω_A is expected (as seen in a combined warming and elevated carbon simulation). In summary, biogeochemical cycles in the region over the Vancouver Island shelf are sensitive to the environmental changes analyzed in Chapter 3, suggesting a potential increasing risk for the development of coastal hypoxia and corrosive conditions in the future.

Chapter 4 examines the role of denitrification in the coupling of the carbon, nitrogen, and O_2 cycles. As discussed in other studies (Fennel et al. 2008, Thomas et al. 2009),

total alkalinity generation in the water column by denitrification within the sediments provides a control on the acidification of the system, especially in the near-bottom layers over the shelf (measured here by an increase in Ω_A). However, the estimated increase in Ω_A due to denitrification is less than 1.5 %, suggesting a marginal impact in the carbonate system off the southern Vancouver Island shelf. Sediment denitrification affects the carbon and O_2 cycles indirectly by reducing primary production and nitrification. In near-bottom layers over the shelf, O_2 concentrations are affected by the balance between enhanced demand by the sediments (due to coupled nitrification/denitrification) and reduced nitrification in the water column. Although changes estimated in O_2 during summer are small ($\pm$ 0.4 %), they may be significant if they are representative of the whole year. In near-surface layers, the decrease in productivity due to sediment denitrification leads to a small increase in pCO_2 ($<$ 2 %), except on the inner shelf where primary production is maintained by nutrients from the VICC. The overall reduction in the net carbon content of the shelf waters due to reduced absorption of CO_2 from the atmosphere is less than 0.5 %. Simulations of the annual cycle and more observations are needed to evaluate the effect of sedimentary denitrification in the region; the experiments examined here for late spring and summer suggest that this process plays a minimal role.

The first part of Chapter 5 analyzes the carbon and nitrogen balance on the shelf as well as fluxes of carbon across the shelf break. In the current model configuration, carbon export to the open ocean occurs in the upper layers (mainly as DIC), with no net offshore flux of carbon in the deeper layers. The second part of Chapter 5 focuses on dissolved organic matter (DOM) cycling in the model. Modelling the semilabile fraction of DOM (DOM_{SL}) increases the residence time of organic carbon in the system, as the

remineralization rate of DOM_{SL} is slower than that of particulate organic matter (POM). Moreover, DOM permits enhanced primary production under nitrogen limited conditions, transforming DIC into semilabile dissolved organic carbon (DOC_{SL}). DOM-related processes can provide important sources of nutrients for the system and introduce deviations from fixed Redfield ratios ($C:N:O_2$) into the model.

The underlying approach behind the development of the model in this dissertation has been to represent both the physical and biogeochemical components with formulations of similar (intermediate) complexity. The planned analyses required a physical configuration that would allow a large number of sensitivity experiments, with an ecosystem model complex enough to represent the main processes involved in nutrient cycling in the coastal ocean. Consequently, I chose to represent summer upwelling off southern Vancouver Island shelf with a quasi-2D physical model, with high resolution in the vertical and across-shelf dimensions and uniform conditions alongshore. This configuration oversimplifies shelf dynamics: it considers only local wind forcing and does not include the effect of coastally trapped waves propagating from the south, net alongshore transport, or the local effect of topographic features such as banks and canyons. Nonetheless, the model domain is set away from the Barkley Canyon and the Juan de Fuca Eddy. In addition, the model includes a representation of the VICC, which is a characteristic oceanographic feature of the region.

Some ecosystem components and processes have been omitted in order to maintain the complexity of the biogeochemical model at a reasonable level, i.e. to have a manageable number of parameters. For instance, particulate inorganic carbon and calcification are not included, as discussed in Chapter 3 (section 3.4); however, blooms of

coccolitophorids appear to be infrequent in the region (Debby Ianson, personal communication). The model does not account for resuspension of sediments in the bottom layers nor does it allow for permanent sequestration of organic matter within the sediment layer. A process not explicitly represented is the autotrophic anaerobic ammonium oxidation or 'anammox' (Mulder et al. 1995), which oxidizes ammonium (NH_4^+, NH_4 hereafter) to dinitrogen gas (N_2) using nitrite (NO_2^-) as an electron acceptor. It has been argued that anammox may be responsible for a greater fraction of the loss of fixed nitrogen in the global ocean than denitrification, although this view has recently been challenged (Ward et al. 2009 and references therein). Because of current uncertainties concerning the importance of this process, anammox is not yet normally included in numerical models of the nitrogen cycle (Hood and Christian 2008).

A common limitation of coastal biogeochemical models is the lack of local in situ observations to tune parameters and improve parameterizations. Data on remineralization and denitrification rates of sediments as well as observations of DOM concentrations were not available on the Vancouver Island shelf. Moreover, the main challenge of introducing DOM into a numerical model lies in the parameterization of still poorly understood processes (Benner 2002, Christian and Anderson 2002). These authors point out that the composition of DOM is variable and still not fully characterized. Here, sediment- and DOM-related parameters were first set to values published in the literature for other regions, and then some were tuned by sensitivity analysis (e.g., remineralization rates of sediments, DON_{SL} and DOC_{SL}; dissolution of detritus to DOM_{SL}). Despite a paucity of observations or gaps in understanding, models are useful tools to investigate the roles and sensitivities of different mechanisms.

Moreover, modelling results can help to identify times and locations where certain observations are needed.

6.2 Future work

The biogeochemical model can still be improved without significant increases to its complexity. The first step would be to introduce a temperature dependence in the remineralization rates of detritus, DOM, and sediments, relevant for investigating potential ecosystem changes associated with global warming, since organic matter decomposition by bacteria is known to vary with temperature (White et al. 1991, Laws et al. 2000, Rivkin and Legendre 2001). Another improvement would be to modify the total alkalinity (TA) calculation within the model to include changes in NH_4. Currently, the computation of TA in the model only considers changes in NO_3 (i.e., new primary production and nitrification), while ignoring sources and sinks of NH_4 (which are assumed to nearly compensate each other; see Chapter 4). If NH_4 changes were incorporated into the TA calculation, both the validity of the assumption and the computational burden of the extra calculations could be assessed.

A major limitation of this study is the 2D representation of a 3D environment. A continuation of the present work could extend the coupling of the current biogeochemical model to a 3D physical representation of the Vancouver Island shelf. Such a configuration would allow studying not only the effect of local wind-driven upwelling, but also the role of remotely-forced phenomena, local topographic features, and mesoscale processes in the nutrient cycling on the shelf.

The present modelling study emphasizes the need for simultaneous observations of carbon and O_2 in coastal systems, both in the form of time series at single stations and frequent cruises monitoring the whole shelf. In addition, the important roles played by DOM and sediments in the model highlight the need to improve our understanding of these components of the ecosystem. Observations of DOM and diagenetic processes are scarce on the Vancouver Island shelf, so future observational efforts need to address this issue.

This thesis describes the state of the ecosystem functioning in terms of the presence of hypoxia and acidified, corrosive waters. The occurrence of these phenomena is deleterious to ocean ecosystems (e.g., Gray et al. 2002, Grantham et al. 2004, Doney et al. 2009). However, the analysis of only hypoxic and corrosive events may not be sufficient to understand the sensitivity of higher animals to a changing climate. Environmental stressors such as decreasing O_2 and increasing pCO_2 narrow the 'thermal window' of marine animals, i.e. the range of body temperatures that allows each organism to function with minimal stress (e.g., Pörtner and Farrell 2008), affecting the animals' performance in growth, reproduction, foraging, etc (Pörtner 2010). Therefore, there is a strong link between ecosystem stressors like ocean hypoxia and acidification and the thermally limited O_2 supply to organisms (Pörtner and Farrell 2008), which our models do not yet include. Such interactions should be addressed in the future, especially in models of the whole trophic foodweb (i.e., 'end-to-end' ecosystem models). The combined effects of O_2 and pCO_2 in the Respiration Index (Brewer and Peltzer 2009) may be a first step into the consideration of this problem.

To conclude, this thesis has demonstrated the strong, and at times subtle, coupling of the carbon, nitrogen, and O_2 cycles in the coastal ocean. Although not unexpected, this result emphasizes the importance of dealing with a coupled system, since ecosystems will be exposed to and will have to adapt to changing conditions in all nutrient cycles simultaneously. This tight coupling should be considered carefully in future studies (both model-based and observational), because studies to date have tended, for example, to focus only on hypoxia or not to consider the effect of changes in the nitrogen reservoir on ocean acidification. This biogeochemical coupling will play a key role as we try to forecast how coastal ecosystems will respond to human modifications of shelf waters as well as to climate change.

Bibliography

Allen, J., Newberger, P. and Federiuk, J. (1995), 'Upwelling circulation on the Oregon continental shelf. Part I: Response to idealized forcing', *Journal of Physical Oceanography* **25**(8), 1843–1866.

Allen, S. E. (2000), 'On subinertial flow in submarine canyons: Effect of geometry', *Journal of Geophysical Research* **105**(C1), 1285–1297. DOI: 10.1029/1999JC900240

Anderson, T. R. and Williams, P. J. l. B. (1998), 'Modelling the seasonal cycle of dissolved organic carbon at Station E1in the English Channel', *Estuarine, Coastal and Shelf Science* **46**(1), 93 – 109. DOI: 10.1006/ecss.1997.0257

Anderson, T. R. and Williams, P. J. l. B. (1999), 'A one-dimensional model of dissolved organic carbon cycling in the water column incorporating combined biological-photochemical decomposition', *Global Biogeochemical Cycles* **13**(2), 337–349. DOI: 10.1029/1999GB900013

Arora, V., Boer, G., Christian, J., Curry, C., Denman, K., Zahariev, K., Flato, G., Scinocca, J., Merryfield, W. and Lee, W. (2009), 'The effect of terrestrial photosynthesis down regulation on the twentieth-century carbon budget simulated with the CCCma Earth System Model', *Journal of Climate* **22**(22), 6066–6088. DOI: 10.1175/2009JCLI3037.1

Auad, G., Miller, A. and Di Lorenzo, E. (2006), 'Long-term forecast of oceanic conditions off California and their biological implications', *Journal Geophysical Research* **111**(C9), C09008–. DOI: 10.1029/2005JC003219

Bakun, A. (1990), 'Global climate change and intensification of coastal ocean upwelling', *Science* **247**(4939), 198–201. DOI: 10.1126/science.247.4939.198

Bakun, A. and Weeks, S. (2004), 'Greenhouse gas buildup, sardines, submarine eruptions and the possibility of abrupt degradation of intense marine upwelling ecosystems', *Ecology Letters* **7**(11), 1015–1023. DOI: 10.1111/j.1461-0248.2004.00665.x

Barth, J. A., Menge, B. A., Lubchenco, J., Chan, F., Bane, J. M., Kirincich, A. R., McManus, M. A., Nielsen, K. J., Pierce, S. D. and Washburn, L. (2007), 'Delayed upwelling alters nearshore coastal ocean ecosystems in the northern California current', *Proceedings of the National Academy of Sciences of the United States of America* **104**(10), 3719–3724. DOI: 10.1073/pnas.0700462104

Bates, N. R. (2007), 'Interannual variability of the oceanic CO_2 sink in the subtropical gyre of the North Atlantic Ocean over the last 2 decades', *Journal Geophysical Research* **112**(C9), C09013–. DOI: 10.1029/2006JC003759

Battisti, D. and Hickey, B. (1984), 'Application of remote wind-forced coastal trapped wave theory to the Oregon and Washington coasts', *Journal of Physical Oceanography* **14**, 887–903. DOI: 10.1175/1520-0485(1984)014<0887:AORWFC>2.0.CO;2

Benner, R. (2002), Chemical composition and reactivity, *in* D. A. Hansell and C. A. Carlson, eds, 'Biogeochemistry of Marine Dissolved Organic Matter', Academic Press, San Diego, pp. 59 – 90. DOI: 10.1016/B978-012323841-2/50005-1

Bianchi, A. A., Bianucci, L., Piola, A. R., Pino, D. R., Schloss, I., Poisson, A. and Balestrini, C. F. (2005), 'Vertical stratification and air-sea CO_2 fluxes in the Patagonian shelf', *Journal of Geophysical Research* **110**, –. DOI: 10.1029/2004JC002488

Biddanda, B. and Benner, R. (1997), 'Carbon, nitrogen, and carbohydrate fluxes during the production of particulate and dissolved organic matter by marine phytoplankton', *Limnology and Oceanography* **42**(3), 506–518.

Bindoff, N., Willebrand, J., Artale, V., Cazenave, A., Gregory, J., Gulev, S., Hanawa, K., Le Quéré, C., Levitus, S., Nojiri, Y., Shum, C., Talley, L. and Unnikrishnan, A. (2007), Observations: Oceanic climate change and sea level, *in* S. Solomon, D. Qin, M. Manning, Z. Chen, M. Marquis, K. Averyt, M. Tignor and H. Miller, eds, 'Climate Change 2007: The Physical Science Basis. Contribution of Working Group I to the Fourth Assessment Report of the Intergovernmental Panel on Climate Change', Cambridge University Press, Cambridge, UK and New York, NY, USA.

Bjørnsen, P. K. (1988), 'Phytoplankton exudation of organic matter: why do healthy cells do it?', *Limnology and oceanography* **33**(1), 151–154.

Blough, N. V. and Vecchio, R. D. (2002), Chromophoric DOM in the coastal environment, *in* D. A. Hansell and C. A. Carlson, eds, 'Biogeochemistry of Marine Dissolved Organic Matter', Academic Press, San Diego, pp. 509 – 546. DOI: 10.1016/B978-012323841-2/50012-9

Bograd, S. J., Castro, C. G., Di Lorenzo, E., Palacios, D. M., Bailey, H., Gilly, W. and Chavez, F. P. (2008), 'Oxygen declines and the shoaling of the hypoxic boundary in the California Current', *Geophysical Research Letters* **35**, –. DOI: 10.1029/2008GL034185

Borges, A. and Gypens, N. (2010), 'Carbonate chemistry in the coastal zone responds more strongly to eutrophication than to ocean acidification', *Limnology and Oceanography* **55**(1), 346–353.

Borges, A. V., Delille, B. and Frankignoulle, M. (2005), 'Budgeting sinks and sources of CO_2 in the coastal ocean: Diversity of ecosystems counts', *Geophysical Research Letters* **32**, –. DOI: 10.1029/2005GL023053

Brewer, P. G. and Peltzer, E. T. (2009), 'Limits to marine life', *Science* **324**(5925), 347–348. DOI: 10.1126/science.1170756

Cai, W.-J. and Dai, M. (2004), 'Comment on "Enhanced Open Ocean Storage of CO_2 from Shelf Sea Pumping"', *Science* **306**(5701), 1477c–. DOI: 10.1126/science.1102132

Cai, W.-J., Dai, M. and Wang, Y. (2006), 'Air-sea exchange of carbon dioxide in ocean margins: A province-based synthesis', *Geophysical Research Letters* **33**, –. DOI: 10.1029/2006GL026219

Cai, W.-J., Wang, Z. A. and Wang, Y. (2003), 'The role of marsh-dominated heterotrophic continental margins in transport of CO_2 between the atmosphere, the land-sea interface and the ocean', *Geophysical Research Letters* **30**(16), 1849–. DOI: 10.1029/2003GL017633

Carlson, C. A. (2002), Production and removal processes, *in* D. A. Hansell and C. A. Carlson, eds, 'Biogeochemistry of Marine Dissolved Organic Matter', Academic Press, San Diego, pp. 91 – 151. DOI: 10.1016/B978-012323841-2/50006-3

Chan, F., Barth, J. A., Lubchenco, J., Kirincich, A., Weeks, H., Peterson, W. T. and Menge, B. A. (2008), 'Emergence of anoxia in the California Current Large Marine Ecosystem', *Science* **319**(5865), 920–. DOI: 10.1126/science.1149016

Chen, C.-T. A. and Wang, S.-L. (1999), 'Carbon, alkalinity and nutrient budgets on the East China Sea continental shelf', *Journal of Geophysical Research* **104**(C9), 20675–20686. DOI: 10.1029/1999JC900055

Chen, C.-T., Liu, K.-K. and MacDonald, R. (2003), Continental margin exchanges, *in* M. Fasham, ed., 'Ocean Biogeochemistry: The Role of the Ocean Carbon Cycle in Global Change', IGBP Book Series, Springer, pp. 53–97.

Christian, J. R. and Anderson, T. R. (2002), Modeling DOM biogeochemistry, *in* D. A. Hansell and C. A. Carlson, eds, 'Biogeochemistry of Marine Dissolved Organic Matter', Academic Press, San Diego, pp. 717 – 755. DOI: 10.1016/B978-012323841-2/50018-X

Christian, J. R., Arora, V., Boer, G., Curry, C., Zahariev, K., Denman, K., Flato, G., Lee, W.G.and Merryfield, W., Roulet, N. and Scinocca, J. (2010), 'The global carbon cycle in the Canadian Earth System Model (CanESM1): Preindustrial control simulation', *Journal of Geophysical Research* . DOI: 10.1029/2008JG000920

Christian, J. R., Lewis, M. R. and Karl, D. M. (1997), 'Vertical fluxes of carbon, nitrogen, and phosphorus in the North Pacific Subtropical Gyre near Hawaii', *Journal of Geophysical Research* **102**(C7), 15667–15677. DOI: 10.1029/97JC00369

Codispoti, L. A., Yoshinari, T. and Devol, A. H. (2005), Suboxic respiration in the oceanic water column, *in* P. del Giorgio and P. Williams, eds, 'Respiration in Aquatic Ecosystems', Oxford University Press, chapter 12, pp. 225–248.

Connolly, T. P., Hickey, B. M., Geier, S. L. and Cochlan, W. P. (2010), 'Processes influencing seasonal hypoxia in the northern California Current System', *Journal of Geophysical Research* **115**(C3), C03021–. DOI: 10.1029/2009JC005283

Crawford, W. (2008), 'Oxygen levels on the Vancouver Island Shelf', State of physical, biological, and selected fishery resources of Pacific Canadian marine ecosystems. Research Document 2008/013. http://www.dfo-mpo.gc.ca/csas/

Crawford, W. and Dewey, R. (1989), 'Turbulence and mixing: Sources of nutrients on the Vancouver Island continental shelf', *Atmosphere-Oceans* **27(2)**, 428–442.

Denman, K. L. (2003), 'Modelling planktonic ecosystems: parameterizing complexity', *Progress in Oceanography* **57**(3-4), 429 – 452. DOI: 10.1016/S0079-6611(03)00109-5

Denman, K. L. and Peña, M. A. (1999), 'A coupled 1-D biological/physical model of the northeast subarctic Pacific Ocean with iron limitation', *Deep Sea Research Part II: Topical Studies in Oceanography* **46**(11-12), 2877 – 2908. DOI: 10.1016/S0967-0645(99)00087-9

Deutsch, C., Emerson, S. and Thompson, L. (2006), 'Physical-biological interactions in North Pacific oxygen variability', *Journal of Geophysical Research* **111**(C9), C09S90–. DOI: 10.1029/2005JC003179

Devol, A. H. (1978), 'Bacterial oxygen uptake kinetics as related to biological processes in oxygen deficient zones of the oceans', *Deep Sea Research* **25**(2), 137 – 146. DOI: 10.1016/0146-6291(78)90001-2

Devol, A. H. (1991), 'Direct measurement of nitrogen gas fluxes from continental shelf sediments', *Nature* **349**(6307), 319–321. DOI: 10.1038/349319a0

Devol, A. H. (2008), Denitrification including anammox, *in* 'Nitrogen in the Marine Environment', 2nd edn, Academic Press, San Diego, chapter 6, pp. 263 – 301. DOI: 10.1016/B978-0-12-372522-6.00006-2

Diaz, R. J. and Rosenberg, R. (2008), 'Spreading dead zones and consequences for marine ecosystems', *Science* **321**(5891), 926–929. DOI: 10.1126/science.1156401

Dickson, A. (1981), 'An exact definition of total alkalinity and a procedure for the estimation of alkalinity and total inorganic carbon from titration data', *Deep Sea Research Part A. Oceanographic Research Papers* **28**(6), 609 – 623. DOI: 10.1016/0198-0149(81)90121-7

Doney, S. C., Fabry, V. J., Feely, R. A. and Kleypas, J. A. (2009), 'Ocean acidification: The other CO_2 problem', *Annual Review of Marine Science* **1**, 169–192. DOI: 10.1146/annurev.marine.010908.163834

Doney, S. C., Mahowald, N., Lima, I., Feely, R. A., Mackenzie, F. T., Lamarque, J.-F. and Rasch, P. J. (2007), 'Impact of anthropogenic atmospheric nitrogen and sulfur deposition on ocean acidification and the inorganic carbon system', *Proceedings of the National Academy of Sciences of the United States of America* **104**(37), 14580–14585. DOI: 10.1073/pnas.0702218104

Dore, J. E., Lukas, R., Sadler, D. W., Church, M. J. and Karl, D. M. (2009), 'Physical and biogeochemical modulation of ocean acidification in the central North Pacific', *Proceedings of the National Academy of Sciences of the United States of America* **106**(30), 12235–12240. DOI: 10.1073/pnas.0906044106

Druon, J., Mannino, A., Signorini, S., McClain, C., Friedrichs, M., Wilkin, J. and Fennel, K. (2009), Modeling the dynamics and export of dissolved organic matter in the northeastern U.S. continental shelf, TM 2009-214177, NASA.

Eppley, R. (1972), 'Temperature and phytoplankton growth in the sea', *Fishery Bulletin* **70**(4), 1063–108.

Fabry, V. J., Seibel, B. A., Feely, R. A. and Orr, J. C. (2008), 'Impacts of ocean acidification on marine fauna and ecosystem processes', *ICES Journal of Marine Science* **65**(3), 414–432. DOI: 10.1093/icesjms/fsn048

Fasham, M. J. R. (1995), 'Variations in the seasonal cycle of biological production in subarctic oceans: A model sensitivity analysis', *Deep Sea Research Part I: Oceanographic Research Papers* **42**(7), 1111 – 1149. DOI: 10.1016/0967-0637(95)00054-A

Federiuk, J. and Allen, J. (1995), 'Upwelling circulation on the Oregon continental shelf. Part II: Simulations and comparisons with observations', *Journal of Physical Oceanography* **25**(8), 1867–1889.

Feely, R. A., Sabine, C. L., Hernandez-Ayon, J. M., Ianson, D. and Hales, B. (2008), 'Evidence for upwelling of corrosive "acidified" water onto the continental shelf', *Science* **320**(5882), 1490–1492. DOI: 10.1126/science.1155676

Fennel, K., Brady, D., DiToro, D., Fulweiler, R., Gardner, W., Giblin, A., McCarthy, M., Rao, A., Seitzinger, S., Thouvenot-Korppoo, M. and Tobias, C. (2009), 'Modeling denitrification in aquatic sediments', *Biogeochemistry* **93**(1), 159–178. DOI: 10.1007/s10533-008-9270-z

Fennel, K., Wilkin, J., Levin, J., Moisan, J., O'Reilly, J. and Haidvogel, D. (2006), 'Nitrogen cycling in the Middle Atlantic Bight: results from a three-dimensional model and implications for the North Atlantic nitrogen budget', *Global Biogeochemical Cycles* **20**, –. DOI: 10.1029/2005GB002456

Fennel, K., Wilkin, J., Previdi, M. and Najjar, R. (2008), 'Denitrification effects on air-sea CO_2 flux in the coastal ocean: Simulations for the northwest North Atlantic', *Geophysical Research Letters* **35**, –. DOI: 10.1029/2008GL036147

Foreman, M. G. G., Callendar, W., MacFadyen, A., Hickey, B. M., Thomson, R. E. and Di Lorenzo, E. (2008), 'Modeling the generation of the Juan de Fuca Eddy', *Journal of Geophysical Research* **113**, –. DOI: 10.1029/2006JC004082

Freeland, H., Crawford, W. and Thomson, R. (1984), 'Currents along the Pacific coast of Canada', *Atmosphere-Ocean* **22**, 151 – 172.

Freeland, H. and Denman, K. (1982), 'A topographically controlled upwelling center off southern Vancouver Island', *Journal of Marine Research* **40**(4), 1069–1093.

Frölicher, T. L., Joos, F., Plattner, G.-K., Steinacher, M. and Doney, S. C. (2009), 'Natural variability and anthropogenic trends in oceanic oxygen in a coupled carbon cycle-climate model ensemble', *Global Biogeochemical Cycles* **23**(1), GB1003. DOI: 10.1029/2008GB003316

García, H. E. and Gordon, L. I. (1992), 'Oxygen solubility in seawater: Better fitting equations', *Limnology and Oceanography* **37**(6), 1307–1312.

Gattuso, J.-P., Frankignoulle, M. and Wollast, R. (1998), 'Carbon and carbonate metabolism in coastal aquatic ecosystems', *Annual Review of Ecology and Systematics* **29**(1), 405–434. DOI: 10.1146/annurev.ecolsys.29.1.405

Goldman, J. and Brewer, P. (1980), 'Effect of nitrogen source and growth rate on phytoplankton-mediated changes in alkalinity', *Limnology and Oceanography* **25**(2), 352–357.

Grantham, B. A., Chan, F., Nielsen, K. J., Fox, D. S., Barth, J. A., Huyer, A., Lubchenco, J. and Menge, B. A. (2004), 'Upwelling-driven nearshore hypoxia signals ecosystem and oceanographic changes in the northeast Pacific', *Nature* **429**(6993), 749–754. DOI: 10.1038/nature02605

Gray, J. S., sun Wu, R. S. and Or, Y. Y. (2002), 'Effects of hypoxia and organic enrichment on the coastal marine environment', *Marine Ecology Progress Series* **238**, 249–279. DOI: 10.3354/meps238249

Gruber, N., Frenzel, H., Doney, S. C., Marchesiello, P., McWilliams, J. C., Moisan, J. R., Oram, J. J., Plattner, G.-K. and Stolzenbach, K. D. (2006), 'Eddy-resolving simulation of plankton ecosystem dynamics in the California Current System', *Deep Sea Research Part I: Oceanographic Research Papers* **53**(9), 1483 – 1516. DOI: 10.1016/j.dsr.2006.06.005

Hales, B., Karp-Boss, L., Perlin, A. and Wheeler, P. A. (2006), 'Oxygen production and carbon sequestration in an upwelling coastal margin', *Global Biogeochemical Cycles* **20**(3), GB3001–. DOI: 10.1029/2005GB002517

Harris, S. L. (2001), Size-fractionated chlorophyll and primary productivity and nutrient distributions off the west coast of Vancouver Island, Master's thesis, University of British Columbia, Vancouver, Canada.

Harris, S. L., Varela, D. E., Whitney, F. W. and Harrison, P. J. (2009), 'Nutrient and phytoplankton dynamics off the west coast of Vancouver Island during the 1997/98

ENSO event', *Deep Sea Research Part II: Topical Studies in Oceanography* **56**(24), 2487 – 2502. DOI: 10.1016/j.dsr2.2009.02.009

Hauri, C., Gruber, N., Plattner, G., Alin, S., Feely, R., Hales, B. and Wheeler, P. (2009), 'Ocean acidification in the California Current System', *Oceanography* **22**(4), 60–71.

Helly, J. J. and Levin, L. A. (2004), 'Global distribution of naturally occurring marine hypoxia on continental margins', *Deep Sea Research Part I: Oceanographic Research Papers* **51**(9), 1159 – 1168. DOI: 10.1016/j.dsr.2004.03.009

Hickey, B., Geier, S., Kachel, N. and MacFadyen, A. (2005), 'A bi-directional river plume: The Columbia in summer', *Continental Shelf Research* **25**(14), 1631 – 1656. DOI: 10.1016/j.csr.2005.04.010

Hickey, B. M. and Banas, N. S. (2008), 'Why is the northern end of the California Current System so productive?', *Oceanography* **21**(4), 91–107.

Hickey, B. M., Thomson, R. E., Yih, H. and LeBlond, P. H. (1991), 'Velocity and temperature fluctuations in a buoyancy-driven current off Vancouver Island', *Journal of Geophysical Research* **96**, 10,507–10,538. DOI: 10.1029/90JC02578

Hill, J. K. and Wheeler, P. A. (2002), 'Organic carbon and nitrogen in the northern California current system: comparison of offshore, river plume, and coastally upwelled waters', *Progress in Oceanography* **53**(2-4), 369 – 387. DOI: 10.1016/S0079-6611(02)00037-X

Hofmann, A. (2008), 'Interactive comment on "Enhanced ocean carbon storage from anaerobic alkalinity generation in coastal sediments" by H. Thomas et al.', *Biogeosciences Discuss.* **5**, S1955–S1962.

Hofmann, M. and Schellnhuber, H.-J. (2009), 'Oceanic acidification affects marine carbon pump and triggers extended marine oxygen holes', *Proceedings of the National Academy of Sciences of the United States of America* **106**(9), 3017–3022. DOI: 10.1073/pnas.0813384106

Hood, R. R. and Christian, J. R. (2008), Ocean nitrogen cycle modeling, *in* 'Nitrogen in the Marine Environment', 2nd edn, Academic Press, San Diego, chapter 33, pp. 1445 – 1495. DOI: 10.1016/B978-0-12-372522-6.00033-5

Hopkinson, C. S., Vallino, J. J. and Nolin, A. (2002), 'Decomposition of dissolved organic matter from the continental margin', *Deep Sea Research Part II: Topical Studies in Oceanography* **49**(20), 4461 – 4478. DOI: 10.1016/S0967-0645(02)00125-X

Ianson, D. and Allen, S. E. (2002), 'A two-dimensional nitrogen and carbon flux model in a coastal upwelling region', *Global Biogeochemical Cycles* **16**, –. DOI: 10.1029/2001GB001451

Ianson, D., Allen, S. E., Harris, S. L., Orians, K. J., Varela, D. E. and Wong, C. S. (2003), 'The inorganic carbon system in the coastal upwelling region west of Vancouver Island, Canada', *Deep Sea Research Part I: Oceanographic Research Papers* **50**(8), 1023 – 1042. DOI: 10.1016/S0967-0637(03)00114-6

Iglesias-Rodriguez, M. D., Halloran, P. R., Rickaby, R. E. M., Hall, I. R., Colmenero-Hidalgo, E., Gittins, J. R., Green, D. R. H., Tyrrell, T., Gibbs, S. J., von Dassow, P., Rehm, E., Armbrust, E. V. and Boessenkool, K. P. (2008), 'Phytoplankton calcification in a high-CO_2 world', *Science* **320**(5874), 336–340. DOI: 10.1126/science.1154122

Ikeda, T. and Hernandez-Leon, S. (2005), Zooplankton respiration, *in* P. del Giorgio and P. Williams, eds, 'Respiration in Aquatic Ecosystems', Oxford University Press, chapter 5, pp. 57–83(27). DOI: 10.1093/acprof:oso/9780198527084.003.0005

Kalnay, E., Kanamitsu, M., Kistler, R., Collins, W., Deaven, D., Gandin, L., Iredell, M., Saha, S., White, G., Woollen, J., Zhu, Y., Leetmaa, A., Reynolds, R., Chelliah, M., Ebisuzaki, W., Higgins, W., Janowiak, J., Mo, K. C., Ropelewski, C., Wang, J., Jenne, R. and Joseph, D. (1996), 'The NCEP/NCAR 40-Year Reanalysis Project', *Bulletin of the American Meteorological Society* **77**(3), 437–471.

Keeling, R. F. and Garcia, H. E. (2002), 'The change in oceanic O_2 inventory associated with recent global warming', *Proceedings of the National Academy of Sciences of the United States of America* **99**(12), 7848–7853. DOI: 10.1073/pnas.122154899

Laursen, A. E. and Seitzinger, S. P. (2002), 'The role of denitrification in nitrogen removal and carbon mineralization in Mid-Atlantic Bight sediments', *Continental Shelf Research* **22**(9), 1397 – 1416. DOI: 10.1016/S0278-4343(02)00008-0

Laws, E. A. (1991), 'Photosynthetic quotients, new production and net community production in the open ocean', *Deep Sea Research Part A. Oceanographic Research Papers* **38**(1), 143 – 167. DOI: 10.1016/0198-0149(91)90059-O

Laws, E. A., Falkowski, P. G., Smith, Walker O., J., Ducklow, H. and McCarthy, J. J. (2000), 'Temperature effects on export production in the open ocean', *Global Biogeochemical Cycles* **14**(4), 1231–1246. DOI: 10.1029/1999GB001229

Levitus, S., Antonov, J., Boyer, T., Locarnini, R., Garcia, H. and Mishonov, A. (2009), 'Global ocean heat content 1955-2008 in light of recently revealed instrumentation problems', *Geophysical Research Letters* **36**(7), L07608. DOI: 10.1029/2008GL037155

Levitus, S., Antonov, J. I., Wang, J., Delworth, T. L., Dixon, K. W. and Broccoli, A. J. (2001), 'Anthropogenic warming of Earth's Climate System', *Science* **292**(5515), 267–270. DOI: 10.1126/science.1058154

Liu, K.-K., Atkinson, L., Quiñones, R. A. and Talaue-McManus, L. (2010), *Carbon and Nutrient Fluxes in Continental Margins*, Global Change — The IGBP Series, 1 edn, Springer Berlin Heidelberg. DOI: 10.1007/978-3-540-92735-8

Álvarez Salgado, X. A., Doval, M. D., Borges, A. V., Joint, I., Frankignoulle, M., Woodward, E. M. S. and Figueiras, F. G. (2001), 'Off-shelf fluxes of labile materials by an upwelling filament in the NW Iberian Upwelling System', *Progress in Oceanography* **51**(2-4), 321 – 337. DOI: 10.1016/S0079-6611(01)00073-8

Macdonald, R. and Pedersen, T. (1991), 'Geochemistry of sediments of the western Canadian continental shelf', *Continental Shelf Research* **11**(8-10), 717 – 735. DOI: 10.1016/0278-4343(91)90076-I

Mackas, D. (1992), 'Seasonal cycle of zooplankton off southwestern British Columbia', *Canadian Journal of Fisheries and Aquatic Sciences* **49**(5), 903–921. DOI: 10.1139/f92-101

Mackas, D. L., Peterson, W. T. and Zamon, J. E. (2004), 'Comparisons of interannual biomass anomalies of zooplankton communities along the continental margins of British Columbia and Oregon', *Deep Sea Research Part II: Topical Studies in Oceanography* **51**(6-9), 875 – 896. DOI: 10.1016/j.dsr2.2004.05.011

Matear, R. J. and Holloway, G. (1995), 'Modeling the inorganic phosphorus cycle of the North Pacific using an adjoint data assimilation model to assess the role of dissolved organic phosphorus', *Global Biogeochemical Cycles* **9**(1), 101–119. DOI: 10.1029/94GB03104

McGregor, H. V., Dima, M., Fischer, H. W. and Mulitza, S. (2007), 'Rapid 20th-Century Increase in coastal upwelling off Northwest Africa', *Science* **315**(5812), 637–639. DOI: 10.1126/science.1134839

Merryfield, W. J., Pal, B. and Foreman, M. G. G. (2009), 'Projected future changes in surface marine winds off the west coast of Canada', *Journal of Geophysical Research* **114**(C6), C06008–. DOI: 10.1029/2008JC005123

Møller, E. F. (2005), 'Sloppy feeding in marine copepods: prey-size-dependent production of dissolved organic carbon', *Journal of Plankton Research* **27**(1), 27–35. DOI: 10.1093/plankt/fbh147

Møller, E. F., Thor, P. and Nielsen, T. G. (2003), 'Production of DOC by Calanus finmarchicus, C. glacialis and C. hyperboreus through sloppy feeding and leakage from fecal pellets', *Marine Ecology Progress Series* **262**, 185–191. DOI: 10.3354/meps262185

Monteiro, P. M. S., van der Plas, A., Mohrholz, V., Mabille, E., Pascall, A. and Joubert, W. (2006), 'Variability of natural hypoxia and methane in a coastal upwelling system: Oceanic physics or shelf biology?', *Geophysical Research Letters* **33**, 37–47. DOI: 10.1029/2006GL026234

Monteiro, P., van der Plas, A., Mélice, J.-L. and Florenchie, P. (2008), 'Interannual hypoxia variability in a coastal upwelling system: Ocean-shelf exchange, climate and ecosystem-state implications', *Deep Sea Research Part I: Oceanographic Research Papers* **55**(4), 435–450. DOI: 10.1016/j.dsr.2007.12.010

Moore, J. K. and Doney, S. C. (2007), 'Iron availability limits the ocean nitrogen inventory stabilizing feedbacks between marine denitrification and nitrogen fixation', *Global Biogeochemical Cycles* **21**, –. DOI: 10.1029/2006GB002762

Morel, F. and Hering, J. (1993), *Principles and applications of aquatic chemistry*, Wiley-Interscience, New York.

Mulder, A., van de Graaf, A. A., Robertson, L. A. and Kuenen, J. G. (1995), 'Anaerobic ammonium oxidation discovered in a denitrifying fluidized bed reactor', *FEMS Microbiology Ecology* **16**(3), 177–183. DOI: 10.1111/j.1574-6941.1995.tb00281.x

Muller-Karger, F. E., Varela, R., Thunell, R., Luerssen, R., Hu, C. and Walsh, J. J. (2005), 'The importance of continental margins in the global carbon cycle', *Geophysical Research Letters* **32**, –. DOI: 10.1029/2004GL021346

Najjar, R. G. (1992), Marine biogeochemistry, *in* K. E. Trenberth, ed., 'Climate System Modeling', Cambridge University Press, Cambridge, England, pp. 241–280.

Najjar, R. G., Sarmiento, J. L. and Toggweiler, J. R. (1992), 'Downward transport and fate of organic matter in the ocean: Simulations with a general circulation model', *Global Biogeochemical Cycles* **6**(1), 45–76. DOI: 10.1029/91GB02718

Nakicenovic, N., Alcamo, J., Davis, G., de Vries, B., Fenhann, J., Gaffin, S., Gregory, K., Grubler, A., Jung, T., Kram, T., Lebre La Rovere, E., Michaelis, L., Mori, S., Morita, T., Pepper, W., Pitcher, H., Price, L., Riahi, K., Roehrl, A., Rogner, H.-H., Sankovski, A., Schlesinger, M., Shukla, P., Smith, S., Swart, R., Van Rooijen, S., Victor, N. and Dadi, Z. (2000), *Special Report on Emissions Scenarios: a special report of Working Group III of the Intergovernmental Panel on Climate Change*, Cambridge University Press, Cambridge, U.K.

Nevison, C., Butler, J. H. and Elkins, J. W. (2003), 'Global distribution of N_2O and the ΔN_2O-AOU yield in the subsurface ocean', *Global Biogeochemical Cycles* **17**, –. DOI: 10.1029/2003GB002068

Orr, J. C., Fabry, V. J., Aumont, O., Bopp, L., Doney, S. C., Feely, R. A., Gnanadesikan, A., Gruber, N., Ishida, A., Joos, F., Key, R. M., Lindsay, K., Maier-Reimer, E., Matear, R., Monfray, P., Mouchet, A., Najjar, R. G., Plattner, G.-K., Rodgers, K. B., Sabine, C. L., Sarmiento, J. L., Schlitzer, R., Slater, R. D., Totterdell, I. J., Weirig, M.-F., Yamanaka, Y. and Yool, A. (2005), 'Anthropogenic ocean acidification over the twenty-first century and its impact on calcifying organisms', *Nature* **437**(7059), 681–686. DOI: 10.1038/nature04095

Osborn, T. R. (1980), 'Estimates of the local rate of vertical diffusion from dissipation measurements', *Journal of Physical Oceanography* **10**(1), 83–89.

Oschlies, A., Schulz, K. G., Riebesell, U. and Schmittner, A. (2008), 'Simulated 21st century's increase in oceanic suboxia by CO_2-enhanced biotic carbon export', *Global Biogeochemical Cycles* **22**(4), GB4008–. DOI: 10.1029/2007GB003147

Overland, J. and Wang, M. (2007), 'Future climate of the North Pacific Ocean', *EOS Transactions AGU* **88**(16), 178–182. DOI: 10.1029/2007EO160003

Paasche, E. (1962), 'Coccolith formation', *Nature* **193**(4820), 1094–1095. DOI: 10.1038/1931094b0

Paasche, E. (2001), 'A review of the coccolithophorid *Emiliania huxleyi* (Prymnesiophyceae), with particular reference to growth, coccolith formation, and calcification-photosynthesis interactions', *Phycologia* **40**(6), 503–529.

Pauly, D. and Christensen, V. (1995), 'Primary production required to sustain global fisheries', *Nature* **374**(6519), 255–257.

Perlin, A., Moum, J. N. and Klymak, J. M. (2005), 'Response of the bottom boundary layer over a sloping shelf to variations in alongshore wind', *Journal of Geophysisical Research* **110**(C10), C10S09–. DOI: 10.1029/2004JC002500

Pörtner, H.-O. (2010), 'Oxygen- and capacity-limitation of thermal tolerance: a matrix for integrating climate-related stressor effects in marine ecosystems', *Journal of Experimental Biology* **213**(6), 881–893. DOI: 10.1242/jeb.037523

Pörtner, H. O. and Farrell, A. P. (2008), 'Physiology and climate change', *Science* **322**(5902), 690–692. DOI: 10.1126/science.1163156

Rabalais, N., Levin, L., Turner, R., Gilbert, D. and Zhang, J. (2010), 'Dynamics and distribution of natural and human-caused hypoxia', *Biogeosciences* **7**, 585–619. DOI: 10.5194/bg-7-585-2010

Raymond, W. H. and Kuo, H. L. (1984), 'A radiation boundary condition for multi-dimensional flows', *Quarterly Journal of the Royal Meteorological Society* **110**(464), 535–551. DOI: 10.1002/qj.49711046414

Redfield, A. C., Ketchum, B. H. and Richards, F. A. (1963), The influence of organisms on the composition of seawater, *in* M. N. Hill, ed., 'The Sea: Ideas and Observations on Progress in the Study of the Seas', Vol. 2. The Composition of Seawater, Wiley, New York, pp. 26–77.

Riebesell, U., Bellerby, R. G. J., Engel, A., Fabry, V. J., Hutchins, D. A., Reusch, T. B. H., Schulz, K. G. and Morel, F. M. M. (2008), 'Comment on "Phytoplankton calcification in a high-CO_2 world"', *Science* **322**(5907), 1466. DOI: 10.1126/science.1161096

Rivkin, R. B. and Legendre, L. (2001), 'Biogenic carbon cycling in the upper ocean: Effects of microbial respiration', *Science* **291**(5512), 2398–2400. DOI: 10.1126/science.291.5512.2398

Sabine, C. and Feely, R. (2007), *Greenhouse gas sinks*, CABI, Oxfordshire, UK, chapter The oceanic sink for carbon dioxide, p. 31.

Sabine, C. L., Feely, R. A., Gruber, N., Key, R. M., Lee, K., Bullister, J. L., Wanninkhof, R., Wong, C. S., Wallace, D. W. R., Tilbrook, B., Millero, F. J., Peng, T.-H., Kozyr, A., Ono, T. and Rios, A. F. (2004), 'The oceanic sink for anthropogenic CO_2', *Science* **305**(5682), 367–371. DOI: 10.1126/science.1097403

Sambrotto, R. N., Savidge, G., Robinson, C., Boyd, P., Takahashi, T., Karl, D. M., Langdon, C., Chipman, D., Marra, J. and Codispoti, L. (1993), 'Elevated consumption of carbon relative to nitrogen in the surface ocean', *Nature* **363**(6426), 248–250. DOI: 10.1038/363248a0

Santana-Casiano, J. M., González-Dávila, M., Rueda, M.-J., Llinás, O. and González-Dávila, E.-F. (2007), 'The interannual variability of oceanic CO_2 parameters in the northeast Atlantic subtropical gyre at the ESTOC site', *Global Biogeochemical Cycles* **21**(1), GB1015–. DOI: 10.1029/2006GB002788

Sarmiento, J. and Gruber, N. (2006), *Ocean Biogeochemical Dynamics*, Princeton University Press, Princeton, NJ.

Schwing, F. and Mendelssohn, R. (1997), 'Increased coastal upwelling in the California Current System', *Journal of Geophysical Research* **102**(C2), 3421–3438.

Seitzinger, S. and Giblin, A. (1996), 'Estimating denitrification in North Atlantic continental shelf sediments', *Biogeochemistry* **35**(1), 235–260. DOI: 10.1007/BF02179829

Seitzinger, S., Harrison, J. A., Bohlke, J. K., Bouwman, A. F., Lowrance, R., Peterson, B., Tobias, C. and Drecht, G. V. (2006), 'Denitrification across landscapes and waterscapes: A synthesis', *Ecological Applications* **16**(6), 2064–2090. DOI: 10.1890/1051-0761(2006)016[2064:DALAWA]2.0.CO;2

Shaffer, G., Olsen, S. M. and Pedersen, J. O. P. (2009), 'Long-term ocean oxygen depletion in response to carbon dioxide emissions from fossil fuels', *Nature Geoscience* **2**(2), 105–109. DOI: 10.1038/ngeo420

Shchepetkin, A. F. and McWilliams, J. C. (2005), 'The regional oceanic modeling system (ROMS): a split-explicit, free-surface, topography-following-coordinate oceanic model', *Ocean Modelling* **9**(4), 347 – 404. DOI: 10.1016/j.ocemod.2004.08.002

Sikes, C., Roer, R. and Wilbur, K. (1980), 'Photosynthesis and coccolith formation: Inorganic carbon sources and net inorganic reaction of deposition', *Limnology and Oceanography* **25**(2), 248–261.

Small, C. and Nicholls, R. J. (2003), 'A global analysis of human settlement in coastal zones', *Journal of Coastal Research* **19**(3), 584–599.

Smith, S. D. (1988), 'Coefficients for sea surface wind stress, heat flux, and wind profiles as a function of wind speed and temperature', *Journal of Geophysical Research* **93(C12)**, 15467–15472.

Smith, S. V. and Hollibaugh, J. T. (1993), 'Coastal metabolism and the oceanic organic carbon balance', *Reviews of Geophysics* **31**, –. DOI: 10.1029/92RG02584

Snyder, M. A., Sloan, L. C., Diffenbaugh, N. S. and Bell, J. L. (2003), 'Future climate change and upwelling in the California Current', *Geophysical Research Letters* **30**(15), 1823–. DOI: 10.1029/2003GL017647

Soetaert, K., Middelburg, J. J., Herman, P. M. J. and Buis, K. (2000), 'On the coupling of benthic and pelagic biogeochemical models', *Earth-Science Reviews* **51**(1-4), 173 – 201. DOI: 10.1016/S0012-8252(00)00004-0

Spitz, Y. H., Newberger, P. A. and Allen, J. S. (2003), 'Ecosystem response to upwelling off the Oregon coast: Behavior of three nitrogen-based models', *Journal of Geophysical Research* **108**, –. DOI: 10.1029/2001JC001181

Steinacher, M., Joos, F., Frölicher, T., Plattner, G. and Doney, S. (2009), 'Imminent ocean acidification in the Arctic projected with the NCAR global coupled carbon cycle-climate model', *Biogeosciences* **6**(4), 515–533. DOI: 10.5194/bg-6-515-2009

Stramma, L., Johnson, G. C., Sprintall, J. and Mohrholz, V. (2008), 'Expanding Oxygen-Minimum Zones in the tropical oceans', *Science* **320**(5876), 655–658. DOI: 10.1126/science.1153847

Taguchi, F. and Fujiwara, T. (2010), 'Carbon dioxide stored and acidified low oxygen bottom waters in coastal seas, Japan', *Estuarine, Coastal and Shelf Science* **86**(3), 429–433. DOI: 10.1016/j.ecss.2009.07.037

Thomas, H., Bozec, Y., Elkalay, K. and de Baar, H. J. W. (2004), 'Enhanced open ocean storage of CO_2 from shelf sea pumping', *Science* **304**(5673), 1005–1008. DOI: 10.1126/science.1095491

Thomas, H., Schiettecatte, L.-S., Suykens, K., M., K. Y. J., Shadwick, E. H., Prowe, A. E. F., Bozec, Y., de Baar, H. J. W. and Borges, A. V. (2009), 'Enhanced ocean carbon storage from anaerobic alkalinity generation in coastal sediments', *Biogeosciences* **6**(2), 267–274. DOI: 10.5194/bg-6-267-2009

Thomson, R. E., Hickey, B. M. and LeBlond, P. H. (1989), The Vancouver Island coastal current: fisheries barrier and conduit, *in* G. McFarlane, ed., 'Effects of Ocean Variability on Recruitment and an Evaluation of Parameters Used in Stock Assessment Models', Canadian Special Publication of Fisheries and Aquatic Sciences, pp. 265 – 296.

Tsunogai, S., Watanabe, S. and Sato, T. (1999), 'Is there a "continental shelf pump" for the absorption of atmospheric CO_2?', *Tellus Series B Chemical and Physical Meteorology* **51**, 701–712. DOI: 10.1034/j.1600-0889.1999.t01-2-00010.x

Vaquer-Sunyer, R. and Duarte, C. M. (2008), 'Thresholds of hypoxia for marine biodiversity', *Proceedings of the National Academy of Sciences of the United States of America* **105**(40), 15452–15457. DOI: 10.1073/pnas.0803833105

Wang, M., Overland, J. E. and Bond, N. A. (2010), 'Climate projections for selected large marine ecosystems', *Journal of Marine Systems* **79**(3-4), 258 – 266.

Wanninkhof, R. (1992), 'Relationship between wind speed and gas exchange over the ocean', *Journal of Geophysical Research* **97**(C5), 7373–7382. DOI: 10.1029/92JC00188

Ward, B. B. (2000), *Microbial ecology of the oceans*, Wiley-Liss, New York, chapter Nitrification and the marine nitrogen cycle, p. 427–453.

Ward, B. B., Devol, A. H., Rich, J. J., Chang, B. X., Bulow, S. E., Naik, H., Pratihary, A. and Jayakumar, A. (2009), 'Denitrification as the dominant nitrogen loss process in the Arabian Sea', *Nature* **461**(7260), 78–81. DOI: 10.1038/nature08276

Waterhouse, A. F., Allen, S. E. and Bowie, A. W. (2009), 'Upwelling flow dynamics in long canyons at low Rossby number', *Journal of Geophysical Research* **114**(C5), C05004. DOI: 10.1029/2008JC004956

Weiss, R. (1974), 'Carbon dioxide in water and seawater: the solubility of a non-ideal gas', *Marine Chemistry* **2**(3), 203 – 215. DOI: 10.1016/0304-4203(74)90015-2

Werner, F. E. and Hickey, B. M. (1983), 'The role of a longshore pressure gradient in Pacific Northwest coastal dynamics', *Journal of Physical Oceanography* **13**(3), 395–410.

Wetz, J. J., Arrington, J. and Wheeler, P. A. (2006), Particulate and Dissolved Organic Carbon and Nitrogen data from the GLOBEC Long-Term Observation Program, 1997-2004, Technical report, College of Oceanic and Atmospheric Sciences, Oregon State University, Corvallis, Oregon.

Wetz, M. S., Hales, B. and Wheeler, P. A. (2008), 'Degradation of phytoplankton-derived organic matter: Implications for carbon and nitrogen biogeochemistry in coastal ecosystems', *Estuarine, Coastal and Shelf Science* **77**(3), 422 – 432.

White, P., Kalff, J., Rasmussen, J. and Gasol, J. (1991), 'The effect of temperature and algal biomass on bacterial production and specific growth rate in freshwater and marine habitats', *Microbial Ecology* **21**(1), 99–118. DOI: 10.1007/BF02539147

Whitney, F. A., Freeland, H. J. and Robert, M. (2007), 'Persistently declining oxygen levels in the interior waters of the eastern subarctic Pacific', *Progress in Oceanography* **75**(2), 179 – 199. DOI: 10.1016/j.pocean.2007.08.007

Whitney, F., Crawford, W. and Harrison, P. (2005), 'Physical processes that enhance nutrient transport and primary productivity in the coastal and open ocean of the subarctic NE Pacific', *Deep Sea Research Part II: Topical Studies in Oceanography* **52**(5-6), 681 – 706.

Williams, P. J. l. B. and del Giorgio, P. A. (2005), Respiration in aquatic ecosystems: history and background, *in* P. del Giorgio and P. Williams, eds, 'Respiration in aquatic ecosystems', Oxford University Press, chapter 1, pp. 1–18(18).

Wolf-Gladrow, D., Zeebe, R., Klaas, C., Körtzinger, A. and Dickson, A. (2007), 'Total alkalinity: The explicit conservative expression and its application to biogeochemical processes', *Marine Chemistry* **106**(1-2), 287–300. DOI: 10.1016/j.marchem.2007.01.006

Wollast, R. (1998), Evolution and comparison of the global carbon cycle in the coastal zone and in the open ocean, *in* K. Brink and A. Robinson, eds, 'The Global Coastal Ocean, Processes and methods', Vol. 10, John Wiley & Sons, p. 213–252.

Wootton, J. T., Pfister, C. A. and Forester, J. D. (2008), 'Dynamic patterns and ecological impacts of declining ocean pH in a high-resolution multi-year dataset', *Proceedings of the National Academy of Sciences of the United States of America* **105**(48), 18848–18853.

Zeebe, R. and Wolf-Gladrow, D. (2001), *CO_2 in Seawater: Equilibrium, kinetics, isotopes*, Elsevier, Amsterdam.

Appendix A. Ecosystem model equations

The ecosystem model consists of 13 state variables to represent the carbon, nitrogen, and O_2 cycles. Phytoplankton (P) and zooplankton (Z) each represent a single functional group (diatoms and mesozooplankton, respectively) expressed in nitrogen units (mmol-N m^{-3}), and assume a fixed C:N Redfield ratio of 106:16 ($R_{C:N}$ = 6.625). The nonliving carbon and nitrogen pools are explicitly modelled as detritus (D_C and D_N) and semilabile organic matter (DOC_{SL} and DON_{SL}), so C:N ratios are variable. On the other hand, the labile fractions of dissolved organic carbon and nitrogen (DOC_{Lab} and DON_{Lab}) are implicitly modelled by assuming instantaneous remineralization to dissolved inorganic carbon (DIC) and ammonium (NH_4), respectively. Nutrients also include a nitrate (NO_3) pool. Oxygen (O_2) is explicitly represented and coupled to the carbon cycle through photosynthetic quotients (PQa = 1.1 and PQn = 1.4; see section 2.2.2). Total alkalinity (TA) is modelled as a non-conservative property (i.e, with biological sources and sinks). The sediment layer contains both carbon and nitrogen components ($Csed$ and $Nsed$), each receiving particulate organic carbon and nitrogen deposited to the seafloor as sinking P, D_C, and D_N. A list of most model parameters, their values, and how they were obtained is given in Table 2.2 (the few not listed are given here in the text).

Most of the equations correspond to ROMS release 3.2; the nitrogen cycle equations were previously described in Fennel et al. (2006) and the carbon equations in Fennel et al. (2008), hereafter referred to as F06 and F08. ROMS O_2 equations have not described in the literature yet. The equations in this Appendix will refer to F06, F08, and ROMS where applicable, and will emphasize changes from the original formulations. Instead of

a small particle detritus pool as in F06, I introduced DOM to the model, mainly based on Druon et al (2009), hereafter D09.

Primary production (new and regenerated) increases *P* biomass, while *P* exudation to DON_{SL} and DON_{Lab}, grazing by *Z*, and *P* mortality reduce it. As well, *P* is allowed to sink through the water column. These processes are represented by

$$\frac{\partial P}{\partial t} = \nu P - \varepsilon_N P - \omega_N P - gZ - m_P P - w_P \frac{\partial P}{\partial z} \qquad \text{A.1}$$

(F06, except exudation formulations adapted from D09) where new and recycled primary production are combined in the first right hand term (νP), ε_N and ω_N are exudation rates of DON_{SL} and DON_{Lab}, respectively, g is the grazing rate of *P* by *Z*, m_P is the mortality rate of *P*, and w_P is the sinking velocity of *P*. The *P* growth rate ν is represented as

$$\nu = \nu^* f_I \left(L_{NO_3} + L_{NH_4} \right) \qquad \text{A.2}$$

(F06) where ν^* is the temperature dependent growth rate (Eppley 1972), f_I represents light limitation, and L_{NO_3} and L_{NH_4} are the nutrient limitation terms for NO_3 and NH_4, respectively (carbon is not considered a limiting nutrient). These terms are given by:

$$\nu^* = \nu_0 \, e^{kT} \qquad \text{A.3}$$

(F06) where ν_0 is the specific maximum growth rate at 0ºC (given in d^{-1} and transformed to Eppley's units of doublings per day by multiplying by 0.59), k = 0.0639, and temperature T is in ºC;

$$f_I = \frac{\alpha \, PAR}{\sqrt{\nu^2 + \alpha^2 PAR^2}} \qquad \text{A.4}$$

(F06) where *PAR* stands for photosynthetically available radiation and α is the initial slope of the primary production rate vs. *PAR* irradiance curve. *PAR* is assumed to be 43 % of the short wave radiation reaching the surface of the ocean and is exponentially

attenuated through the water column by an empirical diffuse attenuation coefficient representing the effects of seawater, phytoplankton biomass *P* (Fasham 1995), and an implicit representation of chromophoric dissolved organic matter (the latter added to the code following Druon et al. (2009); details in section 5.1);

$$L_{NO_3} = \frac{NO_3}{NO_3 + K_{NO_3}} \frac{1}{1 + \frac{NH_4}{K_{NH_4}}} \quad \text{(a)} \quad ; \qquad L_{NH_4} = \frac{NH_4}{NH_4 + K_{NH_4}} \quad \text{(b)} \qquad \text{A.5}$$

(F06) where K_{NO_3} and K_{NH_4} are the half saturation concentrations for uptake of NO_3 and NH_4, respectively. The second factor on the right hand side of equation A.5a represents an inhibition term for uptake of NO_3 in the presence of abundant NH_4 (F06). The total nutrient limitation in equation A.2 is represented by the sum of L_{NO_3} and L_{NH_4} (L_{Tot}), which is always less than one:

$$L_{Tot} = L_{NO_3} + L_{NH_4} = \frac{NO_3}{NO_3 + K_{NO_3}} \frac{K_{NH_4}}{K_{NH_4} + NH_4} + \frac{NH_4}{NH_4 + K_{NH_4}} \leq 1 \qquad \text{A.6}$$

Grazing of *P* by *Z* follows a Holling type III equation:

$$g = g_{max} \frac{P^2}{P^2 + K_P^2} \qquad \text{A.7}$$

(F06) where g_{max} is the maximum grazing rate and K_P is the half-saturation concentration for *P* ingestion. This formulation allows a "refuge" for *P* at very low concentrations, to avoid them becoming extinct due to numerical errors associated with finite time steps.

The time rate of change of *Z* is given by:

$$\frac{\partial Z}{\partial t} = g\beta Z - m_Z Z^2 - \left(l_{BM} + l_E \beta \frac{g}{g_{max}} \right) Z \qquad \text{A.8}$$

(F06) Z biomass increases by assimilating a fraction β of the P grazed and decreases due to quadratic mortality with rate m_Z. Another loss of Z biomass results from excretion of nutrients (NH_4 and DIC), which includes two mechanisms (F06): i) the basal metabolism of Z, represented by a linear rate (l_{BM}), and ii) an excretion rate proportional to the assimilation of P (with maximum rate l_E).

The products from Z and P mortality are transferred to the D_N and D_C pools. Moreover, a fraction $1 - Q$ of the unassimilated grazing ($1 - \beta$) is considered to be feces of Z, thus allocated as detritus as well (the remaining fraction Q of the unassimilated grazing is considered DOM, both labile and semilabile fractions). The loss terms for D_N and D_C are dissolution to DON_{SL} and DOC_{SL} and remineralization to NH_4 and DIC. D_N and D_C can sink through the water column. The equations for D_N and D_C follow:

$$\frac{\partial D_N}{\partial t} = m_P\, P + m_Z\, Z^2 + (1-\beta)(1-Q)\, g\, Z - s_N\, D_N - r_{D_N} D_N - w_D \frac{\partial D_N}{\partial z} \qquad \text{A.9}$$

$$\frac{\partial D_C}{\partial t} = R_{C:N}\left[m_P\, P + m_Z\, Z^2 + (1-\beta)(1-Q)\, g\, Z\right] - s_C\, D_C - r_{D_C} D_C - w_D \frac{\partial D_C}{\partial z} \qquad \text{A.10}$$

(F06 and F08, except $1 - Q$ fraction and dissolution to DOM formulation adapted from D09) where s_N (s_C) and r_{D_N} (r_{D_C}) are the rates for the dissolution and remineralization of D_N (D_C). Note than in equation A.10, P and Z must be multiplied by the $R_{C:N}$ ratio to transform them to carbon units. A fraction Q of the unassimilated ingestion of P is released as DOM according to the equation:

$$Q = 0.71 \frac{g}{g_{\max}} \qquad \text{A.11}$$

(after D09, see section 5.1). The equation for DON_{SL} is:

$$\frac{\partial DON_{SL}}{\partial t} = (1-\beta) Q\, \delta_N\, g\, Z + \varepsilon_N\, P + s_N\, D_N - r_{DON}\, DON_{SL} \qquad \text{A.12}$$

(D09) The parameter δ_N represents the DON_{SL} fraction to total DON, so the fraction of unassimilated grazing $(1 - \beta)$ reaching the DON_{SL} pool is $Q\ \delta_N$ ($\delta_N = 0.3$ after D09 and references therein). Other sources of DON_{SL} already discussed are P exudation with rate ε_N and dissolution of D_N. DON_{SL} decays by remineralization by bacteria with a rate r_{DON}.

The equation for DOC_{SL} is analogous to A.12, with P exudation rate ε_C, a fraction δ_C representing the ratio of DOC_{SL} to total DOC ($\delta_C = 0.55$ after D09 and references therein), a dissolution rate s_C, and a remineralization rate r_{DOC}:

$$\frac{\partial DOC_{SL}}{\partial t} = R_{C:N}\left[(1-\beta) Q\, \delta_C\, g\, Z + \varepsilon_C\, P\right] + s_C\, D_C - r_{DOC}\, DOC_{SL} + \sigma_C\, Excess\text{-}C \qquad \text{A.13}$$

(D09) As in the equation for D_C, P and Z must be multiplied by the $R_{C:N}$ ratio to transform P and Z to carbon units. The main distinction between A.12 and A.13 is the extra source of DOC_{SL} resulting from excess carbon uptake during primary production under nutrient-limited conditions (also referred to as excess carbon production or "*Excess-C*"), which represents carbohydrate over-production that consumes DIC and transforms it into DOC (both labile and semilabile). The parameter σ_C represents the fraction of *Excess-C* that becomes DOC_{SL} ($\sigma_C = 0.45$, after D09); the remaining fraction $1 - \sigma_C$ is directed to DOC_{Lab}. The full expression of *Excess-C* is

$$Excess\text{-}C = \gamma\, \nu^*\, f_I\ \left(1 - L_{Tot}\right)\ P\, R_{C:N} \qquad \text{A.14}$$

(D09) where $\gamma = 0.2$ (after Ianson and Allen (2002) and D09), and ν^* and f_I are described in equations A.3 and A.4 (P is multiplied by $R_{C:N}$ to transform it to carbon units). The term $1 - L_{Tot}$ is close to one when both NO_3 and NH_4 are low and is close to zero when either NO_3 or NH_4 are high (see the upper bound of L_{Tot} in equation A.6).

There is a fraction $1 - \sigma_C$ of *Excess-C* that is directed to DOC_{Lab}. As labile DOM is instantaneously remineralized back to its inorganic constituents, this fraction of the excess consumption of *DIC* is directed back to *DIC* (i.e., there is a net DIC consumption of a σ_C fraction of *Excess-C*, second term on right in A.15). Primary production (new and regenerated, i.e. *vP*) also takes up *DIC*, while the biological sources of recycled *DIC* are: *P* exudation of DOC_{Lab}, a fraction of unassimilated grazing considered to be DOC_{Lab} (instantaneously remineralized to *DIC*), direct *Z* excretion to *DIC*, and remineralization of DOC_{SL} and D_C. The equation for *DIC* is:

$$\frac{\partial DIC}{\partial t} = -\nu\, P\, R_{C:N} - \sigma_C\, Excess\text{-}C + R_{C:N}\left[\omega_C\, P + (1-\beta)\, Q\,(1-\delta_C)\, g\, Z + \left(l_{BM} + l_E \beta \frac{g}{g_{max}}\right) Z\right] + r_{DOC}\, DOC_{SL} + r_{D_C}\, D_C + VICC_{DIC} + \frac{F_{CO_2}}{\Delta z_{surf}} + \frac{F_{DIC}}{\Delta z_{bott}} \qquad \text{A.15}$$

(F08, except *Excess-C* and processes associated to DOC_{Lab} adapted from D09) $VICC_{DIC}$ (which I adapted from the available restoring options in ROMS) represents the restoring term that in the shallowest region of the domain restores DIC to the conditions of the Vancouver Island Coastal Current (VICC). The formulation of this term is

$$VICC_{DIC}(x) = \frac{DIC_{VICC} - DIC}{\tau(x)} \qquad \text{A.16}$$

where DIC_{VICC} are concentrations within the VICC and τ is a restoring time scale, which is a function of the distance (x) from the inshore boundary. Details of the representation of the VICC in the model are given in Appendix B. The term F_{CO_2} is the air-sea flux of CO_2 across the surface (positive into the ocean):

$$F_{CO_2} = k_s\, k_w\, (pCO_{2_{air}} - pCO_{2_{sea}}) \qquad \text{A.17}$$

where the solubility coefficient k_s follows Weiss (1974) and the gas transfer velocity k_w follows Wanninkhof (1992). The atmospheric partial pressure of carbon dioxide ($pCO_{2_{air}}$) is set as a boundary condition and the partial pressure in surface waters ($pCO_{2_{sea}}$) is calculated from temperature, salinity, *DIC*, and *TA,* using the Ocean Carbon-Cycle Model Intercomparison Project (OCMIP2) standard routines. F_{CO_2} is divided in A.15 by the thickness of the near-surface layer, Δz_{surf}. The term F_{DIC} (divided by the thickness of the near-bottom layer, Δz_{bott}) represents the bottom boundary condition for *DIC* and will be explained in detail at the end of this Appendix.

NH_4 is taken up during primary production and during nitrification (the process converting NH_4 into NO_3 by aerobic bacteria, see equation 4.4). The biological sources of NH_4 parallel those for *DIC*: *P* exudation of DON_{Lab}, *Z* losses of unassimilated grazing to DON_{Lab}, direct *Z* excretion to NH_4, and remineralization of DON_{SL} and D_N (as in the case of DOC_{Lab}, DON_{Lab} is assumed to be remineralized instantaneously to NH_4). The time rate of change of NH_4 is:

$$\frac{\partial NH_4}{\partial t} = -\nu^* \, f_I \, L_{NH_4} P - n_{Nit} \, NH_4 + \omega_N \, P + (1-\beta) Q \, (1-\delta_N) \, g \, Z + \left(l_{BM} + l_E \beta \frac{g}{g_{max}} \right) Z + r_{DON} \, DON_{SL} + r_{D_N} D_N + \frac{F_{NH_4}}{\Delta z_{bott}} \qquad \text{A.18}$$

(F06, except processes associated with DON_{Lab} adapted from D09, and n_{Nit}). Nitrification consumes NH_4 (and produces NO_3) at a rate n_{Nit} that varies with O_2 and inversely with light following Denman (2003):

$$n_{Nit} = n_{Nitmax} \, f_{ox} \, \frac{z^{n_z}}{z_{ox}^{n_z} + z^{n_z}} \qquad \text{A.19}$$

where n_{Nitmax} is the maximum rate, z_{ox} is the depth of the half nitrification light level (I_0), and the exponent n_z determines the sharpness of the vertical gradient in n_{Nit}. The function

f_{ox} represents the O_2-dependence of nitrification (new addition to Denman (2003) formulation) and is given by:

$$f_{ox} = \frac{{O_2}^{n_O}}{k_{nit}^{n_O} + {O_2}^{n_O}} \qquad \text{A.20}$$

where k_{nit} is the half saturation constant and n_O is the exponent (analogous to n_z). f_{ox} is 1 for $O_2 > 5$ mmol m^{-3} (details in Chapter 2). The term F_{NH_4} (divided by Δz_{bott}) in A.18 is the bottom boundary condition for NH_4 and will be described at the end of this Appendix.

New primary production takes up NO_3 and nitrification produces it. Moreover, NO_3 is restored in the VICC region ($VICC_{NO_3}$) in the same manner as DIC (equation A.16).

$$\frac{\partial NO_3}{\partial t} = -\nu^* f_I L_{NO_3} P + n_{Nit} NH_4 + VICC_{NO_3} - (1 - f_{ox})\left(r_{DON} DON_{SL} + r_{D_N} D_N\right) R_{NO_3:NH_4} \qquad \text{A.21}$$

(F06, except n_{Nit} and denitrification). The last term on the right hand side of A.21 represents reduction of NO_3 by denitrification when $O_2 < 5$ mmol m^{-3} in the water column (i.e., when $1 - f_{ox} > 0$). The parameter $R_{NO_3:NH_4}$ (84.8:16 = 5.3) is the ratio of NO_3 consumed to NH_4 produced by denitrification of 106 mol-C in organic matter (equation 4.5), following the reactions described by Fennel et al. (2006). Note that the same amount of NH_4 (as well as DIC) is released by the break down of 106 mol-C in organic matter (i.e., 16 mol-NH_4, 106 mol-DIC) whether the process is aerobic remineralization or anaerobic denitrification (compare equations 4.3 and 4.5). The rates of both processes are assumed to be equal (i.e., r_{DON}, r_{DOC}, r_{D_N}, and r_{D_C} also represent the rate of oxidation of organic matter under O_2 limited conditions). A description of the O_2 concentration threshold for the onset of denitrification in the water column is found in section 2.2.2.

New and regenerated primary production, as well as excess carbon uptake, are sources of O_2 in the ecosystem model. P exudation of DOC_{Lab} and the fraction of unassimilated grazing by Z released as DOC_{Lab}, as well as direct Z excretion to DIC, remineralization of DOC_{SL} and D_C, and nitrification are sinks of O_2. Moreover, the VICC O_2 concentrations ($O_{2_{VICC}}$) are restored in the shallow waters (analogously to the restoring of DIC in equation A.16). O_2 exchange with the atmosphere occurs at the surface of the ocean. The O_2 equation is:

$$\frac{\partial O_2}{\partial t} = PQa\left(\nu\, P\, R_{C:N} + \sigma_C\ \ Excess\text{-}C\right)$$
$$- PQa\left(R_{C:N}\left[\omega_C\, P + (1-\beta)\, Q\,(1-\delta_C)\, g\, Z + \left(l_{BM} + l_E \beta \frac{g}{g_{max}}\right) Z\right]\right.$$
$$\left. + f_{ox}\left(r_{DOC}\ DOC_{SL} + r_{D_C} D_C\right)\right) - n_{Nit}\ NH_4\ R_{C:N}\left(PQa - PQn\right)$$
$$+ VICC_{O_2} + \frac{F_{O_{2surf}}}{\Delta z_{surf}} + \frac{F_{O_{2bott}}}{\Delta z_{bott}} \qquad \text{A.22}$$

(ROMS, except DOM associated processes, O_2-dependence of aerobic remineralization, n_{Nit}, and coupling to the carbon cycle rather than to nitrogen). PQn = 1.4 and PQa = 1.1 represent the photosynthetic quotients (i.e., the ratio O_2:C in moles of O_2 produced per mole of carbon assimilated) for new and regenerated production, respectively (equations 4.2 and 4.3). The losses of dissolved O_2 due to remineralization of D_C and DOC_{SL} (first term in the third line of equation A.22) are multiplied by f_{ox}, since aerobic remineralization is reduced when O_2 is scarce (i.e., $f_{ox} \sim 0$). At those low concentrations of O_2, the reduction of NO_3 is activated in the water column (last term of equation A.21). The term F_{O2surf} represents the air-sea flux of O_2

$$F_{O2surf} = \ k_w\,(O_{2_{sat}} - O_2) \qquad \text{A.23}$$

where the concentration of O_2 at saturation ($O_{2_{sat}}$) is calculated after García and Gordon (1992) and the gas transfer velocity k_w follows Wanninkhof (1992). F_{Osurf_2} is positive into the ocean. The last term of equation A.22, $F_{O_{2bott}}$, represents the bottom boundary condition for O_2 (detailed at the end of the Appendix).

Chapter 4 presents an expression for *TA* (equation 4.1) and describes how *TA* is affected by various biogeochemical processes (section 4.1.1):

$$\frac{\partial TA}{\partial t} = \nu^* \, f_I \, L_{NO_3} P + (1 - f_{ox}) \left(r_{DON} \, DON_{SL} + r_{D_N} D_N \right) R_{NO_3:NH_4} - n_{Nit} \, NH_4 \qquad \text{A.24}$$

(F08, except n_{Nit} and water column denitrification). The biological sources of *TA* in the water column that the model includes are new primary production and denitrification (when present in the water column, i.e., at low ambient O_2 concentrations), both consuming NO_3. The only modelled sink of *TA* is nitrification, which produces NO_3. Section 4.2 details the assumptions behind this choice of sources and sinks.

The bottom boundary conditions for the ecosystem model (F_{DIC}, F_{NH4}, and $F_{O_{2bott}}$) are provided by the parameterization of the exchange of carbon, nitrogen, and O_2 between the bottom layer of the water column and a sediment layer. The sediment layer receives sinking organic matter, which is then remineralized, consuming O_2 from the water column in the process (the explicit sediment layer is not part of the original distribution of ROMS). There is no direct flux of *DIC*, NO_3, or NH_4 from the water column to the sediments. The changes in carbon and nitrogen sediment mass (*Csed* and *Nsed*) are represented by:

$$\frac{\partial Csed}{\partial t} = DepositionC - Sediment_{reminDIC} \qquad \text{A.25}$$

$$\frac{\partial Nsed}{\partial t} = DepositionN - Sediment_{reminNH_4} \qquad \text{A.26}$$

(following Soetaert et al. 2000), where *Csed* and *Nsed* are in units of mmol m^{-2}. Then, the bottom boundary conditions for *DIC* and NH_4 in equations A.15 and A.18, respectively, are

$$F_{DIC} = Sediment_{reminDIC} \quad \text{(a)} \quad ; \quad F_{NH_4} = Sediment_{reminNH_4} \quad \text{(b)} \qquad \text{A.27}$$

The deposition rate of organic carbon and nitrogen at the seafloor is equal to the sinking particulate material that exits the lowest layer in the water column:

$$DepositionC = R_{C:N}\ w_P\ P\big|_{z=h} + w_D\ D_C\big|_{z=h} \qquad \text{A.28}$$

$$DepositionN = w_P\ P\big|_{z=h} + w_D\ D_N\big|_{z=h} \qquad \text{A.29}$$

(F06) where P, D_C, and D_N are evaluated at the bottom of the water column of depth h (i.e., reaching the seafloor). The right hand terms in A.28 and A.29 can be obtained formally by integratin equations A.1, A.9, and A.10 from the sea surface to the bottom. Within the sediment layer, organic matter is oxidized by aerobic remineralization and denitrification (O_2 is consumed from the lowest layer of the water column). The remineralization of *Csed* is parameterized with a linear rate, r_{sed_C}:

$$Sediment_{reminDIC} = r_{sed_C}\ Csed \qquad \text{A.30}$$

(Soetaert et al. 2000) $Sediment_{reminDIC}$ produces the same amount of *DIC* from either aerobic remineralization or denitrification (equations 4.3 and 4.5). The oxidation of *Nsed* to NH_4 must account explicitly for denitrification, since for every mole of organic nitrogen remineralized within the sediments, a fraction will be lost to denitrification as N_2 (equation 4.5 and Figure A.1). Therefore, $Sediment_{reminNH_4}$ will have the form

$$Sediment_{reminNH_4} = \Psi\, r_{sed_N}\, Nsed \qquad \text{A.31}$$

(modified from F06 and Soetaert et al. 2000) where r_{sed_N} is the remineralization rate and Ψ represents the fraction of nitrogen converted to NH_4 by oxidation of one mole of organic nitrogen in the sediment layer, after passing through aerobic remineralization and denitrification ($1 - \Psi$ represents the fraction converted to N_2). Processes within the sediments are schematically represented in Figure A.1.

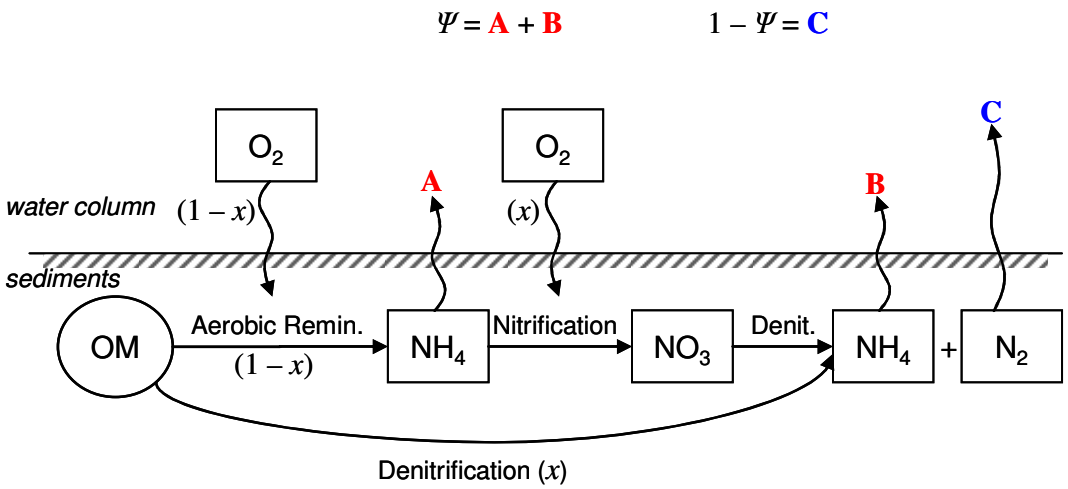

Figure A.1: Nitrogen cycling within the sediments and associated O_2 consumption from the water column. If 106 mol-C in organic matter (OM) are oxidized within the sediments, a fraction $(1 - x)$ is aerobically remineralized, consuming O_2 from the overlying water. A fraction x is denitrified; all NO_3 used in denitrification comes from previous nitrification of NH_4, which requires O_2. Total NH_4 released from the sediments to the bottom of the water column (A + B) represent the fraction Ψ and nitrogen released as N_2 (C) represents the fraction $(1 - \Psi)$.

Ψ is calculated following the approach of F06 and assuming that sediment denitrification occurs by coupled nitrification/denitrification (i.e., all NO_3 denitrified comes first from nitrification of NH_4 in the sediments). Under this assumption, the amount of nitrogen lost to sediment denitrification is linearly related to total O_2 consumption by the sediments by an empirical relationship (Seitzinger and Giblin 1996):

$$N_2 \text{ denitrified (mol-N m}^{-2}\text{ d}^{-1}) = 0.105 \text{ total } O_2 \text{ consumed (mol-O}_2\text{ m}^{-2}\text{ d}^{-1}) \quad \text{A.32}$$

In the denitrification reaction (equation 4.5), 42.4 moles of N_2 (i.e., 84.8 mol-N) are produced per 106 mol-C in organic matter denitrified (organic matter assumed to be $C_{106}H_{263}O_{110}N_{16}P$). Considering that only a fraction x of those 106 mol-C is denitrified (Figure A.1), the total O_2 consumption by oxidation of 106 mol-C in organic matter in the sediments is

$$\text{total } O_2 \text{ consumed} = \frac{84.8\ x}{0.105} \quad \text{A.33}$$

Moreover, the total consumption of O_2 within the sediments can be separated into its aerobic and anaerobic components as

$$\text{total } O_2 \text{ consumed} = (1 - x)\ O_{2remin} + x\ O_{2denit} \quad \text{A.34}$$

where O_{2remin} (O_{2denit}) represents the O_2 consumption by aerobic remineralization (coupled denitrification) of 106 mol-C in organic matter (see Figure A.1). Since the ratio of O_2 to carbon in aerobic remineralization is given by PQa (inverse of the respiratory quotient, RQ^{-1}), $O_{2remin} = 106\ PQa$. The coupled denitrification of 106 moles of organic carbon implies the previous nitrification of 84.8 moles of NO_3 and consequent consumption of O_2. Therefore, $O_{2denit} = 84.8\ R_{C:N}\ (PQn - PQa)$. Merging A.33 and A.34:

$$x\ \frac{84.8}{0.105} = (1 - x)\ 106\ PQa\ +\ x\ 84.8\ R_{C:N}\ (PQn - PQa) \quad \text{A.35}$$

The result yields $x \approx 0.15$, which means that 15 % of organic matter is denitrified and 85 % is remineralized by aerobic bacteria within the sediments. After further calculations described in Table A.1, the oxidation of 106 mol-C in organic matter (consisting of

16 mol-N) yields 3 mol-NH_4 ('A + B' in Figure A.1), while 6.5 mol-N_2 are lost from the bioavailable nitrogen pool ('C' in Figure A.1). Hence, $\Psi = 3/16$ (equation A.31).

Finally, solving for the consumption of O_2 by the sediments, the net ratio (mol:mol) of O_2 consumed to carbon remineralized within the sediments is ≈ 1.17 (compare with $PQa = 1.1$). Therefore, the bottom boundary condition for O_2 in the water column (equation A.22) can be written as:

$$F_{O_{2bott}} = -1.17\ Sediment_{reminDIC} \qquad \text{A.36}$$

Table A.1: Moles of NH_4 produced (positive) or consumed (negative) by (1) coupled denitrification, (2) aerobic remineralization, and (3) total oxidation within the sediments per 106 mol-C in organic matter oxidized. (α) and (β) show the partition between denitrification and nitrification in (1) and $x = 0.15$. Aerobic remineralization, nitrification, and denitrification reactions are given by equations 4.3, 4.4, and 4.5. These processes are shown schematically in Figure A.1 (note that in the figure, NH_4 resulting from denitrification is shown as an efflux from the sediments to the water column (arrow B); however, this table shows that there is net consumption of NH_4 by (1) coupled nitrification/denitrification).

(1) Total NH_4 consumption by coupled denitrification: (α) Partial production by denitrification: $16\ x = 2.4$ (β) Partial consumption by nitrification: $84.4\ x = 12.7$	(α) - (β)	-10.3
(2) Total NH_4 production by aerobic remineralization:	$16\ (1 - x)$	13.5
(3) NH_4 produced by total oxidation within the sediments (equivalent to the net sum 'A + B' in Figure A.1):	(1) + (2)	3.2

Appendix B. The VICC in a quasi-2D model

An important feature of the Vancouver Island shelf system is the buoyancy current that flows northward (poleward) along the coast, known as the Vancouver Island Coastal Current (VICC). In summer it flows against northwesterly winds and a wind-driven shelfbreak current, such that the core of the current is below the surface (Freeland et al. 1984, Thomson et al. 1989, Hickey et al. 1991). In winter, the VICC is stronger near the surface due to prevailing southeasterly winds and fresh water input from rivers and streams along the outer coast of Vancouver Island (Thomson et al. 1989). The main source of the VICC in summer is the low salinity outflow from the Juan de Fuca Strait, resulting from the seasonal maximum in snowmelt input into the mainland rivers (Thomson et al. 1989, Hickey et al. 1991). These fresh waters from runoff (mainly from the Fraser River) are tidally mixed with subsurface ocean waters entering the Strait, becoming nutrient-rich and providing a source of nutrients for the shelf (Crawford and Dewey 1989, Whitney et al. 2005). The VICC represents a boundary between inner and outer shelf waters, providing an alongshore conduit and cross-shore barrier to the transport of biomass (Thomson et al. 1989). This current is between 15 and 25 km wide and is located landward of the 100 m isobath. Its core roughly follows the 50 m depth contour with maximum alongshore velocities (typically > 10 cm s^{-1}) at ~ 20 m in summer (Thomson et al. 1989, Hickey et al. 1991).

The inclusion of the VICC in the model developed here is important for two main reasons:

- Its role as a source of nutrients to the shelf,
- Its role as a barrier to cross-shelf transport.

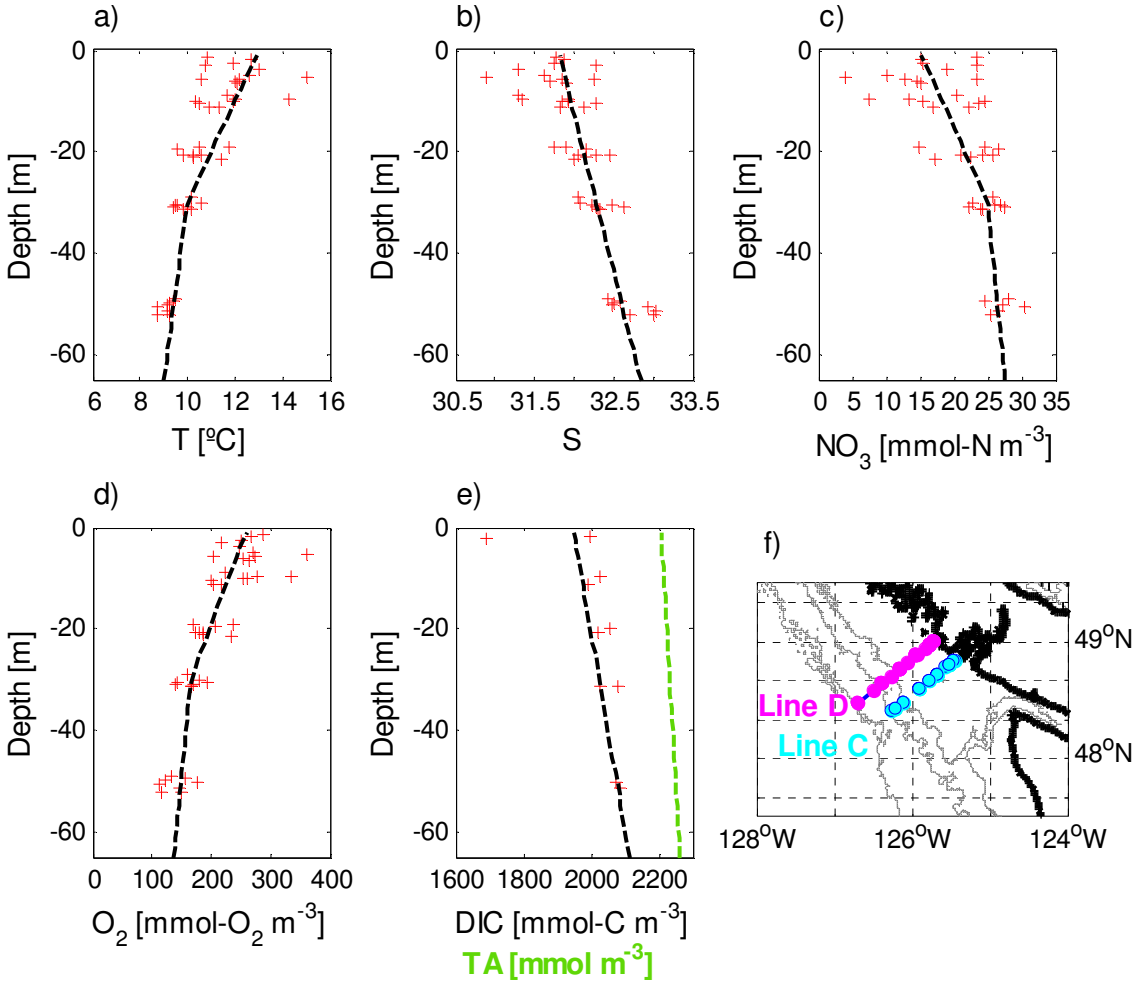

Figure B.1: Profiles used to restore VICC properties: a) Temperature, b) Salinity, c) Nitrate, d) Oxygen, e) Dissolved inorganic carbon and total alkalinity. The red crosses show data from the two shallowest stations of Line C (all stations of Line C shown as cyan circles in panel f; Line D stations are shown as magenta circles for reference); in panel e, data correspond to DIC. The dashed black lines are the linear functions chosen to represent the data profile for each variable. Total alkalinity (green line in panel e) is calculated from salinity following Ianson et al. (2003). Data from panels a to d correspond to six summer transects from 2002 to 2006 (IOS archive); DIC data (panel e) are from a cruise in July 1998 (Ianson et al. 2003).

Formulation of the VICC in a quasi-2D model is challenging because in summertime the main forcing remains outside the model domain (i.e., the Fraser River discharge into the Strait of Georgia, which then flows outward to the Juan de Fuca Strait). After attempting several approaches (detailed at the end of this appendix), I decided to

represent the outer boundary of the current by restoring temperature and salinity near the inshore model boundary, as well as restoring alongshore and cross-shore velocities to values characteristic of the VICC. To represent the VICC biogeochemical properties, I also restore nitrate (NO_3), oxygen (O_2), dissolved inorganic carbon (DIC), and total alkalinity (TA). Here, 'restoring' means adding a term to the right hand of the model equations (as seen in Appendix A)

$$\frac{q_{VICC} - q}{\tau(x)}$$

where q represents any model variable being restored, q_{VICC} is the value of the variable characteristic of the coastal current, and $\tau(x)$ is a restoring time scale that depends on the distance (x) from the inshore boundary. Figure B.1 shows the vertical profiles used to represent VICC properties in the restoring terms, which are linear functions based on observations from shallow stations immediately south (upstream) of the model domain (at another IOS transect, Line C, see cyan circles in Figure B.1f). Total alkalinity (green line in Figure B.1e) was calculated from salinity following Ianson et al. (2003).

A small restoring time τ implies strong nudging and may force q to be almost equal to q_{VICC} (i.e., the above equation becomes the leading term in the right hand side of the equations in Appendix A). The approach to represent the outer boundary of the VICC was to have τ increase with increasing cross-shore distance from the inshore boundary, such that the strongest nudging occurs in the shallowest region of the domain and vanishes within 10 km of the inshore boundary (Figure B.2). The functional form for the decay of the inverse of τ as well as the value of τ at the inshore boundary were decided after running sensitivity experiments, which aimed to represent the outer edge of the VICC in the shallowest ~ 5 km of the domain (i.e., x from 0 to ~ 5 km) and a ~ 5 km

transition between the northward VICC and the southward shelf flow (Rick Thomson, personal communication) from ~ 5 to 10 km. Figure B.3 shows vertical sections of alongshore velocity (averaged over 60 days) for different τ. The middle panel shows the τ used in the model experiments: the transition between northward (positive) and southward (negative) flow extends between ~ 5 km (dashed black line) and ~ 10 km (dashed red line) when $\tau = 0.1$ d at $x = 0$ and its inverse (τ^{-1}) decays as e^{-x^2}. If τ^{-1} decays with the same function of x but $\tau\,(x = 0) = 0.01$ d (left panel Figure B.3), the northward flow occupies nearly all the inshore 10 km region. The right hand panel in Figure B.3 shows the case of $\tau\,(x = 0) = 0.1$ d decaying as a function of e^{-x}: the transition zone between northward and southward flow is narrower and upwelling reaches into shallower waters.

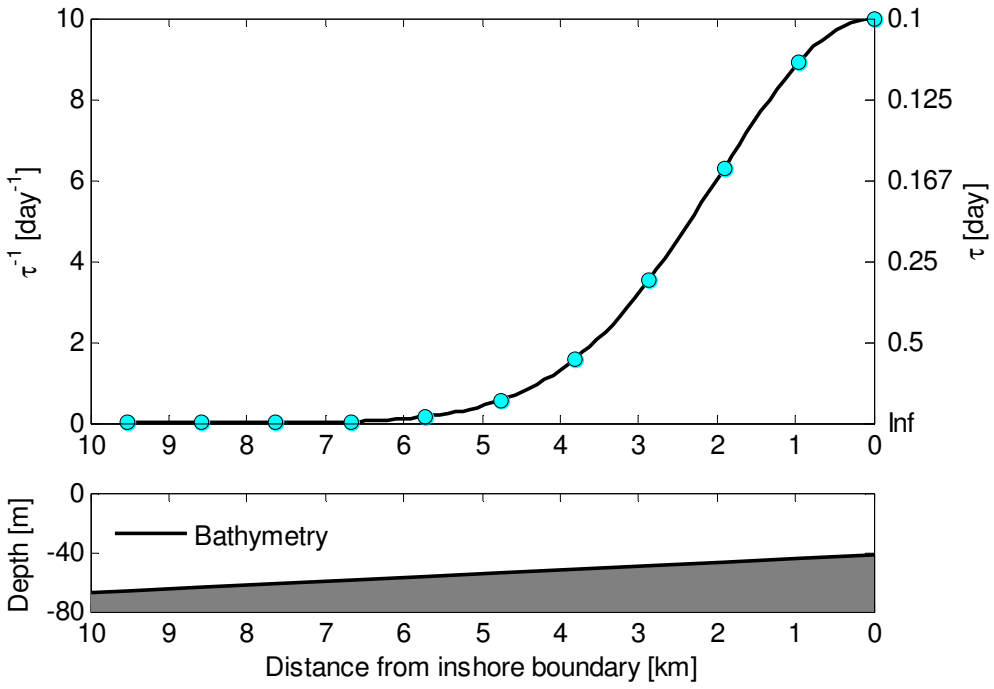

Figure B.2: Upper panel: Decay of the inverse of the restoration time scale (τ) as a function of distance from the inshore boundary: $\tau^{-1} = 10\ e^{-0.13\ x^2}$ (applied to the shallowest 11 grid cells). Y-axis on the left shows the inverse of τ (in days^{-1}); Y-axis on the right shows τ in units of days. Lower panel: Bathymetry profile.

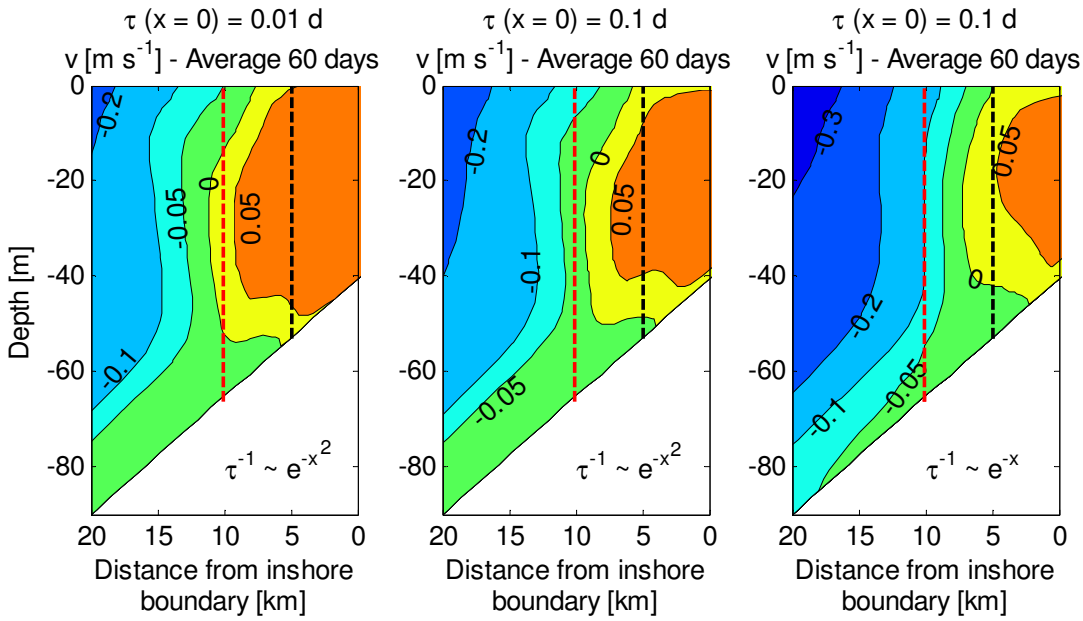

Figure B.3: Vertical sections of alongshore velocity (v, in m s^{-1}) averaged over 60 days for three different τ. Left: $\tau\,(x = 0) = 0.01$ d and $\tau^{-1} \sim e^{-x^2}$; middle: $\tau\,(x = 0) = 0.1$ d and $\tau^{-1} \sim e^{-x^2}$ (as used in this thesis); right: $\tau\,(x = 0) = 0.01$ d and $\tau^{-1} \sim e^{-x}$. The dashed red line indicates the outer boundary of the restoration area ($x \sim 10$ km); the dashed black line denotes 5 km from the inner boundary. Positive (negative) values indicate northward (southward) flow.

DIC concentrations in the VICC

In several sections of this thesis, the DIC concentrations in near-bottom waters of the VICC have been described in the model results as being lower than in the bottom layers over the shelf. This feature results from the profiles used to restore the VICC based on Line C (Figure B.1e) and compares well with the few observations from Line D available to evaluate the model (Figure B.4). Observations closer to the bottom over the shelf are needed to confirm the model results (depths of the each station are given in the caption of Figure B.4).

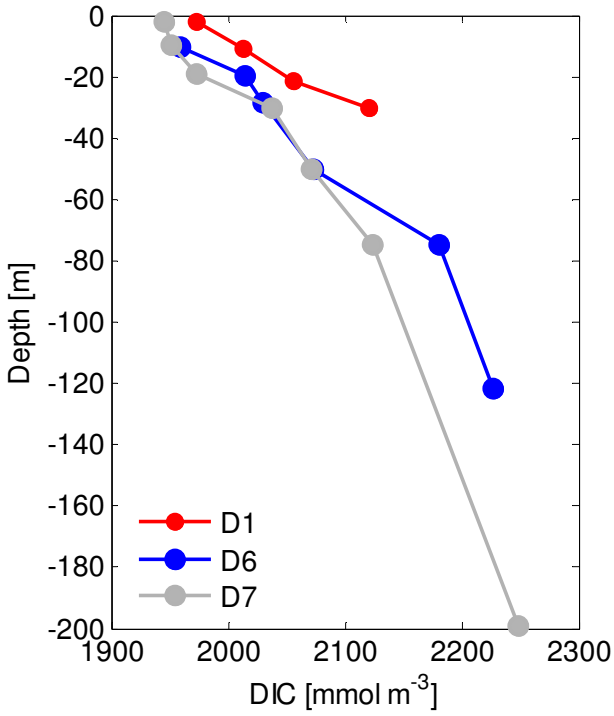

Figure B.4: DIC observations from Line D in July 1998 (Ianson et al. 2003). Station D1 is usually within the VICC. The water column depth at each station is: D1 = 42 m, D6 = 137 m, and D7 = 520.

Other attempts at modelling the VICC

The first approaches to model the VICC aimed at obtaining a geostrophically-balanced current by restoring sea surface height (η) and/or density (i.e., temperature and salinity) to typical VICC values. Below are several shortcomings with these attempted approaches, as well as two other approaches that I chose not to follow.

- Restoring η did not generate a geostrophic northward current, because η is internally calculated in the model to be consistent with the divergence of vertically integrated horizontal velocities. Therefore, the restoring of η was overwhelmed in the presence of wind forcing (even for restoring timescales on the order of a few model time steps).

- Similarly, wind-driven dynamics dominated the VICC region when only T and S were restored to VICC values. If no wind was imposed, the density field produced only a weak northward current (~ 0.05 m s^{-1}).
- Another idea was to model the VICC as a river input (ROMS provides options to set point-sources of water and properties). However, momentum input from a river would have differed from that of the VICC. I abandoned the implementation of this approach after several problems arose in attempts to include mass in the river inflow.

I could have added an explicit body force in the pressure term of the model equations to force η and obtain a geostrophic northward current. However, this would have required major manipulation of the core of the ROMS code, so it was left as a last resort.

Appendix C. Details on the evaluation of model performance

Chapter 2 (section 2.2.4) compares histograms of oxygen and temperature from the model with in situ observations to evaluate whether the quasi-2D model reproduces the main statistical properties of the observations. This Appendix presents histograms of other model variables for which in situ observations were available: salinity (S), nitrate (NO_3), ammonium (NH_4), and chlorophyll-a (Chl-a) data from nine Line D transects (location in Figure 2.1 or Figure B.1f; dates as well as number of stations per transect in Table C.1). Currently, the only dissolved inorganic carbon (DIC) observations available for the Vancouver Island shelf are from a cruise in July 1998 (Ianson et al. 2003). Both Line D and C (location in Figure B.1f) are used to compare with model results. In situ observations for dissolved and particulate organic carbon (DOC and POC) and nitrogen (DON and PON) are taken from seven summer transects off Newport, Oregon (~ 44.65ºN) from 1998 to 2004 (Wetz et al. 2006). These observations, sampled from a coastal upwelling system, are the published data closest to the Vancouver Island shelf.

Table C.1: Dates (dd/mm/yyyy) of Line D transects (see location in Figure 2.1 or Figure B.1f) used to compile the histograms, along with the number of stations per transect.

Transect Date	Number of stations	Transect Date	Number of stations
15/09/1981	1	08/09/2004	5
01/07/1986	1	15/09/2006	7
24/08/1986	4	03/09/2008	2
15/08/1988	1	19/09/2008	8
10/08/1989	1		

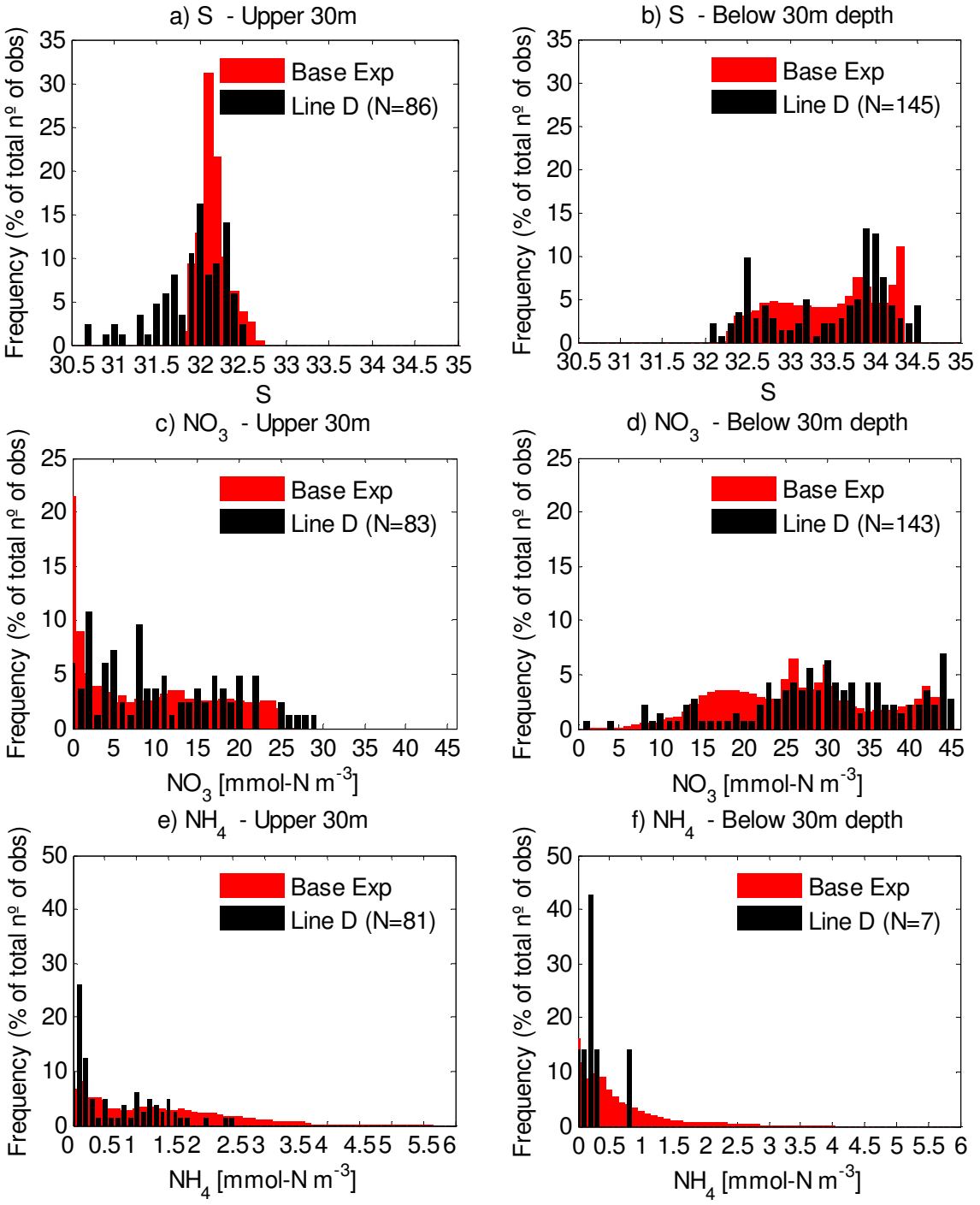

Figure C.1: Histograms of model (red bars) and in situ (black bars) data. Top: salinity (a,b); middle: nitrate (c,d); bottom: ammonium (e,f). Left panels show data for the upper 30 m over the shelf and right panels for data below 30 m. Model results are for the Base Experiment (see description of simulation in section 2.3) omitting the spinup period (50 days). In situ observations are from nine transects along Line D (see location in Figure B.1f) from 1981 to 2008; the legend shows in parentheses the number of observations (N) in each distribution.

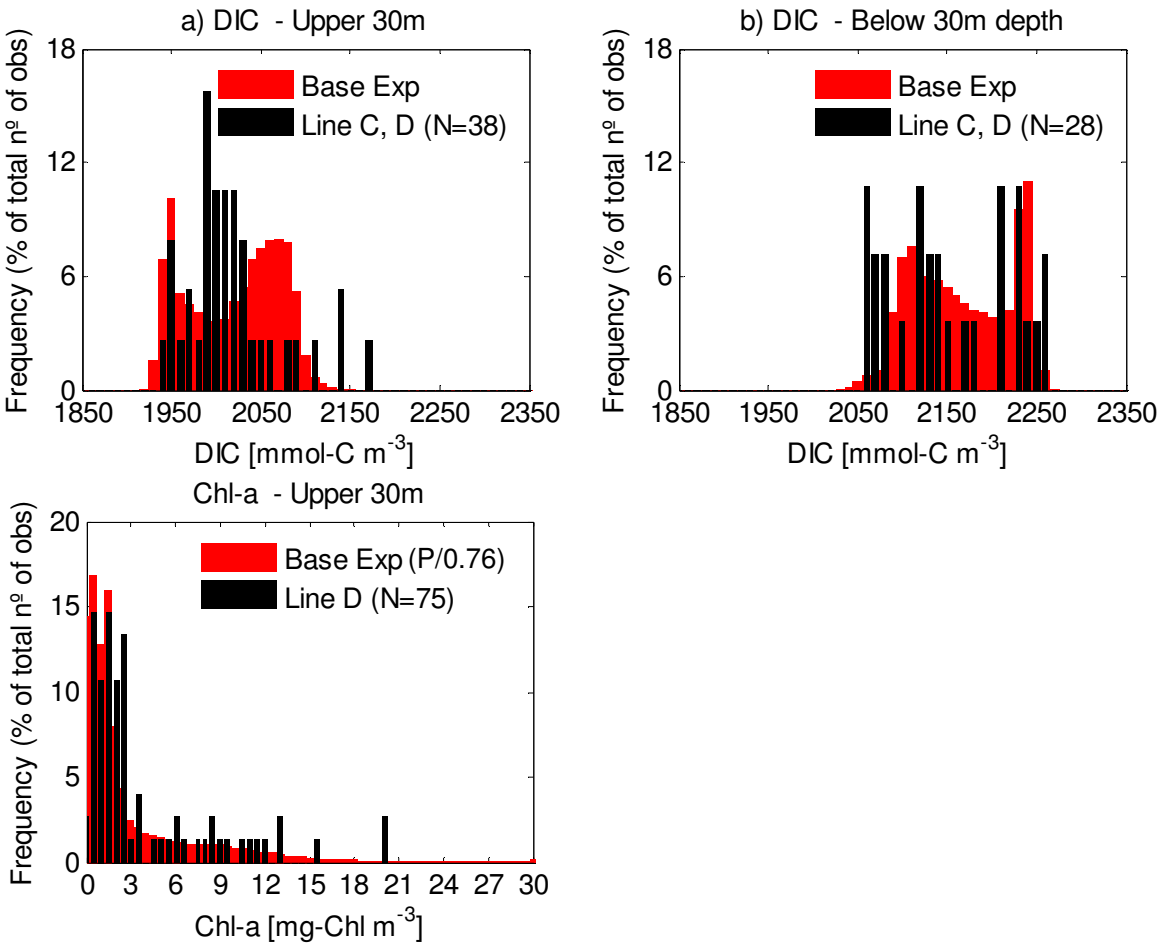

Figure C.2: Histograms of model (red bars) and in situ (black bars) data. Top: dissolved inorganic carbon (a,b); bottom: chlorophyll-a (c). Left panels show data for the upper 30 m over the shelf and right panel for data below 30 m. Model results are for the Base Experiment omitting the spinup period (50 days). In situ DIC observations are from two transects on the Vancouver Island shelf in July 1998 (Line D and C, see location in Figure B.1f). Modelled DIC histograms are for the shelf shallower than 200 m, to match the depth range of the observations. Chlorophyll-a observations are from nine transects along Line D from 1981 to 2008 for the upper 30 m only. Chlorophyll-a in the model is calculated from phytoplankton biomass (P, in mmol-N m^{-3}) assuming a ratio N:Chl = 0.76 mmol-N $(mg\text{-}Chl)^{-1}$ (Denman and Peña 1999). Legends show in parentheses the number of observations (N) in each distribution.

All histograms show the frequency distribution for the model data (red bars) and in situ observations (black bars) over the shelf and slope, for the upper 30 m and the layers below (30 m to the seafloor). Figure C.1a shows that S in the upper 30 m of the model

does not reach values as low as for the in situ Line D observations. This narrower distribution results from the lack of temporal and spatial variability of the VICC in the model ($S < 31.8$ corresponds to VICC waters). For example, the four observations of $S < 31$ correspond to three stations between 65 and 136 m depth from a transect on 19 September 2008 (stations D4 to D6). The modelled VICC (which represents climatological properties, see section 2.2.4) is not as fresh (see salinity profile in Figure B.1b) nor does it extend as far offshore (only restored for depths < 66 m, Figure B.2). Nevertheless, peaks in the model (i.e., the modes) and in situ data histograms are similar as are the upper ranges of S. For the layers deeper than 30 m, S exhibits the same range for both model and Line D observations (Figure C.1b). The model does not show a smooth tail at larger values of S because deep waters over the shelf break are limited to $S = 34.3$, corresponding to initial conditions for S ($S_{initial} = 34.3 - 2.6\ e^{-z/100}$, where z is depth).

Histograms for NO_3 (Figure C.1c and d) show similar ranges for both model and observations. NH_4 (Figure C.1e and f) appears to reach higher concentrations in the model than in the observations, and does not reproduce the preponderance of low concentrations. Note that there are only seven observations below 30 m (Figure C.1f).

As DIC is available from only one cruise in collaboration with the Canadian GLOBEC programme (Ianson et al. 2003), observations from both Line D and C (66 samples in total) are used in Figure C.2 (instead of only using Line D). The model represents relatively well the distributions of DIC observed in both the upper and lower layers (Figure C.2a and b, respectively), although there are a few high concentrations in the upper 30 m that the model represents with lower frequency. Figure C.2c shows a good

correspondence between model and observed Chl-a distributions in the upper 30 m of the water column, despite the fact that Chl-a in the model is calculated from phytoplankton biomass (in mmol-N m^{-3}), assuming a fixed ratio N:Chl = 0.76 mmol-N $(mg\text{-}Chl)^{-1}$ (Denman and Peña 1999).

Figure C.3a and b show the histograms of DOC from the Vancouver Island model (which only accounts for the semilabile fraction, DOC_{SL}) and total DOC (i.e., sum of labile, semilabile, and refractory fractions) measured over the Oregon shelf (Wetz et al. 2006). As DOC_{SL} is abundant in upper layers of the ocean, model and observations exhibit a similar range of concentrations in Figure C.3a, although the shapes of the distributions differ. The lack of refractory DOC in the model explains the bias towards lower values in Figure C.3b, as refractory DOC constitutes most of the bulk DOC in deeper waters (Carlson 2002). If the deepest sample available from the Newport station farthest away from the shore (40 mmol-C m^{-3} at 150 m from a station 1006 m deep) was considered representative of the refractory DOC and subtracted from the observations, the disagreement in Figure C.3b would be sharply reduced. Note, however, that at 150 m not all DOC is expected to be refractory. The model distributions of POC (i.e., sum of phytoplankton, zooplankton, and carbon detritus) are similar to the ones off Oregon, especially in the upper 30 m (Figure C.3c and d). Figure C.4 shows the ratios for DOC:DON and POC:PON. Both ratios are well represented by the model in the upper layers, although histograms are narrower than for observations (Figure C.4a and c). In layers deeper than 30 m, ratios from the model are generally larger than those from the Oregon observations (Figure C.4b and d), especially for dissolved organic matter (DOM; Figure C.4b). The latter may result from the lack of refractory DOC and DON in the

model. The POC:PON ratio exhibits values larger than the Redfield ratio of 6.625 (C:N = 106:16) in both model and observations. The inclusion of DOM in the model is a main contributor to non-Redfield behaviour, along with the explicitly modelled pools of carbon and nitrogen detritus (i.e., D_C and D_N are not linked by a fixed ratio, but the pools are modelled independently).

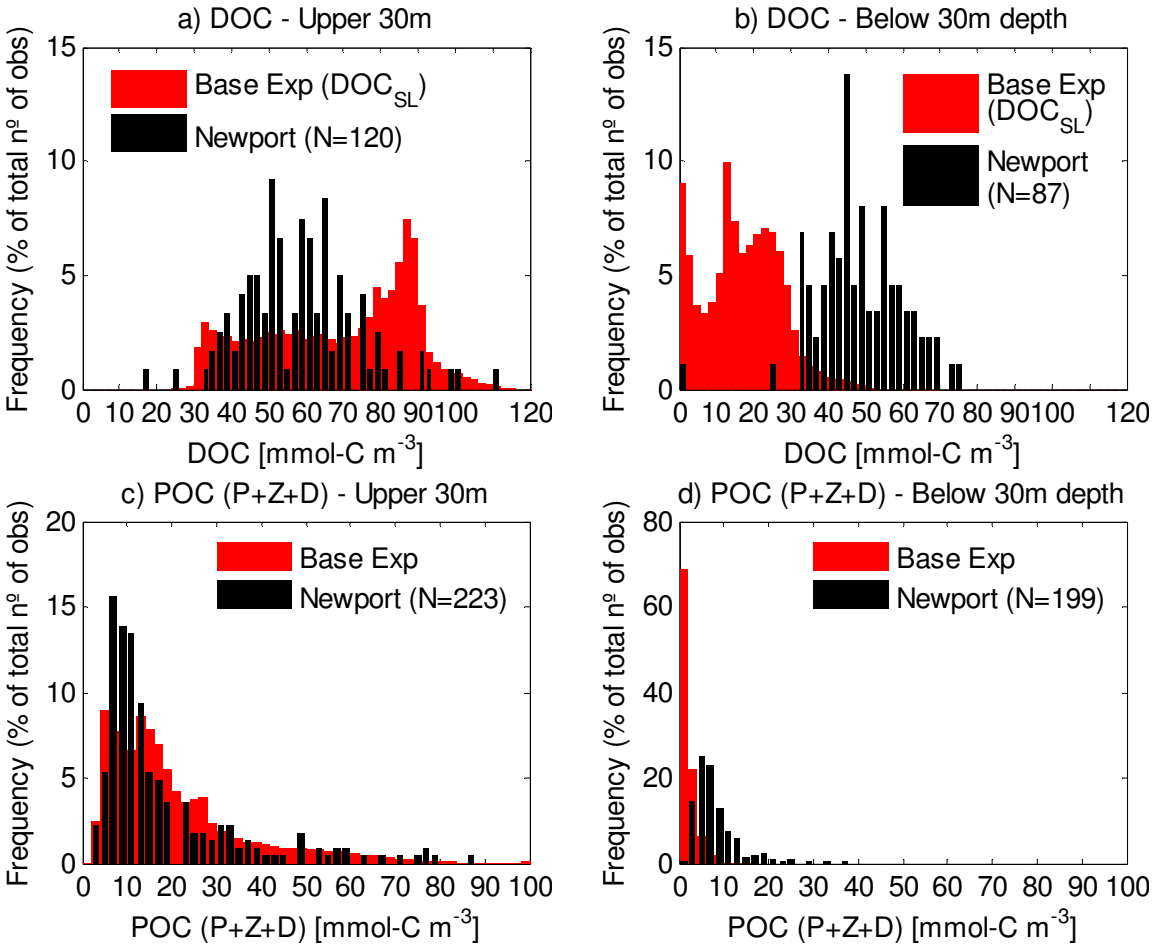

Figure C.3: Histograms of model (red bars) and in situ (black bars) data. Top: dissolved organic carbon (a,b); bottom: particulate organic carbon (c,d). Left panels show data for the upper 30 m of the shelf and right panels for data below 30 m. Model results are for the Base Experiment omitting the spinup period. The model only considers semilabile DOC (DOC_{SL}), and model POC comprises phytoplankton, zooplankton, and carbon detritus. In situ observations are taken from to seven summer transects off Newport, OR (~ 44.65ºN) from 1998 to 2004 (Wetz et al. 2006). Legends show in parentheses the number of observations (N) in each distribution.

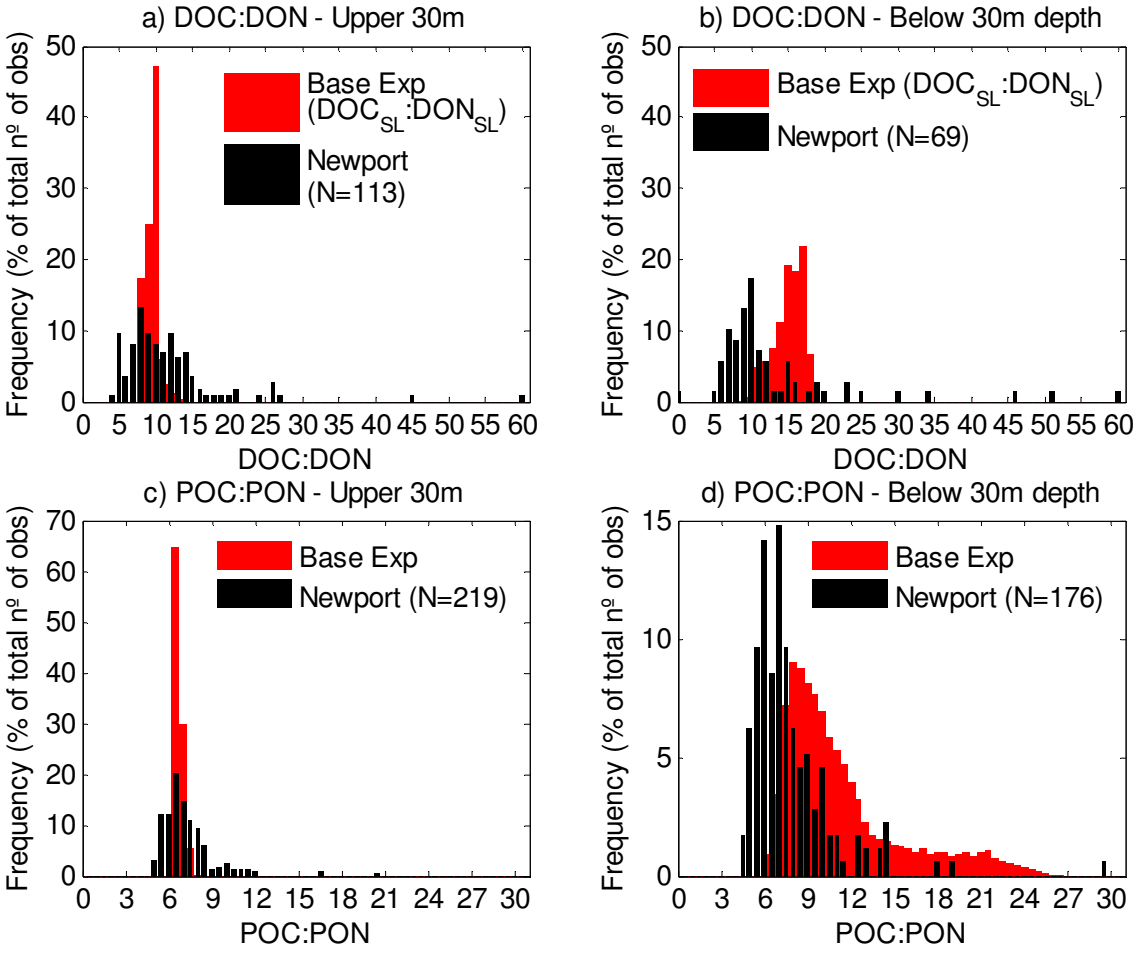

Figure C.4: Histograms of model (red bars) and in situ (black bars) data. Top: dissolved organic carbon to nitrogen ratio (a,b); bottom: particulate organic carbon to nitrogen ratio (c,d). Left panels show data for the upper 30 m of the shelf and right panels for data below 30 m. Model results are for the Base Experiment omitting the spinup period. The model only considers semilabile dissolved organic matter (i.e., DOC_{SL}:DON_{SL}), and model particulate organic matter comprises phytoplankton, zooplankton, and detritus. In situ observations are taken from seven summer transects off Newport, OR (~ 44.65ºN) from 1998 to 2004 (Wetz et al. 2006). Legends show in parentheses the number of observations (N) in each distribution.

Currents in the model and from observations

Alongshore and cross-shelf circulation patterns in the model are represented by the averages during upwelling (days 37 to 44) and downwelling (days 63 to 66) events (Figure C.5a and b, respectively). The cross-shelf circulation occurs mainly in upper and

bottom boundary layers in both cases (although during downwelling, offshore flow occurs in most of the water column below the upper onshore flow). The mid shelf (10 – 30 km from the inshore boundary) alongshore equatorward jet is too strong compared with currents from mooring A1 (Figure C.6). These two features of the model velocity field may be due to the lack of an alongshore pressure gradient and the consequent absence of a poleward subsurface flow at depth over the continental slope, i.e. the California Undercurrent (Werner and Hickey 1983). In a previous 2D model of the upwelling circulation on the Oregon shelf, imposing a constant alongshore pressure gradient reduced the alongshore equatorward jet and distributed the cross-shelf return flow over most of the lower water column rather than in a bottom boundary layer (Federiuk and Allen 1995). However, these authors reported that the correlation between model and observed cross-shelf velocities did not improve significantly by adding the constant alongshore pressure gradient. Furthermore, although the magnitude of the alongshore velocity field was improved, the vertical structure of the jet was represented better by the base model without the additional pressure gradient. Their conclusion, also applicable here, points towards the limitations of a 2D model to represent the characteristically 3D flow field in the coastal ocean. The consequence of the model's representation of the cross-shelf circulation (i.e., mainly forced in the boundary layers) could lead to an overestimation of upwelling and the advection of O_2 and DIC in the bottom layer over the shelf. Nevertheless, although the absolute concentrations observed in these simulations may be sensitive to this feature of the cross-shelf circulation, the directions of change observed in the sensitivity experiments are expected to be robust.

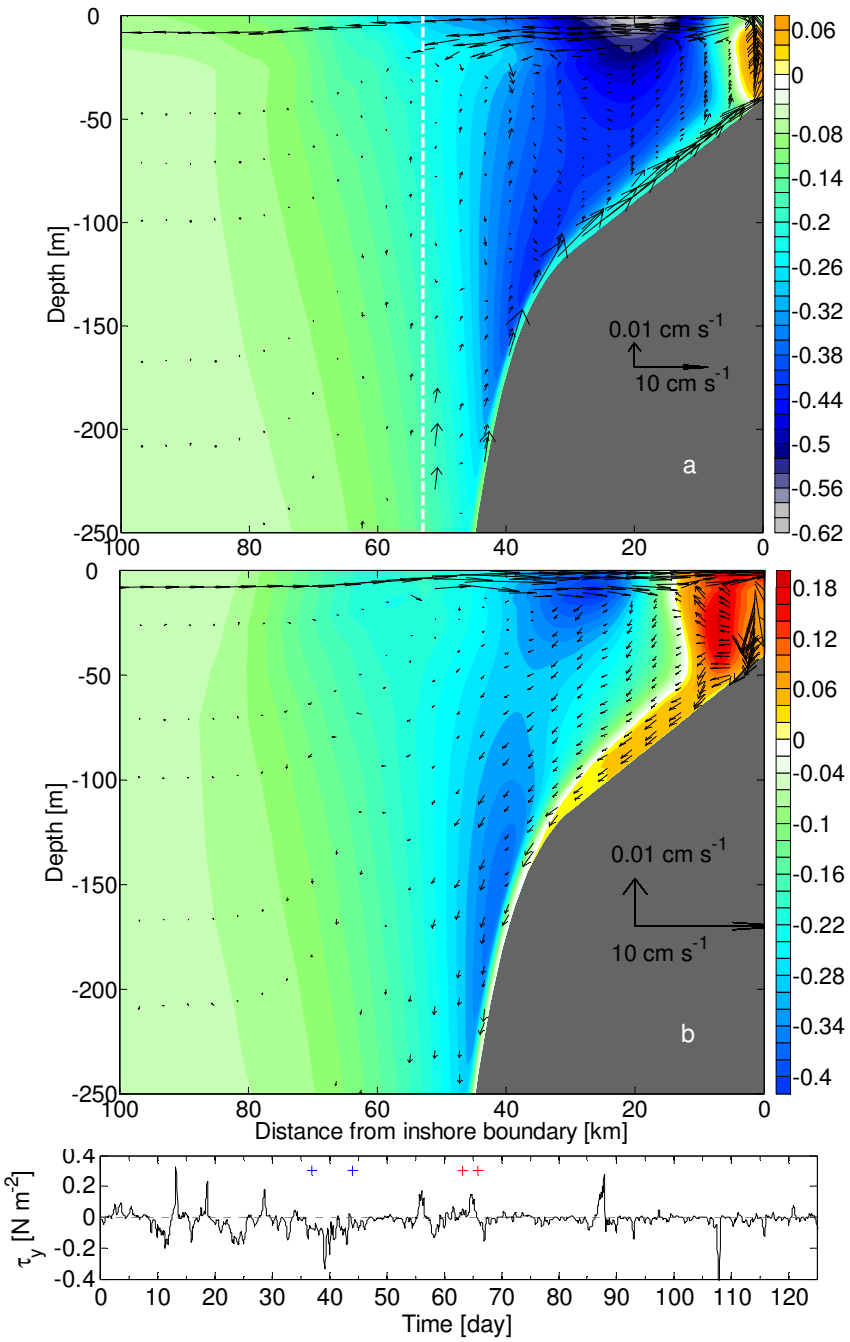

Figure C.5: Mean alongshore currents (colour contours; units are m s^{-1}) and cross-shelf circulation (arrows) during (a) an upwelling event between days 37 and 44 and (b) a downwelling event between days 63 and 66 in the Base Experiment. Plots have the same colour scale but different scales for the arrows (see inset in each panel). The dashed white line in a) indicates the location of mooring A1 (see text and Figure C.6). The bottom panel shows the time series of alongshore wind stress; the initial and final days for the upwelling (downwelling) event are indicated by blue (red) crosses.

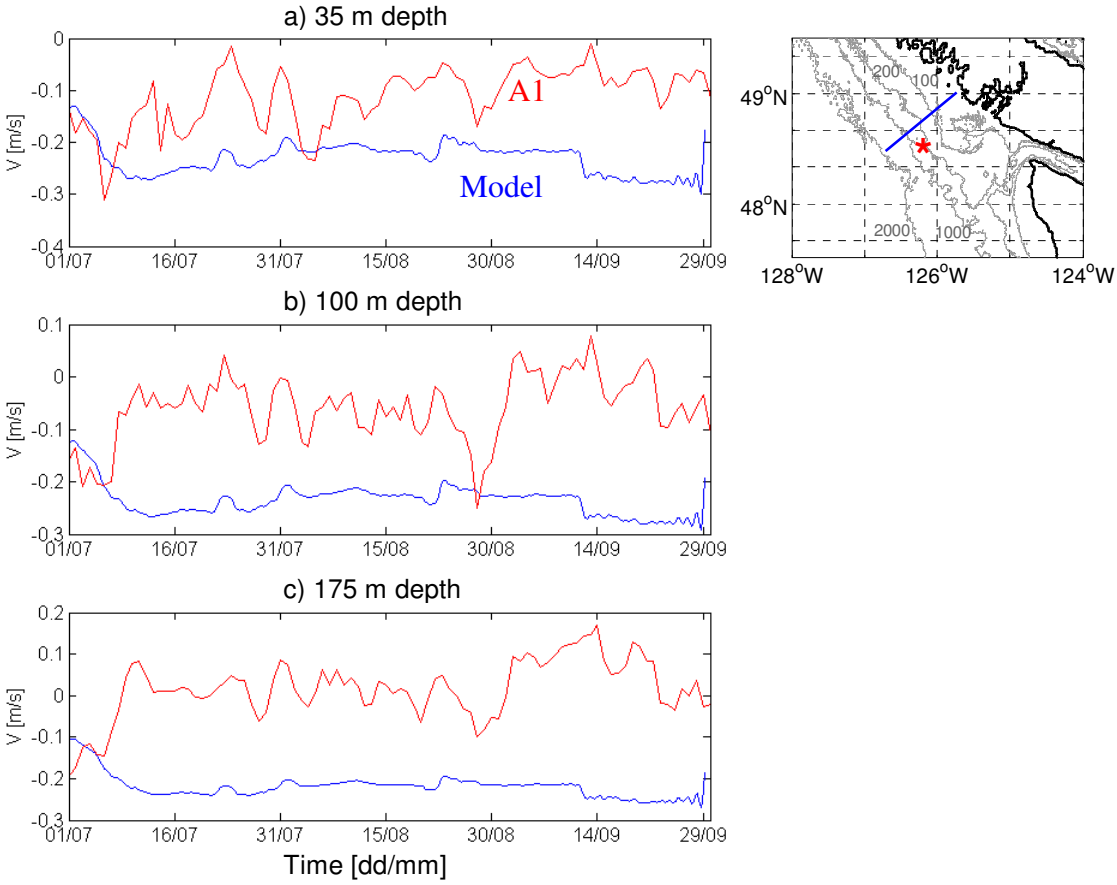

Figure C.6: Time series of alongshore current speed for mooring A1 (red curves) and the model at a location at the same isobath as mooring A1 (511 m; blue curves) for summer 1993. The panels show different vertical levels: a) 35 m, b) 100 m, and c) 175 m depth. The map on the right indicates the location of mooring A1 (red star) and the model transect (blue line).

Appendix D. Interannual variability in the model

Different external forcing datasets, compiled from observations during several different years, were used in the model simulations. Four sets of observed hourly wind stress and NCEP heat fluxes were used to model the summer conditions of 1986, 1993, 2004, and 2008 off the Vancouver Island shelf. To make more meaningful comparisons, initial conditions were the same in all simulations, followed by a 'spinup' period before the period during which results were analyzed. These results were used for the model evaluation described in Chapter 2 (section 2.2.4). Here, a brief discussion of the interannual variability in the model is presented, with emphasis on near-bottom concentrations of oxygen (O_2) and the saturation state of aragonite (Ω_A).

Figure D.1 shows the temperature histograms for the four years (represented by different colour bars) over the shelf for the upper 30 m and below 30 m depth. Modelled temperature distributions for all four years share the same main characteristics (i.e., the temperature ranges and the shape of the histogram), and show some small differences in the tails of the distributions (e.g., upper 30 m in summer 1986 is colder than in the other three years; waters below 30 m are colder in 2008).

A main objective of the thesis is to understand what processes regulate the occurrences of hypoxia and/or corrosive waters on the shelf. As these phenomena typically occur in the bottom layers over the shelf, Figure D.2 shows the histograms of temperature, salinity, O_2, and Ω_A in the near-bottom layer over the shelf. The near-bottom layer shows more interannual variability in temperature (Figure D.2a) than the whole layer below 30 m depth down to the seafloor (Figure D.1b). Near-bottom waters are colder, saltier, and more hypoxic with forcing from summer 2008 (blue bars in all panels of Figure D.2; in

Figure D.2c, vertical dashed line shows the hypoxic threshold, 60 mmol-O_2 m^{-3}). After 2008, summer 2004 forcing (green bars) also yields cold, salty, and more hypoxic conditions 2008, and the 2004 simulation also results in the lowest Ω_A values (Figure D.2d; vertical dashed line shows the aragonite dissolution threshold, $\Omega_A = 1$). Mean alongshore wind stress in the study period (27 May to 29 September) was upwelling favourable for all four years and strongest in 2008, followed by 2004 (Table D.1 shows mean alongshore wind stress and its standard deviation for all simulations). The histogram for 1986 (grey bars) exhibits the highest frequencies near the centre of the distributions, indicating a 'quiet' year with low variability in the near-bottom layer, consistent with the lowest standard deviations in wind stress forcing (see Table D.1).

Table D.1: Mean and standard deviation (SD) of alongshore wind stress (τ_y) during the study period (27 May to 29 September) for the four simulations. Negative mean values indicate upwelling favourable winds.

Simulation for year	1986	1993	2004	2008
Mean τ_y [N m^{-2}]	-0.0151	-0.0175	-0.0183	-0.0231
SD [N m^{-2}]	0.0376	0.0585	0.0492	0.0872

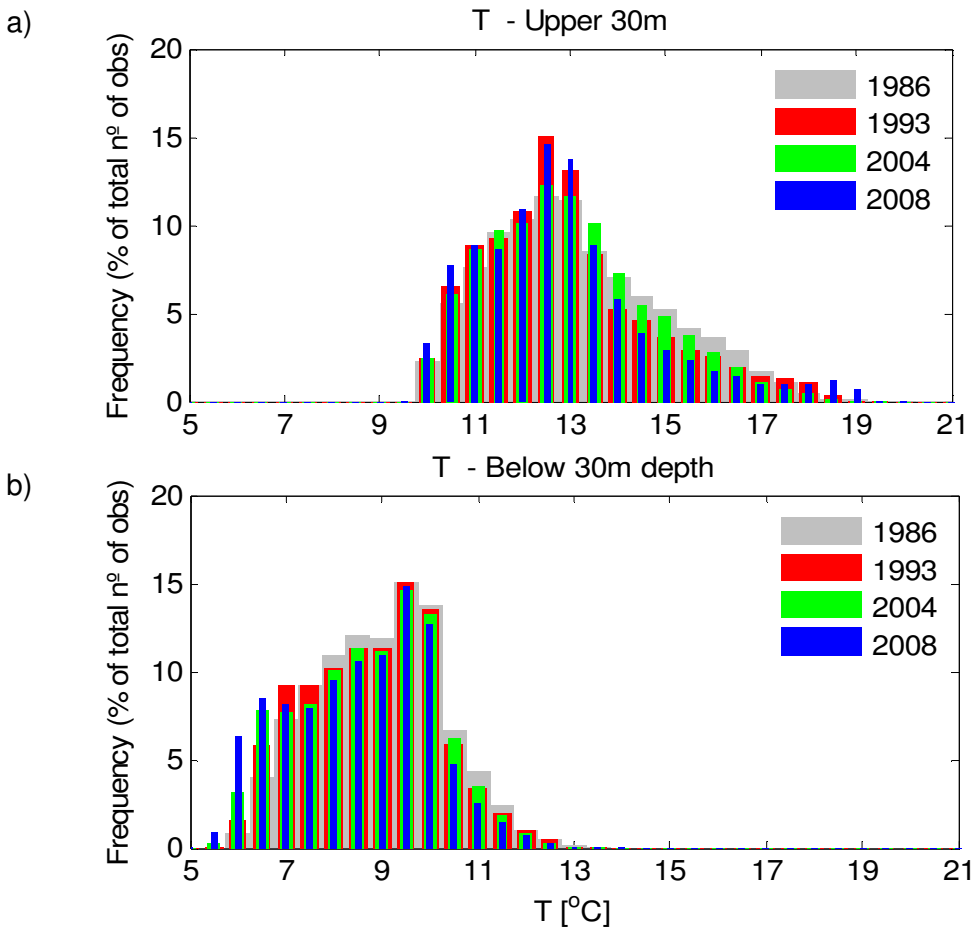

Figure D.1: Histograms of temperature (a) in the upper 30 m of the water column, and (b) below 30 m to the seafloor over the shelf. Colour bars indicate simulations with forcing from 1986 (grey), 1993 (red), 2004 (green), and 2008 (blue).

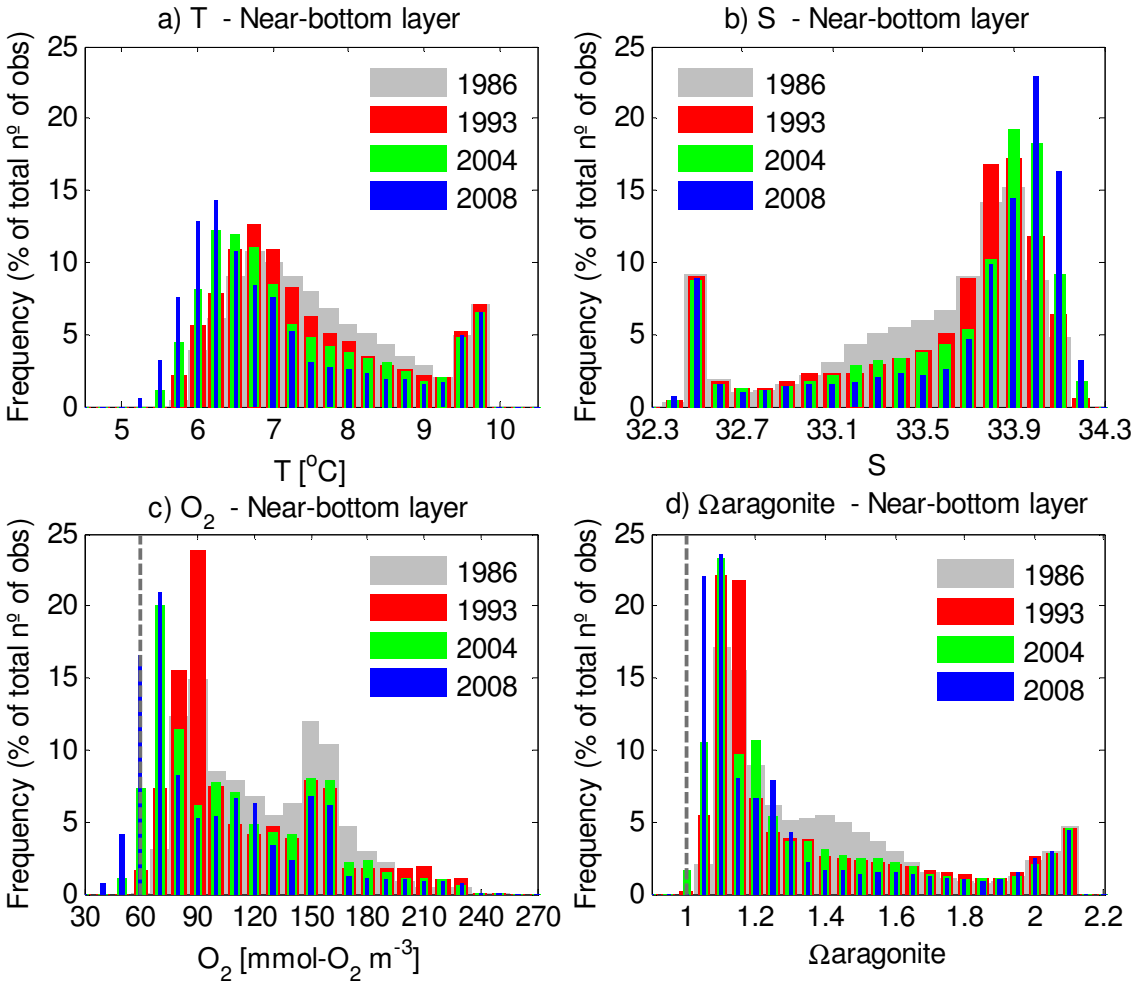

Figure D.2: Histograms of (a) temperature, (b) salinity, (c) oxygen, and (d) saturation state of aragonite in the near-bottom layer of the water column over the shelf. Colour bars indicate simulations with forcing from 1986 (grey), 1993 (red), 2004 (green), and 2008 (blue). Vertical dashed lines in panels c and d indicate the hypoxic threshold (O_2 = 60 mmol-O_2 m^{-3}) and the aragonite dissolution threshold (Ω_A = 1), respectively.

Is the interannual variability in the model comparable with the range of changes in the sensitivity analysis performed in Chapter 3? Figure D.3a shows the histograms of near-bottom layer O_2 concentrations for four experiments:

1) Summer 1993 simulation (referred to as 'Base Experiment' in Chapter 3; red bars),

2) Summer 2008 simulation (blue bars): stronger upwelling relative to 1993

3) The Shallower Oxygen Minimum Zone (OMZ) Experiment: based on the 1993 simulation with a 100-m shallower offshore OMZ (yellow bars),
4) The Shallower OMZ + Strong Upwelling Experiment: as the previous experiment but with stronger upwelling-favourable winds from 2002 for the whole period of the simulation (grey bars; mean alongshore wind stress in 2002 was -0.0225 N m^{-2}).

Simulation 3) differs from 1) only in the depth of the offshore OMZ; the lower O_2 concentrations in 3) (yellow bars) result from the proximity of the hypoxic threshold to the shelf, as discussed in Chapter 3. The stronger upwelling experienced in summer 2008 (2; blue bars) also leads to a decrease in O_2 concentrations, such that the lower O_2 limit is similar to that of 3) (yellow bars). However, the combination of both stronger upwelling and a shoaled OMZ (4; grey bars) produces a pronounced reduction of O_2 concentrations in the near-bottom layer over the shelf. In conclusion, variability of modelled O_2 concentrations between years is comparable with the changes due to a shoaling of the offshore OMZ (i.e., near-bottom O_2 differences between 1993 and 2008 are comparable with differences between 1993 and the Shallower OMZ Experiment). However, if summer upwelling-favourable winds intensify under climate change, the expected changes in near-bottom O_2 concentrations will exceed the range of current interannual variability. Even if summer upwelling does not change significantly in the future, the combined effects of interannual variability and a shoaled OMZ will still increase the expected variability in near-bottom O_2 concentrations.

Figure D.3b compares the histograms of near-bottom Ω_A for simulations of 1993 and 2008 (red and blue bars, respectively) with the Higher Carbon Experiment (increased

DIC and atmospheric pCO_2 conditions expected by 2050). Clearly, changes in Ω_A due to enhanced carbon in the system exceed interannual variability.

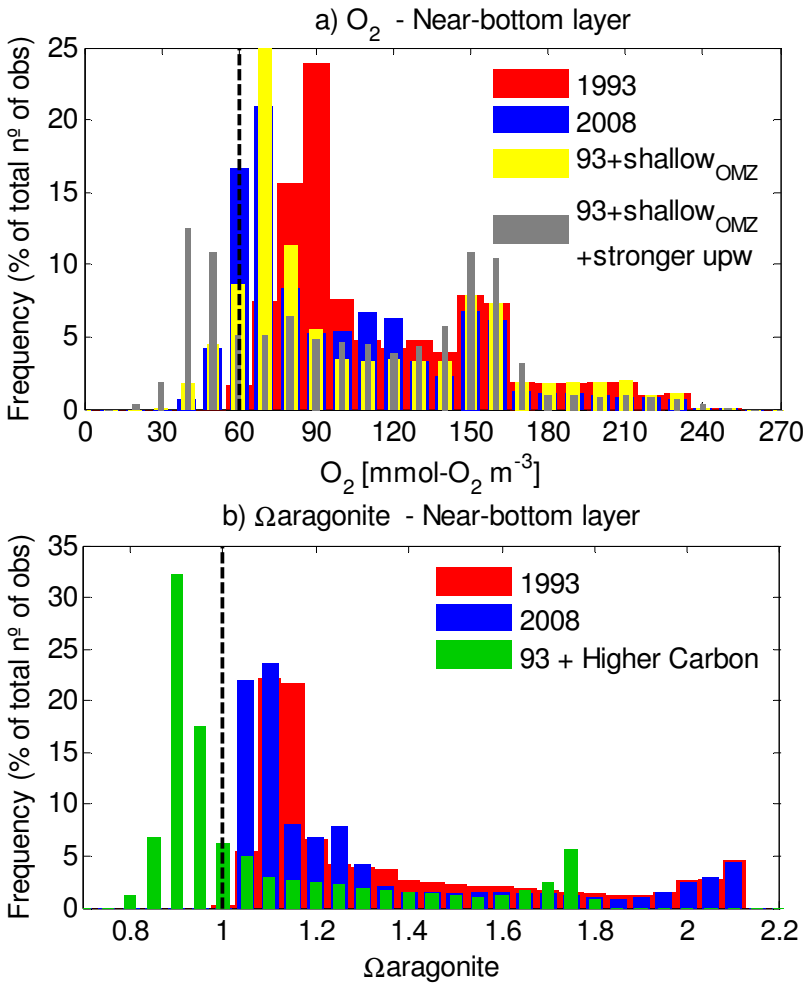

Figure D.3: Histograms of (a) oxygen and (b) saturation state of aragonite in the near-bottom layer of the water column over the shelf. Red and blue bars indicate simulations with forcing from 1993 and 2008, respectively. Panel a also shows the Shallower Oxygen Minimum Zone (OMZ) Experiment (yellow) and the Shallower OMZ + Stronger Upwelling Experiment (dark grey). Green bars in panel b show the Higher Carbon Experiment. Vertical dashed lines indicate the hypoxic threshold (O_2 = 60 mmol-O_2 m^{-3}) and the aragonite dissolution threshold (Ω_A = 1) in panels a and b, respectively.